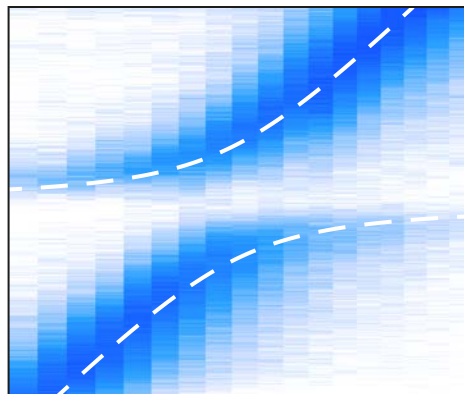# Strong Coupling between Small Atomic Ensembles and an Open Fiber Cavity

Dissertation
zur
Erlangung des Doktorgrades (Dr. rer. nat.)
der
Mathematisch-Naturwissenschaftlichen Fakultät
der
Rheinischen Friedrich-Wilhelms-Universität Bonn

von
Jose C. Gallego Fernández
aus
Murcia, Spanien

Bonn, 2017

Abstract

In this work I present the experimental realization of a versatile platform for the interplay between light and matter at the single-quanta level. In particular, I demonstrate the high cooperativity of small ensembles of rubidium atoms strongly coupled to a state-of-the-art, open fiber-based microcavity, emphasizing the capabilities of the system as an efficient source and storage device for single photons.

The first part of this thesis focusses on the construction and characterization of the microresonator, which is composed of two dielectric mirrors machined on the end-facets of optical glass fibers. Through the implementation of an in-house facility, a large number of fiber-based mirrors are manufactured and precisely characterized. The intrinsic properties of this particular type of resonator are then analyzed and discussed. I present a theoretical model that explains, for the first time, the asymmetry in their reflective line shape and that has important implications for the optimal alignment of fiber-based cavities.

In the following chapter, I introduce the main experimental apparatus, which contains a miniaturized fiber cavity — with small mode volume and a linewidth of $\kappa \approx 2\pi \times 25\,\text{MHz}$ — that is actively stabilized and integrated in a compact assembly. The monolithic structure features several high–numerical aperture (NA) lenses that provide the necessary tools for the trapping, manipulation and high-resolution imaging of atoms inside the resonator. Neutral rubidium atoms are delivered by an optical conveyor belt from the cooling region into the cavity mode, where their deterministic coupling to the resonator is ensured by the tight confinement of a 3D optical lattice. The high linewidth of our open cavity also prevents the manifestation of cavity-heating mechanisms, enabling a constant monitoring of the atom's presence by probing the cavity field without increased trap losses. This atom detection method allows us to perform real-time optical feedback in the transport scheme and to observe the characteristic vacuum Rabi splitting for individual atoms in a non-destructive manner.

The rest of this work focusses on the interplay between atomic and photonic excitations inside the resonator. Due to the small mode volume of the microcavity, coupling strengths up to $g = 2\pi \times 100\,\text{MHz}$ are observed for single atoms, corresponding to light–matter interaction in the strong coupling regime. The system's cooperativity is collectively enhanced more than five times when placing a small atomic ensemble inside the resonator. Such a fast interaction rate — along with the relatively high transmission of the input cavity mirror — provides a rapid, non-destructive readout of the internal hyperfine state of a coupled atom when probing the cavity field. The state-detection method yields fidelities of 99.8 % in 5 ms with less than 1 % population transfer and negligible atom losses.

The last part of the thesis is dedicated to the study of the influence of the cavity on the emission properties of an atom. I show how, despite the small solid angle covered by the cavity mode, the resonator alters the radiation pattern of an externally pumped single atom and increases its emission rate by a factor of 20 due to the process known as cavity back-action. More than 85 % of the emitted photons are collected by the single cavity-mode — as a result of the strong Purcell enhancement — and subsequently channeled out by one of the fiber mirrors. A characterization of the photon statistics of the cavity output shows a clear antibunching dip, confirming that the emission corresponds to a single quantum emitter and that our system can be used as a readily fiber-coupled, efficient single-photon source. The geometry of our fiber-based resonator provides wide optical access that — in combination with the high-NA lenses — allows us to study the free-space emission rate of an atom coupled to the cavity. The various coupling strengths associated to different positions of the atom in the cavity mode lead to a clear visualization of the cavity back-action for all cooperativity regimes.

The high cooperativity, intrinsic fiber coupling and scalability properties of our system make it suitable for the realization of an efficient, high-bandwidth quantum memory and its implementation in quantum networks. Additionally, the ability to couple an ensemble of indistinguishable atoms to the same cavity mode provides a versatile platform for the study of multipartite entangled states.

Parts of this thesis have been published in the following article:

[1] J. Gallego, S. Ghosh, S. K. Alavi, W. Alt, M. Martinez-Dorantes, D. Meschede, L. Ratschbacher, *High-finesse fiber Fabry–Pérot cavities: stabilization and mode matching analysis*, (2016), Appl. Phys. B 122, 47

Contents

Introduction

THREE of the main aspects that set *Homo sapiens* apart from other species on Earth are the development of tools, the ability to communicate, and an abstract ingenuity. Those are believed to be the same factors that, after thousands of years, have shaped the planet into a world dominated by rapidly evolving technology, where fundamental blocks of the universe — like single atoms and photons — are our new tools for the coming era of quantum communication.

The fields of quantum information and communication exploit the unique properties of quantum systems to enhance several aspects of classical information science [2–6]. The widespread implementation of available protocols is subject to the existence of *quantum networks* [7]; namely, a web of quantum nodes — where quantum information is created, processed and/or stored — that are interconnected through fast quantum communication links [8]. Its efficient performance relies on the use of the ideal physical platform for each of the aforementioned tasks. While single photons are the optimum carrier of information in communication links, they represent a poor choice for information processing or storage, which is better performed by neutral atoms [9], ions [10] or solid-state systems [11]. Such a hybrid network requires the use of *interconnection modules* where — by exploiting light–matter interaction — quantum information is transferred from one physical system to another in a reversible way. These interfacing elements also constitute one of the building blocks of quantum repeaters, that allow long-distance distribution of entanglement and quantum information in a network [12–14].

Cavity Quantum Electrodynamics (CQED) provides the ideal setting for the strong coherent interaction between light and matter at the quantum level [15]. By tightly confining and storing light, a cavity or resonator effectively enhances the interaction strength between a photon and a quantum system placed at its core (see Chap. 4). Since its emergence in the 1940s [16], CQED has served as a suitable platform for the investigation of fundamental quantum systems [17]. In recent years, optical CQED with neutral atoms has accomplished many of its envisioned applications as a quantum node: from the realization of basic blocks — quantum memories [18, 19], single photon sources [20] or logic gates [21, 22] — to the implementation of an elementary cavity-based quantum network [23].

Despite the numerous accomplishments, efforts continue in order to realize platforms that fulfill basic requirements such as efficiency, high bandwidth, scalability and robustness. Open cavities, where transmission leakage dominates the intracavity losses (including atomic spontaneous emission), provide the necessary high interaction bandwidths. However, in order to ensure efficient light–matter coupling (i.e. high *cooperativity*), the rate of coherent interaction must be, in general, faster than the leakage (see Sec. 2.1.2 and Chap. 6). Our approach towards a system with both high cooperativity and high bandwidth is to use an open, fiber-based microcavity and to exploit the collective enhancement provided by atomic ensembles [24–26].

Fiber-based Fabry–Pérot Cavities [27] (FFPCs) — which consist of two microscopic concave mirrors machined onto the end facets of optical fibers — are a particularly attractive choice for CQED experiments (see Chap. 2). They offer a small mode volume, high Q factors and wide tunability; additionally, their intrinsic fiber coupling provides convenient access to the intracavity field and facilitates further miniaturization. Their compact size and integrability allows for the realization of robust monolithic designs [1] and make them promising candidates for integration in quantum networks [28]. To date, they have been implemented as photonic interfaces with all kinds of quantum systems including cold atoms [25, 29], ions [30, 31], solid-state emitters [32–34] and optomechanical systems [35].

The microscopic size of the fiber mirrors facilitates wide optical access to the intracavity region, thus allowing the use of versatile optical tools for the control of the coupled atoms (see Chap. 3). Optical lattices [36] are a popular choice for the trapping and localization of neutral atoms, which can be confined in regions on the sub-wavelength scale, thus ensuring a deterministic and constant coupling with the resonator field [37]. Additionally, collections of atoms individually trapped in optical lattices provide a controlled environment for the realization of scalable qubit registers [38] which — when interacting with a common cavity mode — can be exploited for the creation of multipartite entanglement [39] or efficient spin-wave quantum memories [13] (see Chap. 7). With the recent progress in fluorescence imaging, both the internal state [40] and the position [41] of atoms in an ensemble can be detected in a fast and non-destructive way with resolutions beyond the diffraction limit. Such atomic degrees of freedom can be steered with the use of local addressing [42] and optical transport techniques [43, 44], which provide the required logic tools for the initialization and control of the register. Thus, although clouds of cold atoms have been successfully coupled to FFPCs [25, 26], it is of interest to develop systems featuring a more controlled few-body scenario.

In this work I present the realization of strong coupling between a fiber-based microcavity and a small ensemble of (1 to 10) neutral atoms individually confined in a 3D lattice, demonstrating the high cooperativity of the system and its potential use as an efficient quantum memory or single-photon source. Additionally, the implementation of optical tools such as a 2D conveyor belt and an integrated atom-microscope pave the way towards the realization of a well controlled, cavity-coupled qubit register. The detailed structure of the thesis is as follows:

The first half of this work (Chap. 2 and 3) constitutes the technical part, where the development and implementation of the aforementioned tools are described. Chapter 2 contains details on the production and characterization of fiber mirrors, and the properties of the fiber-based resonators built with them [1]. I also present the assembly of a compact system containing a tunable, high-finesse fiber cavity placed at the focal plane of four high-NA lenses, which is the core of the main experimental setup. In Chapter 3 I discuss the confinement and detection of neutral atoms inside the resonator. Atoms are transferred with a conveyor belt from a magneto-optical trap into the cavity mode, where they are tightly confined by a 3D optical lattice. The high-NA lenses are used as an atom-fluorescence microscope, while the cavity reflection provides non-destructive information about the presence of a coupled atom.

Probing the intracavity field is the focus of the two following chapters. In Chapter 4 I show how the spectral properties of the coupled system (in particular the vacuum Rabi splitting) can be observed by weakly pumping the cavity without increasing atom losses. I demonstrate the high cooperativity of our system and how it allows fast, non-destructive detection of the internal atomic state (see Chap. 5).

Finally, in Chapter 6, I explore the influence of the resonator on the emission properties of an externally driven atom. The strong Purcell enhancement of our system allows the cavity to collect most of the atomic radiation, which is then efficiently coupled through one of the fibers and serves as a single-photon source. Furthermore, we will see that the intracavity field imprints a back-action on the local field driving the atom that manifests as an alteration of the total scattering rate, which is severely enhanced.

A Compact Fiber-Cavity System for CQED with Neutral Atoms

B Y confining and storing light, resonators constitute the essence of any cavity QED experiment. The entirety of this chapter is dedicated to the development and characterization of the cavity employed in the experiments presented in this thesis. In order to achieve strong coupling between the cavity photons and optically trapped rubidium atoms, we make use of a fiber-based microcavity consisting of two high-reflectivity mirrors created on the end facets of optical fibers. This type of Fabry–Pérot resonator (introduced in Sec. 2.1) provides micrometric mode volumes and direct fiber coupling to and from the intracavity field. The laser-machining required for the production of such micromirrors is performed at an in-house facility, allowing the manufacturing of a large number of optical-fiber mirrors that meet the requirements of our planned CQED experiments (see Sec. 2.2). This type of resonator exhibits peculiar effects due to the particular laser-polishing technique and the intrinsic fiber coupling. These are investigated in Section 2.3, where relevant mechanisms such as clipping losses and polarization-mode splitting are discussed, including a theoretical model (and its experimental confirmation) that explains the observed asymmetry in the reflective line shape and has important implications for the optimal alignment of the cavity fiber mirrors. Section 2.4 is dedicated to the design, assembly and characterization of a vacuum-compatible compact system that hosts a miniaturized high-finesse resonator and a set of four high-numerical aperture lenses, all integrated in a robust structure. The system, which has been implemented in our main CQED experimental apparatus, provides an active piezo-mechanical stabilization of the fiber cavity and the optical tools and access necessary for the cooling and trapping of neutral atoms inside the resonator. This is facilitated by the integrated lenses, which are also used as an atom microscope (see Chap. 3).

2.1 Optical Fabry–Pérot Microcavities

Devices based on optical microcavities (that confine light to small volumes) are already indispensable for a wide range of applications [45]. In recent years they have become powerful tools for enhancing the interaction between light and matter, which sits at the heart of cavity QED. Amongst the geometries of optical microcavities that are currently investigated, Fabry–Pérot (FP) cavities (described in Section 2.1.1) are particularly attractive for CQED experiments. By confining light with the use of two opposing movable mirrors, they offer ample tunability of the resonator's properties and the possibility to place the quantum system under investigation directly in the region of highest field confinement. Additionally, the high quality dielectric coatings available [46] provide these cavities with Q factors unfeasible in other resonator

types. The paradigm of microscopic FP resonators are fiber-based Fabry–Pérot cavities (FFPCs) [27], which consist of two microscopic concave mirrors machined onto the end facets of optical fibers. Some of the advantages, which are discussed in Section 2.1.2, are small mode volumes with high Q factors, scalability and the convenient access to the intracavity field by its intrinsic fiber coupling. This type of cavity is, thus, a suitable candidate for the implementation of CQED platforms on the microscopic scale for strong coupling with neutral atoms [25].

2.1.1 The Basics of Fabry–Pérot Resonators

To provide a basic understanding of some of the concepts used throughout this thesis, it is necessary to introduce the working principle and basic properties of Fabry–Pérot resonators. The derivations of the results summarized here are well established and can be found in standard textbooks (e.g. [47]).

Spectral properties: the cavity resonance.   An optical FP interferometer (or resonator) consists of a pair of high-reflectivity mirrors facing each other (M_1 and M_2), such that an input light field $\mathcal{E}_{\text{in}}$ injected in the resonator will be reflected back and forth a considerable amount of times (see Fig. 2.1(a)). If the frequency of the input field ($\omega = ck$) fulfills certain conditions, the multiple reflections will interfere constructively leading to an enhancement of the field circulating inside the cavity $\mathcal{E}_{\text{circ}}$ which manifests in the resonator's transmission spectrum as an infinite collection of equidistant longitudinal modes.

In this section we focus in the spectral properties of the system's steady-state solution, therefore do not consider spatial or temporal dependance of the fields. Furthermore, the mirrors' geometry is ignored, and each one is characterized solely by its reflectivity (r_i), transmission (t_i) and losses (l_i) coefficients, and the corresponding amplitudes ($\mathcal{R}_i = |r_i|^2 = 1 - \mathcal{T}_i - \mathcal{L}_i$). We follow the notation from [47] and assume that a phase shift is gained upon transmission (and not reflection), such that the input field injected through mirror M_1 inside the cavity is $i \cdot t_1 \mathcal{E}_{\text{in}}$. The field's amplitude is then reduced upon reflection from both mirrors and — after a full roundtrip inside the cavity with length L_{cav} — a phase shift $\phi = k \cdot 2 L_{\text{cav}}$ is acquired. The steady state of the circulating field is then given by the interference of all consecutive reflections:

$$\mathcal{E}_{\text{circ}} = \mathcal{E}_{\text{in}} \left(i t_1 + r_1 r_2 e^{i\phi} + (r_1 r_2 e^{i\phi})^2 + \ldots \right) = \mathcal{E}_{\text{in}} \frac{i \sqrt{\mathcal{T}_1}}{1 - \sqrt{1 - \mathcal{T}_1 - \mathcal{L}_1} \sqrt{1 - \mathcal{T}_2 - \mathcal{L}_2} \, e^{i\phi}} \, ,$$

which reaches a maximum for every frequency leading to a phase shift multiple of 2π. The resonance condition can be expressed in terms of the lights frequency $\nu = n \cdot 2 L_{\text{cav}} / c = n \cdot \Delta\nu_{\text{FSR}}$, where n is an integer and $\Delta\nu_{\text{FSR}}$ is the so-called Free Spectral Range (FSR) of the resonator. The resulting comb-like spectrum of the intracavity power, shown in Figure 2.1(b), can be expressed as

$$P_{\text{circ}} = P_{\text{in}} \mathcal{T}_1 \frac{\mathcal{F}^2}{\pi^2} \frac{1}{1 + 4 \frac{\mathcal{F}^2}{\pi^2} \sin^2 \left(2\pi \frac{\nu}{2\Delta\nu_{\text{FSR}}} \right)} \, , \tag{2.1}$$

where we assumed $\mathcal{T}, \mathcal{L} \ll 1$ and $\mathcal{L}_1 = \mathcal{L}_2$. The factor $\mathcal{F} = 2\pi / (\mathcal{T}_1 + \mathcal{T}_2 + 2\mathcal{L})$ is known as the finesse of the cavity: a measure of the optical quality of the mirrors and one of the critical figures of merit in the atom–cavity interplay of CQED systems (see Sec. 2.1.2).

Equation (2.1) shows that, on resonance, the injected power $\mathcal{T}_1 \cdot P_{\text{in}}$ is enhanced by a factor of $\mathcal{F}^2 / \pi^2$ due to the resonant interference inside the cavity. The high-power peaks, separated by the FSR, can be described by independent Lorentzian curves displaying a Full-Width Half-Maximum (FWHM) given by $\Delta\nu_{\text{FWHM}} = \Delta\nu_{\text{FSR}} / \mathcal{F}$. This relation constitutes a more experimentally-accessible definition of the finesse,
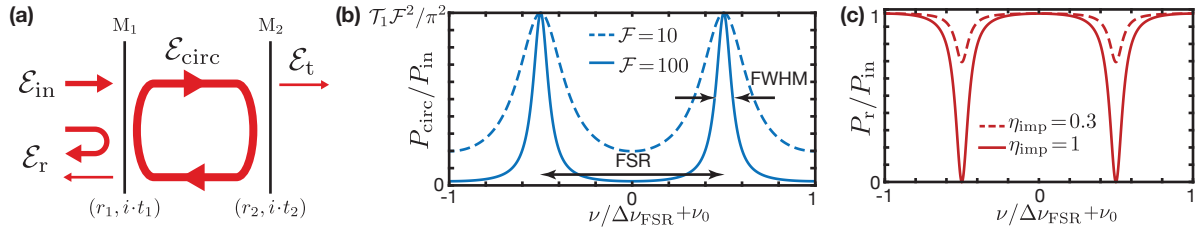
Figure 2.1: Fabry–Pérot (FP) resonator spectrum. **(a)** Simplified diagram of the components of the electric fields involved in a FP interferometer (see discussion in text). **(b)** Normalized intracavity power spectrum showing two consecutive resonance peaks for low (dashed line) and medium (solid line) finesse values. The higher the finesse the thinner are the spectral features and the better is its extinction as an optical filter. **(c)** Normalized reflected power of an impedance-matched (solid line) and a non-matched (dashed line) resonator.

and it is the one used to characterize the optical quality of our cavities in Section 2.3.

The resonator's spectrum can be probed by the fraction of circulating power that gets transmitted through the mirrors at each roundtrip. While the transmission through M_2 is just $\mathcal{T}_2 \cdot P_{\text{circ}}$, the leakage out of the input mirror interferes with the direct reflection of the pumping field (see Fig. 2.1(a)), such that

$$\mathcal{E}_{\text{r}} = r_1 \mathcal{E}_{\text{in}} + it_1 \mathcal{E}_{\text{circ}} \, r_2 e^{i\phi} \approx \mathcal{E}_{\text{in}} \left(1 - \frac{\mathcal{T}_1 e^{i\phi}}{1 - \sqrt{1 - \mathcal{T}_1 - \mathcal{L}_1} \, \sqrt{1 - \mathcal{T}_2 - \mathcal{L}_2} \, e^{i\phi}} \right). \tag{2.2}$$

The reflective spectrum of the cavity is, thus, a similar collection of equidistant features in the form of Lorentzian dips that, on resonance, reach a minimum power

$$P_{\text{r,min}} = P_{\text{in}} \left(1 - \left(\frac{\mathcal{T}_1 - \mathcal{T}_2 + 2\mathcal{L}}{\mathcal{T}_1 + \mathcal{T}_2 + 2\mathcal{L}} \right)^2 \right). \tag{2.3}$$

The particular case when the input transmission $\mathcal{T}_1$ exactly matches the rest of cavity losses ($\mathcal{T}_2 + 2\mathcal{L}$) causes a total destructive interference between both fields in Equation (2.2) and, therefore, results in no reflected power on resonance (see Fig. 2.1(c)). This type of resonator is said to be impedance-matched, due to its equivalence with resonant circuits. For that reason, the factor in brackets of Equation (2.3) is called the impedance-matching efficiency η_{imp}: when it is smaller than unity, the resonator is said to be over-(under-) coupled if $\mathcal{T}_1$ is higher (lower) than the rest of mirror losses. A detailed comparison of the reflective interference problem in standard and fiber-based resonators is presented in Section 2.3.2.

Spatial distribution: the fundamental cavity mode.   The steady-state intensity profile of the circulating intracavity field (also known as *transversal cavity mode*[1]) depends on the geometry of the mirrors. Most resonator types are composed of concave spherical mirrors (with radii of curvature R_i); this configuration yields stable and well defined families of cavity modes which, up to first order, are fully determined by the mirror's curvature and separation. The transversal modes can be described by TEM$_{nm}$ optical waves, the most fundamental of which is the Gaussian (TEM$_{00}$) mode. The Gaussian cavity mode, which is the one presented below, displays the smallest spot size and therefore gives rise to tight cavity mode volumes and reduced losses due to light clipping on finite-size mirrors. As a result of the interference between reflections, the intensity profile is a standing-wave with a spatial distribution

---

[1] In the rest of this thesis, I refer to the fundamental transversal-mode of the cavity simply as *cavity mode*.
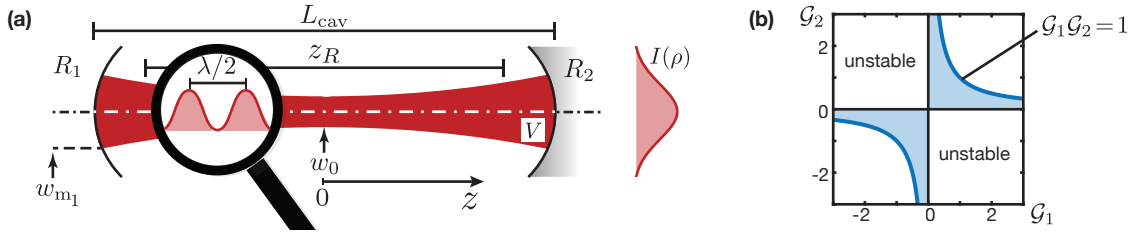
Figure 2.2: **(a)** Geometry of the fundamental TEM$_{00}$ cavity mode. The radius of the Gaussian intensity profile diverges from the waist w_0 and reaches a value w_m at the position of the mirrors. A standing-wave is formed due to the interference between counter-propagating circulating fields. **(b)** Stability diagram of an FP resonator. The colored region represents cavity geometries that allow the hosting of a stable mode.

given by

$$I(x, y, z) = I_0 \frac{w_0}{w(z)} \exp\left(-2\frac{x^2 + y^2}{w(z)^2}\right) \sin^2(kz), \qquad (2.4)$$

where w_0 is the mode's waist. The beam radius diverges along the cavity axis (z) following the expression $w^2(z) = w_0^2(1 + z^2/z_R^2)$ with the characteristic Rayleigh length $z_R = \pi w_0^2/\lambda$, as shown in Fig. 2.2(a).

For a given frequency, the only degree of freedom in the Gaussian profile of Equation (2.4) is the waist w_0. This parameter is fixed by the boundary conditions of the cavity geometry, namely: the radius of curvature of the light's wavefront at the position of mirror M$_i$ must be R_i, such that the mode remains unaltered upon reflection. The requirement can be expressed as [47]

$$w_0^2 = \frac{L_{cav}\lambda}{\pi} \sqrt{\frac{\mathcal{G}_1\mathcal{G}_2(1 - \mathcal{G}_1\mathcal{G}_2)}{(\mathcal{G}_1 + \mathcal{G}_2 - 2\mathcal{G}_1\mathcal{G}_2)^2}} . \qquad (2.5)$$

We have introduced the *resonator g parameters* $\mathcal{G}_i = 1 - L_{cav}/R_i$, which help defining the so-called stability region[2] of the cavity $0 \leq \mathcal{G}_1\mathcal{G}_2 \leq 1$ (plotted in Fig. 2.2(b)) that contains all stable resonator configurations.

The resonator mode presents a spot size at the position of mirror M$_1$ given by

$$w_{m_1}^2 = \frac{L_{cav}\lambda}{\pi} \sqrt{\frac{\mathcal{G}_2}{\mathcal{G}_1(1 - \mathcal{G}_1\mathcal{G}_2)}} . \qquad (2.6)$$

If w_m is comparable to the mirror's size, clipping and diffraction losses may appear after each reflection leading to a decrease in the system's finesse (see Sec. 2.3.1). In order to exclusively excite the fundamental Gaussian mode, the profile of the external field injected into the cavity must be the same as the cavity mode, which is typically achieved with mode-matching optics. However, the small values of w_m present in microresonators are experimentally challenging and, typically, the injected mode differs from that of the cavity. The corresponding mode-matching efficiency ϵ_{in} — given by the overlap of both modes — reduces the resonance incoupling, leading to a reflection on resonance of $P_{r,min} = P_{in}\eta_{imp}\epsilon_{in}$. The mode-matching problem is of particular relevance in the case of fiber-based resonator, where the injected mode is fixed and given by the fiber-core output. A detailed discussion is provided in Section 2.3.2 and Appendix B.

The resonators studied in this thesis provide similar values for both w_0 and w_m (~5 µm), as the Rayleigh length is on the order of the mirrors' separation. This allows us to approximate the volume covered by

---

[2] Points outside stability region give rise to unphysical waist values.

the cavity mode as

$$V = \frac{\pi}{4} w_0^2 L_{\text{cav}} \tag{2.7}$$

As we review in the coming section, the cavity mode volume is a decisive parameter that directly affects the atom-light coherent exchange rate.

2.1.2 Designing an Optical Microresonator for CQED with Neutral Atoms

The confinement of light by its recirculation inside a resonator increases the interaction rate between the intracavity photons and a resonant quantum emitter (e.g. a neutral atom) placed at its center. Furthermore, by employing mirror geometries that lead to fundamental modes with low waist, a bigger overlap of the intensity profile and the atomic cross section ($\sim \lambda^2$) is obtained. As a consequence, the coherent energy-exchange rate g between an atom and a cavity-mode photon — which is proportional to the cavity field amplitude — is inversely proportional to both waist and resonator length, such that $g \propto V^{-1/2}$.

The coupling to the environment leads to irreversible loss of information: an excited atom will spontaneously decay (with a decay rate 2γ) emitting the radiation energy in modes other than the resonator mode; additionally, the finite finesse of the cavity leads to the eventual loss of the cavity photons, which is determined by the cavity field decay rate $\kappa = \Delta\nu_{\text{FWHM}}/2$. The competition between coherent atom–cavity dynamics and incoherent decay processes is captured in the *cooperativity* of the system $C = g^2/(2\kappa\gamma)$ (see Chapter 4.1). This factor represents a crucial figure of merit for the performance of CQED systems in several scenarios. Amongst other, it describes the strength of the Purcell effect (see Chap. 6), the efficiency of an important class of cavity-based single-photon sources [48] and the fidelity of dissipative entanglement protocols [49] (see also Chapter 7). It is therefore a decisive parameter in the process of designing a resonator.

In terms of cavity properties the cooperativity scales as $C \propto \mathcal{F}/w_0^2$, meaning that ultra-high finesse and microscopic mode volumes are in general preferable. Nevertheless, applications of cavities as quantum information nodes (or single photon sources) typically require high communication rates that can only be achieved if the transmission leakage out of the cavity is fast enough. Additionally, "impedance matching" between the linewidth of the cavity and the emitter [50, 51] is necessary when exploiting the enhanced light-matter interaction to perform highly efficient photon storage [13] (see Chap. 7). Both scenarios require *open cavities* with transmission (and therefore κ) values above those of the ultra-high finesse regime ($\mathcal{F} > 10^5$). A reduction of the cavity mode volume is then the only option. According to Equation (2.5), for a fixed resonator length, the volume decreases with the mirrors' Radius Of Curvature (ROC). Standard mechanical-polishing techniques can only provide macroscopic radii (~1 cm) when high finesse values are required [52]. As shown in the next section, the use of laser ablation [53] yields concave structures with ROCs in the micrometer regime and surface roughness comparable to that of superpolished mirrors, offering the possibility to reduce the cavity waist by one order of magnitude [27].

A shorter mirror separation would permit smaller mode waists; however, in most CQED experiments, external optical access to the coupling region is a valuable tool that can be exploited for tight trapping and high-resolution imaging of neutral atoms coupled to the resonator (see Chap. 3). Standard cavity mirrors composed of bulky macroscopic substrates obstruct a considerable fraction of the radial access even when tapered (see Figure 2.3(a)), which becomes relevant at short cavity lengths. The accessibility to the region of interest can be extended by using low cross-section glass surfaces like those offered by optical fibers. Additionally, by using the end facets of single-mode fibers as the mirror substrate, high incoupling mode-matching efficiencies are possible even for cavity-mode waists of a few microns. The intrinsic fiber coupling of the output is of further relevance considering that fiber-optic cables are the ideal candidate for quantum information communication [54]. Combined with the lack of external
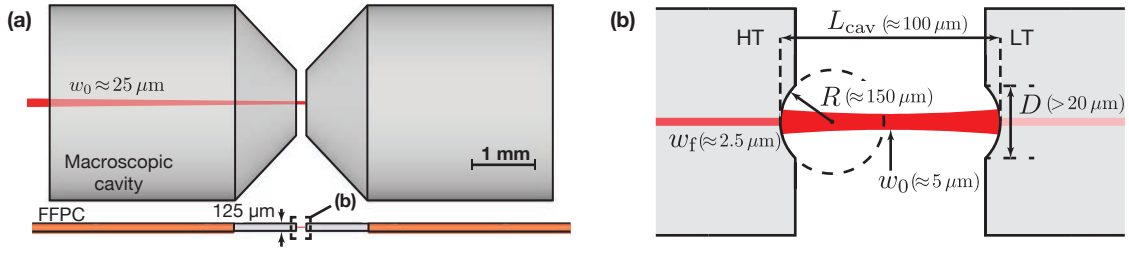
Figure 2.3: Fiber-based Fabry–Pérot Cavities (FFPCs). **(a)** Drawing to scale comparing standard macroscopic cavities (top) with fiber-based resonators (bottom). The latter provide a smaller waist, more optical access, intrinsic miniaturization and direct fiber coupling of the input/output without the need of external mode-matching optics. **(b)** Summary of the typical characteristics and requirements for our FFPC (not drawn to scale). HT: High Transmission mirror, LT: Low Transmission mirror.

mode-matching optics, the fiber coupling enhances the miniaturization and scalability options of the cavity system (see Section 2.4). By coating the fiber end facets such that one of the mirrors displays a much higher power transmission than the other, the directionality of the cavity communication is focussed onto the high transmission mirrors, which serves as an efficient input/output channel.

In summary, in order to obtain a resonator that can provide high-cooperativity light–matter interaction, wide optical access and stable high incoupling efficiencies, the following specifications are required:

- The cavity length must be long enough to provide optical access in the radial directions with an accessible solid angle comparable to that of the lenses employed for fluorescence collection (NA=0.5, see Sec. 2.4.1). This requirement translates into lengths larger than $75\,\mu m$.

- For a fixed length, smaller ROCs lead to bigger spot sizes at the mirror: this decreases the incoupling mode matching (as the fiber mode is fixed) and requires higher mirror diameter (D) to avoid clipping losses. Since R and D are not independent due to the particular mirror machining technique (see next section), it is desirable to create ROCs bigger than $100\,\mu m$. Furthermore it is convenient to stay away from the unstable region of confocal resonators ($R = L_{cav}$), which leads to a target range of $150-200\,\mu m$.

- The diameter of the mirrors must be large enough ($> 4w_0$) to avoid any diffraction/clipping losses of the cavity mode. For typical waist values, this corresponds to $D > 20\,\mu m$.

- One of the two fiber mirrors should fashion a coating with a transmission coefficient much higher than the rest of the losses (which must be minimized to the maximum).

2.2 Production of Microscopic Mirrors through Laser Ablation

The small-radii structures required to achieve ultra-small mode volumes are not within the reach of traditional polishing techniques. Within the last ten years, several methods have emerged capable of achieving such micrometric depressions with reasonable surface quality, the two most successful being surface etching and laser ablation. Wet or ion-based etching of silica substrates has proven to be a useful tool for the scalable production of micrometric spherical depressions suitable for cavity QED [55]. The techniques have been perfected to provide surface roughness on the nanometer scale [56], and radii of curvature below $5\,\mu m$, when combined with laser polishing methods [57]. Nonetheless,

their implementation has only been realized on macroscopic substrates so far, which lack the intrinsic mode-matching capabilities of optical fibers[3].

In contrast, ablation of glass surfaces with CO_2-lasers allows one to carve concave structures directly onto the end facet of optical fibers [27, 53, 59]. This technique is, in general, more versatile and requires less specialized equipment. The low roughness surfaces obtained are comparable to those of superpolished mirrors, making possible the construction of fiber-based cavities with high-finesse (10^5) in the infrared domain [27, 60]. Recent developments in ablation and fiber technologies have provided advances and diversification of all types of microstructures: from the machining of reduced fiber-tip diameters for micrometer-scale cavity lengths [61] to the creation of fiber-resonators in the millimeter range [62, 63], including mode-matching optimization techniques with the use of grin lenses [64].

In this section we present the technical details of our in-house fiber-mirror production facility, based on the concept introduced in references [53, 59]. Keeping in mind the requirements discussed in the previous section, a set of more than a hundred concave micro-structures with ROC between 150 and 200 μm are produced. After applying a high-reflectivity dielectric coating, the resulting fiber-based mirrors can be used to build high-finesse, low-mode-volume resonators.

2.2.1 Carving with Laser Light

Fused silica (SiO_2) displays an absorption peak for wavelengths in the range of 9–11 μm [65]. As a consequence, light from a CO_2-laser (10.6 μm) is efficiently transformed into heat and leads to the melting of the illuminated region where absorption takes place. Local surface tension causes a smoothening of the glass previous to the solidification that provides a typical roughness of 1–2 Å [53, 59, 66], therefore making CO_2-lasers a natural choice for local, controlled polishing of glass surfaces. For temperatures above ~3 000 K (where the depth of the molten layer is reduced to ~1 μm [67]), the evaporation of the material becomes a dominant effect (referred to as *ablation*) and causes a modification of the surface that can be exploited for the formation of microstructures. The basic phenomenological description is that by using a laser beam with a Gaussian intensity profile, we create a temperature distribution on the glass surface that leads to an evaporation pattern with a similar profile. The resulting Gaussian depression offers a spherical smooth surface at the bottom of the structure, which can then be used as a spherical micromirror.

Due to the particular heat dissipation properties of the fiber-surface geometry, and the large amount of conduction channels present in the process, it is challenging to provide a simple analytical model that predicts the ablation results in all scenarios. In this section we focus on the experimental techniques and particular settings that provide us with the required mirror characteristics; a more comprehensive study of the ablation process for a wide scan of the laser's parameters can be found in references [53, 66, 68].

In general, the temperature of the surface depends exponentially on both the power and size of the beam. Therefore, a reasonable control over the laser parameters is necessary in order to obtain consistent results. Although the temperature profile is less sensitive to the exposure time, longer ablation periods lead to a thicker melted layer [67]. The low viscosity layer is modified by surface tensions and manifests as surface-minimizing convex structures around the Gaussian profile, which become more prominent for bigger exposed regions. Further control is required to provide deterministic positioning of the target surface, which is critical when using optical fibers where the laser beam's size is comparable to the fiber end facet.

---

[3] Although this can be solved by using a flat optical fiber as the input mirror [26, 58], the geometry is restricted to semi-planar resonators where the cavity-mode waist sits at the mirror surface.
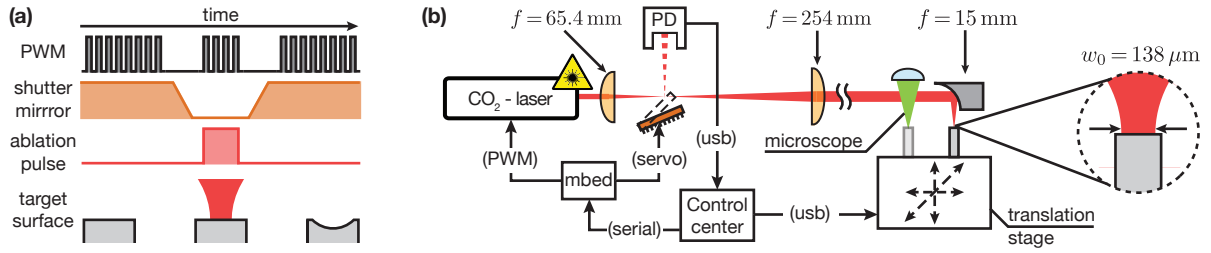
Figure 2.4: CO_2-laser setup. **(a)** Temporal sequence of the laser driving (black), the shutter mirror (orange) and the laser power reaching the target (red) during a single ablation pulse. The PWM driving frequency is 10 kHz and the typical pulse length is 3 ms (not to scale). The buffer time for shutter opening/closing is usually 0.5 s. **(b)** Layout of the main optical and electronic components. The laser output is modified by the two lenses and focussed on the target by a parabolic mirror. The surface is mounted on a 3D stage that can transfer it to the optical inspection zone (green, details in Fig. 2.5(a)). The shutter mirror is placed at the focus of the telescope to make the switching time faster. When closed, it sends the laser beam towards the photodiode (PD). A centralized control center monitors and automatizes the process.

CO_2-Laser Setup

We employ a water-cooled CO_2-laser[4] with a maximum output power of 44 W at 10.6 μm. The laser is driven via a pulse-width modulated signal (PWM) that allows us to control the laser power by modifying the signal's duty cycle [69]. To prevent oscillations in the output power[5] from affecting the reproducibility of the procedure, we monitor the laser output with a thermal photodiode[6] and perform the ablation process only when the power reaches the required value. The constant monitoring is done by deflecting the laser beam with a copper mirror on a motorized mount. When the system is ready to perform the surface machining, the mirror is removed and the laser light is sent to the target according to the time sequence depicted in Figure 2.4(a).

The diameter of the laser beam — which is (2.5 ± 0.5) mm at the output — is modified by an optical setup consisting of two convex lenses and a parabolic mirror (see Fig. 2.4(b)). The ZnSe lenses[7] are placed in a telescope configuration that expands the beam size. This system, combined with the parabolic metallic mirror[8], provides the necessary degrees of freedom to control the final beam waist. In general, we find that for our radius of curvature and diameter requirements it is convenient to use a beam waist that can fully cover the extent of the fiber tip. We place the lenses at the required distance to provide a final beam waist[9] of (138 ± 4) μm. The relative position between the laser focus and the glass surface is controlled by a high-precision three-dimensional translation stage[10] on which the target is mounted. The stage provides positioning with minimum step size of 0.1 μm and sub-micrometer reproducibility in the three directions. The large available travel range of 25 mm facilitates the transfer of the target surface

---

[4] Firestar v30 CO_2-laser: *FSV30SWE* (Synrad, Inc).

[5] For typical output powers of 20 W, we observe intensity fluctuations of ±5 % within a one-minute period (attributed to thermal oscillations). The laser is expected to show power fluctuations on a much shorter time scale [68], but any derived detrimental effect is avoided by performing multiple short ablation processes on the same target (more details in following paragraphs).

[6] Thermal Power Sensor 10 W: *S310C* (Thorlabs, Inc).

[7] Zinc selenite lenses. $f = 2''$: *104370* and $f = 10''$: *236670* (II-VI Infrared Inc).

[8] 90° Off-Axis Parabolic Mirror, Prot. Silver ($f = 15$ mm): *MPD127075-90-P01* (Thorlabs Inc).

[9] The measurement was performed using the razor-blade technique. We integrate the power of the beam when is being blocked by a moving blade. The behavior provides information to reconstruct the spot size at different positions, from which we can extract the waist.

[10] Miniature linear stage with DC motor (×3): *MFA-CC* (Newport Corporation).
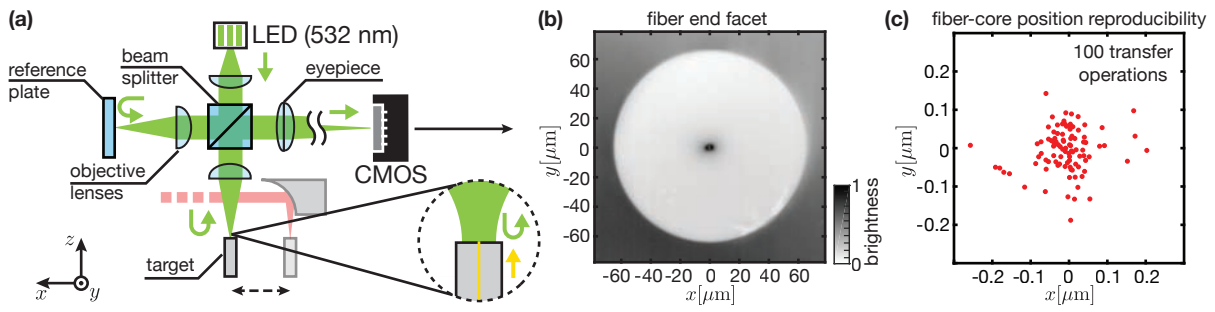
Figure 2.5: Optical inspection setup. **(a)** Layout of the main optical components of the Michelson interferometer microscope. The light from the power LED is split into the two arms: reference and target. Their reflection is focussed onto a camera where their interference emerges as brightness fringes (see next section). In order to locate the fiber-core, we illuminate the other end of the fibers with white light (yellow in the illustration). **(b)** Example of the image (with the reference path blocked) of a cleaved optical SM fiber and the back-illuminated core (brightness inverted for clarity). By fitting a Gaussian to the core brightness we can track its position with sub-micrometer position. **(c)** Position of the fiber core after each of the 100 trips between the microscope focal plane and the CO_2-laser beam. During the procedure the stages display a 2D-reproducibility with an RMS below $0.08\,\mu m$.

from the laser beam to the focal plane of a homemade inspection microscope (part of an interferometric surface reconstruction setup). The control and automation of the entire system is centralized by a computer program, although part of the tasks are performed by an mbed microcontroller[11] [69].

Inspection Microscope

The optical inspection of the target fiber or substrate ensures the correct preparation and alignment of the surface and, more importantly, allows the characterization of the ablation process. In our production facility we employ a self-made, high-resolution microscope (depicted in Figure 2.5(a)) to illuminate the target and project its magnified image onto a CMOS camera[12]. The light source is the collimated output of a green LED[13], which is focussed onto the surface by the microscope's objective. Its high NA of 0.5 along with a long-distance effective focal length of 25 mm, provide a depth of field on the order of ~4 μm. The short depth allows us to locate the axial target position with high precision, while still being big enough to resolve the entirety of the concave structures we aim to create on the fibers. The reflected light, collected by the objective, is separated from the incoming beam by a non-polarizing 50 : 50 beam-splitter and subsequently focussed by an achromatic doublet lens ($f = 500\,mm$) onto the camera. The optical magnification factor of 20 and the size of the sensor's pixels provide a final resolution of $0.26\,\mu m\,pixel^{-1}$.

Figure 2.5(b) shows the microscope image of the end facet of an SM fiber and its core (bright spot at the center of the image) which is imaged by coupling white light into the opposite end of fiber. By fitting a Gaussian to the core's intensity profile we obtain its position with sub-micrometer precision, which can be used to characterize the reproducibility of the translation stages. Their reliability is of critical importance, since they are responsible for transferring the target surface from the microscope's focal plane to the exact location of the CO_2-laser beam waist. When displacing an optical fiber from the imaging plane to the ablation region and back, the fiber-core's final position deviates by less than

---

[11] Microcontroller development board: *mbed NXP LPC1768* (ARM Ltd).
[12] Monochromatic CMOS camera (1280 × 1024): *DCC1545M* (Thorlabs Inc).
[13] Green (530 nm) High-Power LED on Metal Core PCB, 1 000 mA): *M530D1* (Thorlabs Inc).
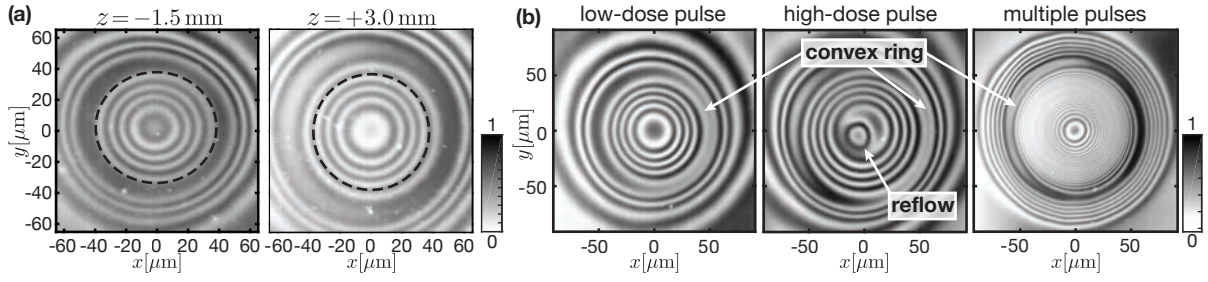
Figure 2.6: Calibration of the ablation procedure. **(a)** Interferogram image of a laser-machined concave structure where the concentric fringes show the rotationally-symmetric height change. The target glass plate is placed at two different points along the CO_2-laser beam axis (z-direction). The ellipticity of 8 % present 1.5 mm before the focus (left) vanishes if we place the glass 3 mm ($0.55\,z_R$) after the focus (right). Pulse parameters: 10 ms at 6.7 W and 14.5 W respectively. **(b)** Interferogram image of three structures created under different pulse configurations (all showing a convex ring due to the pulse length). Left: Low–energy dose pulse (5 ms at 14.5 W). Center: High–energy dose pulse (4 ms at 19 W). The energy deposited is enough to create reflow effects that manifest as a peak at the bottom of the structure. Right: train of 25 low-dose pulses (4 ms at 13.4 W). We obtain steeper features (higher fringe density) without reflow effects.

0.08 μm from the original (see Fig. 2.5(c)), given that the translation motor has enough time to cool down between consecutive trips).

For the precise characterization of the machined structures we install an equivalent objective lens on the free output port of the beam-splitter. By placing a glass plate at its focus, the imaging setup becomes a Michelson interferometer. The reflection from both the target surface and the reference plate (assumed to be perfectly flat) interfere and give rise to fringes in the image brightness. These patterns provide a full surface reconstruction with depth resolutions on the sub-wavelength scale as we show in Section 2.2.2.

Target Preparation and Ablation Procedure

Prior to the ablation of optical fibers, we utilize borosilicate glass plates to perform a coarse calibration of the laser pulse parameters and the location of its focus. The exact axial location of the laser waist can be found by performing several ablations on a glass plate placed at different positions along the beam (z-direction). We find that the beam has a certain ellipticity near its focus — probably due to astigmatism of the beam — which disappears when we displace the target's z-position by 3 mm (see Fig. 2.6(a)). This displaced position is employed in the rest of the procedures.

For pulses of 5 ms or longer, we observe a consistent convex ring around the Gaussian formations machined on the glass plates that is attributed to the surface tension effects discussed in the introduction. When increasing the power of the pulse (in order to reduce the thickness of the absorption region) a similar type of convex profile emerges from the center of the concave depression[14]. This undesired *reflow* effect prevents us from obtaining steeper structures which, typically, are only accessible by increasing the laser power. Therefore, to achieve a small ROC and bigger diameters in the concave depressions we need a more flexible approach that is not limited by the aforementioned process. To that end, we substitute the single ablation procedure by a train of consecutive pulses with smaller energy dose (leaving a cool-down period of 0.5 s in between pulses). Both scenarios are compared in Figure 2.6(b) (the remaining convex

---

[14] Although it seems to be a reflow effect, where the melted material accumulates at the center, it is still not clear why it appears for higher powers. Reflow and general surface-tension effects occur during long exposure times, and are typically reduced by increasing the beam power [53].
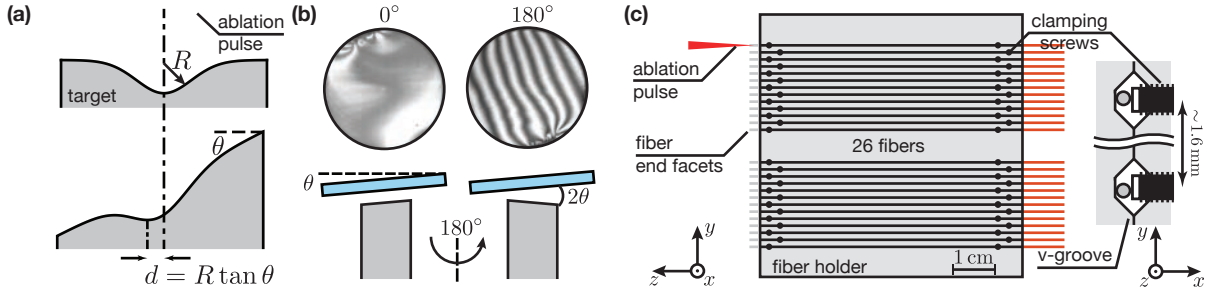
Figure 2.7: Reducing mirror decentration. **(a)** Gaussian profile projected on a flat surface with a tilt of 0° (top) and 3° (bottom). Vertical scale expanded for better clarity. In the second case a decentration (d) appears between the minimum of the profile and the original center. **(b)** Interferogram images of a cleaved fiber aligned to the reference plate (left) and then rotated by 180° around its axis (right). The number of appearing fringes yields and inclination of $\theta \approx 0.5°$ (using the rule of thumb: $\theta = 0.06° \times$ fringes). **(c)** Technical drawing of the side view of the fiber holder. The plate, mounted on the translation stage, can hold up to 26 fibers that are clamped at the two ends by screws (protected with a piece of teflon). Left: close up of the front view showing the position of the fibers in the V-grooves and the clamping method.

ring is finally prevented by using shorter pulses).

Once a coarse parameter-scan is realized on glass plates, the fine adjustment of the pulse characteristics must be performed with optical fibers in order to account for their particular heat dissipation properties. The fibers employed in our setup are copper-coated single-mode (SM) and multi-mode (MM) fibers[15]. The metallic coating — which provides better mechanical stability and is vacuum compatible — can be removed by placing the fiber in an iron(III) chloride solution for 15 min. Subsequently, we use a fiber cleaver[16] to obtain a clean and flat fiber end facet. The fibers are then placed in groups of 26 inside a custom-made fiber-holder [70] mounted onto the translational stage, where each fiber can be independently machined. We find that by using a train of 45 pulses of 3 ms each (and 20 W of power) we can produce fiber mirrors with radii of curvature in the range of 150 to 200 μm (see next section).

Misalignments between the SM-fiber core and the center of the laser-machined depression become critical when using the fiber mirrors to form a cavity. As we shall see in Section 2.3.2, the amount of light that can be pumped from the fiber core into the cavity decays exponentially with the displacement between both modes. In fact, for our typical resonators, a decentration of 2.5 μm would lead to a reduction of 50 % in the mode-matching efficiency[17]. Due to the high reproducibility of the translation stages, the origin of any distribution of decentration values is attributed to an inclination in the target's surface. As shown in the simplified case of Figure 2.7(a), if the glass surface is tilted, the bottom of the depression is displaced from the axis of the Gaussian beam (which is overlapped with the fiber core). For a typical ROC of 170 μm, a small angle of 1° will already cause a decentration of $d = 3$ μm. It is therefore necessary to reduce the uncertainty of the surface's relative angle as much as possible.

An inclination of the glass surface can be caused by either a tilt of the fiber itself, or a slanted cleaved end facet. Although the fiber cleaver is specified to provide a cutting angle below 0.5°, we have observed that in most of the cases this angle is actually bigger than 1°. The measurement of the end facet inclination is performed by rotating the fiber around its axis[18] and observing the evolution of the surface's tilt on the interferogram images. If the reference plate of the interferometer is aligned parallel to the initial fiber

---

[15] Cu-coated optical fibers. Ge-doped single-mode: *Cu800*. Pure silica, step-index multi-mode: *Cu100/110* (IVG Fiber).

[16] Optical-fibers cleaver: *S324* (Furukawa Electric Co Ltd).

[17] The efficiency can be partially recovered by a misalignment between the fibers that conform the cavity.

[18] Fiber Rotator for Bare Fiber with 125 μm Cladding Diameter: *HFR007* (Thorlabs Inc).

surface, a subsequent fiber rotation of 180° will show interference fringes corresponding to twice the cleaving angle (see Fig. 2.7(b)). This technique allows us to improve the cleaving process[19] and post select those fibers with perpendicular end facets. In general, an average of 2.5 cleaving procedures is required to obtain a fiber with potential decentrations below 1 μm.

To ensure that the optical fibers do not present arbitrary angles when placed in the ablation setup, we equipped the custom-made holder with V-grooves that tightly host the fibers, as depicted in Figure 2.7(c). Due to the bigger diameter of the the the groove, the fiber tips can still freely move a few tens of micrometers; the typical displacements within the groove after clamping the fiber with teflon-protected screws are on the order of 20 μm which implies potential decentrations of 1 μm[20]. By making sure that the reference plate is parallel to the surface of those fibers with a perpendicular end facet, any systematic angle between the fiber holder and the CO_2-laser beam will result in a fixed decentration that can be taken into account before the ablation. An additional and more active approach is performed right before the ablation to reduce the decentration due to residual fiber angles: When a mounted fiber is tilted due to the clamping conditions mentioned above, a quick inspection of the direction and number of fringes on its surface tells us how much we must displace the ablation location in order to counter decentration effects. Altogether, with the techniques presented here we achieved a reduction of 0.7 μm on the average decentration.

2.2.2 Interferometric Surface Reconstruction

The inspection microscope is employed as an optical profilometer for the precise experimental characterization of each of the laser-machined structures. With the use of phase-shifting interferometry, the setup offers vertical resolutions of ~25 nm. Although this accuracy is not enough to characterize the surface roughness (expected to be ~0.2 nm), it nevertheless provides a precise estimation of the mirrors' global characteristics, namely: radius of curvature, diameter, decentration, etc. In addition — due to its long-working distance — the optical inspection realizes non-contact estimations that can be performed fast and in-situ, immediately after the surface treatment (as opposed to AFM measurements).

Phase-Shifting Interferometry and Phase Unwrapping

The fringes observed in the interferograms emerge due to changes in the relative phase ϕ between the two interferometer arms. When examining the machined structures, the intensity modulation of the image corresponds directly to height variations in the fiber mirror (assuming that the glass plate employed as a reference is a perfectly flat surface). A 2D map of $\phi(x, y)$ (and therefore of the surface's height) can, in principle, be obtained from a single interferogram image. In the simplest case of perfectly balanced and homogeneous illumination of both arms, the relation between the relative phase and the light's intensity $I(x, y)$ is given by

$$I(x, y) = I_0 \left[1 + \cos\left(\phi(x, y)\right)\right] .$$

The variations of the intensity from 0 to twice the average (I_0) are directly mapped into changes of the relative phase (expressed in modulo 2π). The phase can then be unwrapped and the reconstructed surface is obtained.

In a more realistic scenario, low contrast and inhomogeneous illumination produce spatial alterations of the intensity map that are not related to height variations[21]. Since the illumination conditions tend

---

[19] The copper coating needed to be etched for at least 3 mm to avoid undesired bending of the fiber within the cleaver.

[20] This is assuming the worst case scenario in which the angle comes from the closest clamping point (at around 4 mm from the fiber tip). For such displacements the estimated fiber angle is on the order of 0.3°.

[21] The amount of reflected light is not perfectly balanced for both arms, leading to a reduced contrast. Furthermore, since the LED employed is not a point-source, it generates spatially inhomogeneous illumination at the focus of the microscope.
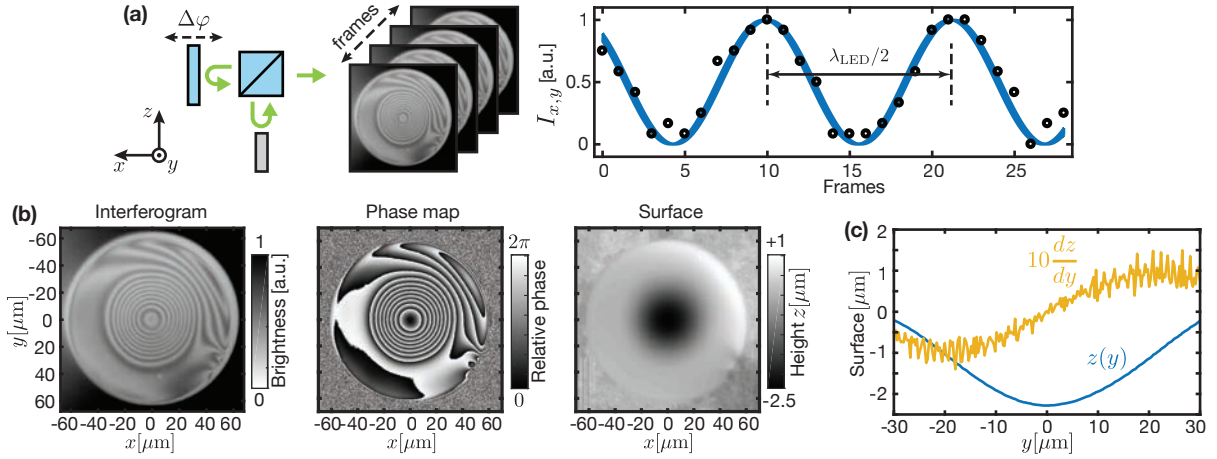
Figure 2.8: Phase-shifting interferometry and surface reconstruction of fiber mirror #656. **(a)** Right: Simplified sketch of the in-situ PSI procedure. At each of the 30 steps, the reference plate is displaced by 23.5 nm and an interferogram is taken. Left: intensity modulation of a single pixel during the scan. The data is fit to a sinusoidal curve of the type $A + B \sin(4\pi z/\lambda + \phi)$ (blue curve, thickness represents 95 % confidence interval). The fit is done individually for each pixel, from which the relative-phase map $\phi(x, y)$ is extracted (modulo 2π). **(b)** Sequence of the profilometry, from left to right: single histogram, wrapped-phase map from PSI and reconstructed surface from unwrapping algorithm (rescaled as $z = \phi \lambda_{\mathrm{LED}}/4\pi$). **(c)** Vertical cross section of the reconstructed surface (blue) and its derivative (orange, amplified ×10). The maximum noise level (extracted from the oscillations in the derivative) limits the resolution to 26 nm (RMS).

to vary for different targets, the effect cannot be precisely countered and the relative phase map is too noisy to be properly unwrapped. This is solved using *phase-shifting interferometry*, which consists in examining the behavior of the intensity map while displacing the axial position of the reference plate in steps $\Delta z < \lambda_{\mathrm{LED}}/2$ (with $\lambda_{\mathrm{LED}} = 532$ nm). After each displacement, every point (x, y) of the intensity map acquires a phase shift $\varphi(z) = 4\pi\Delta z/\lambda_{LED}$, such that

$$I(x, y, z) = I_{\mathrm{r}}(x, y) + I_{\mathrm{f}}(x, y) + 2\sqrt{I_{\mathrm{r}}(x, y)I_{\mathrm{t}}(x, y)} \cos\left[\phi(x, y) + \varphi(z)\right].$$

where $I_{\mathrm{r}}(x, y)$ and $I_{\mathrm{f}}(x, y)$ are the unknown illumination-intensity maps of reference and fiber surface, respectively. In practical terms, the displacement leads to an oscillation of the brightness of each pixel. Since the illumination inhomogeneities do not change during the (z) displacements, they do not affect the sinusoidal behavior. An examination of the initial phase at each point then provides the required $\phi(x, y)$ map (plus an arbitrary offset). The technique is described in Figure 2.8(a), where the brightness of a single pixel is shown for different positions of the reference plate (which is mounted in a high-precision piezo stage[22], controlled by the mbed). The retrieved map, containing the phase difference with full $0 - 2\pi$ contrast, can be fed to a phase-unwrapping algorithm [71] that retrieves the true phase map, as shown in Figure 2.8(b).

The vertical resolution of the setup is in principle determined by the sensitivity of the camera and the precision of the translation stage. Nevertheless, noise in the interferograms due to vibrations of the system (for instance, a nearby flow box) limit the measurement precision. As a consequence, the resulting phase maps become particularly noisy at the $\phi = 2\pi \to \phi = 0$ discontinuities, which leads to smooth artifacts during the unwrapping procedure on the scale of 26 nm, as shown in Figure 2.8(c).

---

[22] High Resolution Translation Stage: *TRITOR102V*. Controller and voltage amplifier: *ENV40CAP* (piezosystem jena GmbH).
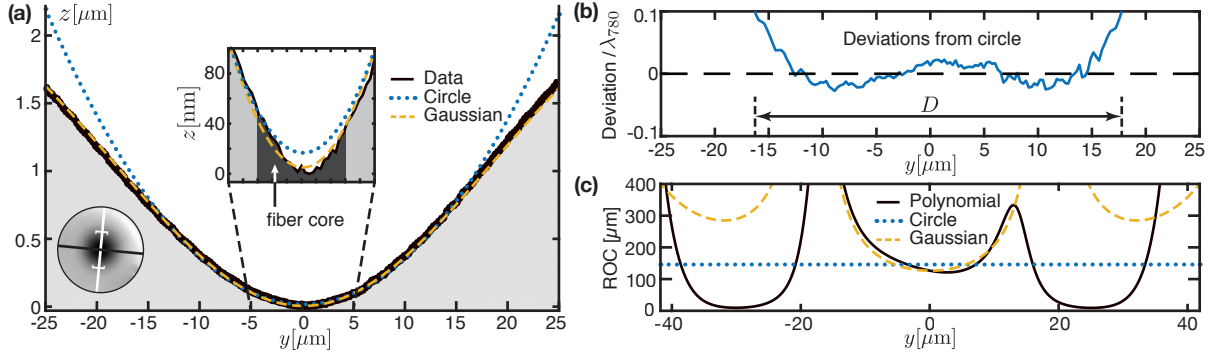
Figure 2.9: Mirror surface evaluation of fiber mirror #656. **(a)** Cross section of the surface along one of the two main axes (vertical white line in the inset, at the bottom left). The surface height (solid, black line) is fitted to both a Gaussian (dashed, orange line) and a circular curve (dotted, blue line). The vertical scale is augmented by a factor of 20. The inset shows a closeup of the central region including the 6 μm-diameter fiber core (axial decentration of 0.1 μm). **(b)** Difference between the mirror surface and the spherical model. The range within the boundaries $\pm\lambda/10$ marks the mirror diameter D according to our definition. The variation at the central region is attributed to the core-cladding transition [62, 63]. **(c)** Estimations of the ROC from the a fit of an 8th-order polynomial (solid, black line), a Gaussian and a circle (same color code as in (a)). Although the Gaussian and polynomial estimations are more precise, the spherical fit gives a better estimation of the average ROC over the central region. Notice the longer horizontal range of the plot (±40 μm).

Surface Evaluation

Once the concave depression is reconstructed, a preliminary fit to a 2D-Gaussian curve is used to identify possible ellipticities. Subsequently, a more detailed evaluation of the surface is performed along its two main axes by fitting both a Gaussian and a circle to the central region of the depression (see example in Fig. 2.9(a)). The Gaussian curve describes the surface behavior much better throughout the whole region, as expected from the intensity profile of the ablation pulse. The circular fit (here also referred to as spherical) drifts from the profile as we separate from the central area where the fit is performed (±15 μm). Since a sphere represents the desired mirror shape, the deviations between the fiber-surface and the circular fit contain information about the quality of the mirror's geometry. In fact, this residual profile (example shown in Fig. 2.9(b)) can be used to estimate the effective diameter of the depression. This is given by the region of the mirror that is spherical, which is not well defined in a Gaussian surface. We follow a conservative approach[23] by defining the diameter as the area where the deviations to a perfect sphere are smaller than $\lambda/10$ (with $\lambda = 780$ nm being the wavelength of the light used in the experiments discussed in this thesis). Under this consideration, the estimated mirror diameters for our fibers are on the order of 30 μm, which fulfills our requirements.

Due to the Gaussian-like behavior of the depressions, their curvature varies along the surface. This becomes clear when fitting a high-order polynomial to the surface and retrieving its local ROC for different positions[24]. Although the variations in radius are negligible in the core region (±5 μm), they increase considerably as we move away from the center, as shown in Figure 2.9(c). An analytical expression of the effective ROC of the mirror is not well defined, and it must be retrieved by experimental

---

[23] An alternative choice is that of defining the diameter by the turning points of the Gaussian curve, which associates the size of the mirror to the region where the structure is still concave. This leads to overestimations of the true diameter, as not all the concave region presents the spherical behavior required to maintain the resonator mode.

[24] For an arbitrary function $f(x)$, the ROC is defined as $R(x) = |(1 + f'^2)^{3/2}/f''|$.
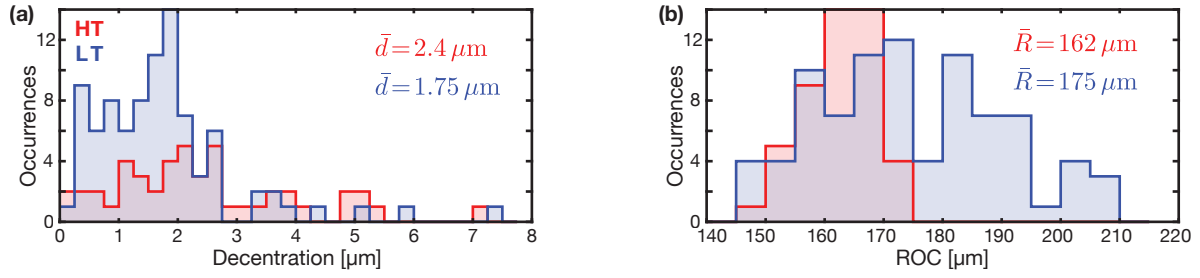
Figure 2.10: Distribution of the relevant figures of merit for the SM fibers of both runs: HT = 47 (red) and LT = 88 (blue). Ablation parameters: train of 45 pulses of 3 ms duration and 20 W of power. **(a)** Histogram of the decentration with average values of $d_{HT} = (2.4 \pm 0.2)\,\mu$m and $d_{LT} = (1.75 \pm 0.13)\,\mu$m. **(b)** Histogram of the spheric radii of curvature (average from both main axes). Average values of $R_{HT} = (162.6 \pm 0.7)\,\mu$m and $R_{LT} = (175.2 \pm 1.9)\,\mu$m.

means. The measurements shown in Section 2.3.1 typically yield estimations in accordance to the radius of curvature of the spherical fit, which is the value used in the rest of this chapter. The relative difference in curvature along the two main axes ($|\Delta R|/R_{max}$) yields the ellipticity of the structure which in our mirrors is below 5 % on average. This geometrical distortion becomes relevant when the mirrors are used to form a resonator, as it can break the degeneracy of the linearly polarized eigenmodes of the cavity (see [72] and measurements in next section).

Additionally, the position of the core — obtained by imaging the light coupled to the fiber — is compared to the center of the structure (extracted from the corresponding fits[25]), thus yielding the decentration for each mirror. A summary of the typical values and their distribution is presented in the following.

Fiber Mirror Production Results

Two main batches of fiber mirrors were manufactured in February and July 2014, referred to as HT (high-transmission) and LT (low-transmission) respectively, due to their coating characteristics (see below). The final number of laser-machined optical fibers was 47(SM)/15(MM) and 88(SM)/7(MM) for HT and LT sets, respectively. Identical ablation parameters were employed for both runs, although the manufacturing of LT mirrors includes the techniques of cleaving post-selection and active prevention of decentration. As a result, we obtained a reduction of the average decentration from 2.4 µm to 1.75 µm and more than 24 (LT-) fiber end facets with less than 1 µm displacement (see histograms in Fig. 2.10(a)). An equivalent histogram is displayed in Figure 2.10(b) for the spherical ROCs. There is a wide distribution of radii due to fast power instabilities of the laser and similar fluctuations due to the constant switching during the train of pulses. As a result, the ablation procedure provides a range of values[26] which is considerably larger for the LT batch. The origin of the discrepancy is unknown, although the most probable cause is a degradation of the laser's water cooling system between both production periods.

A high-reflectivity dielectric coating was deposited on the fibers by employing ion-beam sputtering (*Laseroptik GmbH*). The two coating runs were designed to exhibit transmissions of $\mathcal{T}_{HT} = 120$ ppm and $\mathcal{T}_{LT} = 10$ ppm in order to enhance the directionality of the cavity output (see Sec. 2.1.2). A high

---

[25] The decentration estimation assumes that the reference glass plate is perpendicular to the fiber's axis. As previously discussed, this is ensured by aligning the plate parallel to the surface of a flat-cleaved fiber.

[26] An equivalent distribution is expected for the mirror diameters, since the ratio between ROC and diameter is given by the ablation-beam waist, and it's only slightly dependent on laser power [68].

Table 2.1: Main parameters of the two coating runs for 780 nm light. The specified values for transmission ($\mathcal{T}$) and losses $\mathcal{L}$ (absorption and scattering) were provided by Laseroptik GmbH. Experimental transmission coefficients measured after annealing procedure (see App. A.1). Losses extrapolated from finesse measurements of Sec. 2.3, with this technique absorption and scattering losses are indistinguishable.

	Fibers (SM/MM)	$\mathcal{T}$ (spec./meas.)	$\mathcal{L}$ (spec./meas.)
HT	53/27	$(120 \pm 20)/(126 \pm 13)$ ppm	$20/(26 \pm 5)$ ppm
LT	95/9	$(10 \pm 2)/(13 \pm 3)$ ppm	$16/(25 \pm 5)$ ppm

reflectivity is maintained for a broad spectrum of frequencies of approximately $770 - 820$ nm that covers the two main spectroscopic (D_1 and D_2) lines of rubidium and the the 770 nm laser used to stabilize the cavity length (Sec. 2.4.2). Appendix A.1 contains a detailed description of the coating properties and their experimental characterization, including the mirror annealing technique necessary to reduce the initial high losses present the coated fibers. The relevant properties for 780 nm are summarized in Table 2.1.

2.3 Effects Specific to Fiber Cavities

This section contains a study on the properties of resonators formed by the fiber mirrors produced in our facilities, focussing on those characteristics which are specific to FFPCs[27], either due to the surface laser-machining procedure or due to their inherent fiber-coupling. In Section 2.3.1 the optical quality of the mirrors is examined by monitoring the resonance linewidth of the cavity. In particular, we observe a finesse dependance on cavity length (due to mirror clipping) and polarization-mode splittings, both effects emerging due to the finite and non-spherical nature of laser-machined depressions. Additional challenges — specific to FFPCs — arise from the intrinsic direct fiber coupling of light to the resonator mode [1, 73]. For instance, the efficiencies to couple light into and from the cavity mode are set by the relative alignment of the fiber mirrors. In order to achieve optimal cavity alignment it is therefore important to find strategies to accurately characterize the coupling efficiencies already during the assembling of the resonator. Thus, in Section 2.3.2, we analyze the connection between the cavity alignment, cavity mode matching and asymmetric reflective line shapes for fiber resonators (the results shown there are an adaptation from reference [1]).

A Setup for Cavity Characterization

Due to the high finesse and small size of our fiber-based resonators, a certain mechanical and optical stability is required when studying their spectral properties. To that end, an optical setup was developed to serve as both a test bed to characterize different fiber mirrors and cavity configurations (this section), and to assemble a compact cavity system suitable for neutral-atom experiments (Sec. 2.4).

The observables to be monitored during the initial alignment and the subsequent examination of the resonator are its transmissive and reflective properties. These are probed by coupling light from a diode laser (780 nm or 850 nm depending on the measurements) into the corresponding input fiber mirror and measuring both reflection and transmission of the cavity with corresponding photodiodes at the end of

---

[27] In this section we use of the acronym FFPC (instead of *fiber cavity*) to emphasize the difference from macroscopic cavities.
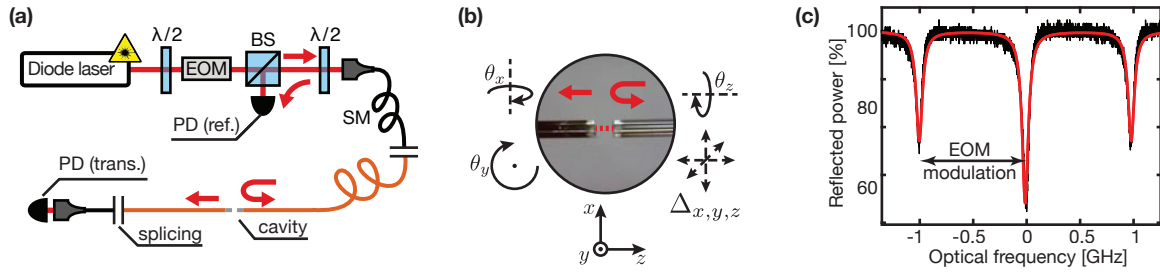
Figure 2.11: Cavity-characterization setup. **(a)** Simplified layout of the main optical components. The output of a diode laser (780 nm or 850 nm) is modulated to create 1 GHz sidebands and then coupled into the spliced input-fiber. The half-wave plates ($\lambda/2$) provide control over the linear polarization of the light. The reflection (separated from the input by a 50 : 50 beam-splitter (BS)) and the transmission are monitored by photodiodes. **(b)** The precise alignment of the cavity (observed by two microscopes in x and y directions) is done in all three directions and angles by the corresponding stages. The system can also host hybrid cavities with macroscopic substrates. Fiber mirrors in the picture: #708 (LT, left) and #304 (HT, right). **(c)** Reflection dip of an HT-LT FFPC for the modulated input light (780 nm). A fit (red) to three equidistant Lorentzian curves provides the required frequency calibration and an estimation of the linewidth (here $\kappa = 2\pi \times (34.9 \pm 0.2)$ MHz).

each of the optical fibers (see Figure 2.11(a)). For a typical SM-SM fiber-cavity configuration, the fiber tips are initially placed facing each other (separated by a few tens of micrometers) in order to ensure the formation of a stable cavity mode (the process is monitored by two perpendicular microscopes). Once a resonance dip (peak) is observed in the reflection (transmission), the incoupling is optimized by displacing the input fiber in the plane perpendicular to the cavity axis. This is performed with a sub-micrometric-precision translation stage[28] on which the input fiber is held with the help of a custom-made V-groove. A fiber rotator can be added in order to change the relative angle of one of the mirrors around the fiber axis (see the polarization-mode splitting analysis in Sec. 2.3.1). The output fiber — mounted in a similar V-groove block — can be rotated along the two remaining axis[29] (θ_x, θ_y) to ensure that the two fibers are parallel to each other (Fig. 2.11(b)).

Either the laser frequency or the length of the cavity must be scanned in order to resolve more than one of its optical resonances. Due to the large Free Spectral Range (FSR) of these short resonators (~2 THz) it is more convenient to modify the cavity length, which only requires displacements bigger than $\lambda/2$. This displacement can be performed by a piezo-electric element inside the translation stage. Nevertheless — due to the low resonance frequency of the stage platform — when a precise measurement is required, it is more convenient to scan the cavity length by gluing the fibers to a small shear-piezo (see Sec. 2.4). To retrieve the spectral figures of interest like the linewidth (κ) or the FSR in frequency domain, a conversion must be made from piezo voltage to optical frequency. This is done by using sideband modulation of the input light as a frequency marker. The output of the laser is sent through a homemade[30] resonant Electro-Optic Modulator (EOM), which modulates the phase of the input field, effectively creating frequency sidebands 1 GHz away from the carrier. Figure 2.11(c) shows the reflection dip of an HT-LT fiber cavity probed by modulated light at 780 nm. Since the linewidth of the laser is considered much smaller than that of the resonator, the half-width of the reflected dip corresponds directly with the cavity-field decay rate κ. The linewidth contains rich information, not only about the cavity, but also about the independent fiber mirrors. In the following paragraphs we characterize certain

---

[28] 3-Axis NanoMax Stage, Differential Drives, Open-Loop Piezos: *MAX312D/M* (Thorlabs Inc).

[29] High-Precision Rotation Mount: *PR01/M*. Large Goniometer, 25.4 mm to Point of Rotation: *GNL10/M* (Thorlabs Inc).

[30] The building and characterization of the EOM and corresponding electronics was performed by my colleague S. Gosh.

properties of the mirrors (optical losses and ellipticity) by observing how the reflection dip behaves under different cavity lengths or input polarizations.

2.3.1 Clipping Losses and Mode Splitting

Finesse for Different Cavity Lengths

The finesse of a resonator is a measure of the optical quality of its mirrors and, as described in Section 2.1, is inversely proportional to the power losses upon reflection. The processes considered so far included transmission $\mathcal{T}$, absorption and scattering, which are coating-specific and do not depend on the global geometry of the mirror. In this section we study how the finite size of the laser-machined mirrors and its Gaussian-like structure contribute to the optical losses via clipping. Such processes emerge when a fraction of the light is reflected into a mode other than that of the cavity, and become relevant if the size of the cavity mode at the fiber surface (w_m) is comparable to the diameter D of the mirror (a feasible scenario for fiber cavities). In particular, the clipping losses per mirror C can be estimated as [27]

$$C = \exp\left(-\frac{D^2}{4w_\mathrm{m}^2}\right).$$

It is reasonable to assume that the cavity hosts a Gaussian mode in most of the cases, which leads to a beam radius at the mirror w_m given by Equation (2.6). Since the illuminated region of the fiber surface increases with the cavity length L_cav, the finite size of the mirror manifests as a corresponding drop in the finesse:

$$\mathcal{F} = \frac{2\pi}{\mathcal{T} + \mathcal{L} + C(L_\mathrm{cav}, D, R)}, \tag{2.8}$$

where $\mathcal{L}$ denotes losses due to absorption and scattering and R is the mirror's ROC. For our typical cavity lengths ($<100\,\mu\mathrm{m}$) the mirror's spot size is $w_\mathrm{m} \approx 5\,\mu\mathrm{m}$ and, as we shall see, clipping is negligible. However, this effect plays a critical role in systems where long resonators are required, such as those hosting ion traps where the effect of the fiber's dielectric surface must be avoided. The characterization of clipping processes is therefore of relevance in the community, and has been recently studied in several scenarios [27, 60, 62, 63, 74].

Since the finesse is phenomenologically defined as the ratio between the FSR and the Full-Width Half-Maximum (FWHM) of the cavity resonance, a single scan over two consecutive spectral features provides the necessary information. Figure 2.12 contains examples of a measurement of both quantities (and the incoupling efficiency η_dip) for a HT-LT fiber cavity. Since the output cavity mirror in this case is a fiber, it is not possible to obtain information about the transversal profile of the modes corresponding to each peak. Nevertheless, taking into account that we typically obtain incoupling efficiencies of ~90 % when using the Gaussian mode of an SM-fiber as an input, it is safe to assume that the deep reflection features correspond to the fundamental TEM$_{00}$ mode. In order to evaluate the spectral properties for increasing cavity lengths, a scale is required to gauge the different mirror distances. This is provided by converting the FSR to frequency space ($\Delta\nu_\mathrm{FSR}$) with the previously mentioned sideband modulation: as the distance between mirror increases, the separation between sidebands and carrier is reduced proportionally[31].

A measurement of the finesse for different cavity lengths for the same type of HT-LT fiber-resonator is shown in Figure 2.13(a); despite the scattered nature of the data points[32] the plot displays a gradual

---

[31] One should keep in mind that the piezo scan used to estimate the FSR might not be linear, and therefore for precise estimations of the finesse and the cavity length (like those to characterize the final assembled cavity used in the rest of the experiments) should be performed by other methods, as we point out in Sec. 2.4.

[32] The deviation from the expected plateau for short cavity lengths might occur due to the presence of degenerated higher-order
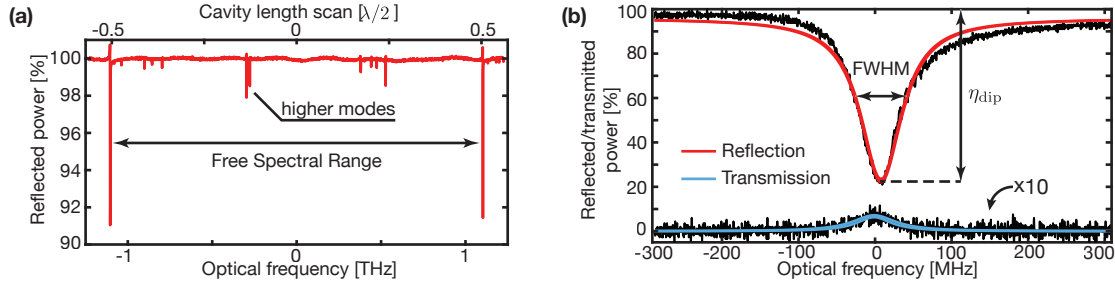
Figure 2.12: Scan over the cavity resonances. **(a)**. A wide scan of the piezos shows two consecutive resonances of the fundamental mode. The fibers are aligned by reducing the power coupled to higher transversal modes (small peaks at the center). The depth of the large peaks appears reduced due to the resolution of the oscilloscope. The top axis is not a real calibration of the piezo stroke, but a scale to guide the eye (fiber mirrors used: #318 and #652). **(b)**. Reflection dip and transmission peak of a HT-LT fiber cavity (fiber mirrors used: #304 and #708). Only the reflection dip is used in the following analyses due to its prominent depth (caused by the HT input configuration). Lorentzian curves (red and blue) are used to fit the data, the discrepancies of the fit with the reflected dip (both the asymmetric shape and the small horizontal offset) are a consequence of the fiber-core mode filtering (see Section 2.3.2).

decay for distances longer than ~120 μm due to the expected clipping losses. The sudden drop at the end of the scan is caused by the cavity entering the unstable region determined by $R_{min} < L_{cav} < R_{max}$ where no resonance peak is observed. The curve is a fit to Equation (2.8), which shows a reasonable agreement between the data and the clipping losses model. By using some of the coating and geometrical properties of the mirrors as free parameters, we obtain an estimation for the minimum of the two ROCs of (172 ± 4) μm[33] and an average mirror diameter of (28.2 ± 1.0) μm. While the radius of curvature is in excellent agreement with the estimation from the surface reconstruction for that specific fiber (169.5 μm), we find that our definition of the spherical-mirror diameter overestimates the mirror's size by 30 % when compared to the effective experimental value. The initial plateau of the finesse for short cavities, which is dominated by the coating properties, provides an estimation of the total losses of (18 ± 5) ppm per mirror. This includes absorption and scattering (which cannot be distinguished with this method). A similar analysis for different coating combinations yields the estimated values previously presented in Table 2.1.

The widening of the spot size at the mirror's surface for different cavity lengths does not only affect the finesse but also the incoupling efficiency. Recalling the definition in Section 2.1, the incoupling efficiency is the relative drop of reflected power on resonance (here designated by η_{dip}), given by the product of both the impedance (η_{imp}) and mode-matching (ϵ_{in}) efficiencies. Since the resonator under inspection is composed of a HT input mirror with a transmission higher than the rest of the losses, the cavity is said to be overcoupled. An increase in losses (such as the one appearing for long cavities) will lead to a initial growth of the impedance matching until it reaches unity. However, the mode matching displays an opposite behavior: The difference in size between the fiber-core and the cavity modes increases with the cavity length.

The expression for η_{imp} is given by Equation (2.3) (adding the clipping effect to the total losses); however, the calculation of the mode-matching efficiency requires a more thorough study of the system's geometries. As discussed, ϵ_{in} is given by the overlap integral between the Gaussian modes of the fiber core ψ_f with waist w_f and the cavity mode at the position of the mirror ψ_m with beam radius w_m. In the

---

[33] transversal modes that suffer higher clipping losses [75].

[33] Since there is no data beyond the unstable region, only the minimum ROC can be estimated. We compare it to the one of the fiber presenting the smaller ROC of the two.
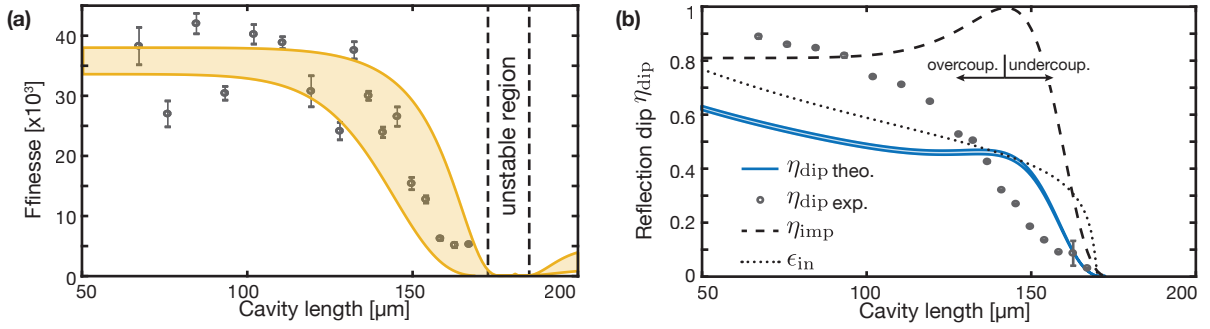
Figure 2.13: Finesse and incoupling for different cavity lengths (fiber mirrors used: #304 and #708). **(a)** Finesse decrease due to clipping losses. Each data point (gray) corresponds to 10 measurements, the error bars represent the standard deviation of the mean. A fit (orange) to Equation (2.8) shows the agreement with the model, the thickness of curve represents the one-sigma confidence interval. The free parameters are the total losses, the average mirror diameter and the minimum ROC of the two mirrors. The dashed lines represent the unstable cavity region for the extracted ROC. **(b)** Incoupling efficiency for increasing cavity lengths. The data (gray) is compared to our simple model (blue), which consist on the product of η_{imp} (dashed) and ϵ_{in} (dotted). The discrepancies are attributed to filtering of the fiber-core, which leads to higher incoupling values for overcoupled cavities. The transition between over- and undercoupling ($\eta_{\mathrm{imp}} = 1$) is a consequence of the increasing clipping losses.

simplest scenario, considering the expression for w_m from Equation (2.6), the mode-matching factor is given by [76]

$$\epsilon_{\mathrm{in}} = |\langle \psi_{\mathrm{m}} | \psi_{\mathrm{f}} \rangle|^2 \approx \frac{4\, w_{\mathrm{m}}^2 w_{\mathrm{f}}^2}{\left(w_{\mathrm{m}}^2 + w_{\mathrm{f}}^2\right)^2}\,, \tag{2.9}$$

any decentration or relative angle between the fiber axis and the resonator mode implies an additional decrease in the efficiency. A more detailed description of mode matching for different geometrical scenarios can be found in App. B, however for this particular analysis Equation (2.9) suffices. The combination of both effects predicts an almost flat incoupling that only gets reduced when approaching the unstable cavity region. The model is represented in Figure 2.13(b), using the previously estimated values of the mirror geometries and fiber-core waist size[34]. When compared to the experimental data, it becomes clear that the simplified model underestimates the incoupling efficiencies for most of the scan range. Such discrepancies are a direct consequence of the mode filtering done by the fiber-core, which alters the interference between the light reflected off the fiber-surface and the cavity leakage and, therefore, the behavior of the reflection dip (see Sec. 2.3.2). In general, the mode filtering leads to a lager η_{dip} for particular alignments of the fibers if the cavity is overcoupled. Since said alignment was performed by optimizing the incoupling, the effect is always present and leads to the higher value than the one predicted by the simple model for the region where the resonator is overcoupled.

Polarization-Mode Splitting: Birefringence and Mirror Ellipticity

The degeneracy of orthogonal linear-polarization modes inside the cavity is of crucial importance for CQED applications where quantum information is encoded in the polarization degree of freedom. Furthermore, the ability to inject and maintain arbitrary polarizations in the resonator allows the creation of σ-polarized cavity modes, which can then be used to address the strongest atomic transitions or to

---

[34] The mode field diameter of the SM fiber output was independently measured by a colleague yielding a value of $w_{\mathrm{f}} = (2.61 \pm 0.03)\,\mu m$ at 852 nm. Assuming linear dependence on the wavelength, we estimate $w_{\mathrm{f}} = (2.53 \pm 0.03)\,\mu m$ at 780 nm.

perform precise preparation of the atomic state via optical pumping (see e.g. Chap. 4). It is therefore necessary to minimize any effect that might lead to a lift of such a degeneracy, which occurs when the phase shift acquired by the light after a cavity round trip depends on its polarization. In general, a differential phase-shift $\Delta\varphi$ between both linearly-polarized modes leads to a splitting $\Delta\nu_{spl}$ of their resonance frequencies which, when normalized by the cavity FWHM ($\Delta\nu_{FWHM} = 2\kappa$), is given by (see e.g. [52, 77]):

$$\frac{\Delta\nu_{spl}}{\Delta\nu_{FWHM}} = \frac{\mathcal{F}}{2\pi}\Delta\varphi \,. \tag{2.10}$$

The accumulation of the roundtrip phase-shifts after each reflection leads to a splitting which is enhanced by the cavity, making high-finesse systems particularly sensitive to small phase differences[35].

There are two main mechanisms that can lead to such frequency splittings. The first is the presence of birefringence in the last coating layers, which can emerge due to inhomogeneous coating depositions or be induced by stress on the mirror due to its mounting conditions. The intracavity field penetrates into a small fraction of the coating [79], and the different refractive index of the two optical axes gives rise to a polarization-dependent penetration depth (and therefore different phase-shifts). To prevent such a scenario, we typically glue or clamp the optical fibers a few millimeters away from the mirror end facet[36]. The second cause of mode splitting, more prominent in fiber-based cavities, is related to the ellipticity of the laser-machined mirrors. As discussed in reference [72], corrections to the paraxial resonator theory show that the resonance frequency of a linearly polarized mode depends on the radius of curvature of the mirrors along the polarization direction. As a consequence, an elliptical mirror with radii R_a and R_b will induce a polarization-dependent phase-shift of

$$\Delta\varphi = \frac{\lambda}{2\pi}\frac{R_a - R_b}{R_a R_b} \,. \tag{2.11}$$

When combining the effect of both mirrors with the cavity enhancement of Equation (2.10), resulting mode splittings can be on the order of hundreds of MHz for FFPCs [27, 60].

Independently of its origin, the mode splitting can be reduced by rotating one of the fibers — and therefore its optical/elliptical axis — such that the phase shift induced by one of the mirrors ($\Delta\varphi_1$) is compensated by the other ($\Delta\varphi_2$). By following the Jones formalism used in [72], the effective roundtrip phase-shift for a relative angle θ between the axes of the two mirrors is given by

$$\Delta\varphi_{eff} = \sqrt{\Delta\varphi_1^2 + \Delta\varphi_2^2 + 2\Delta\varphi_1\Delta\varphi_2\cos(2\theta)} \,. \tag{2.12}$$

A relative rotation of one of the mirror can reduce the total splitting from $\Delta\varphi_1 + \Delta\varphi_2$ to $|\Delta\varphi_1 - \Delta\varphi_2|$. A perfect balance of the phase shifts will only occur for mirrors with the same degree of birefringence or ellipticity; in general it does not take us more than few combinations before finding a pair of mirrors that can provide splittings considerably smaller than the linewidth.

As a proof of principle and to characterize the usual mode-splitting present in our resonators, we analyze the degeneracy lift of the modes in a HT-HT fiber cavity and show its effective reduction when rotating one of the fibers with respect to the other. Figures 2.14(a,b) show the reflection dip of the cavity when the input fiber is rotated such that the splitting is either maximized or minimized, respectively[37]. By measuring the peak separation for several rotation angles of the input fiber one obtains

---

[35] This effect can be exploited to detect birefringence of coated substrates with a few ppm resolution [78].

[36] Regarding the coating procedure, the ion-beam sputtering is performed under continuous rotation of the coated surface to ensure its homogeneity.

[37] In order to ensure enough resolution when estimating the splitting from the closely overlapped curves, we assume that
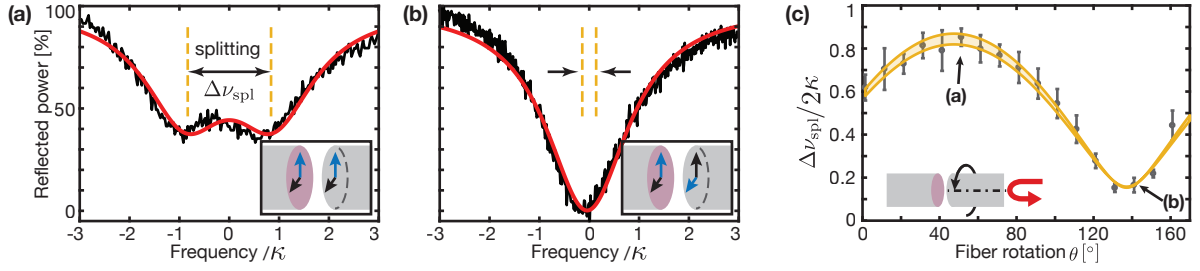
Figure 2.14: Polarization-mode splitting (fiber mirrors used: #223 and #402). **(a)** Reflection dip with the maximum splitting obtained when rotating the input fiber. The red curve indicates a fit to two Lorentzian curves with the same amplitude and width. The inset shows the relative angle between the elliptical axes (blue and black arrows) of the mirrors (here their phase shifts add to each other). For the opposite case, when the rotation minimizes the total phase shift, the splitting is not visible anymore **(b)**, and it is mainly estimated by the total amplitude of the dip. **(c)** Mode-splitting for different relative angles between the fibers normalized to the cavity FWHM. Each data point (gray) represents 10 measurements with a standard deviation given by the error bars. The fit to Eq. (2.12) (orange) is performed with the two mirrors' phase-shift and an angle offset as free parameters; its width represents the one-sigma confidence interval.

an oscillating behavior between splittings of $0.9\,\Delta\nu_{\text{FWHM}}$ and $0.2\,\Delta\nu_{\text{FWHM}}$. The data shows excellent qualitative agreement with the model of Equation (2.12), which suggests relative phase shifts of our mirrors of $\Delta\varphi_1 = (142 \pm 3)\,\mu\text{rad}$ and $\Delta\varphi_2 = (98 \pm 4)\,\mu\text{rad}$. These values are three times higher than the ones expected due to mirror ellipticities (Eq. (2.11)). Given the accuracy of our surface reconstruction and spherical ROC estimations, we attribute the discrepancies in $\Delta\varphi$ either to a tilt of the cavity mode that can change the effective ellipticity or to additional mode-splitting mechanisms like the aforementioned stress-induced birefringence.

A splitting of $\sim 0.2\,\Delta\nu_{\text{FWHM}}$ was obtained for the specific cavity used in the experiments of the coming chapters. To characterize the polarization-mode splitting with higher resolution than the one provided by the Lorentzian fits, a Hänsch–Couillaud optical setup [80] was implemented by my colleague S. Ghosh that provided an estimated final mode-splitting of $(9.0 \pm 0.3)\,\text{MHz}$. This value was confirmed by the 5 % variations in amplitude of the reflected dip observed when varying the input light polarization.

2.3.2 Asymmetric Reflective Line Shape and Optimal Alignment

The direct coupling of light from optical fibers to the cavity mode and vice versa is an important feature of FFPCs that can strongly benefit integration and miniaturization of optical cavities. The intrinsic fiber connection, however, can also give rise to adverse effects that do not occur for traditional macroscopic Fabry–Pérot cavities coupled by free-space beams. For FFPCs, the spatial mode matching between the cavity mode and the incoming and outgoing fiber-guided light fields are intrinsically determined by the relative alignment of the fiber mirrors. Once the fiber mirrors have been fixed in position, the coupling into the cavity cannot be altered any more. The two spatial mode matching efficiencies $\epsilon_{\text{in}} = \epsilon_{\text{HT}}$ and $\epsilon_{\text{out}} = \epsilon_{\text{LT}}$ are important figures of merit that enter the resonant transmission efficiency of a fiber cavity

$$\frac{P_{\text{T,max}}}{P_{\text{in}}} = \epsilon_{\text{HT}}\,\epsilon_{\text{LT}} \cdot \frac{4\,\mathcal{T}_{\text{LT}}\mathcal{T}_{\text{HT}}}{(\mathcal{T}_{\text{HT}} + \mathcal{T}_{\text{LT}} + \mathcal{L}_{\text{HT}} + \mathcal{L}_{\text{LT}})^2} \tag{2.13}$$

the two peaks have the same half-width (κ) and amplitude. This is a reasonable consideration given that we do not expect polarization-dependent mirror losses and that the input polarization was modified such that both modes where equally populated.

and determine the probability to retrieve a cavity photon

$$p_{i,\text{out}} = \epsilon_i \cdot \frac{\mathcal{T}_i}{\mathcal{T}_{\text{HT}} + \mathcal{T}_{\text{LT}} + \mathcal{L}_{\text{HT}} + \mathcal{L}_{\text{LT}}}$$

at the fiber output $i = $ HT or LT. For cavity-based light-matter interfaces, ϵ_i furthermore sets an upper limit to the efficiency of mapping photons from mirror side i into the cavity-coupled quantum system. Many applications of FFPCs therefore rely on a method to determine and optimize a particular mode matching efficiency (in our case ϵ_{HT}) during the alignment of the cavity.

Measurements of the fiber-cavity transmission depend (according to Eq. 2.13) on the product $\epsilon_{\text{HT}} \cdot \epsilon_{\text{LT}}$ and can therefore not be applied to separately determine the mode matching efficiencies of FFPCs consisting of two single-mode fibers. Naturally, the simple transmission method also fails for one-sided FFPCs with one non-transparent mirror substrate. Reflection measurements, on the other hand, offer the possibility to characterize and optimize the individual mode-matching efficiencies. Their evaluation, however, requires a more careful analysis than has previously been considered, in order to extract ϵ_i from the observed drop in the power of the reflected light on resonance (see e.g. Fig. 2.12(b)). The treatment of the reflective coupling problem in terms of the interference of spatially mode-filtered light fields (see App. B for details and [81, 82] for earlier related works on the topic) gives rise to two important practical results for FFPCs:

First, the model explains, for the first time, the origin of the asymmetry of FFPC resonance line shapes that are observed in reflection but not in transmission (as we saw in the previous section Fig. 2.12(b)). The asymmetry is found to be an intrinsic property of FFPCs and independent of the power and polarization of the incident light, and can be described by the sum of a Lorentzian and its corresponding dispersive function. We find good agreement between theory and experimental measurements, thereby confirming our model of the effects of spatial mode filtering in FFPCs.

Second, our calculations show that for strongly overcoupled FFPCs, where the transmission of the incoupling mirror strongly exceeds the sum of all other contributions to the round trip losses ($\mathcal{T}_{\text{HT}} \gg \mathcal{T}_{\text{LT}} + \mathcal{L}_{\text{LT}} + \mathcal{L}_{\text{HT}}$), the alignment that maximizes the depth of reflected incoupling dip does not maximize the spatial mode matching efficiency ϵ_{HT}. In fact, for this experimentally very relevant type of one-sided cavity, the maximum depth of the incoupling dip will approach unity for misalignments that significantly reduce the mode matching efficiency. This is in agreement with the discrepancies observed in the previous analysis of incoupling efficiency for different cavity lengths (see Figure 2.13(b)). We experimentally confirm this result with additional measurements on a strongly overcoupled test cavity and find good agreement with the theoretical predictions.

Notation: To keep our notation compact, we write all electric fields involved in the formulation of the problem (see Fig. 2.15) as

$$E_i = \mathcal{E}_i \cdot |\psi_i\rangle,$$

where the Dirac notation is used for the description of the spatial mode components [76] and $\mathcal{E}_i$ contains the complex amplitude of the field, including the time dependence $e^{i\omega t}$. The overlap integrals of normalized spatial-mode functions can thus be basis-independently expressed as $\langle \psi_i | \psi_j \rangle$.

For the description of the mode matching geometry (shown in Figure. 2.16(a)) we introduce four spatial modes: the forward and backward propagating modes in the single mode fiber $|\psi_f^\pm\rangle$, the spatial mode $|\psi_r\rangle$ corresponding to the fiber-mirror reflection of the forward propagating fiber mode $|\psi_f^+\rangle$, and the forward and backward propagating cavity modes $|\psi_{\text{cav}}^\pm\rangle$.
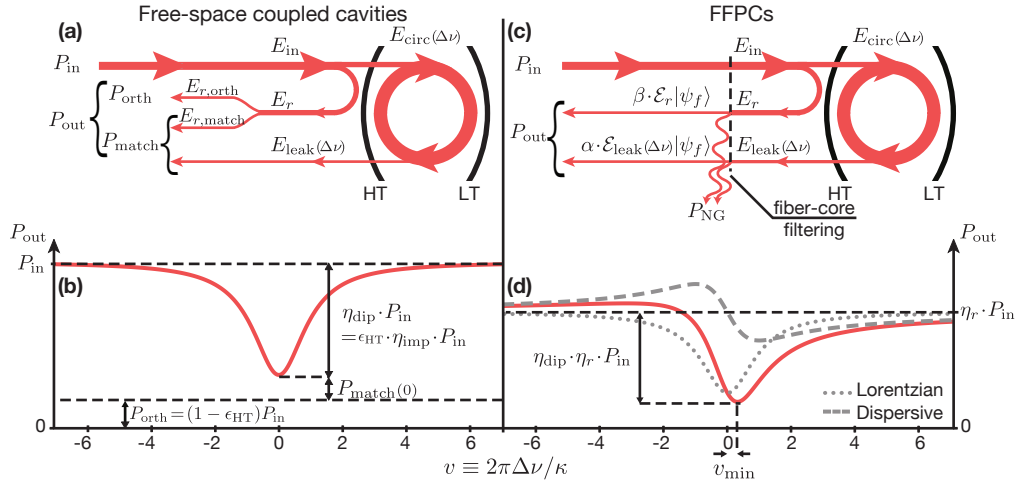
Figure 2.15: Illustration of the contributions to the reflective cavity line shapes. For free-space coupled cavities, the interference of the spatially mode matched part of the directly reflected field E_r interferes with the cavity leakage field E_{leak} **(a)** and gives rise to the Lorentzian dip in the cavity reflected power at resonance **(b)**. For FFPCs, the mode filtering of the reflected light by the single mode fiber implies that the two fields can fully interfere **(c)** and the depth of the asymmetric line shape is no longer directly related to the spatial mode efficiency ϵ_{HT} **(d)** (see main text for details).

We name their mutual overlap integrals

$$
\begin{aligned}
\langle\psi_{\text{cav}}^{+}|\psi_{f}^{+}\rangle &= \alpha \\
\langle\psi_{\text{cav}}^{-}|\psi_{r}\rangle &= \langle\psi_{\text{cav}}^{+}|\,R^{\dagger}R\,|\psi_{f}^{+}\rangle = \langle\psi_{\text{cav}}^{+}|\psi_{f}^{+}\rangle = \alpha \\
\langle\psi_{\text{cav}}^{-}|\psi_{f}^{-}\rangle &= (\langle\psi_{\text{cav}}^{+}|\psi_{f}^{+}\rangle)^{*} = \alpha^{*} \\
\langle\psi_{f}^{-}|\psi_{r}\rangle &= \beta,
\end{aligned}
\tag{2.14}
$$

with the overlap amplitudes $\alpha,\beta\in\mathbb{C}$. The mode matching efficiency from the fiber mode to the cavity is then given by [76]

$$
\epsilon_{\text{HT}} = |\langle\psi_{\text{cav}}^{+}|\psi_{f}^{+}\rangle|^{2} = |\alpha|^{2}.
\tag{2.15}
$$

Furthermore, in Equation 2.14 we utilize the fact that reflection (from the incoupling mirror) is a unitary transformation ($R^{\dagger}R=\mathbb{1}$) and that overlap amplitudes are conjugated when the directions of propagation of both modes are changed [38].

Mode Matching in Free-Space Coupled Cavities

We start by revisiting the reflective mode matching problem for the well known case of free-space coupled cavities [79]. Fig. 2.15(a) illustrates that for the incident light field

$$
E_{\text{in}} = \mathcal{E}_{\text{in}}\,|\psi_{f}^{+}\rangle
$$

---

[38] This is evident for the overlap integral of Gaussian beams, where for the complex spatial mode functions the relation $\psi_{i,\vec{k}}(x,y,z) = \psi_{i,-\vec{k}}^{*}(x,y,z)$ holds and hence $\int_{-\infty}^{\infty}\int_{-\infty}^{\infty}\psi_{1,\vec{k}_{1}}^{*}(x,y,z)\psi_{2,\vec{k}_{2}}(x,y,z)\,dxdy = (\int_{-\infty}^{\infty}\int_{-\infty}^{\infty}\psi_{1,-\vec{k}_{1}}^{*}(x,y,z)\psi_{2,-\vec{k}_{2}}(x,y,z)\,dxdy)^{*}$ (see App. B for details).

the reflected signal on a photodetector can be understood from the interference of the two light fields $E_{\text{leak}}(\Delta\nu)$ and E_r (where $\Delta\nu = \nu_{\text{laser}} - \nu_{\text{cav}}$).

The transmission of the detuning-dependent intracavity field

$$E_{\text{circ}}(\Delta\nu) = \mathcal{E}_{\text{in}} \frac{i\, t_{\text{HT}} \langle \psi_{\text{cav}}^+ | \psi_f^+ \rangle}{1 - r_{\text{HT}}\, r_{\text{LT}}\, e^{i\phi}} | \psi_{\text{cav}}^+ \rangle$$

through the incoupling mirror gives rise to the leakage field

$$
\begin{aligned}
E_{\text{leak}}(\Delta\nu) &= i\, t_{\text{HT}} \cdot \mathcal{E}_{\text{circ}} \cdot r_{\text{LT}}\, e^{i\phi} | \psi_{\text{cav}}^- \rangle \\
&= -\mathcal{E}_{\text{in}} \frac{t_{\text{HT}}^2\, r_{\text{LT}}\, e^{i\phi}}{1 - r_{\text{HT}}\, r_{\text{LT}}\, e^{i\phi}} \langle \psi_{\text{cav}}^+ | \psi_f^+ \rangle | \psi_{\text{cav}}^- \rangle \\
&= -\mathcal{E}_{\text{in}} \cdot \zeta(\Delta\nu) \cdot \langle \psi_{\text{cav}}^+ | \psi_f^+ \rangle | \psi_{\text{cav}}^- \rangle,
\end{aligned}
\tag{2.16}
$$

where a phase factor $\pi/2$ upon mirror transmission and the round-trip phase $\phi = 2\pi\Delta\nu \cdot c/2L_{\text{cav}} = 2\pi\Delta\nu/\Delta\nu_{\text{FSR}}$ have been considered (see [47] or Sec. 2.1). r_i, t_i are the reflection and transmission coefficients of cavity mirror i. c and $\Delta\nu_{\text{FSR}}$ denote the speed of light and the cavity free spectral range, respectively. Additionally, the complex quantity $\zeta(\Delta\nu)$ is introduced in Eq. 2.16 to describe the leakage field's dependence on mirror properties and the cavity length.

The field directly reflected from the incoupling mirror

$$E_r = r_{\text{HT}} \cdot \mathcal{E}_{\text{in}} | \psi_r \rangle \simeq \mathcal{E}_{\text{in}} | \psi_r \rangle,$$

can be decomposed into a part

$$E_{r,\text{match}} = \left(\langle \psi_{\text{cav}}^- | E_r \rangle \right) | \psi_{\text{cav}}^- \rangle = \mathcal{E}_{\text{in}} \langle \psi_{\text{cav}}^- | \psi_r \rangle | \psi_{\text{cav}}^- \rangle$$

that is mode matched to the cavity and therefore interferes with $E_{\text{leak}}(\Delta\nu)$, and a part

$$E_{r,\text{orth}} = E_r - E_{r,\text{match}} = \mathcal{E}_{\text{in}} \left(| \psi_r \rangle - \langle \psi_{\text{cav}}^- | \psi_r \rangle | \psi_{\text{cav}}^- \rangle \right)$$

that is orthogonal to the cavity mode and by definition does not interfere.
The total power recorded at the detector is then given by

$$
\begin{aligned}
P_{\text{out}} &= P_{\text{orth}} + P_{\text{match}}(\Delta\nu) \\
&= E_{r,\text{orth}}^\dagger E_{r,\text{orth}} + (E_{r,\text{match}} + E_{\text{leak}}(\Delta\nu))^\dagger (E_{r,\text{match}} + E_{\text{leak}}(\Delta\nu)) \\
&= P_{\text{in}}(1 - \epsilon_{\text{HT}}) + P_{\text{in}}\left(\epsilon_{\text{HT}} \left| 1 - \zeta(\Delta\nu) \right|^2 \right).
\end{aligned}
\tag{2.17}
$$

The Taylor expansion of Eq. 2.17 around the resonance ν_{cav} (for $\Delta\nu/\Delta\nu_{\text{FSR}} \ll 1$) yields the familiar result of Lorentzian dips in the reflected power at the cavity resonances

$$\frac{P_{\text{out}}(\nu)}{P_{\text{in}}} = 1 - \eta_{\text{dip}} \frac{1}{1 + \nu^2}, \tag{2.18}$$
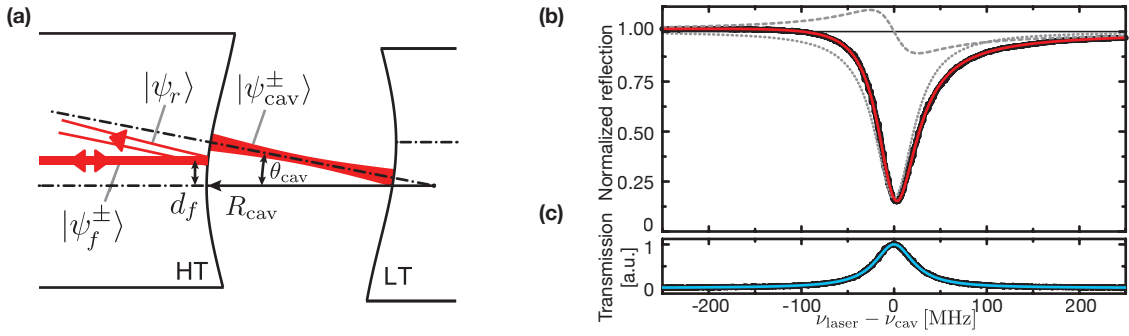
Figure 2.16: **(a)** Geometry of the FFPC mode matching problem. The relative alignment of the forward and backward propagating fiber ($|\psi_f^\pm\rangle$) and cavity ($|\psi_{\mathrm{cav}}^\pm\rangle$) modes and the mode ($|\psi_r\rangle$) corresponding to the fiber-mirror reflection of $|\psi_f^+\rangle$ is shown along one spatial dimension. An equivalent description holds for the other transverse direction. **(b)** Normalized reflective and transmissive line shapes of the FFPC (experimental data and fits). The power and polarization independent asymmetry in the reflected light results from spatial mode filtering of the interfering fields reflected from the cavity by the single mode fiber (fiber mirrors used: #304 and #708). The fit function (red solid line, Eq. 2.21 normalized to the off-resonantly detected power) predicted by the mode matching model is the sum of a Lorentzian (dotted line) and its corresponding dispersive function (dashed line). The extracted mode-overlap coefficients from the fit are: $\alpha = 0.735 - 0.157i$ and $\beta = 0.93 - 0.256i$. **(c)** The transmitted power follows a Lorentzian curve.

where $v = 2\pi(\nu_{\mathrm{laser}} - \nu_{\mathrm{cav}})/\kappa$ is the normalized detuning. The dip amplitude

$$\eta_{\mathrm{dip}} = \epsilon_{\mathrm{HT}} \cdot \left(1 - \left|1 - \zeta(0)\right|^2\right) \tag{2.19}$$

$$= \epsilon_{\mathrm{HT}} \cdot \left(1 - \frac{(\mathcal{T}_{\mathrm{HT}} - \mathcal{T}_{\mathrm{LT}} - \mathcal{L}_{\mathrm{HT}} - \mathcal{L}_{\mathrm{LT}})^2}{\mathcal{L}_{\mathrm{sum}}^2}\right) = \epsilon_{\mathrm{HT}} \cdot \eta_{\mathrm{imp}}$$

$$\text{with} \quad \mathcal{L}_{\mathrm{sum}} = \mathcal{T}_{\mathrm{HT}} + \mathcal{T}_{\mathrm{LT}} + \mathcal{L}_{\mathrm{HT}} + \mathcal{L}_{\mathrm{LT}}$$

is directly proportional to the spatial mode matching ϵ_{HT}, which can thus be easily determined once the mirror parameters are independently measured. According to Eq. 2.19, the depth of the reflective dip η_{dip} is maximum for cavity mirrors that satisfy the impedance matching condition ($\mathcal{T}_{\mathrm{HT}} = \mathcal{T}_{\mathrm{LT}} + \mathcal{L}_{\mathrm{HT}} + \mathcal{L}_{\mathrm{LT}}$; $\eta_{\mathrm{imp}} = 1$) and decreases symmetrically for equally overcoupled and undercoupled cavities.

Mode Matching in FFPCs and Spatially Mode-filtered Cavities

The reflective mode matching for FFPCs can be imagined as the case of a free-space coupled cavity followed by spatial mode filtering of the returning light by the single mode fiber (see Fig. 2.15(b)). Only light that couples back into the fiber mode is guided back to the detector, whereas the light entering the cladding modes is lost and does not reach the detector. The light field that is guided back in the fiber mode

$$E_{\mathrm{out}}(\Delta\nu) = \left(\langle\psi_f^-| E_r + \langle\psi_f^-| E_{\mathrm{leak}}(\Delta\nu)\right)|\psi_f^-\rangle$$

$$= \mathcal{E}_{\mathrm{in}}\left(\langle\psi_f^-|\psi_r\rangle + \zeta(\Delta\nu)\langle\psi_{\mathrm{cav}}^+|\psi_f^+\rangle\langle\psi_f^-|\psi_{\mathrm{cav}}^-\rangle\right)|\psi_f^-\rangle$$

thus results in the detected power

$$P_{\text{out}} = E_{\text{out}}^{\dagger}E_{\text{out}} = P_{\text{in}}\left|\beta - \alpha^2 \cdot \zeta(\Delta\nu)\right|^2 \tag{2.20}$$

$$= P_{\text{in}}\left|\frac{1}{\epsilon_{\text{HT}}}\left(\beta \cdot (\alpha^2)^* - \epsilon_{\text{HT}}^2 \cdot \zeta(\Delta\nu)\right)\right|^2.$$

The Taylor approximated ($\Delta\nu/\Delta\nu_{\text{FSR}} \ll 1$) solution

$$\frac{P_{\text{out}}(\nu)}{P_{\text{in}}} = \eta_r - \eta_{\mathscr{L}}\left(\frac{1}{1+\nu^2} - \mathscr{A}\frac{\nu}{1+\nu^2}\right) \tag{2.21}$$

features an asymmetric dip in the reflected power at the cavity resonance that consists of a Lorentzian of amplitude

$$\eta_{\mathscr{L}} = \frac{4\mathcal{T}_{\text{HT}}}{\mathcal{L}_{\text{sum}}}\left(\text{Re}\left[\beta \cdot (\alpha^2)^*\right] - \epsilon_{\text{HT}}^2\frac{\mathcal{T}_{\text{HT}}}{\mathcal{L}_{\text{sum}}}\right)$$

and its corresponding dispersive curve with relative amplitude

$$\mathscr{A} = \frac{\text{Im}\left[\beta \cdot (\alpha^2)^*\right]}{\text{Re}[\beta \cdot (\alpha^2)^*] - \epsilon_{\text{HT}}^2\frac{\mathcal{T}_{\text{HT}}}{\mathcal{L}_{\text{sum}}}},$$

where $\text{Re}\left[...\right]$ and $\text{Im}\left[...\right]$ denote the real and imaginary part.

The comparison of Equations 2.21 and 2.18 in Figure 2.15 illustrates that spatial mode-filtering fundamentally changes the reflective spectral line shape. In the off-resonant case, the divergence and deflection upon reflection on a curved and decentered fiber mirror lead to power losses P_{NG} into non-guiding fiber cladding modes that reduce the fraction of incident light that reaches the detector by $\eta_r = |\beta|^2$. The depth η_{dip} of the asymmetric FFPC dip is no longer limited by ϵ_{HT}, is not maximum for the impedance matched condition ($\mathcal{T}_{\text{HT}} = \mathcal{T}_{\text{LT}} + \mathcal{L}_{\text{HT}} + \mathcal{L}_{\text{LT}}$) and responds differently to overcoupling or undercoupling. In particular for significantly overcoupled cavities, the state $\eta_{\text{dip}} = 1$ can always be reached for sufficient misalignment, i.e. reduction of ϵ_{HT}. No differences arise in the line shape of the circulating power and the transmission of FFPCs, which are Lorentzian as in the case of free-space coupled cavities. The minimum of the reflective power $P_{\text{out}}(\nu_{\text{min}})/P_{\text{in}} = \eta_r(1 = \eta_{\text{dip}})$ is hence shifted relative to the (transmissive) cavity resonance frequency by $\nu_{\text{min}} = \left(1 - \sqrt{1+\mathscr{A}^2}\right)/\mathscr{A}$. The validity of the model is confirmed by the excellent agreement with the experimental reflective and transmissive line shapes shown in Figure 2.16(b). The FFPC in use is an HT-LT fiber cavity (characterized in Section 2.4 and used in the experiments of following chapters) that displays an estimated mode-matching efficiency of 0.60 ± 0.02.

Optimal FFPC alignment

The geometry of FFPC alignments is sketched in Figure 2.16(a). By factoring the overlap integrals along two orthogonal directions $\langle\psi_i\rangle\psi_j = \langle\psi_{i,x}|\psi_{j,x}\rangle\langle\psi_{i,y}|\psi_{j,y}\rangle$, the problem can be analyzed by considering two individual one-dimensional alignments [76]. Optimal alignment for a one-sided cavity corresponds to maximizing the spatial mode matching efficiency $\epsilon_{\text{HT}} = |\alpha|^2$ from the cavity mode to the HT-fiber. This is achieved by adjusting the cavity angles $\theta_{\text{cav},x}$ and $\theta_{\text{cav},y}$ using the transversal displacement or the relative inclination of the fiber mirrors.

For the theoretical modeling of the alignment-dependent mode matching and reflective line shapes (with Equations 2.15 and 2.21) the mode overlap amplitudes α and β need to be evaluated in terms of the
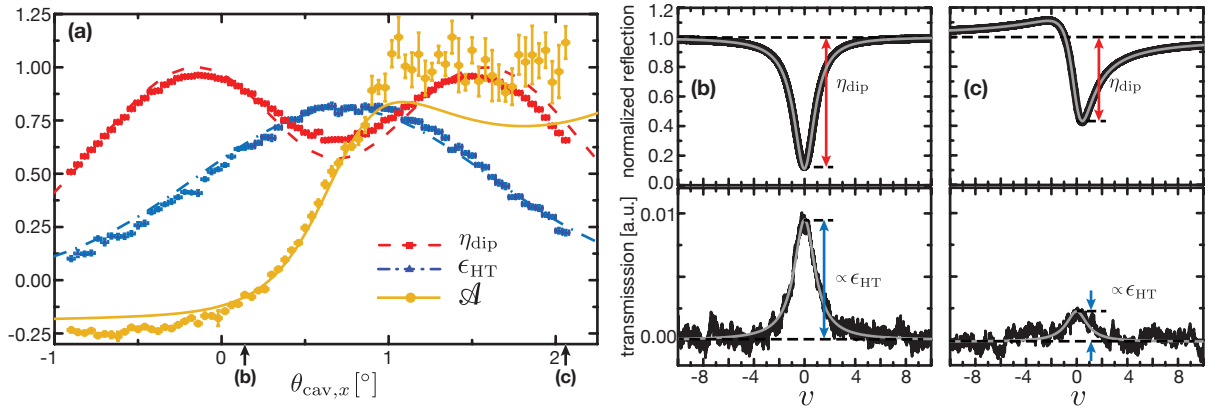
Figure 2.17: Experimental verification of the FFPC alignment model. **(a)** Spatial mode matching efficiency ϵ_{HT}, depth of dip in reflection η_{dip} and asymmetry parameter $\mathscr{A}$ as a function of the cavity alignment. The theoretical model (lines) agrees well with the experimental data points for the strongly overcoupled FFPC. The error bars in y-direction denote the one-sigma *standard error of the mean* from 10 identical measurements. x-errors denote the estimated precision of the rotation stage. The optimal cavity alignment occurs for a cavity mode angle of $0.8°$ due to the significant decentration of the mirror fiber. The experimentally observed maximum of η_{dip} is reduced compared to the theoretically predicted value $\eta_{\mathrm{dip, max}} = 1$ due to the background light from reflections along the optical path. Parameters extracted from the fit: $\mathrm{CT} = 0.82$, $\theta_{\mathrm{cav},y} = 0.15°$, $\theta_{\mathrm{cav},x0} = -2.1°$ and $\phi = 5.4°$. Reflective and transmissive line shapes are shown for the cavity angles $\sim0°$ **(b)** and $\sim2°$ **(c)**. The curves (gray) represent a fit of the data (black) to the model of Eq. (2.21).

cavity mirror parameter (radii of curvature R_{HT}, R_{LT}, mirror decentrations $d_{f,x}$, $d_{f,y}$ and fiber mode field radius w_f) and the alignment parameters (cavity length L_{cav} and cavity alignment angles $\theta_{\mathrm{cav},x}$ and $\theta_{\mathrm{cav},y}$). We find analytic expressions for α and β by performing the overlap integration of the modes $|\psi_f^{\pm}\rangle$, $|\psi_{\mathrm{cav}}^{\pm}\rangle$ and $|\psi_r\rangle$ represented as inclined and displaced Gaussian beams, from where we finally obtain analytic expression for $\mathscr{A}$, η_{dip} and ϵ_{HT} (for details of the calculation see App. B).

To experimentally confirm the calculation we perform measurements on a strongly overcoupled hybrid cavity that is formed by the combination of an HT fiber mirror and a macroscopic mirror substrate with ultra-low transmission ($\mathcal{T}_{\mathrm{ULT},850\,\mathrm{nm}} = 0.9\,\mathrm{ppm}$, $\mathcal{L}_{\mathrm{ULT},850\,\mathrm{nm}} = 4\,\mathrm{ppm}$, $R_{\mathrm{ULT}} = 50\,000\,\mu\mathrm{m}$ [52]). We record the reflective as well as the transmitted line shape as a function of the inclination angle θ_m of the mirror substrate by adapting the cavity-characterization setup introduced in the previous section. Due to the gimbal mounting of the nearly flat ($R_{\mathrm{ULT}} \gg R_{\mathrm{HT}}$) ULT mirror, we can make the approximations $\theta_m \simeq \theta_{\mathrm{cav},x}$ and $L_{\mathrm{cav}}(\theta_{\mathrm{cav},x}) \simeq L_{\mathrm{cav}}(0)$. By fitting Eq. 2.21 to the the reflective line shapes we obtain $\mathscr{A}$ and η_{dip} (see Fig. 2.17(b,c)). Moreover, since the mode matching efficiency on the ULT mirror side can be assumed as independent of the alignment ($\epsilon_{\mathrm{ULT}} \approx 1$), it follows from Eq. 2.13 that the fiber to cavity mode matching efficiency $\epsilon_{\mathrm{HT}}(\theta_{\mathrm{cav},x}) = C_T \cdot P_{\mathrm{T,max}}(\theta_{\mathrm{cav},x})$ is proportional to the resonant cavity transmission signal $P_{\mathrm{T,max}}$.

We simultaneously fit the three sets of data with their corresponding model functions $\mathscr{A}(\theta_{\mathrm{cav},x})$, $\eta_{\mathrm{dip}}(\theta_{\mathrm{cav},x})$ and $\epsilon_{\mathrm{HT}}(\theta_{\mathrm{cav},x})$ by minimizing the (unweighted) sum of all least-square residuals (see Fig. 2.17(a) and Supplemental Material in [1]). In addition to the independently measured constants $R_{\mathrm{HT}} = (150 \pm 15)\,\mu\mathrm{m}$, R_{ULT}, $L_{\mathrm{cav}} = (16.9 \pm 0.5)\,\mu\mathrm{m}$[39], $d_f = (2.0 \pm 0.4)\,\mu\mathrm{m}$, $w_f = (2.60 \pm 0.05)\,\mu\mathrm{m}$, $\mathcal{T}_{\mathrm{HT},850\,\mathrm{nm}}$ and $\mathcal{L}_{\mathrm{sum},850\,\mathrm{nm}}$, the model functions depend on four experimentally unknown or inaccurately constrained factors, which we use as free parameters of the fit. These are the alignment angle $\theta_{\mathrm{cav},y} \approx 0$ along the

---

[39] The length was estimated by tuning two independent lasers such that their wavelengths λ_1 and λ_2 are resonant with consecutive longitudinal cavity modes which allows one to obtain the cavity length by the relation $L_{\mathrm{cav}} = \lambda_1\lambda_2/(2(\lambda_2 - \lambda_1))$.

y-axis, the absolute zero position of the scan of the alignment angle along the x-axis ($\theta_{\text{cav},x0}$), the orientation ϕ of the fiber-mirror decentration axis relative to the x-axis ($d_{f,x} = d_f \cdot \cos(\phi)$, $d_{f,y} = d_f \cdot \sin(\phi)$) and the absolute calibration constant C_T of the mode matching efficiency. We find good agreement between the experimental data and the theoretical model for the hybrid cavity (see Fig. 2.17). Significantly better agreement is found for a fiber-mirror decentration of $d_f = 2.7\,\mu\text{m}$ (see App. B), which could indicate that our characterization of the fiber mirror by interferometric imaging ($d_f = (2.0 \pm 0.4)\,\mu\text{m}$) underestimates the fiber-mirror decentration. Our investigation makes it possible to determine and therefore optimize individual mode matching efficiencies ϵ_{HT}, ϵ_{LT} using the easily accessible quantities $\mathcal{A}$ and η_{dip} from cavity reflection measurements.

2.4 Vacuum-compatible Integrated Fiber-Cavity System

Due to their intrinsic properties, FFPCs are the ideal platform for future applications of high finesse micro-resonators and the implementation of scalable and robust CQED systems. Thus, the development of compact portable FFPC-based devices and novel technical solutions for their assembly and stabilization will be required. In this section we show how the miniaturization of the fiber mirrors can be exploited by integrating them in a small vacuum-compatible assembly that includes the necessary high-NA optics for neutral-atom experiments. The optical system does not only facilitate a stable and tight confinement of atoms inside the resonator, but can also be used as a high-resolution atom microscope. While being compact, the assembly displays wide optical access to the cavity and the ability to externally tune and precisely stabilize its length.

2.4.1 A Miniaturized Optical System

To provide intrinsic stability to our cavity and imaging system, we developed a compact and monolithic structure to which — after a precise alignment — the components are glued together forming a robust assembly. This type of mounting, where the fiber mirrors and high-NA lenses are permanently glued in a fixed position, provides higher stability and increases the scalability of the system, as no additional precision stages or macroscopic piezo-electric elements are necessary inside the vacuum system[40]. The robustness is ensured by the short cavity length ($<100\,\mu\text{m}$) and low thermal expansions of the ceramic and glass components used, which prevent severe misalignments in the system due to slow temperature drifts or external tensions. However, the precise alignment and curing process must be carefully performed since critical parameters like the cavity length, its mode matching efficiency or the focal plane of the optical system cannot be modified after the assembly. In the following we discuss the details of the main components and steps necessary for a successful construction, along with a summary of the properties of the resulting system.

Assembling the Fiber Cavity

The assembly procedure begins by preparing the selected fiber mirrors with the annealing and splicing techniques discussed in Appendix A.1. After a quick characterization of their transmission properties, both fibers are placed in the cavity-characterization setup employed in Section 2.3 where the mirrors, mounted facing each other, can be aligned to form a resonator with sub-micrometric precision. The process is at all times monitored by recording the reflection and transmission of the cavity for 780 nm

---

[40] The option to realign the cavity after it has been placed in vacuum is nevertheless relevant for systems with long resonators which are more sensitive to thermal or tension misalignments. This also applies to scenarios where it is convenient to move the mirrors by macroscopic distances, as it is recommended during the trapping of ions (see e.g. [30, 60]).
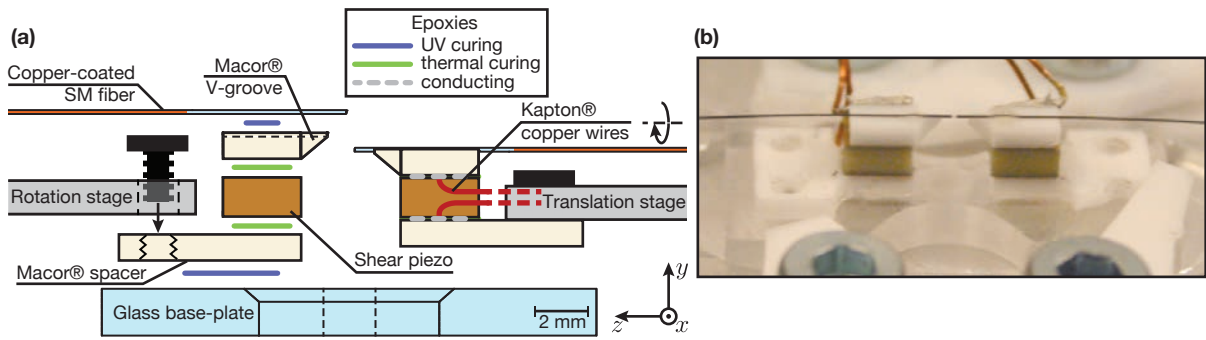
Figure 2.18: Assembly of the FFPC system. **(a)** Sketch of the main components of the alignment and assemblage procedure. Left: Individual parts of the stack and different gluing layers. The thermal curing of the stack is done before gluing the fibers to it. Right: glued piezo–Macor bundle attached to the stage. The stages keep the cavity aligned during the last gluing to the base-plate, while the piezos scan over the resonance to monitor the incoupling. **(b)** Photograph of the assembled and baked-out FPPC system employed in the following neutral-atom experiments.

laser light and, additionally, observed by two perpendicular microscopes. After reducing any polarization-mode splitting by rotating one of the mirrors with respect to the other (see Section 2.3.1) each fiber is glued onto a ceramic Macor® V-groove with vacuum-compatible UV-cured glue[41]. These V-grooves are part of a custom-made vertical stack additionally composed of a shear piezoelectric actuator[42] (piezo) and a Macor T-shaped spacer, which are glued together using thermally-cured epoxy[43]. Both surfaces of each piezo element are connected to Kapton®-protected copper wires[44] by means of an electrical conductive paste[45] thus allowing their external driving. Figure 2.18(a) summarizes the main components of the cavity assembly.

Each of the piezo–Macor bundles is screwed onto their respective alignment stages (translational for the incoupling mirror, rotational for the outcoupler). Once the fiber has been glued onto the groove, the assemblage can be used to scan the cavity resonance while both stacks are being aligned to the desired resonator length and glued onto a common plate. Monitoring the cavity resonance — by scanning the high voltage driving of the shear piezos — is necessary to maintain the resonator aligned during this critical gluing step, where the FFPC coupling and length are finally fixed. The base-plate where both stacks are mounted (also referred to as cavity bridge) acts as the monolithic element keeping a constant spacing and alignment of the fibers. The bridge is made out of glass to allow UV light through, in order to cure the glue used in the last step. The use of light-cured glue is important to maintain and correct the alignment during the procedure, which would not be possible with thermally-cured composites.

Once the cavity system has been fully assembled (see Fig. 2.18(b)), it is clamped onto a temporal metallic base and baked out at around 100 °C for a few hours to ensure the proper curing of the glues. In order to avoid misalignment due to hysteresis during the thermal expansion of the system, we keep the thickness of the glue layers to a minimum. For the FPPC used in the present experiments, the transmission peak was slightly reduced after the thermal curing. However, no major change was observed in the reflection signal.

The compact assembly is designed to fulfill the optical access requirements for trapping and cooling

---

[41] UV curable epoxy adhesive: *EPO-TEK® OG116-31* (Epoxy Technology Inc).
[42] Shear piezo electric actuator: *PIC255* 3×3×1.5 mm (PI Ceramic GmbH).
[43] Two-components high temperature epoxy: *EPO-TEK® 353ND* (Epoxy Technology Inc).
[44] Kapton® insulated, 0.3 mm diameter wire for UHV: *311-KAP-025* (Allectra GmbH).
[45] Two-components silver filled epoxy: *EPO-TEK® H20-E* (Epoxy Technology Inc).
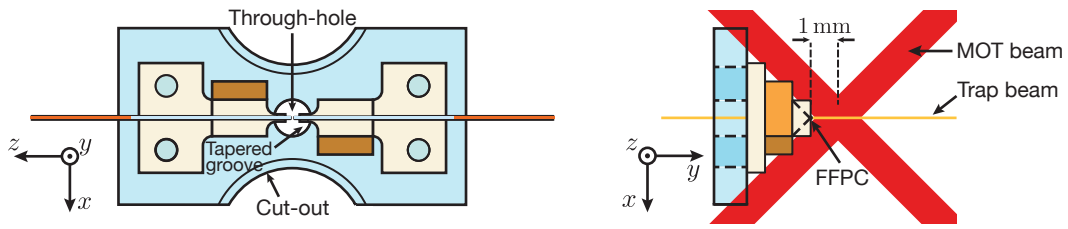
Figure 2.19: Optical access of the FPPC system. Left: Top view showing the through-hole and side circular cut-outs of the cavity bridge. The tapered end of the V-grooves is also visible. Right: Side view showing the optical layout of the MOT (red) and one of the dipole-trap beams (orange). A detailed description can be found in Sec. 3.1.

neutral atoms in the vicinity of the cavity. As will be discussed in detail in Sec. 3.1, a Magneto-Optical Trap (MOT) must be created as close as possible to the cavity to provide efficient atomic transport; with MOT beams with radii on the order of 700 μm, it is critical that enough optical access is provided to avoid their clipping or distortion. This conditions are ensured by tapering the end of the V-grooves where the fibers sit, and grinding out circular sections on both sides of the glass base-plate (see Fig. 2.19). Furthermore, the confinement of atoms inside the cavity is provided by external dipole trap beams which are focussed at the center of the cavity (see next section for details about the integrated focussing optics). The cavity length must be enough to provide clearance to the high-power trapping beams, in order to avoid scattering, diffraction or — most importantly — absorption of the light that could lead to instabilities in the cavity length or damage of the mirrors. The size of the beams at the position of the resonator is designed to be 13 μm which — given our typical cavity lengths around 100 μm — is small enough to avoid any of those adverse effects. The strong divergence associated with such small waists leads to a spot size of the dipole trap beams of ~200 μm at the position of the base plate, which requires a 2 mm through-hole at its center to ensure negligible clipping and certain freedom of alignment.

Integration with a High-NA Imaging System

The tight confinement of neutral atoms inside the resonator requires strongly focussed dipole trap beams. Although this can be achieved by long working distance microscopes [83], it is in general more convenient to use lenses with short a focal length. Their small working distance provides high beam-pointing stability and makes these lenses the ideal optical element for the miniaturization of the system, as their compact design allows the integration with the fiber-cavity assembly. By employing lenses with high NA that collect a considerable fraction of the fluorescence emitted by the atoms, the system provides a much better signal-to-noise ratio and resolution of single atom images (see Section 3.2.1).

We equip our fiber cavity with an imaging system composed of four aspheric lenses[46] with NA = 0.5 and a working distance of 5.9 mm (effective focal length of 8 mm). The lenses sit in a custom-made vacuum-compatible holder (made out of PEEK®), such that all of them are focused at the same virtual point (eventually the center of the cavity mode). In order to avoid clipping or distortion of the MOT beams, parts of the outer rim of the lenses are removed by smooth grinding (as seen in Fig. 2.20). The system is a modification of an earlier version (without cavity) used and extensively described in reference [84], which also contains a description of the lens alignment technique. After each lens is aligned to the correct position (with a precision below 5 μm), it is fixed to the bottom half of the holder by UV-cured glue (see Fig. 2.20(b)). The fiber cavity is then placed at the center (see Fig. 2.20(c)) and aligned to the common focal plane by looking at the shadow casted by the fiber mirrors when they clip a

---

[46] Unmounted Geltech Aspheric Lens, AR (600-1 050 nm): *352240-B* (Thorlabs Inc).
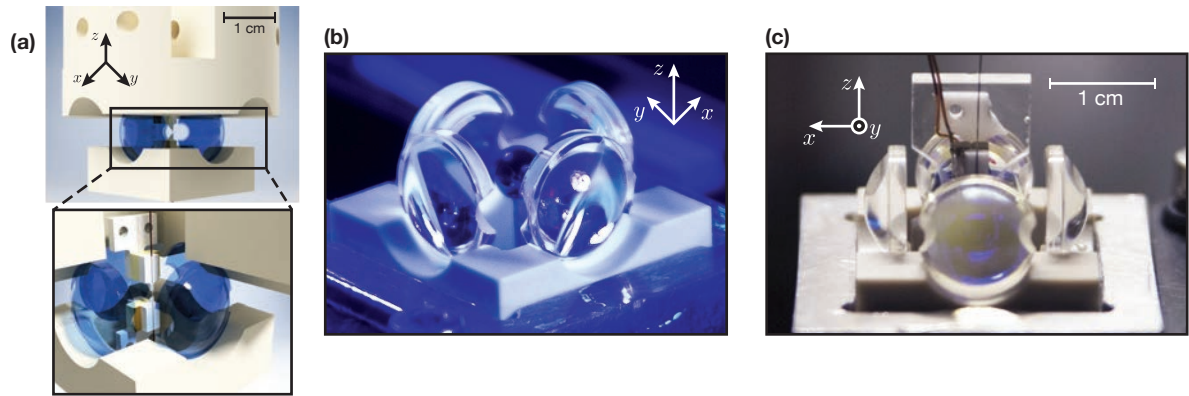
Figure 2.20: Integration of the FPPC in a high-NA imaging system. **(a)** Rendering of the integrated system composed of the PEEK holder (yellow), the four high-NA lenses (blue) and the cavity assembly at its core (see inset). **(b)** The image shows the four lenses glued to the bottom holder while UV illumination curing is taking place. The ball at the center is a smooth reflective sphere used to align all lenses to the same virtual point (see [84]). **(c)** Image of the cavity assembly (mounted vertically) after being attached to the lens holder. A picture of the whole system including the full holder and the metallic structure can be found in Sec. 3.1.1.

beam focused by the lenses[47]. The cavity bridge is previously provided with a thin layer of UV-curable glue, such that when the optimal alignment is achieved the system can be directly cured without further mechanical disturbances. The remaining top half of the holder is then attached and the final assembly is connected to a metallic structure that provides support in the vacuum apparatus (see Sec. 3.1.1). All the components are baked-out in a high-vacuum environment to ensure the proper outgassing of the glues.

   Although alignment precisions below $10\,\mu$m can be achieved for the positioning of the cavity, we observed — after several bake-outs and its insertion in the vacuum vessel — a displacement of around $50\,\mu$m between the fiber cavity and the focal plane of, at least, one of the lenses[48]. The misalignment is attributed to thermal expansion of the (thick) layer of glue required to attach the cavity bridge to the PEEK holder.

Characteristics of the Fiber Cavity Used in the Neutral Atoms Experiment

For the construction of the FPPC used in the experiment, we follow the requirements exposed in Section 2.1.2. The optical fibers must be single-mode fibers in order to obtain high incoupling efficiencies and maintain the transversal mode of the cavity output. Additionally, we aim to form cavities with asymmetric coating properties (HT–LT) to ensure a highly directional input-output channel (provided by the high transmission mirror). For that reason we chose two single-mode fiber mirrors (with high and low transmission respectively) that display the required radii of curvature and no apparent clipping losses for distances of ~$100\,\mu$m. They where selected due to their small decentration and after making sure that their intrinsic polarization-mode splitting could be reduced to a small fraction of the resonator linewidth (by the rotation of one of the mirrors). After the construction of the cavity, several characterization

---

[47] A wide beam of 1 cm waist is sent to two of the perpendicular lenses and strongly focussed down to $w \approx 1\,\mu$m at the common focal plane. The fiber cavity is then displaced with micrometrical resolution around the central region where the alignment is performed by monitoring the clipping effects of the fiber mirrors on the transmitted beams.

[48] This is observed by the fact that an extra compensation lens was required outside the vacuum in order to collimate the output beam. The estimation, performed by a colleague, was realized by simulating in OSLO® the misalignment that would correspond to such a scenario.

Table 2.2: Relevant parameters of the FPPC used in the neutral-atom experiments. All properties are measured or derived for 780 nm unless otherwise specified. The error bars correspond to either direct or propagated experimental uncertainties. All methods and quantities have been introduced in the previous sections, except those involving the lock laser which are described in Sec. 2.4.2. The cavity QED rates are calculated for a single atom at the center of the cavity mode.

Parameter		Value	Extracted from
Mirrors (HT/LT)			
Fiber-mirror ID		#304(SM)/#708(SM)	
Core mode waist	w_f	$(2.53 \pm 0.03)\,\mu\mathrm{m}$	output beam profiling
Radius of curvature	R	$(170 \pm 5)/(186 \pm 5)\,\mu\mathrm{m}$	surface reconstruction
Effective diameter	D	$(28.2 \pm 1.0)\,\mu\mathrm{m}$	clipping losses
Mirror decentration	d_f	$(0.7 \pm 0.3)/(0.2 \pm 0.3)\,\mu\mathrm{m}$	surface reconstruction
Transmission	$\mathcal{T}$	$(126 \pm 13)/(13 \pm 3)\,\mathrm{ppm}$	direct measurement
Losses (scat. and abs.)	$\mathcal{L}$	$(26 \pm 5)/(25 \pm 5)\,\mathrm{ppm}$	finesse and transmission
Cavity geometry			
Length	L_cav	$(93.36 \pm 0.03)\,\mu\mathrm{m}$	lock–probe beat length
Mode waist	w_0	$(4.40 \pm 0.04)\,\mu\mathrm{m}$	cavity geometry
Mode volume	V	$(1\,420 \pm 25)\,\mu\mathrm{m}^3$	cavity geometry
Mode radius at mirror	w_m	$(5.26 \pm 0.01)\,\mu\mathrm{m}$	cavity geometry
Input mode matching	ϵ_HT	0.60 ± 0.02	reflection dip asymmetry
Cavity spectroscopy			
Free spectral range	$\Delta\nu_\mathrm{FSR}$	$(1\,606.7 \pm 0.5)\,\mathrm{GHz}$	cavity length
Cavity full width	$\Delta\nu_\mathrm{FWHM}$	$(50.8 \pm 1.0)\,\mathrm{MHz}$	sideband-modulated dip
Finesse (780 nm)	$\mathcal{F}$	$32\,800 \pm 1\,100$	FSR–FWHM ratio
Finesse (770 nm)	$\mathcal{F}_\mathrm{lock}$	$27\,200 \pm 1\,000$	FSR–FWHM ratio
Pol.-mode splitting	$\Delta\nu_\mathrm{spl}$	$(9.0 \pm 0.3)\,\mathrm{MHz}$	Hänsch–Couillaud setup
Lock–probe beat length	d_beat	$(31.12 \pm 0.01)\,\mu\mathrm{m}$	
CQED parameters			
Atom–light coupling	$g_0/2\pi$	$(121.6 \pm 1.1)\,\mathrm{MHz}$	^{87}Rb D$_2$-line cycling transition
Cavity field decay	$\kappa/2\pi$	$(24.5 \pm 0.8)\,\mathrm{MHz}$	cavity linewidth
Atomic dipole decay	$\gamma/2\pi$	$3.03\,\mathrm{MHz}$	rubidium natural decay [85]
Cooperativity	C_1	100 ± 4	

measurements took place including estimations of the final resonator length[49], the input mode-matching efficiency and the cavity finesse. A summary of the main properties of the mirrors and the cavity, along with the derived relevant QED parameters, is shown in Table 2.2.

It must be pointed out that the finesse values described here were measured while the cavity was exposed to air atmosphere. When placed in the high-vacuum conditions of our experiment, the finesse of the cavity degrades with time. The type of decay and the time scales involved are strongly influenced by the presence of ultraviolet (UV) light shone onto the mirrors; in particular we observe that UV radiation

---

[49] An estimation of the length was realized by a colleague by precisely measuring the frequency required for the lock light (see next section) such that the cavity in on resonance with both lock and probe light.
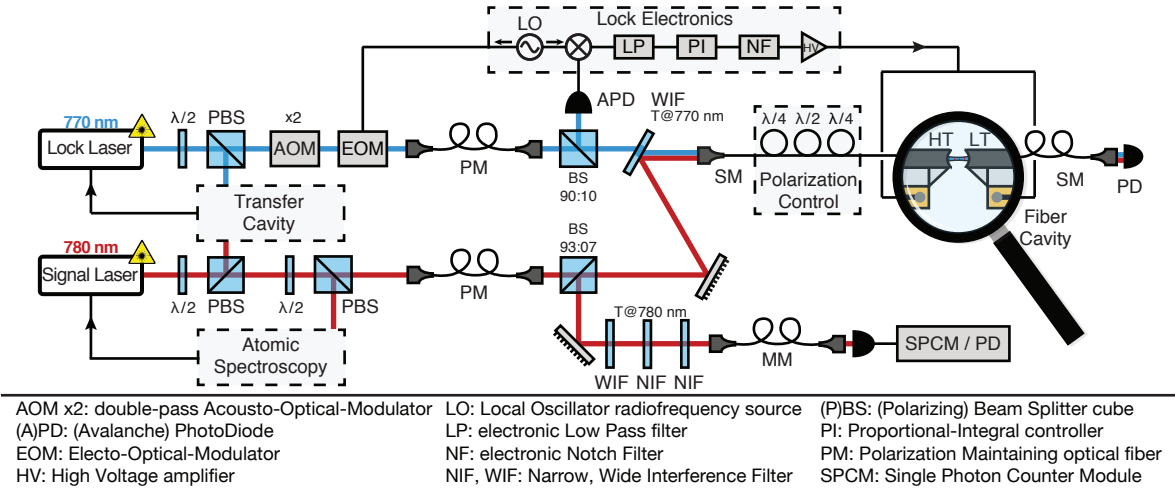
Figure 2.21: Fiber-cavity locking scheme for cavity QED experiments with neutral atoms. An optical resonance of the fiber cavity is stabilized at the ^{87}Rb D$_2$ line at 780 nm by locking a resonator mode with a frequency separation of three free spectral ranges to a far detuned *lock* laser at 770 nm. The lock laser itself is stabilized via a transfer cavity to a rubidium-referenced *signal* laser that is used to resonantly address the cavity. Signal and lock photons enter and exit the one-sided cavity through the fiber mirror with high transmission. A series of band-pass interference filters is employed to separate the 1 μW lock light from single photon signals at 780 nm prior to detection (figure taken from [1]).

can turn a rapid exponential decay of the finesse into a slower decline with a time constant orders of magnitude larger. Appendix A.2 contains a detailed record of the finesse in the time span covering the experiments presented in this thesis, along with a description of the techniques employed to partially recover the original low mirror losses.

2.4.2 Active Stabilization of the Cavity Resonance

The resonator-enhanced light-matter interaction in CQED experiments relies on the precise tuning of a cavity resonance to an optical transition of the quantum system under investigation. In even more miniaturized and integrated experimental setups the task of stabilizing high-finesse FFPCs to within a small fraction of their optical linewidth (corresponding to mirror displacements on the order of 10 pm) can pose significant challenges. In this section we present a summary of the techniques and the optical setup employed for locking our piezo-mechanically actuated FFPC. The implementation and characterization of the setup was performed by my colleague Sutapa Ghosh; the following description is, thus, just a summary of the critical components which will be of relevance in the coming chapters.

First, the signal external-cavity diode laser at 780 nm wavelength is referenced onto a Doppler-free polarization spectroscopy in a rubidium vapor cell. The stability of this laser is transferred onto a *lock* laser near 770 nm by means of an actively stabilized Fabry–Pérot transfer cavity with 1.5 m length

---

[50] *Signal* photons and laser are also referred to as *Probe* in the following chapters.

Figure 2.22: **(a)** The Pound–Drever–Hall error signal (black, bottom) and the reflected lock (blue, middle) and signal power (red, top) are shown for a single scan of the cavity length (figure taken from [1]). The modulated lock reflection dip is also employed as a monitor of the finesse degradation (see App. A.2). **(b)** The effective coupling of the trapped atoms is given by the phase difference between the lock field nodes (trapp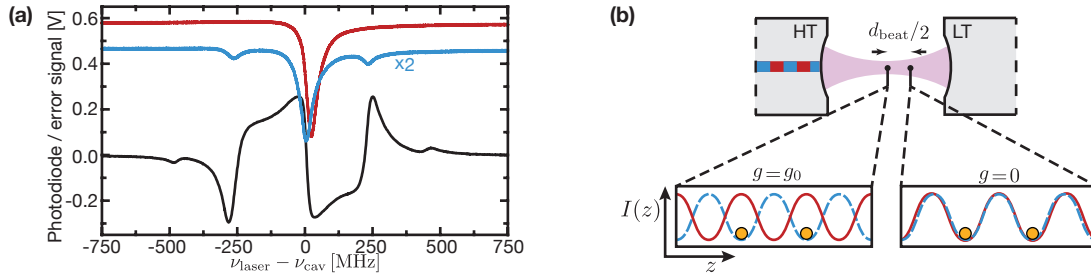ing regions, dashed blue lines) and the signal antinodes (high coupling of the cavity to the atomic resonance, solid red lines). The distance between maximum and zero effective coupling is given by half the beat length between both fields.

and finesse 50. The frequency separation of the lock and the signal laser $\nu_{lock} - \nu_{signal}$ can be fine-tuned with an Acousto-Optical Modulator (AOM) in double-pass configuration to exactly three free spectral ranges of the FFPC, such that both waves are simultaneously resonant with the cavity. Both fields are combined by an interference filter and enter the FFPC through the high-transmission fiber mirror. Sidebands at 248.2 MHz are electro-optically-modulated onto the lock light, which is detected in reflection by a resonant avalanche photodiode (APD) to generate an error signal with the Pound–Drever–Hall method [87] (see Fig. 2.22). To improve the bandwidth of the lock, the analog proportional–integral controller that supplies feedback to the shear piezos features passive electronic notch filters in order to compensate for mechanical resonances of the cavity assembly at 18 kHz and 70 kHz. The stabilized FFPC features frequency noise of less than $0.04\,\kappa$ (1 MHz) RMS on short time scales (20 Hz to 2 MHz bandwidth) and peak-to-peak drifts of less than $0.36\,\kappa$ (8.8 MHz) over the course of 2 h. The dominant source of drifts of the locked cavity is the fluctuation of the FFPC relative to the lock laser, probably caused by residual interferences in the fiber.

Most of the optical components of the setup are placed in a light-sealed environment, in order to reduce the background noise of the signal single photons detected by the SPCM. The separation of those photons from the strong lock light (typically $1-3\,\mu$W) relies on spectral filtering, since the polarization degree of freedom is typically reserved for other purposes. Experimentally, we find that — after the suppression of lock laser photons by a series of band-pass interference filters — the photon background is limited to ~1 000 counts s^{-1} by frequency conversion from 770 nm photons inside the single mode fiber, attributed to spontaneous Raman scattering in optical fibers (see [1] and references therein). The polarization of the light entering the cavity (which is a resource of particular relevance in many CQED protocols) is tailored by employing a set of a half-wave and two quarter-wave plates[51]. As discussed in Chapter 4, it is convenient to send well-defined circularly-polarized light into the resonator, which is done by tuning the polarization-control setup such that — when combined with the effect of the optical fiber — it behaves as a quarter-wave plate. In particular we send linearly-polarized light and rotate the corresponding waveplates such that the reflection displays a perpendicular polarization angle[52].

Additional frequency shifts of the lock laser by an AOM — before it is overlapped with the input

---

[51] The initial fiber-based polarization control was substituted by two free-space equivalents in the path of probe and lock, such that their polarization could be changed independently.

[52] Additionally, one must ensure that an input beam polarized at 45° returns with exactly the same polarization.

signal photons — can be used to precisely modify the cavity length and tune its resonance frequency to arbitrary values within a ±250 MHz. Furthermore, the intracavity lock light is also employed as a confining field for neutral atoms inside the cavity. As discussed in Section 3.1.2, by exploiting the intracavity power enhancement and the small waist of the resonator mode, the blue detuned lock laser creates a tight repulsive potential that confines the atoms in the nodes of its intensity standing wave. By choosing a frequency separation between signal and lock of an odd number of FSR (three in our case), the two fields are out of phase at the center of the cavity (see Fig. 2.22(b)). This configuration ensures that the atoms in the central region are trapped in the maxima of signal intensity (and therefore of maximum coupling to the resonant cavity field). The effective coupling seen by the atoms will be reduced as we move from the midpoint and vanish when both fields are in phase. The distance between both extremes is half the beat length d_{beat} of lock and signal fields which — given the three FSR separation — is given by[53] $L_{\text{cav}}/3 \approx 31\,\mu\text{m}$.

---

[53] It cal also be calculated as $d_{\text{beat}} = \lambda_1\lambda_2/2(\lambda_1 - \lambda_2)$, which provides the estimation of the cavity length used in Table 2.2.

Controlled Delivery and Detection of Individual Atoms inside a Fiber Cavity

E XPLORING the dynamics of the enhanced light–matter interaction requires the deterministic coupling of neutral atoms to the mode of our fiber cavity. To obtain optimal control over the atomic degrees of freedom, the particles must be well confined in traps, isolated from their environment and any perturbation to their internal state must be minimized. The conservative potentials offered by optical dipole traps are the natural candidate to achieve the required confinement and long coherence times. The employment of such manipulation techniques is the subject matter of Section 3.1. We show the implementation of a small Magneto-Optical Trap (MOT) as a neutral-atom source, capable of trapping and cooling tens of ^{87}Rb atoms in the vicinity of the resonator (Sec. 3.1.1). The cooled atoms are then transferred into a movable optical lattice that provides the controlled delivery of individual atoms into the cavity mode (Sec. 3.1.3). Inside the resonator, a three-dimensional configuration of optical lattices ensures the localization of the atoms in sub-micrometric regions (Sec. 3.1.2) to guarantee a constant atom–cavity coupling.

We retrieve information on the presence of atoms in the cavity mode region through two complementary detection techniques. By using the high-NA lenses to efficiently collect the atom's fluorescence, our system provides high resolution images allowing us to extract the number and relative positions of small atomic ensembles in the region of interest within tens of milliseconds (as shown in Sec. 3.2.1). An alternative detection method is presented in Section 3.2.2, where the cavity field is used as a probe to monitor the presence of coupled atoms in a non-destructive way (i.e. with no trap losses). Furthermore, this information is exploited to perform real-time feedback on the optical transport, thus obtaining deterministic loading of single atoms coupled to our fiber-resonator.

3.1 Confinement and Transport of Neutral Atoms

The development of magnetic and optical tools in the last few decades opened a wide range of possibilities for the control and manipulation of neutral atoms. Of singular importance was the successful implementation of the magneto-optical trap [88], a keystone in the field of ultracold atoms that gave rise to experimental breakthroughs such as the first observation of a Bose-Einstein Condensate (BEC) [89, 90]. With the appearance of optical dipole traps [91, 92], it became possible to individually trap particles in a confined region of space in the absence of external disturbances, and to perform all-optical controlled transport and delivery of individual atoms [43, 44, 93].

The integration of this manipulation tools with high-finesse cavities opened a number of new ap-

proaches focussed on the enhancement and control of the atom–light interaction. The first instance of an atom optically-trapped in a resonator was performed by utilizing the intracavity field as a dipole trap [94–96]. The subsequent addition of external optical lattices provided higher degrees of confinement and cooling [97, 98], along with the possibility to deterministically transport atoms to the cavity mode [37, 99, 100]. The achieved level of control on the atomic degrees of freedom allows these systems to perform operations at the single quanta level, including single-photon all-optical switches [21] and quantum gates [22]. In addition to single atoms, these techniques can also be employed to host BECs inside a resonator [25, 101] to study many-body dynamics in different scenarios [102, 103].

3.1.1 A Small Magneto-optical Trap

Typical velocities of single particles in room-temperature gases are on the order of $100 \, \mathrm{m \, s^{-1}}$. Even when considering the lower end of the Boltzmann distribution, the trap depths provided by optical traps — usually on the order of 1 mK — are not sufficient to contain atoms with such a kinetic energy. In addition, to reduce collisions of the atoms under investigation with the background gas, low pressures below 10^{-9} mbar are required. As a consequence, a process is required that can both "cool" the atoms down to a few tens of μK and, simultaneously, confine and compress them in a high density cloud. In the following we show how a magneto-optical trap [88, 104, 105] provides the required compression of the phase-space by generating force fields that are dependent on both velocity and position of the particular atomic species.

Working Principle

To reduce the velocity of an atom, one can exploit the interchange of momenta that takes place when the atom scatters photons from a laser beam. The absorption of a photon imprints on the atom a recoil parallel to the propagation of the incoming light. Since the subsequent spontaneous emission process is isotropic, the atom gains a nett momentum in the direction of the laser beam after several scattering events. Due to the Doppler effect associated with the motion of the atom, if the laser beam (frequency ω) is red-detuned with respect to the atomic transition (i.e. : $\omega < \omega_{\mathrm{at}}$), the photons propagating against the atomic motion will be closer to resonance — and have a higher probability of absorption — than those moving with the atom. The effective recoil results in a reduction of the atomic velocity (see Fig. 3.1(a)). The technique can be trivially expanded to all directions by shining three orthogonal pairs of counter-propagating beams. Such a beam configuration gives rise to a friction force known as *optical molasses*. For ^{87}Rb, this cooling method can provide temperatures as low as $T_{\mathrm{D}} = \hbar\Gamma/2k_{\mathrm{B}} \approx 146 \, \mu\mathrm{K}$, where $\Gamma = 2\pi \times 3$ MHz is the natural linewidth of the D_2 line of rubidium, k_{B} is Boltzmann's constant and $\hbar$ is Planck's constant. This lower bound is known as the *Doppler limit* [106] and is caused by the always present recoil of the spontaneous emission processes.

Cooling mechanisms do not prevent the atoms from diffusing and leaving the molasses region, therefore a trapping potential is required. This is achieved by introducing a magnetic field gradient and employing circularly polarized light (Fig. 3.1(c)). The presence of a magnetic field lifts the degeneracy of the Zeeman sublevels (see Sec. 5.3) and its gradient gives rise to an energy splitting that increases linearly with the distance from the trap center. In this picture, the Zeeman splitting can be understood as the analogue of the Doppler shift in position space: Atoms located at one side of the trapping region will display a sublevel splitting that will make then resonant with photons of a particular polarization. By providing the counter-propagating beams with orthogonal polarizations, the atoms absorb with higher probability the photons that have a momentum towards the trap center, as shown in Figure 3.1(b). This gives rise to an additional position-dependent radiation pressure. The restoring force is expandable to
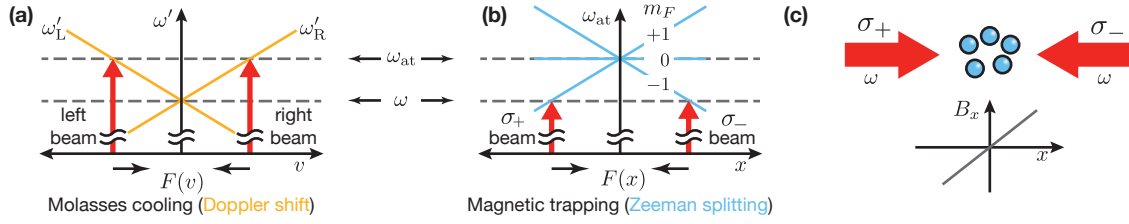
Figure 3.1: Working principle of a MOT in one dimension. **(a)** Molasses cooling. The Doppler effect shifts the apparent frequency $\omega' = \omega + k \cdot v$ of the right (ω'_{R}) and left beams (ω'_{L}), such that they are only resonant with atoms moving against their propagation direction at certain velocity v, giving rise to a friction force $F(v)$. **(b)** Magnetic trapping. The linear Zeeman splitting shifts the energy of the m_F-sublevels such that an atom at the side of the trap is closer to resonance with photons with momenta towards the trap center. **(c)** One dimension of the experimental configuration. Two counter-propagating laser beams which are circularly polarized and red-detuned with respect to the atom provide the cooling mechanism, while the trapping force is obtained in combination a radial magnetic field gradient.

three dimensions by, for example, using magnetic coils in anti-Helmholtz configuration to realize a magnetic quadrupole field.

Implementation

The main experimental requirements for implementing a MOT are sufficient environmental isolation (vacuum system), narrow linewidth light sources (lasers) and controlled magnetic fields (electromagnets). In our setup we use the components from a previous version of the experimental apparatus, with a few modifications to host the cavity-assembly. A more detailed and comprehensible description of the system can be found in the thesis of Miguel Martinez-Dorantes [84]. In the following paragraphs we review the relevant characteristics of the MOT setup, focussing on the main additions implemented during my thesis.

Vacuum system. We employ an ultra-high vacuum system (UHV) at pressures of 10^{-9}–10^{-10} mbar. The main components of the apparatus are depicted in Figure 3.2(a,b). The system was opened under nitrogen atmosphere to remove and modify a few components (as compared to [84]). The pressure of the closed system — evacuated from atmospheric pressures with two turbo-molecular pumps[1] in series — is preserved by an all-metal valve and an ion pump that maintains pressures on the order of 1×10^{-9} mbar[2]. A titanium sublimation pump[3] was included in the apparatus to reduce any buildup of pressure due to contaminated surfaces introduced with the cavity assembly.

The required background gas is supplied by an appended rubidium source. The reservoir contains a broken glass ampule with ^{87}Rb in order to expose the alkali atoms to the vacuum environment. The flow of rubidium towards the main chamber is controlled through an edge valve and, if necessary, by a heating wire that controls the temperature of the reservoir.

The cavity assembly is positioned at the center of a glass cell, which has eight anti-reflection coated windows to supply the necessary optical access (Fig. 3.2(b)). The cavity is attached through a metallic connector to a passive vibration-isolation stage that provides acoustic damping of frequencies from

---

[1] Turbomolecular drag pumping station: *TSU 071E* and Turbomolecular drag pump: *TMU 071P* (Pfeiffer Vacuum).
[2] This pressure is one order of magnitude higher than the one in the original apparatus. We attribute the increase to outgassing of the multiple components and glues utilized in the cavity assembly.
[3] Titanium sublimation cartridge: *916-0050* (Agilent Technologies).
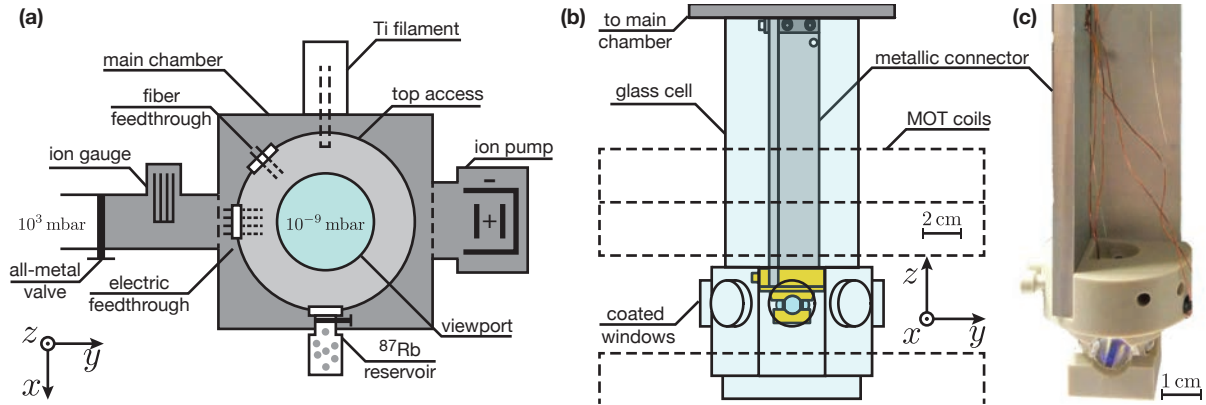
Figure 3.2: Vacuum System. **(a)** Simplified sketch of the vacuum system (top view, not to scale). The elements in white represent the additions to the previous version of the apparatus. **(b)** Technical drawing of the glass cell and the in-vacuum cavity assembly (side view). The octagonal glass cell is directly attached to the main chamber, while the cavity assembly is connected to a vibration-damping stage (not shown). The dashed lines indicate the position of the surrounding coils that create the magnetic gradient at the cavity position. **(c)** Photo of the cavity assembly and its connector to the damping stage. The Kapton wires and copper optical fibers (visible in the picture) are attached to the metallic structure with vacuum-compatible glue (*STYCAST 2850FT + Catalyst 24VL*, Emerson and Cuming).

100 Hz onwards. Residual acoustic disturbances at lower frequencies are compensated by the optical table that supports the entire apparatus and by the active stabilization of the cavity length (see Sec. 2.4.2). In Figure 3.2(c) the cavity construction including the copper-coated optical fibers of the resonator and the Kapton wires of the piezo-elements are shown. The cables are connected to the copper pins of a high-voltage electric feedthrough[4] that allows us to address the piezo-elements from the outside. Likewise, the optical fibers exit the vacuum apparatus through a homemade feedthrough hole sealed by UHV-compatible glue[5] after the cavity insertion.

Magnetic field generation. The magnetic quadrupole field required for the atom trap is provided by two strong electromagnets; each of them is comprised of a pair of coils of flat copper wire that surround the glass cell (Fig. 3.2(c)). The coil stacks are placed in an anti-Helmholtz configuration resulting in a magnetic gradient $dB_z/dz = 4 \,\mathrm{G\,cm^{-1}} \times I(A)$ at the cavity position. Driving currents I on the order of a few amperes are enough to produce the highly confined MOT required in our setup. In addition, three pairs of smaller coils are placed around the cell in a Helmholtz configuration to generate magnetic bias fields or to compensate for residual magnetic disturbances (see experiments in Chap. 5); we refer to them as *compensation coils*.

Optical system. According to the working principle previously introduced, a single closed atomic transition is required for a MOT. In our case, we employ the D_2 line of ^{87}Rb and, in particular, the hyperfine transition $|F = 2\rangle \rightarrow |F' = 3\rangle$ (represented as the red arrow in Figure 3.3(a)). This is known as the *cycling transition*, since dipole–selection rules only allow the atom to decay back into $|F = 2\rangle$ from the excited hyperfine state $|F' = 3\rangle$. We avoid the population of the $F = 1$ ground state caused by off-resonant scattering events of the type $|F = 2\rangle \rightarrow |F' = 2\rangle$ through so-called *repumper* laser beams resonant with the

---

[4] Feedthrough instrumentation/power (1.5 kV): *9340-05-CF* (Hositrad).
[5] UHV-compatible, sealing thermal glue: *Epotek H77* (Epoxy technology).
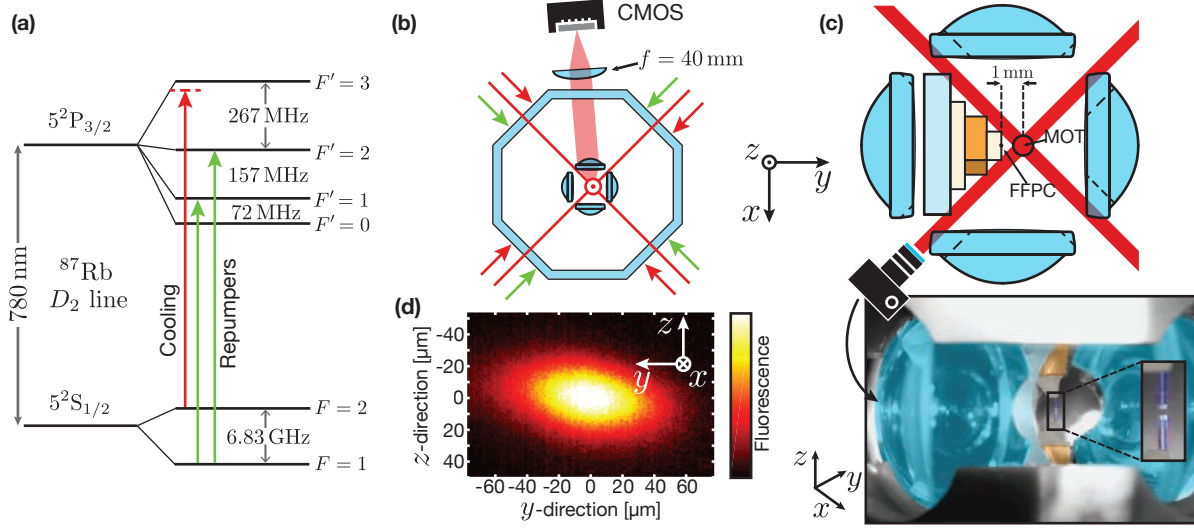
Figure 3.3: Optical setup of the MOT. **(a)** Simplified energy-level scheme of the D_2 line of ^{87}Rb (not to scale), including the hyperfine splitting. The transitions addressed by the cooling and repumper lasers are depicted by the red and green arrows respectively. Their frequency can be scanned by a few tens of megahertz with the use of an AOM. **(b)** Top view of the layout of the MOT beams. Two crossed pairs of counter-propagating beams enter the glass cell through the optical windows along the diagonal axes, while the vertical beams are delivered through the top viewport and the bottom of the glass cell. All beams carry both cooling and repumping light. The fluorescence of the MOT is collected by one of the in-vacuum aspheric lenses; the output image beam is tilted due to the MOT being 1 mm away from optical axis. A convergent lens focusses the light onto a CMOS camera (a typical MOT image of 500 ms exposure time is shown in **(d)**). **(c)** Technical drawing of the MOT beams in the cavity assembly. Dashed lines mark the lenses' cut-outs removed for increased optical access. Inset: Photo of the assembly from the point of view of a MOT beam. False colors are applied for consistency with the top diagram. The cavity can be seen in the zoom-in region.

$|F=1\rangle \rightarrow |F'=\{1,2\}\rangle$ transitions. Note that the high transition strength of the cycling transition renders it as an ideal candidate for the coupling with the cavity, thus the *cooling light* is used as *probe light* (see Sec. 2.4.2).

Both laser sources are delivered into the vacuum system from three pairs of counter-propagating beams by exploiting the optical access through the glass cell windows and the top viewport of the apparatus (Fig. 3.3(b)). Details about the light sources and the optical setup that distributes the six laser beams with the required polarization can be found in [84][6]. The radius of the vertical beams at the position of the MOT amounts to 1 mm, while the size of the horizontal beams is limited to ~0.7 mm by the constrained optical access between the high NA lenses (inset of Fig. 3.3(c)). Due to restricted optical access to the cavity mode, the MOT is created at a distance of 1 mm from the fiber cavity as it is depicted in the technical drawing of Figure 3.3(c). The tools necessary to transport the cooled atoms to the resonator will be discussed in Section 3.1.3.

The fluorescence emitted by the atoms during the cooling and trapping is effectively collected by the in-vacuum lenses and imaged onto a CMOS camera[7] to observe the MOT region. Additionally, as described in Section 3.2.1, the region of interest at the cavity mode is observed by a highly sensitive

---

[6] Although the setup had to be removed and re-implemented due to the bake-out of the system, no major changes were performed.

[7] Monochromatic CMOS camera (1280 × 1024): *DCC1545M* (Thorlabs Inc).

EMCCD camera. Although the low sensitivity of the particular CMOS chip does not allow us to perform calibrated fluorescence measurements at the single-atom level, we are able to determine the full-width of the cloud to be around $32\,\mu\mathrm{m} \times 66\,\mu\mathrm{m}$. In Figure 3.3(d) we see an image of the MOT for typical laser power and detunings and a field gradient of $26\,\mathrm{G\,cm^{-1}}$. The ellipticity of the cloud is a consequence of the gradient created by the coils[8]. Similar measurements performed with an EMCCD camera for a MOT of the same characteristics show that the typical trap will contain a few tens of atoms at sub-Doppler temperatures as low as $40\,\mu\mathrm{K}$ [84, 107].

3.1.2 A Three-dimensional Optical Lattice in the Cavity

In contrast to radiation pressure traps such as the MOT — where trapping relies on spontaneous emission events every few nanoseconds — far-detuned optical dipole traps provide a nearly conservative potential based on the dispersive interaction between the atomic dipole and the light's electric field, with only a few scattering events per second [36]. The longer coherence times and versatility thus make dipole traps an ideal platform for quantum-enabled technologies with neutral atoms [108, 109]. Of particular relevance are the so-called *optical lattices*. Through the interference of two laser beams, they display a landscape of numerous potential wells that provides individual localization and manipulation of neutral atoms [110]. When implemented in all directions, they result in a compact, three-dimensional network of lattice sites with ideal scalability properties. By creating a 3D optical-lattice in our system, we achieve tight confinement of individual neutral atoms in the region of the fiber-cavity mode.

The Dipole Potential

A full description of the dipole interaction between an atom and a electromagnetic field requires the use of the quantum-mechanical treatment (see e.g. [111]). Nonetheless, for all practical purposes, the classical model provides an intuitive picture which successfully describes the basic dynamics[9]. In Lorentz's model, the atom is considered as an electron elastically bound to the core by a harmonic potential of frequency ω_0. The effect of a classical electromagnetic field (of frequency ω and intensity distribution $I(\mathbf{r})$) in this picture is reduced to an induced electric dipole on the atom. The interaction between the field and the dipole it induces can be separated into a dispersive behavior that gives rise to a conservative potential U, and a photon absorption and re-emission process described by the absorption scattering rate R_{sc}. For the typical case where $\Delta = \omega - \omega_0 \ll \omega$, the expression for both figures of merit can be reduced to (see e.g. [107])

$$U(\mathbf{r}) = \frac{\hbar\Gamma^2}{8\Delta}\frac{I(\mathbf{r})}{I_{\mathrm{sat}}} \tag{3.1a}$$

$$R_{\mathrm{sc}}(\mathbf{r}) = \frac{\Gamma}{\hbar\Delta}U(\mathbf{r})\,, \tag{3.1b}$$

where $I_{\mathrm{sat}} = \pi h \Gamma c / 3\lambda^3$ is the saturation intensity of the atomic transition with decay rate Γ.

The light field intensity distribution creates a spatial variation of the atomic ground-state energy[10]

---

[8] The anti-Helmholtz configuration produces a linear gradient of the vertical component of the field (B_z) that is two times that of the horizontal ones.

[9] This approximation fails to predict certain effects that might be of relevance in other scenarios, like a quantitative description of the atomic natural linewidth Γ, or the *AC Stark shift* of the excited state of an atom (also referred to as *light shift*).

[10] A more complete version of the effect emerges, in the quantum-mechanical formalism, as a shift of the atomic energy levels known as the AC Stark shift, which depends on the particular Zeeman state of the electron and the polarization of the light field.
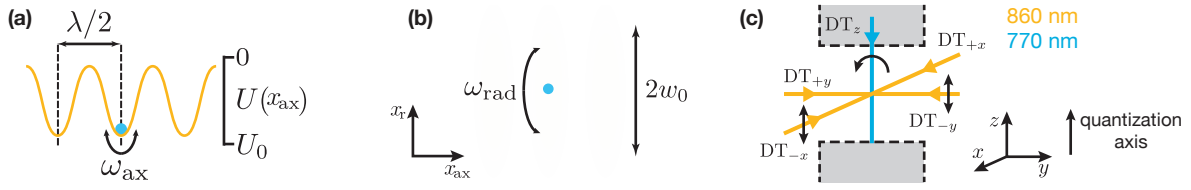
Figure 3.4: Working principle and implementation of an optical lattice. **(a)** Attractive dipole potential in the axial direction (x_{ax}). A collection of equidistant wells (of depth U_0) keep the atoms trapped with a frequency ω_{ax}. **(b)** 2D representation including one of the radial directions (x_r) where the confinement is less tight. **(c)** Layout of the five beams necessary for our 3D optical lattice. Two pairs of counter-propagating red-detuned beams (orange) create a 2D attractive lattice in the (x, y)-plane. The blue-detuned intracavity field (blue) creates a repulsive periodic potential in the remaining z-direction. The black arrows indicate the polarization of the electric field.

and the absorption rate. Relation (3.1b) implies that, in order to avoid undesired scattering processes, one must use far-detuned light fields; the resulting decrease of depth can then be compensated by using a higher intensity. In addition, it is worth noticing that the dipole potential has the same sign as the detuning of the light. Thus, for red-detuned fields ($\Delta < 0$), the atom will feel attracted to regions of high intensity; contrarily, blue-detuned beams will create a repulsive potential and expel the atoms away from the high-field regions.

In its simplest version, a dipole trap can be created by using a red-detuned laser field, such that the atoms experience attraction towards the beam. This type of tractor beam can trap, move and rotate particles without mechanical contact, which gives it the name of *optical tweezers*. They are particularly useful tools in fields such as biology, photochemistry or nano-fabrication, as the mechanism introduced above applies to any polarizable objects even on the macroscopic scale [112]. However, the single potential-well provided by such dipole traps is not sufficient to individually confine several particles and perform single-qubit operations in a many-body system [110] without inter-particle collisions. Such conditions can be met by employing a series of independent optical tweezers [113], a less demanding option is that of using the net of potential wells provided by an optical lattice.

A 3D Optical Lattice

By exploiting the interference effects between two coherent laser fields, one can create standing-wave intensity patterns that supply arrays of identical potential wells with sizes on the wavelength scale. The particular case of a Gaussian beam interfering with its retro-reflection — that was introduced already in Section 2.1.1 when discussing the fundamental cavity mode — represents the intensity distribution of the dipole traps employed in our system. The pattern consists of a sinusoidal distribution with a periodicity of $\lambda/2$, with an envelope given by the Gaussian profile of the laser beam. For red-detuned light, the atoms will experience an array of pancake-shaped potentials (see Fig. 3.4(a,b)). Since the cavity region is much smaller than the Rayleigh range of our trapping beams ($\sim 250\,\mu m$), we can consider all potential wells to be identical to each other. A typical approximation is to consider each lattice site as a harmonic potential: A trapped atom will oscillate around the minimum-energy point with a frequency that depends on the direction of motion. The axial confinement is typically stronger than the radial one (as $w_0 > \lambda/2$), thus the motion of the atom is described by both the axial ω_{ax} and radial ω_{rad} frequencies, the two of them being proportional to $\sqrt{U_0}$.

Since the optical lattice represents a conservative potential, any atom approaching the trap from "infinity" distance will have a total energy bigger than any bound-state of the potential well. In other words, one cannot trap atoms by dropping or ejecting them into the optical lattice, as they will fly by
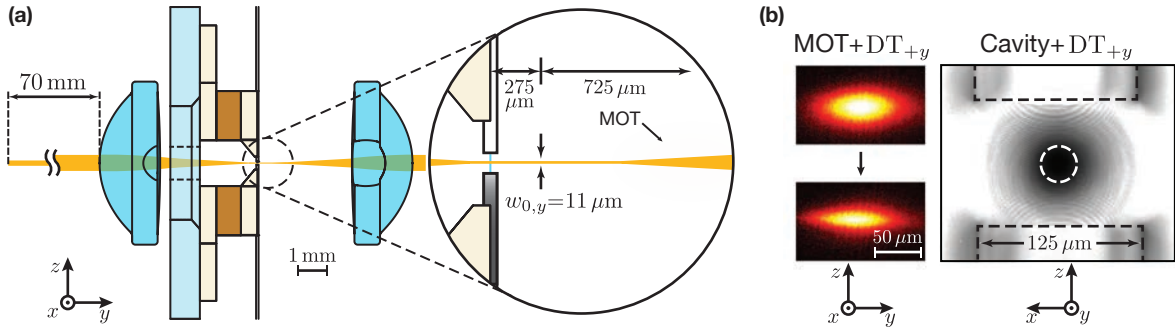
Figure 3.5: Optical alignment of the transport optical lattice DT_y. **(a)** Technical drawing of the optical path. The lattice connects the loading region of the MOT with the fiber cavity. The beam propagating from the left (DT_{+y}) is focussed down to 170 µm at a distance of 70 mm before the in-vacuum lens in order to displace the focus of the trap towards the MOT. **(b)** Left: Image of the effect of the single dipole-trap beam DT_{+y} on the MOT. Right: Image of the position of DT_{+y} at the cavity region (beam profiling camera). For this particular picture we illuminated along the dipole trap optical path with 780 nm light.

and continue their journey even if their temperature is below the trap depth. Instead, the optical lattice must be formed directly in the midst of the cooling region of the MOT, such that atoms are cooled down to a total negative energy. To deliver the atoms from this loading area to the region of interest (i.e. the cavity), one of the optical lattices must be overlapped with the line connecting the MOT and the center of the cavity mode. This dipole trap, referred to as DT_y, is the key tool of our atom delivery system as it takes on the duty of loading, transporting and trapping the atoms into the cavity mode. Two other optical lattices, DT_x and DT_z, are additionally implemented to add axial confinement in the remaining directions (see Fig. 3.4(c)). These are provided, respectively, by a pair of red-detuned beams focused at the cavity along the x-direction ($w_{0,x} = 13$ µm) and by the blue-detuned intracavity field of the lock laser ($w_{0,z} = 4.4$ µm).

Figure 3.5(a) contains a technical drawing describing the optical path of DT_y through the cavity assembly. The two counter-propagating laser beams are focussed by two of the high-NA lenses (as in the case for DT_x). These do not only provide a high pointing stability but also allow us to focus the incoming beams down to a waist of $w_{0,y} \sim 11.2$ µm. The size and location of the waist represents a compromise between the ability of trapping a whole atomic ensemble at the cavity (trapping volume much bigger than λ^3) and sufficiently large trap depth for the efficient loading of atoms at the MOT position. Both conditions require a trapping beam with a Rayleigh length on the order of the cavity–MOT distance. By pre-focussing the incoming beam (DT_y) before it reaches the high-NA lens, we displace the position of the waist from the center of the cavity towards the MOT by 275 µm. As a result we obtain a relatively small beam radius at the cavity position (13 µm) while providing enough loading efficiency at the MOT (where the spot size is 21 µm).

The alignment of the dipole traps $DT_{x,y}$ with respect to the 3D confining region is done by imaging the central plane of the cavity mode on a beam profiling camera[11], with the use of the high-NA lenses. The dipole trap beam appears as a Gaussian spot surrounded by the cavity, while the fibers are imaged by applying external illumination with red light[12]. By monitoring the lattice influence on the shape and brightness of the magneto-optical trap, we can align the DT_y beams such that they overlap with the MOT

---

[11] High-Resolution Laser Beam Profiling System: *LaserCam-HR II* (Coherent Inc).

[12] The waist extracted from these images will depend on the wavelength of the light employed along the dipole trap beam and the position of the focal plane of the beam profiling system, and thus is not considered for characterizing the trap beams size.
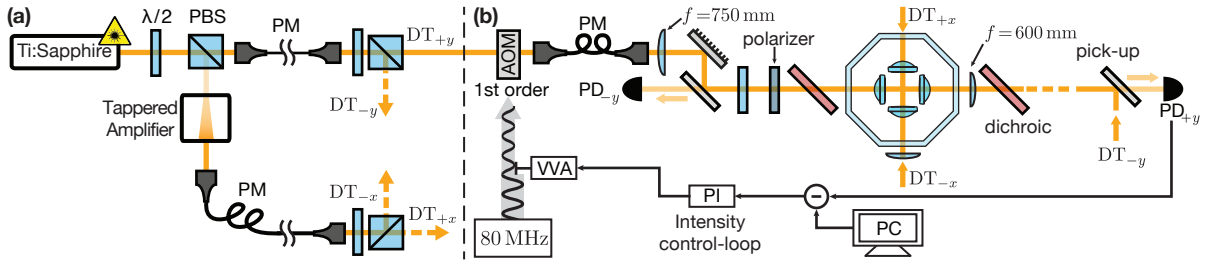
Figure 3.6: Simplified layout of the optical setup for the distribution and stabilization of the dipole trap power. **(a)** The power from the Ti:Sapphire laser is partially amplified and distributed into four arms that later form the horizontal 2D optical lattice. **(b)** Main components on the optical path of each one of such arms (here illustrated for DT_{+y}). The beam passes through an AOM that controls the optical frequency and power of the first diffractive order. This is then polarized and focussed onto the glass cell. The dichroic mirrors (two of them not shown) separate the trapping light from the atomic fluorescence at 780 nm, which is collimated by the compensation lenses ($f = 600$ mm). Bottom: scheme of the electronics involved in the intensity control-loop of a single dipole-trap arm.

and pass through the center of the cavity region at the same time (see Fig. 3.5(b)).

The Light Sources

The lock laser (770 nm) used to stabilize the cavity length forms a standing wave inside the resonator that is also utilized to confine the atoms along the cavity axis (z-direction). Both the power and frequency of the lock light are actively stabilized. Furthermore, the power enhancement of the high-finesse cavity — along with the small detuning of 10 nm — provides trap depths above 1 mK for a few microwatts of input power used in the locking mechanism. The circular polarization of the trapping light can, in principle, lead to vectorial light-shifts and scrambling of the Zeeman population. However, the corresponding effects are considerably reduced since the laser is blue-detuned and the atoms are confined at the nodes of the standing wave (see Sec. 5.3).

Ideally, one would avoid red-detuned dipole traps to reduce detrimental effects such as varying AC Stark shifts and spontaneous photon scattering events. However, at least one red-detuned attractive potential is needed to have a stable trapping configuration that allows optical transport. For that reason, our free-space dipole traps are constituted by light at 860 nm, emitted from a Titanium:Sapphire laser[13] with a typical output power of 700 mW. To facilitate the loading and transport, most of the output is used to create DT_y, although a small fraction is picked and amplified by a Tapered Amplifier[14] to provide the light for DT_x. Both sources are coupled into polarization-maintaining fibers (PM) and later split equally into two paths that form the counter-propagating beams of the corresponding trap. A simplified scheme showing the power distribution is shown in Figure 3.6(a). Each of the four arms is linearly polarized[15] in the direction of the quantization axis (z-direction) and its frequency and intensity are controlled by an acousto-optic modulator[16] (AOM) operating at 80 MHz in single-pass configuration (before entering the glass cell). A small fraction of the transmitted light is picked off by a partially transmitting mirror and focussed onto a homemade amplified photodiode (PD) to stabilize the power of the dipole traps to a computer-controlled set-point. The active stabilization is performed by a Proportional-Integral servo circuit (PI), shown in Figure 3.6(b). The output signal addresses a voltage-variable attenuator (VVA)

---

[13] CW tunable Ti:Sapphire laser: *MBR 110/10* (Coherent Inc).
[14] 850 nm Tapered amplifier (2.2 W): *EYP-TPA-0850-02000-4006-CMT04-0000* (Eagleyard photonics).
[15] VIS-IR polarizer: *IR 950 BC4 CW02* (Codixx AG).
[16] AO Modulator at 80MHz central frequency: *3080-122* (Crystal Technology LLC).

Table 3.1: Main parameters of the three optical lattices at the center of the cavity for typical power settings. P is the power per arm in free-space, or the circulating intracavity power for DT_z (for an input at the fiber of $3\,\mu W$ and $\kappa = 2\pi \times 50\,MHz$). U_{max} represents the trap-depth or the wall-height depending on the light being red- or blue-detuned. ΔE_0 denotes the AC Stark shift at the center of the trap, which vanishes for blue-detuned lattices.

Trap	λ (nm)	w (μm)	P (mW)	U_{max} (mK)	R_{sc} (s^{-1})	$\Delta E_0/2\pi$ (MHz)	$\omega_{ax}/2\pi$ (kHz)
DT_x	860	13	50	-0.31	7.4	6.2	281
DT_y	860	13	90	-0.55	13.4	11.2	377
DT_z	770	4.4	6.2	1.70	~ 0	–	740

that controls the amplitude of the RF signal driving the AOM (and therefore its output optical power). This closed intensity control-loop provides a bandwidth of ~1 kHz. To avoid undesired interference effects between the two crossed dipole traps DT_x and DT_y, we create a 160 MHz relative shift between them by using the negative and positive first-order of the AOM, respectively. Typical optical powers and corresponding trap parameters for the three lattices are summarized in Table 3.1.

3.1.3 An Optical Conveyor Belt

The ability to transport neutral atoms is an essential requirement in experiments where the trapping and cooling mechanisms cannot be implement in the location of interest. Only a few approaches have managed to perform this operation in a controlled and efficient way, such that the atoms are deterministically delivered into the target without considerably increasing their temperature. The emerging technology of atom chips [114] provides a convenient platform for the manipulation and control of atomic clouds by the use of magnetic forces generated in nano-fabricated structures [115]. For systems where only a small number of particles is required, optical lattices represent a more convenient choice: they can deliver individually trapped atoms, they can be steered and their implementation is less invasive. These *optical conveyor belts* can efficiently cover up to centimeter distances with sub-micrometer precision [43, 44, 93]. In the following paragraphs we outline the implementation of a two-dimensional conveyor belt that allows us to control the position of an atom inside the cavity mode. Appendix C contains a detail description of the electronic components involved, while a demonstration of the transport is shown in Section 3.2, where the different schemes to detect the atomic position are introduced.

Moving a Standing Wave

To implement our two-dimensional optical conveyor belt we make use of the red-detuned optical lattices introduced in the previous section[17]. The standing-wave trapping potential can be shifted by temporally detuning the frequency ν_0 of the counter-propagating beams by $+\Delta\nu/2$ and $-\Delta\nu/2$ respectively. An intuitive picture of the mechanism appears when changing to the reference frame moving at a velocity $v = \lambda\,\Delta\nu/2$. In that frame, the Doppler effect shifts the frequency of the beams by the same amount in opposite directions, such that both of them recover the original value ν_0 and a steady standing-wave forms. This results in a lattice moving at velocity v in the reference frame of the laboratory.

In order to keep the atoms trapped during the process, the acceleration must be performed adiabatically. The force applied to the atoms tilts the trapping potential of the lattice and reduces its effective depth;

---

[17] In the following we will describe the mechanism to transport in one dimension, while the expansion to 2D is straightforward.

if the atomic temperature or the acceleration are to high, the axial trapping will not be strong enough and the atom will escape the trap. For our typical settings of trap depths and MOT temperatures, the maximum acceleration is on the order of 10^5 m s^{-2}, which allows the transport of atoms over a 1 mm distance within a few hundreds of microseconds [116]. In order to perform feedback on the transport sequence (see Sec. 3.2.2) we typically use smaller accelerations ($\sim$100 m s^{-1}) and transport velocities of 1 μm ms^{-1}.

Flexible Tuning of Optical Frequencies

The necessary control over the frequency of the dipole trap beams is achieved through the AOMs that also steer the trapping power (see previous section). We use the first refractive order of each AOM in single-pass configuration, resulting in a change $\Delta\nu$ of the RF driving frequency and, equivalently, a shift of the optical frequency of the beam. Therefore, to achieve sub-micrometer precision during the transport, the differential driving frequency between both AOMs must be controlled well below 1 Hz. In addition, their relative phase is directly mapped onto the spatial phase of the dipole trap: sudden changes or jittering in that phase will shake the lattice and can lead to heating or even the loss of the atom [117].

As detailed in Appendix C, we use a Dual Digital Frequency Synthesizer (DDFS) to control the AOMs of each of the red-detuned dipole traps. Each DDFS board provides two independent RF outputs with well defined frequency (0.09 Hz) and a low relative phase-noise that leads to negligible heating-induced trap losses. The boards are directly addressed by an mbed microcontroller which contains the information about the type and duration of the desired frequency shift, and that can halt the atom transfer in real-time on command. This becomes a useful tool to achieve deterministic single-atom loading into the resonator, as shown in Section 3.2.2.

3.2 Fast Detection of Atoms in the Cavity Mode

The transport and confinement tools presented in the previous section are not sufficient to ensure a deterministic coupling of an atom with the fiber cavity and to estimate the number of atoms present in the region of interest due to random loading of atoms into arbitrary positions in the trap. To provide the necessary information about the atoms relative position, we present and characterize two complementary detection methods in the following section. The first technique, discussed in Section 3.2.1, consists in imaging the fluorescence emitted by the atoms with the high-NA lenses of the cavity assembly onto a detector with spatial resolution. In this way, we obtain information about the number of atoms and their relative positions in a few tens of milliseconds. However, some of the atoms may eventually leave the trap during the detection procedure due to heating processes originated from the illumination light. An alternative method based on using the intracavity field as a probe, presented in Section 3.2.2, provides continuous monitoring of the presence of the atom with no detectable losses. We exploit the fact that the fully dispersive coupling of an atom to the resonator can drastically change the reflective properties of the cavity. This information is used to perform real-time feedback on our transport scheme, allowing us to deterministically couple a single atom into the cavity mode.

3.2.1 Fluorescence Imaging

Fluorescence detection is a standard technique extensively used in quantum optics community (see e.g. [41, 84, 118, 119]). It consists in illuminating the atoms with near-resonant light, and gathering a fraction of the scattered photons to form an image of the emitters. In our setup, we collect the fluorescence

with one of the in-vacuum lenses. The collected light is focussed onto an EMCCD camera with single-photon sensitivity to provides images of sub-micrometer resolution. The information derived from those images is used to estimate the number of atoms coupled to the resonator (Sec. 4.2.3) or to investigate the scattering properties of the atom–cavity system (Chap. 6). This method also constitutes a stepping stone towards optical addressing of single atoms, since the combination of high resolution images with a strongly focussed addressing beam can provide the generation of particular atomic patterns inside the cavity [120].

The Imaging Setup

The essence of fluorescence detection is to observe photons that have been previously scattered by the atom(s). As mentioned in the previous section though, photon scattering decreases the coherence and, more importantly, the trapping times. For that reason, the optical lattice was designed to reduce the rate of scattering events to a few per second. As a consequence, an additional optical field is required to image the atoms. The optical molasses employed in the MOT are the ideal candidate since they assure a constant streaming of scattered photons and keep the atom at low temperatures thus preventing trap losses. Imaging with 3D optical molasses is a standard technique that — with suitable detection and collection capabilities — can provide information about the position of the atoms within a few tens of milliseconds [84]. In our case, we are restricted to a 1D equivalent of the molasses along the transport direction (see Fig. 3.7(a)). The reason being that the resonator region has limited optical access along the cavity axis and that we cannot send molasses laser beams in the direction of the camera (in order to prevent stray light).

We employ the MOT cooling and repumper fields as light sources delivered through the same optical path as the dipole-trap beams DT_y, which ensures a large overlap between illumination and trapping regions. The homogeneity of the illumination is further guaranteed by avoiding intensity interference between the counter-propagating beams, by providing them with linear polarization in perpendicular directions (lin⊥lin configuration). Furthermore, by strongly focussing the optical molasses with the high-NA lenses, we prevent contamination of the images due to stray light scattered off the fiber tips. A considerable fraction of the fluorescence (∼3.8 %) is collected by one of the other in-vacuum lenses and collimated by a compensation lens outside the glass cell. This light is separated from the co-propagating trapping beam by a dichroic mirror[18] and subsequently focussed onto the EMCCD chip[19] by an $f = 300$ mm lens[20]. To avoid detection of residual trapping light, two laser-line filters[21] are placed in front of the camera. The expected magnification of the entire optical system amounts to 37.5. This factor is experimentally confirmed within uncertainties by imaging the transport of single atoms, yielding a magnification of 34 ± 3 which is used to scale all images shown in this section).

Figure 3.7(b) shows an example of a 40 ms picture taken under typical molasses configuration. We can see a string of atoms that have been successfully transported from the MOT into the imaging region. The ∼4° vertical tilt of the lattice is caused by the alignment constraint of connecting the MOT, the cavity center and the access hole in the cavity spacer. A similar tilt in the x-axis can be inferred from the defocussing of the atoms at different positions, although it might also be a consequence of the divergence of the optical lattice (since the waist is 275 μm away). Atoms trapped only by the transport lattice display a clearly elliptical shape, which is a direct consequence of the disparities between axial and radial confinement. Indeed, the shape of the atom's wave-packet is given by the geometry of the trapping

---

[18] Dichroic beamsplitter: *HC BS 801* (AHF analysentechnik AG).
[19] iXon EMCCD camera: *Ixon 3 DU-897-BV* (Andor Technology Ltd).
[20] An additional $f = -1\,000$ mm lens is used in order to allow the fine focussing of the atom's plane.
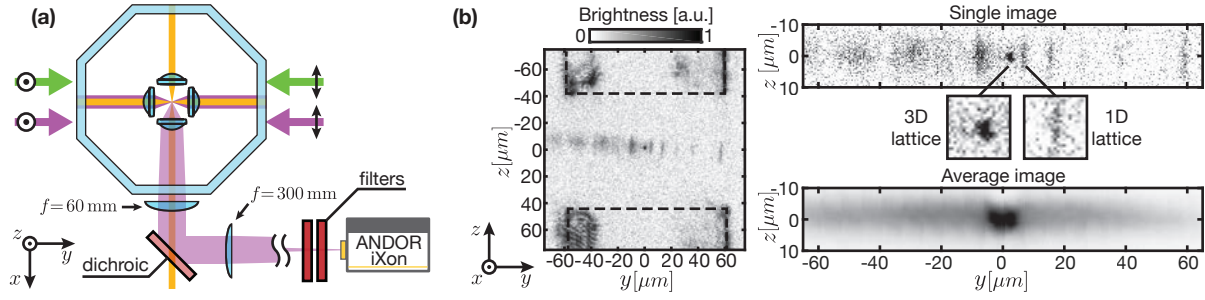[21] 780 nm MaxLine® laser clean-up filter: *LL01-780-25* (Semrock Inc).

Figure 3.7: Imaging setup. **(a)** Simplified layout of the optical setup for fluorescence imaging. The repumper (green) and illumination beams (purple) are delivered in a lin⊥lin configuration, and no bias magnetic field is applied. The high-NA lenses focus the beams to a waist similar to that of the co-propagating dipole-trap beams (orange). See main text for more details. **(b)** Single image of 40 ms exposure time with the optimum illumination parameters described in the text. The brightness code represents detected counts in the EMCCD camera. Left: Full image showing the fiber tips and the atoms trapped at the center. Top right: zoom in the lattice after rotating the image (sub-pixel resampling) to correct the tilt. Atoms in the central region are trapped in a 3D-lattice configuration and present a more symmetric and smaller wave-packet (insets). An average of several images is shown at the bottom to display the clear disparity between 3D (center) and 1D lattice (sides).

potential. Additionally, its radial extension is proportional to the temperature of the atom. That is not the case for the atoms in the 3D-lattice region. The tight axial confinement provided by the three lattices gives rise to a symmetric single-atom image which — in the absence of hopping — does not depend on the temperature. The smaller footprint increases the brightness per pixels as compared to those on the 1D-lattice, this is easier to see in the average images shown at the bottom. As we discuss in the next paragraphs, this brightness difference is enhanced when no cooling is available since weakly trapped atoms leave the trap earlier during the illumination process. The confinement effect of the 3D lattice on the fluorescence scattering can be used to determine the position of the cavity mode and to align the dipole trap beams with respect to its location. With this technique we estimate that the final location of the 3D lattice is displaced by ~6 μm from the center of the resonator along the cavity axis (*z*-direction). Due to the beating length of 30 μm between the probe and lock lasers (see Sec. 2.4.2), we estimate that such a deviation can lead to a 20 % reduction of the average effective coupling.

Heating Effects in 1D Molasses

Our imaging configuration differs from the standard molasses illumination in that we only utilize one dimension. If the light is red-detuned, the Doppler cooling introduced in Section 3.1.1 will keep the axial velocity of the atoms from increasing. This is not the case for the remaining radial directions, where the scattered photons imprint a constant random recoil on the atom that accumulates due to the absence of cooling. For a typical total trap depth of 0.75 mK, the average number of photons that an atom can scatter before leaving the trap is around 1000 if we consider no cooling[22]. Including the total detection efficiency of our system this translates into 20 detectable photons (13 for atoms in the 1D trap), which is sufficient to obtain a clear image of an atom. However, the process is generally destructive in the sense that the atom's temperature in the radial directions will be higher or — in the worst case — the atom will have left the trap after an image has been taken. If the imaging process is longer than a few tens of milliseconds, the difference in trapping potential will translate into a difference of detected photons per

---

[22] We neglect heating due to dipole force fluctuations, which only becomes relevant in deeper traps [121]. We also assume that the atom is originally at the vibrational ground state.

atom, and the regions with deeper traps will appear brighter. In general, we observe many more photons per atom than the expected in a 1D cooling scenario. This might imply that, due to its tilting angle, the illumination beams partially address the two remaining directions and effectively reduce the total heating rate.

We optimize the illumination[23] parameters to maximize the cooling effects by taking several pictures successfully. In this case, the total fluorescence of consecutive frames decreases exponentially. The extracted trapping lifetime of the atoms during the illumination can then be obtained for different optical powers and detunings of the light. In general the optimum detuning is around -40 MHz with respect to the free atom resonance[24], for optical powers from 50 to 150 nW per arm. This configuration yields illumination lifetimes of a few hundred milliseconds (in the 3D lattice), and is used in the images shown here unless otherwise specified.

Characterizing the Atomic Fluorescence

In this section we perform a qualitative analysis of how to obtain the number of atoms and their position from fluorescence images. Nonetheless, this technique can be adapted to perform spatially-resolved measurements of other quantities that would be less accessible otherwise, such as the atoms' temperature [107] or their internal hyperfine state [40]. In the following analysis we assume an ideal scenario where the atoms remain cold and tightly confined in a single lattice site during the illumination process. In this case, the extension of the atomic wave-packet in the axial direction is only a small fraction of the trapping and fluorescence light's wavelength and, thus, beyond the the system's resolution. The most relevant limitations to the optical resolution are those generated by diffraction effects, the limited resolution of the detector and the magnification of the system, which we discuss in the following.

The technically-limited finite size of the optical elements in our setup give rise to small diffraction-induced aberrations of the image, which typically still result in Airy patterns that can be characterized by a corresponding Point Spread Function (PSF). The PSF corresponds to the image of a perfect point source, and it therefore sets a lower bound for the imaged size of an identical object, e.g. the trapped atoms. The final atom images obtained are thus the result of the convolution between the atomic wavepacket and the PSF, combined with discretized image sampling of the pixel detector [41]. A detailed characterization of an identical imaging system has been presented in [84], using single atoms as a point source to yield a PSF width of $\sigma_{\mathrm{PSF}} \approx 0.4$ μm (slightly deteriorated due to aberrations). We can safely assume an identical PSF for the atoms within the aplanatic region of the focussing plane (~55 μm).

As we previously mentioned, heating caused by the illumination gives rise to a wider spread of the atomic wavefunction in radial directions for atoms trapped in a 1D lattice configuration. Additionally, any power unbalance between the counter-propagating illumination beams results in random hopping between different lattice sites. Both effects mask the resolution of our system and generally lead to spot sizes of around 1.45 μm for 3D trapped atoms, which is larger than the lattice constant $\lambda_{\mathrm{DT}}/2 = 0.43$ μm. We show in Figure 3.8(a) a sample image for two atoms in a 1D and a 3D optical lattice respectively, which have been selected due to the absence of hopping. Both their widths and positions can be extracted by fitting two-dimensional Gaussians to their brightness. On the one hand, atoms trapped by a single lattice display the expected elliptical shape with an aspect ratio of around three. On the other hand, atoms located in the 3D lattice result in a symmetric image of ~0.5 μm spot size in this particular case. Using these hopping-free atom images we confirm that our system is capable of resolving point-like sources with sub-micrometric resolution.

---

[23] In this section we refer to the beams employed in the imaging as both *illumination* or *molasses* beams.

[24] This value is only valid for 3D trapped atoms, the 1D trap configuration requires a larger detuning due to the smaller light shift.
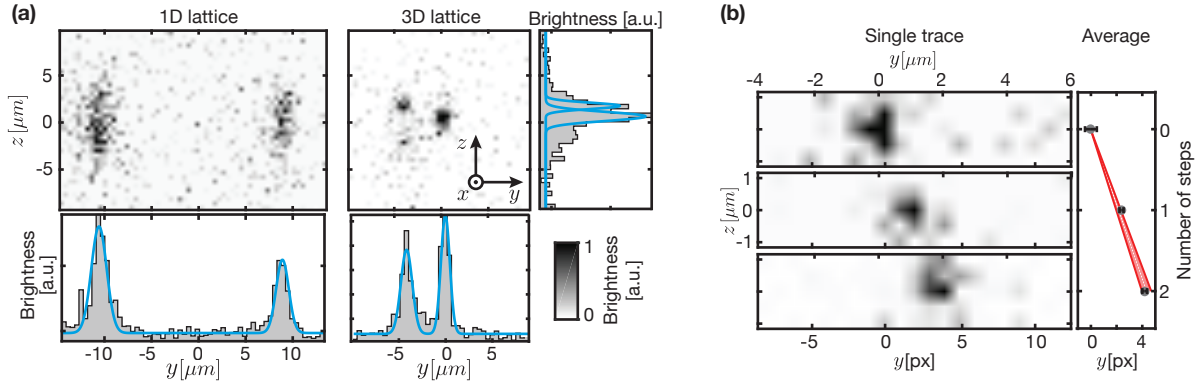
Figure 3.8: Imaging optical resolution. **(a)** Left: 10 ms image of two atoms trapped in a 1D lattice, with average widths of $\sigma_{ax} = 0.75\,\mu m$ and $\sigma_{rad} = 2.4\,\mu m$. The bottom graph shows the integrated counts in the vertical direction. We estimate a separation of approximately 45 lattice sites. Right: 10 ms image of two cold atoms trapped in a 3D lattice. Their shape is now symmetric with an average width of $\sigma_{ax} = 0.47\,\mu m$, which is close to the expected PSF of our optical system. The total distance between both atoms is estimated to be 4.2 μm. **(b)** Calibration of the magnification through 1 μm transport steps. Left: sample picture of a single atom being transported. The resolution is enough to precisely fit its position, but hopping and atom losses require more statistics. Right: average of 2000 measurements. We obtain the average position for each of the three situations (black error bars) and perform a linear fit (red line) to obtain the correspondence between pixel number and micrometers. The thickness of the fit represents the one-sigma confidence interval.

The minimum spot size does not represent the current limit to the precision in the estimation of the atom's position (if atoms are well separated from one another). As it has been shown in reference [41], the position of an atom in an optical lattice can be determined beyond the diffraction limit and with sub-pixel resolution when the optical transfer function is properly characterized and the signal-to-noise ratio is high enough. In our system, it translates into a precision of ~40 nm within a few tens of milliseconds of illumination time [84]. However, this does not hold completely for dense ensembles where atoms are close to each other. In that scenario the Rayleigh criterion provides an approximation to the minimum separation between point sources necessary to optically resolve them (although it can be overcome). For our optimal resolution, this distance is on the order of ~1 μm. As a result, our imaging system is in principle able to resolve more than 50 atoms in the 2D plane of the cavity mode region, which is significantly more than the maximum number of atoms typically loaded into the cavity (see Sec. 4.2.3).

The magnification of our system has been chosen such that we prevent information loss due to the spatial averaging performed by the discretized pixels of the sensor. This is achieved by ensuring that the PSF is imaged onto more than two pixels [122]. In our case, the requirement corresponds to a magnification of at least 35. Larger magnifications reduce the signal-to-noise ratio of the images due to background noise. Thus, we chose a factor of 37.5 for our imaging system. To confirm this value we perform a calibration by imaging the transport of atoms in the lattice [120, 123]. The individual atoms are transferred into the 3D lattice region and where a series of 1 μm transport steps are performed, each one followed by a 10 ms imaging period. Figure 3.8(b) shows an example of a single atom being transported two times in the horizontal direction. To compensate for hopping or atom loss due to the illumination-induced heating, we repeatedly perform the measurement 2000 times and measure the displacement of the average atom position, resulting in a correspondence of $(2.15 \pm 0.18)\,\text{pixel}\,\mu m^{-1}$ and a magnification of 34 ± 3[25].

---

[25] This factor has been independently confirmed by measuring the width in pixels of the fiber tips (125 μm), which yields
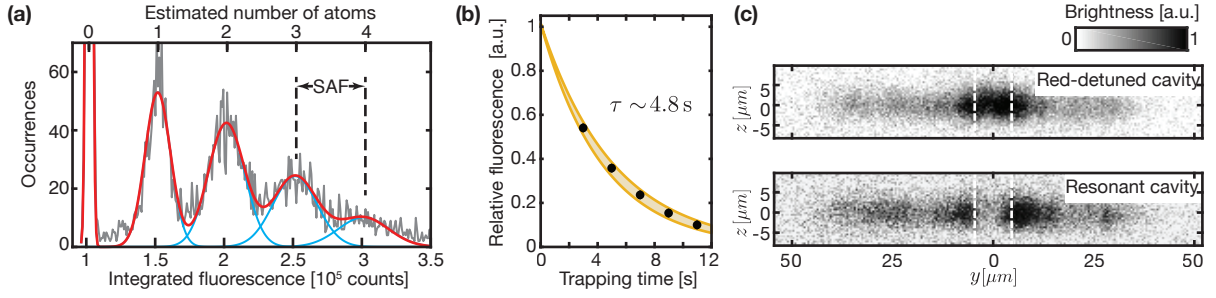
Figure 3.9: Information from the integrated fluorescence. **(a)** Fluorescence histogram obtained from 7000 atom images of 20 ms duration in a $9\,\mu\mathrm{m} \times 9\,\mu\mathrm{m}$ patch of the cavity region. A vertical zoom is applied in the bottom diagram. The data (gray) is fit to the model described in the text (red). We also plot the Gaussian curves corresponding to each number of atoms (blue). As a result we obtain a SAF of $\sim$2 500 counts ms^{-1}. **(b)** Exponential decay of the average number of atoms in the (1D) transport optical-lattice. Each data point corresponds to 900 images of an atomic ensemble after the corresponding waiting time. The statistical error bars are smaller than the markers. The thickness of the fit curve (orange) represents the one-sigma confidence interval. **(c)** Average of 300 fluorescence images of an atomic ensemble with the cavity being red-detuned by 150 MHz (top) or near resonance at 50 MHz (bottom). The effect of the cavity emerges as short illumination lifetime (and therefore a lack of fluorescence) in the region of the cavity mode (white dashed lines).

While images with strong thermal hopping do not contain useful spatial information, we can still determine the number of atoms by considering the amount of scattered photons. Assuming that all the atoms are trapped and illuminated in the same way, each one will contribute to the total fluorescence with an amount of photons given by the single-atom fluorescence (SAF). Hence, there exists a linear relation between number of atoms in an image and its total brightness. To estimate the SAF for particular settings of the illumination, we take several images and integrate their fluorescence over the region of interest (in this case, the 3D trapping area). Figure 3.9(a) shows the results when plotting a histogram of all the integrated counts. As expected, we obtain a series of equidistant peaks separated by the SAF. The first one corresponds to the background counts when no atom in present in the picture, while the rest stand for images with a growing number of atoms N (each Gaussian peak with a width that increases as $\sigma_\mathrm{N} = \sqrt{N}\sigma_1$). A fit to a simple model[26] provides the required calibration.

Using the relatively simple method of setting thresholds on the fluorescence, we can quickly determine the number of atoms in a picture with a precision that is limited by the overlap of the independent Gaussian curves. This, in turn, depends on their width and amplitude. While the amplitude is given by the average number of atoms in the region (which is usually fixed by the particular experimental procedure), the relative width can be reduced by increasing the exposure time of the image. In our case, though, we are limited by the trapping lifetime of the atoms during illumination and cannot perform arbitrarily long images. In addition, inhomogeneous trapping or scattering conditions within the region of interest lead to a spatial variation of the SAF which — when integrating over the image — will result in further overlap between the curves. Although a more thorough analysis could potentially improve the estimation precision, it would need to be adapted to each experimental scenario, which is beyond the scope of this section.

The determination of the number of atoms in a specific region will be used in Chapter 4, where it is employed to correlate the amount of atoms coupled to the cavity and the collective cooperativity

---

$\sim$2.1 pixel μm^{-1}

[26] We use the function $\sum_{N=0}^{4} = A_N \exp\left(-(F - F_{N,0})^2/2\sigma_\mathrm{N}^2\right)$, assuming a maximum four atoms per picture.

of the system. Another practical application — that does not require spatial resolution — is that of determining the average trapping time of the atoms in the optical lattice. This is done by estimating the average number of atoms present in the optical lattice after different trapping times and characterizing the corresponding decay. For the measurement shown in Figure 3.9(b) we load a ensemble of atoms from the MOT to the dipole trap, transport them to the imaging region and wait a certain amount of time before taking a single image. This is performed hundreds of times for five different waiting periods. As a result we observe a decay with a time constant of (4.8 ± 0.4) s that we attribute to background gas collisions[27]. A similar measurement employing the cavity reflection to detect the trapping lifetime of a single atom yields identical values (as discussed in Sec. 3.2.2).

The Effect of the Cavity and How to Prevent It

Most of the images shown in this section were taken with the cavity resonance being shifted by more than 1 GHz away from the illumination light frequency. This setting ensures that the scattered photons are not resonant with the cavity and that no coherent interaction takes place. In cases where the resonator is near resonant the atom and the illumination light, the scattering properties of the coupled atoms — both the rate and the emission pattern — will be modified. This considerably affects the imaging outcome in the region of interest. As an example, the total scattering rate of an atom coupled a blue-detuned cavity can get enhanced by more than an order of magnitude (for detunings of a few tens of megahertz). This increases the heating rate accordingly and results in typical illumination lifetimes on the millisecond scale. As a consequence, images recorded with a long exposure time show areas with low brightness at the position of the cavity mode, which is in stark contrast to red-detuned or off-resonant cavity configurations (see Fig. 3.9(c)).

This effect does not only depend on the detuning, but also on the atom–cavity coupling strength. Since atoms at the center of the cavity mode are more strongly coupled than those in the outer regions, the fluorescence rate becomes spatially inhomogeneous. This in itself represents an interesting scenario and shows how tailoring the electromagnetic environment of an atom can modify its scattering properties. We dedicate indeed the entirety of Chapter 6 to explore the processes involved and how to exploit them. Nonetheless, the strong dependency on the position of the atom and the resonance of the cavity — along with the large heating rates — become detrimental effects when a consistent and systematic fluorescence imaging technique is required. This situation can be avoided either by shifting the cavity resonance away (as we did to record the previous images) or by changing the frequency of the illumination field. The shift necessary in the resonance of the cavity in order to prevent its influence must be much bigger than the resonator linewidth ($\sim$100 MHz). This is achieved by locking the cavity length arbitrarily far away from any resonance. However, since our experiments require a locking of the cavity frequency to the atomic D_2 line, we can maximally shift it by $\pm$250 MHz due to the limited by the bandwidth of the AOMs. The fluorescence detection discussed in Chapter 4 makes use of such a large detuning. Nevertheless, the residual effects of the cavity cannot be completely prevented at those detunings, requiring a different approach for future experiments.

The solution can be provided by illuminating the atoms with light resonant with the D_1 line (795 nm). As shown in a recent implementation [120], we can indeed record fluorescence imaging using this atomic transition, while the D_2 line is exclusively used for the atom–cavity interaction. This configuration will not perturb the imaging, since the new illumination frequency is far from any cavity resonance. In summary, this alternative scheme allows us to image atoms that are strongly coupled to the cavity without affecting their scattering properties or collecting most of the illumination photons.

---

[27] Such a lifetime is expected for the pressures in our vacuum setup ($\sim 10^9$ mbar). We neglect the heating induced by phase-noise in the trapping beams, which we estimated to be above 20 s (see App. C).

The absence of 3D cooling is of course still present if we restrict ourselves to the 1D molasses configuration. An alternative would be to perform a two-dimensional illumination with beams at a 45° angle with respect to the *x*–*y* axes. This would lack cooling in the cavity direction, which can be achieved by using the intracavity field (see discussion at the end of Sec. 4.1). In the absence of heating detrimental effect, we expect precise estimation of the number of atoms and their position within the cavity region. By additionally collecting the fluorescence from a perpendicular direction (using one of the other in-vacuum lenses), a 3D reconstruction of the ensemble would be possible, expanding the possibilities of our system (see Chap. 7).

3.2.2 Cavity Reflection Monitoring

Fluorescence imaging represents an ideal method to detect the spatial distribution of atomic ensembles. However, in spite of taking only a few tens of milliseconds, the illumination-induced heating effects make it an invasive procedure with low repeatability. A non-destructive alternative, which is particularly suitable in the single-atom regime, is given by detecting the presence of an atom through its coupling to the cavity (see e.g. [58, 124, 125]). A strongly coupled atom can drastically change the intracavity power of a resonator that is being externally pumped with resonant light. This can be understood in a simplified picture where the atom modifies the effective length of the cavity due to its refractive index. As a consequence, monitoring the reflective and transmissive properties of the resonator with an external probe provides valuable information about the system: not only the presence of an atom, but also its coupling strength to the cavity, its internal state, etc. When combined with our optical transport capabilities, this detection scheme can also be used to estimate the relative position between a string of atoms. The dispersive nature of the interaction ensures negligible repercussions on the atom's trapping conditions, which is of crucial importance in our setup. An extended version of this technique is employed in the measurements of Chapter 4 to obtain the spectrum of the coupled atom–cavity system and in Chapter 5 to perform fast detection of the internal hyperfine state of an atom.

We begin this last section with a description of the working principle of the detection scheme, followed by an introduction to the experimental setup. We show estimations of the coupling strength and the relative position between atoms by using the cavity field as a spatial probe. The flexibility of our optical transport allows us to deterministically place an atom in the cavity region by stopping the transfer as soon as an atom is detected. Finally, the non-intrusive character of the probing technique allows the continuous monitoring of the atom's presence in the cavity without any observable influence on its trapping time, as we will show at the end of this block.

An Atom Moving through the Cavity

Let us assume a cavity with perfect mode- and impedance-matching, that is being externally probed by a weak light field on resonance with the atoms. When scanning the cavity length, the reflection of the probe field will show the typical dip introduced in the previous chapter. If the cavity length is locked at the resonance point, the light will enter the cavity and the reflection will vanish due to the corresponding interference effects. The scenario is different in the presence of an atom coupled to the resonator. As we will see in Section 4.2.1, the reflected power when the system is on resonance with an atom (with coupling constant *g*) is given by

$$P_{\text{ref}} = P_{\text{in}} \left[1 - (1 + g^2/\kappa\gamma)^{-2} \right], \tag{3.2}$$

where again κ and γ represent the decay rate of the cavity field and of the atomic excited state, respectively. If the coupling is strong enough, the atom will cause a visible change in the reflected power, which
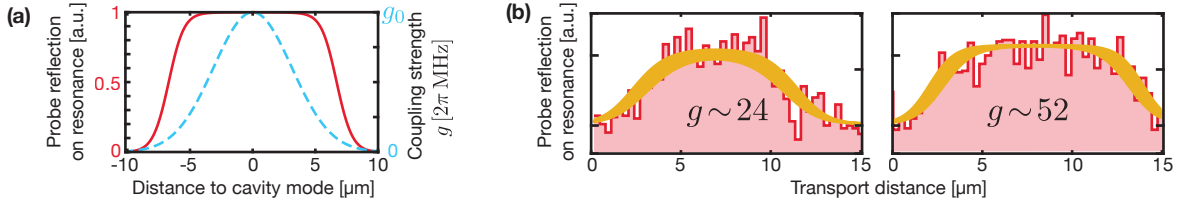
Figure 3.10: Cavity reflection in the presence of an atom. **(a)** Reflection signal for an atom with $g_0 = 2\pi \times 80\,\text{MHz}$ placed at different radial positions in the resonant cavity mode (solid red) with $(\kappa, \gamma) = 2\pi \times (50, 3)\,\text{MHz}$. The saturated curve is a consequence of the underlying coupling-position correspondence given by the Gaussian profile of the cavity mode (dashed blue). **(b)** Two examples of transient signals due to a single atom passing through the cavity. The count rate (red, 2 ms bins) is fitted to the model from Eq. (3.2) (orange), the thickness of the line represents the 95 % confidence interval. The estimated couplings are $2\pi \times (24 \pm 3)\,\text{MHz}$ and $2\pi \times (52 \pm 12)\,\text{MHz}$, respectively. The distance has been calibrated using a transport velocity of $0.16\,\mu\text{m}\,\text{ms}^{-1}$ (see text for details).

eventually reaches the saturation value of P_{in}. The precision with which one can estimate the coupling strength gets quickly reduced for our typical values of $g > 2\pi \times 40\,\text{MHz}$ (which are standard in our case) and is limited by the SNR of the reflected counts. A better approach to determine the coupling is to transfer the atom through the area covered by the cavity mode. The Gaussian profile of the intracavity field provides a correspondence between position and coupling strength. Therefore, monitoring the reflected light while the atom passes through the cavity allows us to extract the maximum coupling of the atom despite the saturation of the signal. Figure 3.10(a) depicts the reflected power expected from the transit of an atom according to Equation (3.2), along with the underlying profile of the intracavity field. When using this method to detect relative distances between atoms, it is the size of the cavity mode ($\sim 4.4\,\mu\text{m}$) that limits the resolution, as the Gaussian profile plays the role of the PSF in the imaging method. Furthermore, due to the saturation of the signal, it is impossible to distinguish the number of atoms in a certain region if their separation is smaller than the cavity mode (as opposed to fluorescence imaging, where the total integrated counts do not saturate). Thus, this technique performs better in the single-atom case (see example in Fig. 3.10(b)). A more powerful approach consisting in scanning the frequency of the probe instead of the position of the atom allows us to estimate the coupling strength even for dense ensembles (see Chap. 4).

In the following paragraphs we will consider the atoms as two-level systems (cycling transition), which yields the highest coupling with the cavity (g_0). The technical details about the preparation of atoms in such a state is discussed in detail in Section 4.2.2, and it only requires the presence of the probe field and an external repumper. For now we make the assumption that all atoms interact in the same way with the cavity, and that the variations in the estimated effective coupling strength g arise from different positions of the atoms in the cavity field.

The Detection Setup

The experimental layout required for the cavity-based detection is similar to the one described in Section 2.4.2 in the context of cavity stabilization. The relevant optical and electronic components are shown in Figure 3.11(a). The cavity is pumped through the high-transmission fiber by the probe laser, which is resonant with the rubidium D_2 line and stabilized in intensity. The signal reflected from the cavity mirror is separated from the incoming light by a 97%/3% beam-splitter and coupled into the multi-mode fiber of a Single-Photon Counter Module[28] (SPCM). The single-photon clicks of the detector

---

[28] SPCM: *COUNT-250N* (Laser Components).
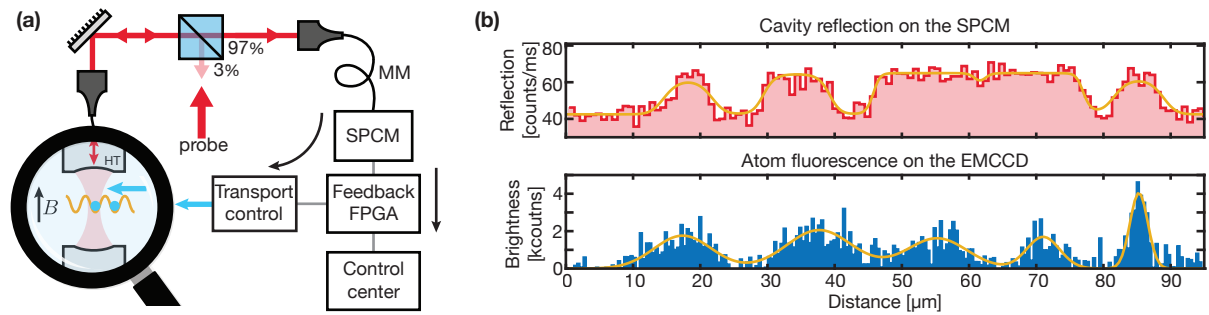
Figure 3.11: Atom detection setup. **(a)** Layout of the main experimental components for the cavity-based detection. The probe light (red) is reflected off the cavity and sent to the SPCM. The photon counts are processed by the FPGA-based card which can communicate to the transport control in order to apply real-time feedback (see text). The lock laser and the dipole-trap and repumper beams are not shown here for simplicity. **(b)** Detection of a string of atoms passing through the cavity. Top: reflection counts detected on the SPCM. To perform the fit we assume the number of atoms given by the fluorescence measurement. Bottom: Vertically-integrated counts of a 20 ms fluorescence image taken after the transit. The Gaussian peaks display a width that increases as we move from the cavity region (left end), attributed to aberrations outside the aplanatic region.

are time-tagged by an FPGA-based card[29] with 10 ns resolution. The self-made counting software provides a graphic interface showing the detected counts and stores the arrival time of every photon in a compressed binary file. The device allows us to react in real time to specific changes in the reflection by sending a trigger signal to the transport control, which is the basis of the transport feedback scheme presented later.

When scanning the length of the resonator we observe the dip in the reflected power signal, which allows us to lock the cavity on resonance where the counts on the detector reduce to a minimum. The entire detection procedure works as follows: By loading atoms in the dipole trap and transporting them into the cavity, the atoms emerge as transitory increases in the count rate (see Fig. 3.10(b)). Due to its non-linear behavior and the poissonian noise of the photon counts, the uncertainties on the estimation of g are bigger than the ones from our alternative method based on the observation of the band splitting. Since the atoms that couple stronger saturate the reflected signal during a longer period, it is challenging to distinguish strongly coupled atoms from a dense string of weakly coupled atoms. This becomes clear in Figure 3.11(b) where we show the cavity-based detection counts of a string of atoms transported through the cavity, and compare it to the fluorescence signal of an image taken directly after the transport. Due to the saturation effect, we cannot determine the number of atoms in the dense region, requiring the fluorescence imaging to provide the additional information. Yet, the reflective detection does not induce hopping nor does it suffer from spatial inhomogeneities (e.g. atoms located outside the aplanatic region in the fluorescence image).

Placing and Monitoring a Single Atom into the Cavity

Despite the fact that this method is not suitable for multiple-atom scenarios, the technique provides a valuable platform for the detection and monitoring of a single atom coupled to the cavity. As a consequence of the sensitivity of the SPCM and the high contrast of the signals, only a few femtowatt of probe light are usually required for this technique. Furthermore, as discussed in the following chapter, only a small fraction of the photons sent to the cavity are actually scattered by the atom [124]. This

---

[29] PXI FPGA Module for FlexRIO: *PXIe-7966* (National Instruments Ltd).

Figure 3.12: Continuous monitoring of a single atom. **(a)** Example trace of an atom passing through the cavity and a second one triggering the stop me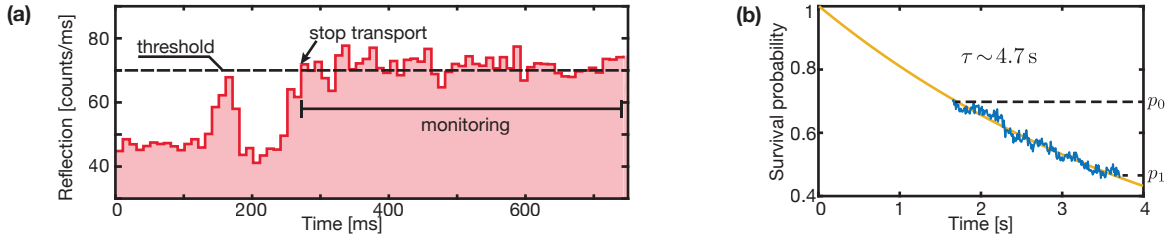chanism, which causes constant high level of the reflection (bin time of 10 ms and threshold of 70 counts ms^{-1}). **(b)** Decay curve of the survival during a monitoring period of 2 s after 1.5 s of transport. The blue data is the average of 35 traces. The extracted decay coincides with the one originated from background-gas collisions. The two free parameters of the fit (orange) are the decay time τ and the initial amplitude p_1.

absence of photon recoil implies that probing the cavity does not induce any detectable heating and, therefore, enables a non-destructive monitoring of the atom's presence.

A prerequisite for this procedure is the deterministic loading of a single atom into the resonator. This is achieved by combining our optical transport capabilities (Sec. 3.1.3) with the information provided by the cavity reflection. As an atom approaches the center of the cavity mode and the signal raises, the FPGA card stops the transport once a threshold (typically ∼90 % of the maximum reflected power) is reached.

The final position of the atom depends on three basic factors: the effective coupling, the threshold for the reflected power and the reaction time of the feedback system. The latter is mainly limited by the typically low power of the probe laser, thus requiring a binning time of at least 10 ms to obtain a decent contrast on the atom signals. The atom continues moving up to 2 μm at our usual transport speed after the threshold has been exceeded. Strongly coupled atoms will trigger the stop mechanism at a position further away from the cavity center. In this case, the remaining transport distance of 2 μm might not be enough to place it at the optimum position. Atoms with weaker effective coupling, though, might trigger the system only when they have reach the desired position and the consecutive transport delay reduces the final coupling. However, we observe that the final average coupling is rather insensitive to additional transport distances of a few micrometer after the feedback process[30]. It is important to keep in mind, that by using this transport procedure we perform a pre-selection of the coupling strengths in a certain range. This becomes relevant when measuring the distributions of g values in Section 4.2.2.

An advantage of the relatively short stopping distance of 2 μm is that it ensures the presence of only one atom in the cavity. Events where the effective coupling of several weakly coupled atoms mimic a strongly coupled one are prevented by sparsely loading the dipole trap (e.g. using short MOT-loading times and temporarily reducing the trap depth to get rid of hot atoms). An estimation of the remaining two-atom cases is done by measuring fluorescence histogram in the cavity region (similar to the one presented in Fig. 3.9(a)). For typical parameters we observe that usually less than 15 % of the cases contain more than one atom in the cavity[31] (see results presented in Fig. 4.7(b)).

Figure 3.12(a) shows an example of a typical transport trace. A first atom passing through the cavity does not exhibit a coupling strong enough to surpass the threshold, thus causing further transport until a second atom triggers the stop mechanism. Further on, the atom is held in the cavity while its presence is

---

[30] To estimate the average coupling here, we used the technique introduced later in Section 4.2.

[31] This is still a conservative estimation, as we are not taking into account atoms that are in the region of interest of the image but not coupled to the cavity.
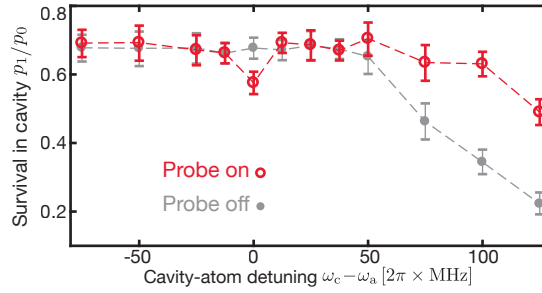
Figure 3.13: Relative survival rate (p_1/p_0) for atoms under continuous monitoring (red) or in the darkness (gray); the error bars represent the Clopper-Pearson confidence intervals (each data point corresponding to measurements of 300 to 1000 traces). The comparison is done for several frequencies of the monitoring cavity field. We attribute the discrepancies for far blue detunings to technical reasons (see text).

being continuously monitored. If the atom escapes the trap, the steady high level of the reflection counts will drop to the initial minimum. By averaging over several of such measurements, the telegraph-like signals transform into an exponentially decaying curve that describes the survival rate of the trapped atom under cavity probing (see Fig. 3.12(b)). The behavior during this time period (taking into account the time elapsed before the atom reached the cavity) corresponds to a trapping lifetime of (4.67 ± 0.10) s. This is in agreement with the independently measure lifetime in the 1D lattice, which confirms that indeed the cavity field is a non-destructive probe since any induced heating effect is negligible compared to the background collisions.

To confirm the results we also perform a reference measurement where the probe light is off while the atom is in the cavity[32]. The survival rate during this procedure (p_1/p_0 in the figures) appears to be the same as the one extracted for the continuously monitored case. Furthermore, this similarity holds even for different frequencies of the cavity probe field, as represented in Figure 3.13. The corresponding measurement sequence starts by transporting a single atom into the cavity and subsequently changing the frequency of the probe as well as the cavity length in order to keep it resonant with the light's frequency. After a period of 2 s both the cavity and probe are brought back to resonance to check the presence of the atom. The same is done without the probe light for the survival in the dark.

The relevance of this measurement relies on the fact that the survival is not affected by the presence of the cavity field or by its frequency. This implies the absence of *cavity cooling* and *cavity heating*, which are a consequence of the interplay between the motion of the atom and its interaction with the cavity field. In Section 4.1 we present a short description of these types of processes, and the reason why they do not emerge in our particular system. Although there is a clear drop on both survival rates for the blue-detuned cavity field, we do not observe heating effects in similar measurements (like those of Sec. 4.2) where we scan over the cavity frequency. We attribute the discrepancy to technical disturbances of the system during this particular measurement, e.g. intrinsic power instabilities of the probe laser in the far, blue-detuned region caused by the AOM being driven far off-resonance. This would deteriorate the atom detection at the end of the process (especially for the reference measurement, where probe is suddenly switched prior to the detection). Other sources could be parametric heating of the atoms due to oscillations in the locking mechanism of the cavity. Although the particular reasons are still not clear, we can rule out cavity-cooling/-heating processes, since they would occur at frequencies much closer to resonance.

---

[32] The probe is on during a short time at the beginning and the end of the 2 s window in order to detect the atom during the transport and to check if it survived the process, respectively.

Strong Coupling between Individual Atoms and a Fiber Cavity

Having combined the microcavity platform and the single-atom facility, the rest of this thesis is dedicated to the investigation of the basic properties of the coupled system and its potential applications. We begin in Section 4.1 by exploring the dynamics of a coupled atom–cavity system and its interactions with the environment, walking through the different regimes of coupling strength. The quantum-mechanical formalism introduced here serves as the basic framework on which the results discussed in following chapters are based.

One of the fundamental features of the coupled dynamics in strongly interacting systems is the visible splitting in their energy band structure. To access the underlying energy spectrum one must externally probe the coupled system by exciting any of its constituents: either the atom or the cavity. In Section 4.2 we show how the splitting can be clearly observed by pumping the cavity with a coherent field and monitoring its reflection, providing us with a fast and non-destructive estimation for the coupling strength g. We characterize the distribution of g due to different positions of the atoms in the resonator, and observe an enhancement of the effective cooperativity of the system when placing a small atomic ensemble in the cavity mode.

The effect of the coupled atom in the cavity reflective properties can also be used to obtain information about the internal atomic structure, which allows one to detect the hyperfine state of an atom in a non-intrusive manner by weakly pumping the resonator. This cavity-based state detection is discussed in the following Chapter 5, where it is shown that it entails a faster and more robust choice than the equivalent free-space fluorescence state detection [40], with a higher detection fidelity.

The system can be alternatively probed by externally driving the atom, instead of the cavity. This scenario is the focus of investigation of Chapter 6, where we monitor the photons scattered by the driven atom in both free space and the cavity mode. The results show that, in the same way that an atom can modify the reflective properties of the resonator, the cavity does alter the scattering properties of the atom. By varying the cavity resonance, the total scattering rate of an atom can be either reduced or enhanced considerably.

4.1 A Brief Introduction to Cavity QED

In 1946, E. M. Purcell inaugurated the era of cavity QED by introducing one of its most notable aspects: The rate of spontaneous emission of an excited atom can be modified by placing it inside a resonator [16]. In free space and with no photons present, an excited atom relaxes back to its ground state by emitting a

photon with a decay rate of Γ. Fermi's Golden Rule states that such a rate is proportional to density of final states ρ [111], which in this case is the density of radiation modes of the surrounding environment. It is clear then that modifying the properties of the electromagnetic modes with a resonator can indeed affect the atom's properties. For a Fabry–Pérot cavity of finesse $\mathcal{F}$, the density of states resembles the spectrum of Lorentzian peaks discussed in Section 2.1; it can be shown [126] that the ratio between the decay rate inside the resonant cavity and in free space is given by:

$$ f_P = \frac{6}{\pi^3} \frac{\lambda^2}{w_0^2} \mathcal{F} \, , $$

where w_0 stands for the cavity-mode waist and λ is the wavelength of the emission. If the cavity possesses high reflectivity mirrors and a small mode volume, this ratio becomes comparable to unity, thus yielding an increased atomic decay rate given by

$$ \Gamma' = \Gamma(1 + f_P) \, , \tag{4.1} $$

the so-called *Purcell enhancement*.

Despite the fact that this effect emerges already for weak interaction between the atom and the cavity, it still denotes a clear change on the atom's behavior at the single photon level. This suggests the question: Under which conditions does a single quantum entity (atom or photon) significantly alter the properties of the system? [77] Interestingly enough, one can reinterpret the Purcell factor f_P as the cavity-enhanced optical depth of a single atom: The cross-section of the atom $(3\lambda^2/2\pi)$ divided by the area of a cavity photon $(\pi w_0^2/4)$ and multiplied by two times the photon round-trips $(\mathcal{F}/\pi)$ [124]. If we require a single atom to act as a non-linear medium in the cavity, it must be optically thick, which results in the condition $f_P > 1$.

In the more recent literature, the Purcell factor also receives the name of *cooperativity* of the system, which for a single atom is generally defined as $C_1 = f_P/2$. This figure of merit can be re-expressed in a more generic form as the ratio between the rate of coherent and incoherent processes [127]

$$ C_1 = \frac{g^2}{2\kappa\gamma} \, , \tag{4.2} $$

where g stands for the coupling strength, κ is the cavity-field decay rate and $\gamma = \Gamma/2$. This is a universal definition which is valid for all platforms and more convenient for the following derivations. The inverse of the cooperativity is defined as the *critical atom number* N_0, and it represents the amount of atoms required to switch from a dispersive to an absorptive optical response to a resonant cavity field.

The alternative situation, where a single photon has a non-linear effect on the atom, can also occur. To saturate an atomic transition, the field's Rabi frequency must be bigger than the atomic decay rate (see e.g. [111]). The Rabi frequency for a single photon in the cavity turns out to be $2g$, which gives rise to yet another figure of merit: the *saturation photon number* $n_0 = \gamma^2/2g^2$. In summary, for an atom–cavity system to display non-linear effects already at the level of a single quantum excitation, one must impose the condition that the critical numbers (N_0, n_0) are indeed smaller than unity [128]. This does not necessarily imply strong coupling $(g \gg \kappa, \gamma)$ as we will discuss at the end of this section.

Many of the features of cavity QED (including the Purcell effect [129]) can be described via a fully classical framework of linear atomic absorption and dispersion [130]; this includes some of the results shown below as well as in the following experiments. However, a quantum treatment becomes necessary for several scenarios that contain saturation effects, coherent population evolution, single-photon correlations, etc. For that reason, in the pages ahead, we present a brief description of the quantum

system dynamics, including the irreversible effects of the environment as well as a short journey through the different coupling regimes of the non-driven system. The results for an externally driven system will be provided afterwards along with the corresponding measurements. For the sake of readability we avoid minor details; an introduction to the quantization of light (see e.g. [126]) as well as a more thorough description of certain calculations can be found in Appendix D.

4.1.1 A Single Atom Meets a Single Photon

The Jaynes-Cummings Hamiltonian [131] describes the spin-spring interaction between a two-level atom and a quantized mode of the electromagnetic field. In the absence of dissipative processes, the energy of the atom–cavity system is described by

$$\hat{H}_{\mathrm{JC}} = \hat{H}_{\mathrm{a}} + \hat{H}_{\mathrm{c}} + \hat{H}_{\mathrm{int}} .$$

where $\hat{H}_{\mathrm{a}}$ stands for the atomic energy, $\hat{H}_{\mathrm{c}}$ is the Hamiltonian of the cavity mode and $\hat{H}_{\mathrm{int}}$ describes the interaction between the atom and the cavity field.

Let us consider a two-level atom with ground $|g\rangle$ and excited $|e\rangle$ states of energies $E_{\mathrm{e}} = E_{\mathrm{g}} + \hbar\omega_{\mathrm{a}}$. For convenience one can choose $E_{\mathrm{g}} = 0$ such that the Hamiltonian is reduced to one term proportional to the population of the excited state

$$\hat{H}_{\mathrm{a}} = \hbar\omega_{\mathrm{a}} |e\rangle\langle e| = \hbar\omega_{\mathrm{a}} \hat{\sigma}^{\dagger}\hat{\sigma} .$$

We have introduced the raising and lowering operators $\sigma^{\dagger} = |e\rangle\langle g|$ and $\sigma = |g\rangle\langle e|$ which describe the excitation and deexcitation of the atomic spin, respectively.

To describe the energy of the cavity field we resort to the second quantization formalism (see App. D.1). The Hamiltonian of the electric field, after quantization, displays the energy spectrum of a mechanical oscillator:

$$\hat{H}_{\mathrm{c}} = \hbar\omega_{\mathrm{c}}\left(\hat{a}^{\dagger}\hat{a} + \frac{1}{2}\right),$$

where $\hat{a}^{\dagger}$ and $\hat{a}$ represent the ladder operators of the field with frequency ω_{c}.

The spectrum shows a collection of eigenstates called *Fock states* $|n\rangle$ (with eigenenergies $n\hbar\omega_{\mathrm{c}}$) which represent n photons in the cavity mode. The operators $\hat{a}^{\dagger}, \hat{a}$ are thus referred as creation and annihilation operators, since they respectively add or remove an excitation (photon) from the system.

The dipole moment of the atom $\hat{\mathbf{d}}$ couples to the electric field of the cavity mode $\hat{\mathbf{E}}$ (given in Eq. (D.5)), such that the interaction term in the Heisenberg picture reads

$$\hat{H}_{\mathrm{int}} = \hat{\mathbf{d}}\cdot\hat{\mathbf{E}} = d\left(\hat{\sigma} e^{-i\hbar\omega_{\mathrm{a}}} + \hat{\sigma}^{\dagger} e^{i\hbar\omega_{\mathrm{a}}}\right)\mathscr{E}_0\left(\hat{a}\, e^{-i\hbar\omega_{\mathrm{c}}} + \hat{a}^{\dagger} e^{i\hbar\omega_{\mathrm{c}}}\right); \tag{4.3}$$

where $\mathscr{E}_0$ is the electric field amplitude of a single photon (see Eq. (D.3)). Under the right approximations[1] and after applying a unitary transformation to get rid of the time dependence, we obtain the conventional form of the Jaynes-Cummings Hamiltonian [131]:

$$\hat{H}_{\mathrm{JC}} = \hbar\omega_a\, \hat{\sigma}^{\dagger}\hat{\sigma} + \hbar\omega_c\, \hat{a}^{\dagger}\hat{a} + \hbar g_0\left(\hat{\sigma}^{\dagger}\hat{a} + \hat{\sigma}\, \hat{a}^{\dagger}\right). \tag{4.4}$$

We introduce once more one of the key parameters of the system, which is the coupling strength g_0

---

[1] We apply the dipole approximation by assuming that the atomic dipole is much smaller than the light wavelength ($\mathbf{k}\cdot\mathbf{r}_{\mathrm{atom}} \ll 1$), and the rotating wave approximation by neglecting the terms oscillating at frequencies $(\omega_{\mathrm{a}} + \omega_{\mathrm{c}}) \gg |\omega_{\mathrm{a}} - \omega_{\mathrm{c}}|$.
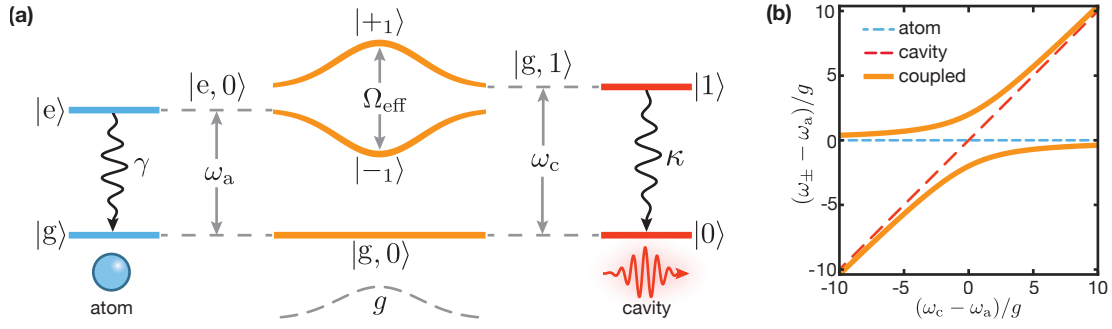
Figure 4.1: Interacting atom–cavity system with a single excitation. **(a)** Energy-level schemes ($\hbar = 1$) for the atom (blue, left), the cavity (red, right) and the lowest three states of the Jaynes-Cummings ladder (orange, center). The decay constants γ and κ represent the environmental coupling of the atom and the cavity respectively (wavy arrows). The red background and the dashed gray line in the central region represent the Gaussian profiles of the cavity mode and the coupling strength respectively; as we move towards higher values of g (center) the band splitting Ω_{eff} increases and the new eigenstates $|\pm_1\rangle$ depart from the original uncoupled states (sides). **(b)** Energy bands for both the uncoupled and coupled atom–cavity system (same color code as in (a)). On resonance, the degeneracy is lifted and a band gap of $2g$ appears. In the dispersive regime though only a shift reveals the weakened interaction.

between an atom and a single cavity-photon

$$g_0 = d \sqrt{\frac{2\omega_c}{\hbar\varepsilon_0 V}}, \tag{4.5}$$

where ε_0 is the vacuum permittivity and V represents the cavity mode volume[2]. The coupling constant is also referred as half the *single-photon Rabi frequency* since it represents the rate of coherent energy exchange between the atom and a single photon in the cavity. The effect of the position of the atom can be included by considering the TEM$_{00}$ cavity-mode spatial distribution (see Sec. 2.1) such that

$$g = g_0 |\sin(kz)| e^{-(x^2+y^2)/w_0^2}. \tag{4.6}$$

This incorporates the radial Gaussian profile of waist w_0 and the standing wave pattern in the propagation direction. From now on we will thus reserve the symbol g_0 for the coupling strength of a single atom placed at the center of the cavity mode, and use g to represent the real or effective coupling of the system in general.

The ground state of the new coupled system is given by the tensor product of the uncoupled original ground states $|g, 0\rangle := |g\rangle_a \otimes |0\rangle_c$. In the presence of n excitations, $\hat{H}_{\text{int}}$ couples only the states $|g, n\rangle$ and $|e, n-1\rangle$; it is therefore enough to diagonalize $\hat{H}_{\text{JC}}$ in the subspace spanned by those states which results in a ladder of doublets $|\pm_n\rangle$ also known as the Jaynes-Cummings ladder[3]. The ground state along with the lowest doublet $|\pm_1\rangle$ (see Fig. 4.1(a)) are enough to describe most of the experiments presented in this chapter since we will always assume a maximum of one excitation in the system (also known as *weak excitation approximation*).

---

[2] Expression (4.5) allowed us to claim in the introduction that $f_P = g^2/\kappa\gamma$.

[3] For high values of n we reach the semi-classical regime and the ladder transitions give rise to the well known Mollow triplet [132] spectrum of a strongly driven atom with $\Omega = \sqrt{n}\,\Omega_{\text{eff}}$.

The eigenenergies of the coupled system are no longer $\hbar\omega_a$ and $\hbar\omega_c$ but the symmetric bands

$$\omega_\pm = \frac{\omega_a + \omega_c}{2} \pm \frac{\Omega_{\text{eff}}}{2}, \tag{4.7}$$

where we have introduced the effective single-photon Rabi frequency $\Omega_{\text{eff}}^2 = 4g^2 + (\omega_c - \omega_a)^2$. This bands feature an avoided crossing, as shown in Fig. 4.1(b); the value of the energy splitting which lifts the degeneracy of the original bands at resonance corresponds to $2\hbar g$ and is typically referred as to *vacuum Rabi splitting* (VRS). In the time domain picture, this coherent exchange of energy can be seen as an oscillation between the atom being excited and the cavity containing a photon, with a periodicity of $2g$.

When the system is far off-resonance ($\Delta_{\text{c-a}} := (\omega_c - \omega_a) \gg g$) one recovers the atomic and photonic energy bands of the uncoupled system, except for a small dispersive frequency shift given by $|\Delta_{\text{shift}}| = g^2/\Delta_{\text{c-a}}$. On the one hand the cavity resonance shift can be viewed as a dispersive effect of the atom changing the effective refractive index of the cavity. On the other hand the atom experiences an AC Stark shift produced by an off-resonant field with driving strength $2g$.

The appearance of the splitting at resonance is a sign of the interaction between the individual subsystems [133]. However, when dissipation is present in the dynamics, the avoided crossing is washed out by incoherent processes. The splitting is then visible only if the coherent exchange of energy is faster than the decay rates (i.e. the system is said to be strongly coupled).

4.1.2 The Open Quantum System: from Weak to Strong Coupling

The Master Equation Approach

Closed quantum-systems are a convenient abstraction that simplifies the dynamics while keeping basic physical insights. However, in any realistic scenario where the aim is to describe a feasible experiment, one must account for dissipative processes which describe the interaction between the system of interest and its environment. Furthermore, in the experiments that we perform, the atom–cavity system is probed by external fields that constantly pump excitations into the system, which cannot be considered closed anymore.

The joint evolution of the system can be obtained by adding the environment to the Hamiltonian and calculating the unitary time evolution. Unfortunately, the reservoir that surrounds the closed system usually contains an infinity amount of degrees of freedom, the dynamics of which are not necessarily known. Since we are not interested in those environmental states, one can use the density matrix formalism to trace them out. In this case the Schrödinger equation is replaced by the master equation [134], which provides the time evolution of the density matrix $\hat{\rho}$ of the closed system[4]:

$$\frac{d\hat{\rho}(t)}{dt} = \hat{\mathcal{L}}\hat{\rho}(t). \tag{4.8}$$

The Liouvillian superoperator $\hat{\mathcal{L}}$ contains both the coherent evolution given by the unitary Hamiltonian of Equation (4.4) and the Linbland terms associated with the relaxation processes of the system:

$$\hat{\mathcal{L}}\hat{\rho} = -\frac{i}{\hbar}\left[\hat{H}_{\text{JC}}, \hat{\rho}\right] + \hat{C}\hat{\rho}\hat{C}^\dagger - \frac{1}{2}\left(\hat{C}\hat{C}^\dagger\hat{\rho} + \hat{\rho}\hat{C}\hat{C}^\dagger\right),$$

where we have introduced the Jump or Collapse operator[5] accounting for the two decay channels of our

---

[4] This approximation holds as long as the reservoir has enough degrees of freedom such that it has no *memory* (i.e. is Markovian), which is reasonable when the environment is the continuum of electromagnetic modes.

[5] We use the expression for zero temperature, since the contribution of thermal photons at our wavelength (780 nm) is negligible.

atom–cavity system [17]:

$$\hat{C} = \sqrt{2\gamma}\,\hat{\sigma} + \sqrt{2\kappa}\,\hat{a}\,.$$

The solution to the master equation yields a complete description of the system, allowing us to obtain critical information. For example, the cavity output field can be calculated by multiplying the leakage time of a cavity-photon (2κ) times the intracavity photon number $\langle\hat{a}^\dagger\hat{a}\rangle$. Equivalently, the population of the atomic excited state $\langle\hat{\sigma}^\dagger\hat{\sigma}\rangle$ multiplied by the decay rate Γ provides the free-space scattering rate of the atom.

Nevertheless, the complexity of the system and the size of the Hilbert space make it computationally challenging to solve Equation (4.8) unless certain approximations are considered. In the presence of decoherence, the master equation has a steady state solution ($\hat{\mathcal{L}}\hat{\rho}_\mathrm{s} = 0$); in the case of externally driven systems such a solution is not the trivial one, and therefore provides relevant information. To reduce furthermore the complexity, we can assume the already mentioned weak-excitation approximation that allows us to truncate the Hilbert space. With such considerations it is possible to obtain the steady state solution via affordable numerical computations [135, 136] for any range of decay and coherent rates and for different external-driving schemes, without further approximations required. In addition, one can include different polarization modes inside the cavity and/or hyperfine and Zeeman substructures of the atomic energy levels [137]. We will make use of such numerical computations whenever a detailed simulation of the system is required (more details can be found in App. D.3).

Part of the physics and relevant dynamics during the transient processes, however, remain hidden when performing such computations. To obtain a deeper insight of the dynamics we will derive analytical approximations whenever is possible. With such intention in mind, in the coming paragraphs we explore the time evolution of the open atom–cavity system for different coupling strengths.

A Dissipative Two-Level System: The Different Regimes

Let us assume an interacting, open atom–cavity system with maximum one excitation (much as the one described in Figure 4.1) and consider the doublet $|\pm_1\rangle$ as our closed two-level system. In that case, any decay process (including transitions to the ground state) will be regarded as a loss from our system of interest. This can be described heuristically by a non-Hermitian Hamiltonian[6] $\hat{H}_\mathrm{diss}$ (see e.g. [138, 139]) that includes the losses of the system such that

$$\hat{H}_\mathrm{diss} = \hat{H}_\mathrm{JC} - i\hbar(\gamma\hat{\sigma}^\dagger\hat{\sigma} + \kappa\hat{a}^\dagger\hat{a})\,.$$

The eigenvalues $\tilde{\omega}_\pm$ of this new Hamiltonian differ from those of the closed system in Equation (4.7), and are actually complex numbers given by (see e.g. [26, 140])

$$\tilde{\omega}_\pm = \omega_\mathrm{a} + \frac{\Delta_\mathrm{c-a} - i\,(\kappa + \gamma)}{2} \pm \sqrt{g^2 + \left(\frac{\Delta_\mathrm{c-a} - i\,(\kappa - \gamma)}{2}\right)^2}\,. \tag{4.9}$$

Their real part describes the resonance frequency, while the imaginary component reveals the linewidth of such a resonance. A plot containing both the energy bands and their widths for different values of the coupling strength g is included in Figure 4.2(a) for the resonance case ($\Delta_\mathrm{c} = 0$).

Our goal is to use the knowledge from Equation (4.9) to explore the different dynamics that arise as we increase the interaction strength [26, 141]. To this end we will assume that the system is initially composed of an excited atom in an empty cavity (the state $|e, 0\rangle$ in the original basis), and then analyze

---

[6] It can be interpreted as the quantum equivalent of introducing losses in a system by adding an imaginary term to the energy.
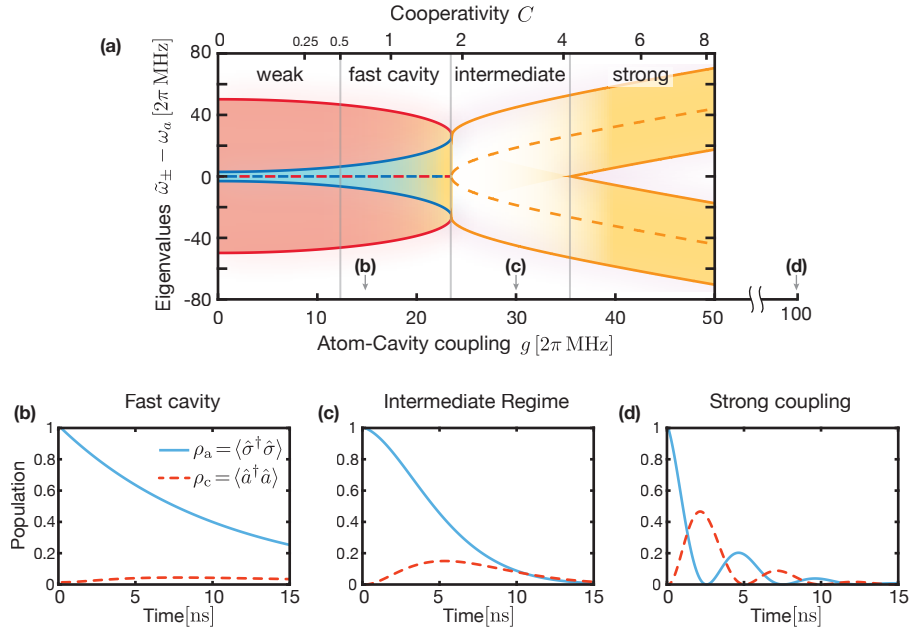
Figure 4.2: Frequency spectrum and time evolution of the open, non-driven atom–cavity system for different coupling regimes, with $\omega_a = \omega_c$ and $(\kappa, \gamma) = 2\pi \times (50, 3)$ MHz. **(a)** Complex eigenvalues of the non-Hermitian Hamiltonian: Dashed lines mark the resonance frequencies ($\mathrm{Re}(\tilde{\omega}_\pm)$). Solid lines represent their full-width half-maximum ($\pm\mathrm{Im}(\tilde{\omega}_\pm)$). Atom- and cavity-like states are indicated by blue and red respectively; orange represents the intermediate to strongly-coupled system. The regions separated by the vertical lines are (from left to right): weak-coupling, fast-cavity, intermediate and strong-coupling regime. The bottom row depicts the time evolution of both atom and cavity populations for the different interaction strengths: **(b)** Fast-cavity exponential decay given by Eq. (4.11), with $g = 2\pi \times 15$ MHz. **(c)** Intermediate domain behavior from Eq. (D.8) with $g = 2\pi \times 30$ MHz. **(d)** Strong-coupling oscillations of Eq. (4.12) with $g = 2\pi \times 100$ MHz.

the time evolution of the population of both the atom $\rho_a = \langle \hat{\sigma}^\dagger \hat{\sigma} \rangle$ and the cavity $\rho_c = \langle \hat{a}^\dagger \hat{a} \rangle$. We will always assume that the system is in resonance ($\omega_c = \omega_a$) and focus on the interpretation of a few selected results, although a full analytical solution to this problem can be found in Appendix D.2.

When classifying different regions according to the interaction strength, one should not restrict the possibilities to either weak ($g \ll \kappa, \gamma$) or ultra-strong coupling ($g \gg \kappa, \gamma$). There are more scenarios rich in physics than just the two extreme cases of poorly coupled systems described by classical laws, and fast coherent dynamics that can be explained by a closed-system approach.

For the low strength values of the **weak-coupling domain** one still finds non-trivial properties like that of optical bistability [142]; however we are mostly interested in the scene where quantum effects clearly manifest. As discussed, this occurs when the critical atomic number N_0 and the saturation photon number n_0 are smaller than unity; this implies $g > \gamma$ but not necessarily $g > \kappa$, which is then compatible with the cavity decay rate being the highest. Such conditions define the so-called **fast-cavity domain**, and can be rewritten as $\kappa > (g^2/\kappa) > \gamma$. The eigenfrequencies in this approximation are fully imaginary:

$$i\,\tilde{\omega}_+ \approx \kappa - g^2/\kappa$$
$$i\,\tilde{\omega}_- \approx \gamma + g^2/\kappa\,.$$

This means that the coupled system is still degenerate, as opposed to the non-dissipative case where the

splitting appears as soon as $g > 0$ (see Eq. (4.7)). The coherent coupling is still much smaller than the cavity decay and therefore the interaction can be considered perturbative. In other words, the eigenmodes still conserve their original atomic and photonic identities, but with a modified linewidth. The change is negligible in the case of the cavity, yet the atomic decay rate experiences a considerable enhancement. One can rewrite the atomic linewidth $i\tilde{\omega}_-$ in terms of the cooperativity defined in (4.2), and in fact we recover the expression for the Purcell effect of Equation (4.1), namely:

$$\gamma' = \gamma(1 + 2C_1). \tag{4.10}$$

The time evolution of both populations is found to be

$$\rho_a \approx e^{-2\gamma't} \quad \text{and} \quad \rho_c \approx \frac{g^2}{\kappa^2}\left(e^{-\kappa t} - e^{-\gamma't}\right)^2. \tag{4.11}$$

The initial atomic excitation preferably decays into the cavity mode with the higher rate γ'; yet, the transient population of the cavity is negligible ($g^2/\kappa^2 \ll 1$). This is to be expected, as for this kind of fast cavities, the photon leaves the resonator as soon as the atom emits it, without a chance of being reabsorbed (see Fig. 4.2(b)). Although in this regime the cavity decay is much faster than any coherence, it has been shown that if one probes the system by pumping photons into the resonator, the underlying coherent effects can still be observed [26] (even though it is clearly an over-damped system).

As we turn up the coupling, we reach a particular point when $g = (\kappa - \gamma)/2$. The eigenstates are no longer photon- and atom-like, but an equal mixture of both with a linewidth given by the average of the originals: $i\tilde{\omega}_\pm = (\kappa + \gamma)/2$. This is the region often referred as to the **intermediate regime**, and it displays a transitional behavior, somewhere between the Purcell-enhanced decay of the atomic excitation and the coherent Rabi oscillations expected for a strong interaction. As depicted in Figure 4.2(c), the cavity population exhibits a transient build-up since the coherent exchange is now on the order of the cavity leakage, which is not an uncommon experimental scenario.

From this point onwards the width stays constant and a splitting appears; however it is not until $g^2 > (\kappa^2 + \gamma^2)/2$ that both bands are properly resolved. This marks the beginning of the **strong-coupling domain** which is also the regime where we perform the majority of our experiments. For couplings much higher than this transition value, we recover the non-dispersive result of a splitting of $2g$ given that

$$i\tilde{\omega}_\pm \approx \frac{\kappa + \gamma}{2} \pm i g.$$

As expected, at this point the roles of atomic and photonic excitations are equivalent, and the populations perform several Rabi oscillations before the energy dissipates into the environment (see Figure 4.2(d)):

$$\begin{aligned} \rho_a &\approx \cos^2(gt)\, e^{-(\kappa+\gamma)t} \\ \rho_c &\approx \sin^2(gt)\, e^{-(\kappa+\gamma)t}. \end{aligned} \tag{4.12}$$

The effect of the slow damping terms is still there, represented by the exponential envelope with a decay rate of $\kappa + \gamma$. This means that, in this regime, the effective decay time of the dressed atom does not increase linearly with the cooperativity (Eq. (4.10)), as it is limited by the cavity linewidth. Instead, for strongly-coupled systems the decay rate scales as $\gamma' = \gamma(1 + \kappa/\gamma)$. Nonetheless, the probability of the atom emitting the photon into the cavity mode instead of in free space is still given by

$$\eta = 2C_1/(1 + 2C_1). \tag{4.13}$$

This expression applies in all regimes, meaning that the collection efficiency of the resonator is not limited and does, indeed, increase for stronger couplings. This effect is not exclusive to spontaneously emitted photons, but also applies to coherent scattering of light shone onto the atom, as we will discuss and show in Chapter 6.

As we move away from resonance the eigenstates recover their original identity and linewidth, and the interaction is reduced to an energy shift. This can be observed when we weakly drive the cavity, as we demonstrate in the measurements performed in Section 4.2.

The External Atomic Degrees of Freedom: a Comment on Cavity Cooling

In the model used so far, we have focussed on the energy exchange between the cavity field and the internal degrees of freedom of the atom, thus excluding any effects related to the atomic motion. However, due to the shallow optical traps employed in our particular setup, the influence of the cavity on the kinetic behavior of the atom can be crucial. When externally driving the system with a weak classical field, the interplay between the intracavity photons and the atomic motion along the resonator gives rise to a rich panorama of effects. The complexity of the dynamics involved can be exploited to "cool" the motional state of the atom, either along the cavity axis by pumping the resonator mode [143–146] or in all three directions by trapping and driving the atom with external fields [97, 147, 148]. A detail understanding of the underlying mechanisms is beyond the scope of this work; intuitive pictures for both scenarios can be found in the aforementioned references (e.g. [146, 148]).

The critical feature that all cavity-cooling techniques share is the limit on the final temperature. In the same way that Doppler cooling cannot provide temperatures below $T_D \approx \hbar\gamma/k_B$ [106], the steady-state limit of cavity cooling is set by $T_{cav} \approx \hbar\kappa/k_B$. Effective cavity cooling is, therefore, experimentally challenging in the regime of open resonators with $\kappa \gg \gamma$, since the external trapping forces must be strong enough to contain atoms with temperatures on the order of T_{cav}. In our case, it translates into optical lattices with trap depths around ∼2.5 mK which are not within our reach in terms of optical power[7]. Thus, cavity-induced cooling processes cannot be exploited in the present system due to the high bandwidth of the cavity. Nonetheless, this also means that we do not face the detrimental effects that may appear when the system's settings are not the optimal for cooling. The lack of this so-called *cavity-heating* processes allows us to freely use any combination of detunings without the resonator increasing the heating rate, as it was demonstrated in Section 3.2.2.

A different approach is necessary in order to provide cooling in the three directions, especially along the cavity axis. In a previous experimental setup, we showed that cooling in the cavity axis can be provided either by EIT techniques [149] or by using the intracavity lock laser to perform cavity-assisted Raman cooling [150]. The latter, which is now being implemented in our system, constitutes a promising candidate for the realization of 3D cooling.

Our Experimental Parameter Range

The expression of the coherent rate g_0 introduced in Equation (4.5) yields the maximum theoretical value of the coupling strength of a single atom. If we consider the mode volume of the fundamental cavity mode (see Eq. (2.7)) and the cycling transition of the ^{87}Rb D$_2$ line[8], we expect $g_0 \approx 2\pi \times 120$ MHz. Experimentally, we observe lower values generally attributed to the different positions of the atom in

---

[7] In addition, heating processes like dipole-force fluctuations would become predominant when illuminating atoms in such deep traps [121].

[8] The atomic dipole d can be calculated from the atomic transition frequency and natural lifetime, see e.g. Eq. (D.10) (where $d = \mu$).

the cavity mode (Sec. 4.2.2). In addition, when applying external illumination (as in Section 6) the effective coupling might be reduced further due to delocalization of the atom (hopping) and population of sublevels others than the one involved in the cycling transition (optical pumping). Both effects depend on a wider range of parameters like the particular illumination settings or the trapping potential, giving rise to a wider distribution of possible strengths. The reduced coupling can nevertheless be collectively enhanced by coupling more than one atom to the cavity (Sec. 4.2.3). All things considered, we observe effective coupling factors going all the way from 0 to $2\pi \times 200$ MHz.

Although the free-space atomic decay γ is fixed, the cavity losses represented by κ depend on the characteristics of the resonator and its mirrors. As described in Appendix A.2, the finesse of our cavity has decayed with time, and in the rest of this thesis we show experiments where κ takes on values from the wide range of $2\pi \times (40-100)$ MHz. Considering the extent of coupling strengths and cavity linewidth observed during the experimental procedures, we face different coupling regimes in our system, which motivates the spectrum of relative strengths that we covered in the previous paragraphs.

4.2 The Spectrum of the Strongly-coupled System

The most prominent aspect of the spectrum of a coupled atom–cavity system is the avoided crossing of the energy bands, which we have introduced as the vacuum Rabi splitting [133]. In the presence of decoherence processes, the resonance features broaden and the band gap only becomes apparent when the system is strongly coupled, such that $g > (\kappa+\gamma)/2$. As a consequence, the observation of the VRS constitutes the hallmark of strong coupling in cavity QED.

To access this underlying energy structure one must externally probe the coupled system. The natural approach in optical CQED is to drive the cavity field instead of the atom, as it has a smaller impact on the thermal motion of the latter, and therefore is less restrictive in terms of required trapping forces. In this case, all the relevant spectral information is contained in the intracavity power, which can be interrogated by detecting the photons leaving the cavity mirrors (in either transmission or reflection). The VRS with single neutral atoms was first measured using the cavity transmission via transient measurements of thermal [151, 152] and cooled [153] atomic beams with one atom on average, while the first observation of the splitting for a trapped atom was not accomplished until 2004 [154, 155] (and 2010 for fiber cavities [156]). In particular, Boca *et al.* [154] showed that it was possible to uncover the energy band gap from a single measurement performed on one and the same atom. Due to the lack of a three-dimensional lattice and the presence of cavity-induced heating effects, the measurement required intervals of Raman cooling applied onto the atom.

In this section we show that the full confinement provided by our three optical lattices, combined with the lack of cavity effects on the atom's mechanical degrees of freedom, allows us to observe a clear single-atom VRS signal from a single trace, without the need for additional cooling techniques. As a result, we measure a two-dimensional spectrum of the energy bands of our system thus demonstrating that the atoms are indeed strongly coupled. Moreover, we show that the cooperativity of the system is not limited by the experimental design, as it can be enhanced by exploiting the collective enhancement provided by an atomic ensemble. In particular, we obtain a twofold boost of the average coupling strength by placing a small group of atoms inside the resonator.

4.2.1 Reflective Properties of the Dressed Cavity

To investigate the properties of the dressed system we probe the cavity with a weak laser; theoretically this is depicted by a pumping of the intracavity field with a coherent state described by a photon rate ε.

If the probe beam is faint enough ($\varepsilon \ll \kappa$) one can still use the weak-excitation model introduced in the previous section, where the external driving is reduced to a single term in the new effective Hamiltonian:

$$\hat{H}_\varepsilon = \hat{H}_{\mathrm{JC}} - i\hbar(\gamma\hat{\sigma}^\dagger\hat{\sigma} + \kappa\hat{a}^\dagger\hat{a}) + \varepsilon\,(\hat{a}^\dagger + \hat{a})\,. \tag{4.14}$$

Schrödinger's equation provides the population dynamics of both the cavity ($\langle\hat{a}^\dagger\hat{a}\rangle$) and the atom ($\langle\hat{\sigma}^\dagger\hat{\sigma}\rangle$). In particular, in the steady state one finds an analytical solution for the photon number inside the driven cavity (see App. D.2):

$$\langle\hat{a}^\dagger\hat{a}\rangle = \frac{\varepsilon^2}{\left|(\kappa + i\Delta_{\mathrm{c}}) + g^2/(\gamma + i\Delta_{\mathrm{a}})\right|^2}\,,$$

where $\Delta_{\mathrm{a,c}} = \omega_{\mathrm{a,c}} - \omega_{\mathrm{p}}$ are the frequencies of the system in the picture rotating at the probe frequency ω_{p}.

The imaginary components that appear in the denominator indicate the dispersive behavior that gives rise to a shift in the system resonances; thus, this expression for the intracavity power contains the spectrum of the open system discussed in the theoretical introduction. Before we move on with the details for the observation of the splitting, let us write down the cavity field in a more transparent way as

$$\langle\hat{a}^\dagger\hat{a}\rangle = \frac{\varepsilon^2/\kappa^2}{1 + (\Delta_{\mathrm{c}}/\kappa)^2}\frac{1}{|1 + 2\tilde{C}|^2}\,. \tag{4.15}$$

We have now separated the expression into two factors: The first term is the Lorentzian curve expected for a pumped, empty cavity while the second stands for the dressing induced by the atom. We have introduced a convenient term called the *complex cooperativity* [157]

$$\tilde{C} = \frac{g^2}{2(\kappa + i\Delta_{\mathrm{c}})(\gamma + i\Delta_{\mathrm{a}})}\,, \tag{4.16}$$

which is, in essence, an extension of the cooperativity for an externally driven system. This new quantity depends on the different detuning parameters and it recovers the original value C_1 when on resonance. We will use it from now on, as it will simplify the expressions of the system's spectrum in the rest of the chapter and facilitate comparisons when we drive the atom, instead of the cavity (see Chap. 6).

It is now easier to see the effect of a coupled atom in terms of the cooperativity of the system: if $\tilde{C}$ is high enough, the cavity field will be depleted in the presence of the atom. This effect is what allowed us to detect the presence of the atom while performing the feedback transport and, as we will see in the next chapter, to distinguish between different atomic internal states.

The information about the spectrum is also contained in the photons that the atom scatters into free space. A quick calculation shows that the scattering rate of the atom, when externally pumping the cavity, is given by

$$R_{\mathrm{a}} = \frac{\varepsilon^2}{\kappa C_1}\frac{4|\tilde{C}|^2}{|1 + 2\tilde{C}|^2}\,,$$

which, for a cooperativity bigger than unity, can be approximated by $\varepsilon^2/\kappa C_1$ (on resonance). This means that the atom scatters in free space a fraction of approximately C_1^{-1} of the photons sent to the cavity.

Due to the low critical photon number in our system ($n_0 \approx 10^{-3}$), we have to drive the cavity with low powers on the order of femtowatts to keep the atom from saturating. Collecting and detecting the few photons scattered in free space with the EMCCD camera requires long measurement times that would reduce the duty cycle of the typical experiments presented in this section[9]. Thus, we only observe the

---

[9] This is not the case when using higher pumping powers [158] or low cooperativity systems [152], where the free-space atomic scattering can be substantial, and the splitting can be observed.
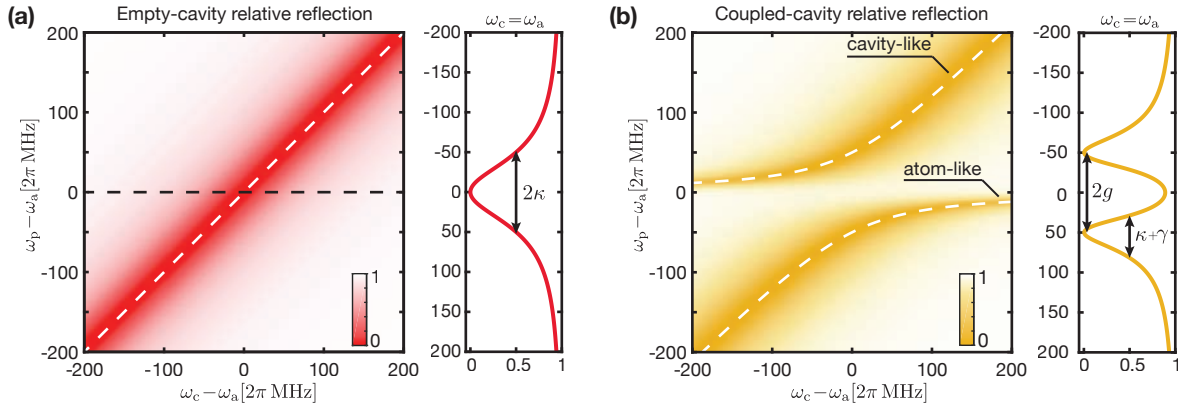
Figure 4.3: Theoretical model for the power reflected off a weakly driven cavity (with $\alpha = \beta = 1$ and $\eta_{HT} = 0.5$), normalized to the far off-resonant cavity reflection. **(a)** Reflected power from an empty cavity for different resonator frequencies (horizontal axis) and probe frequencies (vertical axis). The typical Lorentzian dip of width 2κ, shown in the lateral section for $\Delta_{c-a} = 0$, appears when both cavity and probe are on resonance (diagonal dashed line). The atomic transition is represented here by the black horizontal line. **(b)** Reflection spectrum of a coupled atom–cavity system with typical values of $(g, \kappa, \gamma) = 2\pi \times (50, 50, 3)$ MHz. The crossing point of the two uncoupled bands has now disappeared due to the vacuum Rabi splitting, where the system is a mixed entity part atom and part cavity with a linewidth given by the average of the originals (shown in the lateral section for $\Delta_{c-a} = 0$). For large cavity detunings, the system's eigenbands (represented by the dashed lines) converge to both the initial atomic and cavity eigenfrequencies of (a), and so do their widths. The amplitude of the atom-like reflection dip gets reduced due to the atom-induced losses, although the effect is not clearly visible in this particular parameter regime.

system's spectrum by detecting the leakage of photons from the intracavity field (E_{leak}).

Due to the design of our system we only have access to the the reflected counts, and not the transmitted. When interpreting the power reflected from the resonator, we must take into account the interference between the cavity reflection and the leakage field (as we did in Chap. 2), this time adding the effect of the coupled atom. The interference between both fields results in a cavity output power $P_{out} = |\beta E_{in} - \alpha E_{leak}|^2$, where the complex amplitudes α and β represent the mode matching of the fiber-core mode with the leaked and reflected fields respectively (see Sec. 2.3.2). The intracavity field leaks out of the high-transmission mirror with an amplitude $E_{leak} = \sqrt{2\eta_{HT}\kappa}\langle \hat{a}\rangle$, where η_{HT} is the ratio between the transmission coefficient $\mathcal{T}_{HT}$ and the total losses of the resonator. The amplitude $\langle \hat{a}\rangle$ can be extracted from Equation (4.14) taking into account that the coherent pumping in this case is given by $\varepsilon = \sqrt{\eta_{HT}\kappa}\,\alpha E_{in}$. This leads us to the final expression for the reflected power of a coupled atom–cavity system:

$$P_{out} = P_{in}\left|\beta - \alpha^2\,\frac{\sqrt{2}\,\eta_{HT}}{(1 + i\Delta_c/\kappa)}\,\frac{1}{(1 + 2\tilde{C})}\right|^2 . \tag{4.17}$$

For $\tilde{C} = 0$ we recover the asymmetric Lorentzian line-shape typical of the reflection dip in fiber cavities, while in the presence of an atom the factor $|1 + 2\tilde{C}|^{-2}$ introduces the spectral properties previously discussed. In particular, this denominator describes two Lorentzian curves that follow the eigenbands given by $\Delta_c = g^2/\Delta_a$, featuring the avoided crossing when cavity and atom are on resonance. The effect of the decoherence processes is inscribed in the widths of both Lorentzians, which vary between 2κ and 2γ; in fact, by changing the system's detunings one can steer the system's behavior from an atom- to a cavity-like excitation. The amplitude of the reflection dip gets reduced for the atom-like states; in those

cases, the excitation of the atom results in a bigger fraction of photons being scattered into free space, which is equivalent to an increase of the mirror losses of the resonator.

An example of both empty- and dressed-cavity spectra can be seen in the example plotted in Figure 4.3. Although in the theoretical description it is more convenient to use the probe frequency ω_p as a reference, in practical terms it is more natural to describe the system detunings with respect to the fixed atomic resonance ω_a. In that case, the variables $\Delta_{p\text{-}a} = \omega_p - \omega_a$ and $\Delta_{c\text{-}a} = \omega_c - \omega_a$ are more convenient, since they are experimentally independent of each other as they correspond to changes in the frequency of the probe light or the cavity length respectively. These are the axes shown in the figures where, for a constant cavity frequency, a scan of the probe detuning shows the expected band splitting.

The spectrum of the coupled system is then fully accessible through the probe reflected counts. Although the driving field must be weak, the cavity reflection is effectively funneled through the high-transmission fiber and a considerable fraction of the photons reach the SPCM detector. As a result, the observation of the vacuum Rabi splitting in our system is a straightforward measurement, as we show in the following paragraphs.

4.2.2 Observing the Vacuum Rabi Splitting

Experimental Considerations

As in the cavity reflection monitoring introduced in Section 3.2.2, the resonator is driven by a circularly-polarized probe laser at 780 nm which is sent through the input (high-transmission) fiber; the reflection, which carries information about the cavity spectral properties, is separated from the input beam via a 97/03% beam splitter and sent through the laser-line filters onto the fiber-coupled single-photon detector. In addition, the frequencies of both the cavity and the driving field can be independently tuned. This basic experimental layout, depicted in Figure 4.4(a), represents the basic foundation upon which all the experiments presented in this last chapter are based.

The theoretical model introduced earlier to describe the dressed-cavity spectrum is only valid if the system fulfills the underlying assumptions of weak excitation and two-level atom. The first condition is achieved by driving the cavity with a probe field which is faint enough, i.e. $n_{\text{cav}} = \langle \hat{a}^\dagger \hat{a} \rangle \ll n_0$. By evaluating Equation (4.15) on resonance and with no atom, we find that the cavity contains an average number of photons $n_{\text{cav}} = \varepsilon^2/\kappa^2 = \epsilon \, \eta_{\text{HT}} \, P_{\text{in}}$, where $\epsilon = |\alpha|^2$ is the cavity mode-matching coefficient and P_{in} is the power impinging on the cavity mirror. Our weak probe generates count rates on the level of 70 counts ms^{-1} after being reflected from the cavity. Taking into account 62 % of losses in the optical path due fiber coupling, filters and other elements, this leads to an estimated driving power of $P_{\text{in}} \approx 45$ fW and a corresponding $n_{\text{cav}} \approx n_0/30$ if one assumes $g = 2\pi \times 50$ MHz. The number of photons is then far away from the saturation limit and the system will indeed behave linearly[10].

The two-level approximation is realized by making sure that the cavity field addresses always the cycling transition $|2, 2\rangle \rightarrow |3', 3'\rangle$, which additionally provides the strongest coupling. This is achieved using the probe field itself to optically pump the atom into the outermost m_F-sublevel of the ground state (see Fig. 4.4(b)). The combination of the quantization axis provided by a bias magnetic field and the circular polarization of the intracavity photons result in the atom undergoing σ-type transitions. Independently of the initial Zeeman sublevel, after a few scattering processes the atom will end up in $m_F = \pm 2$ and effectively behave as a two-level system. In the case of undesired off-resonant pumping onto the lower $F = 1$ manifold, the atom is readily brought back to the upper ground state by a π-polarized

---

[10] Notice that on average we only have 6×10^{-5} photons in the cavity! That is the reason of the word *vacuum* in vacuum Rabi splitting
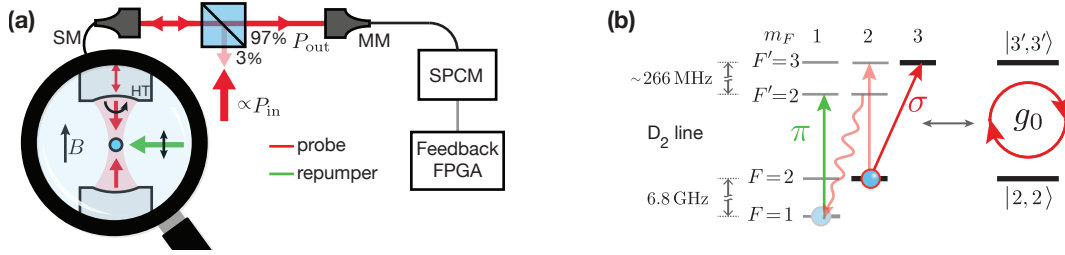
Figure 4.4: Experimental setup for the monitoring of the cavity reflection. **(a)** Layout of the main components for probing the cavity. A faint, circularly polarized probe-laser (P_{in}) is sent to the cavity through its high-transmission fiber. The reflection is separated from the incoming light via a 97/03% beam-splitter and afterwards sent to the single-photon detector (SPCM). The signal is read by the FPGA, which is used to monitor the reflected counts during the transport and the spectrum measurement. When the atom is transported into the cavity mode (magnified area), a strong repumper field is applied to maintain it in the $F=2$ manifold. A bias magnetic field of $B \approx 0.5\,\mathrm{G}$ is used to determine the quantization axis. **(b)** Simplified level scheme of the relevant atomic transitions. The cavity field (solid-red arrow) optically pumps the atom into its outermost m_F-sublevel via consecutive σ-transitions; once there, the atom can be reduced to a two-level system with a single resonance on the cycling transition (thick-black levels). Residual unwanted polarizations (shaded-red arrow) might pump the atom into the $F=1$ manifold, which is not coupled to the cavity. This is quickly corrected by a strong $1 \rightarrow 2'$, π-polarized repumper field that is always present.

repumping beam ($I \approx 20 I_{sat}$) applied from free space. More details regarding the pumping processes are investigated in Chapter 5 when using the cavity reflection as a detector of the atomic hyperfine state.

A final technical remark must be made regarding the effect of the transport scheme and data post-selection on the following estimations of the coupling strength. As discussed in Section 3.2.2, the threshold technique employed in the transport feedback pre-selects on atoms with a specific range of cooperativities and those with particularly low coupling will not trigger the mechanism. Additionally, during the analysis, we post-select on traces where the atom has survived the measurement, which is decided again by looking at the reflected counts from the cavity. In both cases, we neglect the traces where the atom was weakly coupled due to its relative position in the cavity mode, and this will artificially increase the average coupling. Although these effects will be present in the following procedures, we get rid of them when performing the measurements on a small ensemble (Sec. 4.2.3).

The Energy Spectrum of the Dressed System

The splitting of the energy bands in the coupled system are observed when, for a particular cavity length, the frequency of the probe is swept around resonance. We typically perform a 500 ms scan of $\pm 200\,\mathrm{MHz}$ with the corresponding probe-light AOM while keeping the power stabilized. Due to the lack of cavity-induced cooling or heating effects, the temperature of the atoms does not increase when modifying the frequency of the probe or of the cavity and the trapping lifetime is still limited by the background collisions (see Sec. 3.2.2).

A simplified diagram of the measurement sequence is shown in Figure 4.5(a). After a short loading of the MOT, the atoms are transferred into the optical lattice which is then temporarily lowered to expel out most of them and ensure that the transport-feedback scheme provides maximum one atom in the cavity mode. After the deterministic transport (which requires both cavity and probe in resonance with the atom), the cavity is shifted to the particular length for which we desire to measure the energy bands. The new cavity resonance is kept fixed during the subsequent probe scan; this yields a single measurement
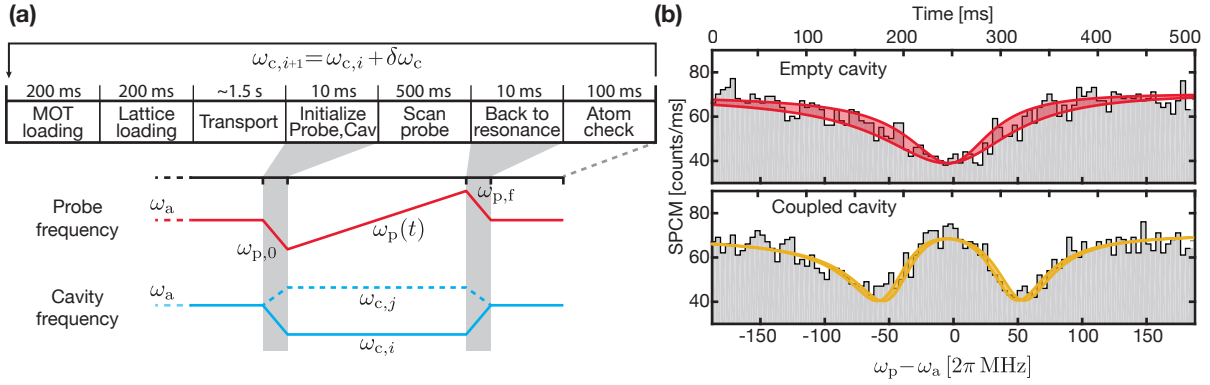
Figure 4.5: Measurement of the vacuum Rabi splitting. **(a)** Block diagram of the main steps in the experimental sequence. A short MOT loading and a temporal lowering of the dipole trap ensure a reduced number of atoms in the lattice. The optical conveyor-belt transports a single atom into the cavity via the FPGA-based feedback scheme. Next, the cavity is shifted to the frequency where we want to perform the spectral measurement ($\omega_{c,i}$) and the probe is initialized ($\omega_p = \omega_{p,0}$) before the 500 ms frequency scan ($\omega_{p,0} \rightarrow \omega_{p,f}$). At the end, both cavity and probe are tuned to resonance (ω_a) to check the presence of the atom. The whole procedure is repeated for different cavity lengths ($\omega_{c,j}$). **(b)** Example of a single measurement-trace for an empty (red) and a coupled (orange) cavity on resonance with the atom. The gray bars represent the detected count rate (5 ms bins), to which we attribute a Poissonian error of ± 3 counts s^{-1}. The curves represent a fit to the model from Equation (4.17) and their width is given by the one-sigma confidence interval of the estimation of $\kappa = 2\pi \times (49 \pm 5)$ MHz and $g = 2\pi \times (53.7 \pm 1.3)$ MHz respectively. In both cases we use the values for α and β obtained from our previous analysis of the reflective line shape in Section 2.3

trace of the reflected counts where a double dip signals the presence of the band splitting. Finally, both cavity and probe are brought back to resonance to confirm that the atom remained trapped.

Figure 4.5(b) displays an example of a single measurement trace for either zero or one atom in the resonant cavity. The first case represents a standard cavity line-shape measurement like those performed in the preceding chapters; a fit to the model provides an estimation of the linewidth of $\kappa = 2\pi \times (49 \pm 5)$ MHz and of the coefficient $\eta_{HT} = 0.31 \pm 0.20$[11]. Alternatively, in the presence of a single atom, the vacuum Rabi splitting emerges as a clear double dip which is in excellent agreement with the theoretical model, even though it is extracted from a single measurement. For this particular case, we extract a coupling strength of $g = 2\pi \times (53.7 \pm 1.3)$ MHz which provides a single-atom cooperativity of $C_1 = 9.8 \pm 1.2$. This value, much higher than unity, was expected from the clear separation of the Rabi sidebands and it constitutes the first proof that our atom–cavity system is strongly coupled.

The coupling strength estimated here depends on the position of the particular atom (during this measurement we assume no hopping due to the absence of heating/cooling mechanisms). In order to characterize the distribution of coupling strengths and to, furthermore, retrieve a full spectrum, we perform the measurement of the energy splitting for several cavity frequencies with a few tens of single-atom traces each. The results of the measurement are displayed in Figure 4.6. As expected, the energy band of the uncoupled resonator does not show any particular feature as we sweep the cavity length. Nonetheless it provides us with a precise estimation of unknown system parameters like the driving power, the mirror transmission or the linearity of the cavity frequency scan. We extract a more conservative

---

[11] This suggests that the increase in mirror losses has not severely affected the original transmission of the input mirror. If one assumes that the new losses that reduce the reflectivity do not change the transmission coefficient, one obtains $\eta_{HT} = \mathcal{T}_{HT}/(\mathcal{T}_{HT} + \mathcal{T}_{LT} + 2\mathcal{L}_{new}) \approx 0.33$ which agrees with the single measurement estimation.
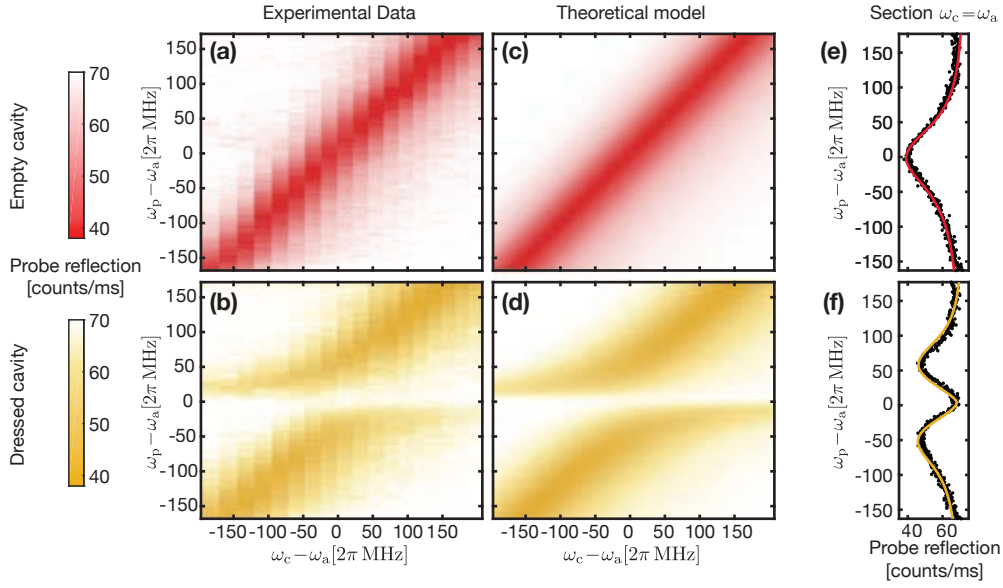
Figure 4.6: Measurement of the coupled-system spectrum. Top row (in red) corresponds to the energy band of the empty cavity; bottom row (in orange) displays the dressed-cavity case. The experimental measurements **(a)** and **(b)** show a probe-frequency scan for 18 different cavity lengths, with each data column corresponding to an average from around 40 traces. **(c)** and **(d)** are the corresponding fits to the models of Equations (4.17) and (4.18) respectively. For a more direct comparison between theory and experiment we show a particular section for the case of the resonant cavity in **(e)** and **(f)**. The latter shows the vacuum Rabi splitting, in this case the amplitude of the dips is not as big as in the empty-cavity case; this is a consequence of averaging over atoms with different coupling strengths.

value of the linewidth of $\kappa = 2\pi \times (57.5 \pm 0.2)$ MHz which, along with the line-shape asymmetry factors, describes the measurement precisely as one can see in the cross section presented in Figure 4.6(e).

The measured spectrum of the dressed cavity clearly displays the avoided crossing of the bands, showing that by driving the resonator one can pump both atom- and cavity-like excitations of the system. The data is in excellent agreement with the theoretical fit shown beside it, even though we performed only 40 measurements per cavity length. We have used an extension of the original model for P_{out} where we introduce a distribution of coupling strengths; this is done by performing a convolution of Equation (4.17) with a normalized Gaussian of mean $\bar{g}$ and width σ_g:

$$P'_{\text{out}}(\bar{g}, \sigma_g) = \frac{1}{\sqrt{2\pi}\Delta g} \int_{-\infty}^{\infty} P_{\text{out}}(g') \, e^{-(g'-\bar{g})^2/2\sigma_g^2} \, dg' \, . \qquad (4.18)$$

As we will see in the next paragraphs, this distribution is a reasonable assumption. The mean and variance of the strength are the only free parameters in the fit (along with a slight correction of the AC Stark shift) since the rest of the variables are taken from the empty-cavity case. As a result we observe that the average coupling strength for a single atom in this measurement is $\bar{g} = 2\pi \times (49.94 \pm 0.12)$ MHz with individual measurements deviating by $\sigma_g = 2\pi \times (18.2 \pm 0.2)$ MHz from the mean value. Thus, depending on the particular atomic coupling, the system presents cooperativities in the range $C_1 \in [2.9, 13.5]$. We expect small variations in the distribution depending on the settings of the feedback-transport scheme and the data post-selection (both effects are removed in the measurements of the following section).

In summary, we have demonstrated a robust and repeatable procedure that allows us to estimate with

precision the coupling strength of a particular atom to the resonator. The measurement time could be drastically reduced by directly changing the frequency of the diode-laser output, instead of using an AOM[12]. This would ensure that no atom is lost during the procedure and allow one to "monitor" g at different stages of any measurement where the coupling of the atom with the cavity is relevant. In addition, the vacuum Rabi splitting could be used as a probe to estimate other system parameters like light shifts or the atom's position. We also showed that indeed an atom can be strongly coupled to our fiber cavity and that single-atom cooperativities on the order of 10 or more can be routinely obtained. The estimations for the average g presented here are still below the expected theoretical value of $2\pi \times 120\,\mathrm{MHz}$ due to the random position of the atom and, possibly, due to a non-optimal overlap of the 3D-lattice[13]. Nonetheless we will show in the following that we can obtain couplings closer to the optimum one — or even beyond — if we couple several atoms to the resonator.

4.2.3 Collective Coupling of a Small Ensemble of Atoms

So far we have focused on the simple scenario provided by the single-atom case; nonetheless, using an ensemble of atoms provides several advantages, the most important being that they can collectively contribute and enhance the total cooperativity of the system. If we consider a group of N_{at} atoms, all equally coupled to the a single mode of the resonator, the Jaynes-Cummings Hamiltonian of Equation (4.4) becomes

$$\hat{H}_{\mathrm{TC}} = \hbar\omega_c\,\hat{a}^\dagger\hat{a} + \hbar\omega_a \sum_{i=1}^{N_{\mathrm{at}}} \hat{\sigma}_i{}^\dagger\hat{\sigma}_i + \hbar g_0 \sum_{i=1}^{N_{\mathrm{at}}} \left(\hat{\sigma}_i{}^\dagger\hat{a} + \hat{\sigma}_i\,\hat{a}^\dagger\right).$$

where σ_i is the lowering operator of the corresponding two-level atom and TC stands for Tavis-Cummings, as they were the first to propose and solve this Hamiltonian [159].

The collective effect of the ensemble can be simplified due to the indistinguishability of the atoms and the fact that they interact with the resonator in the same way. In this particular scenario, the dynamic of the system resembles that of a cavity interacting with a single "super atom" with a coupling constant of $g_N = g_0 \sqrt{N_{\mathrm{at}}}$. That means that the cooperativity of the system increases linearly with the number of atoms in the resonator, as $C_N = C_1 N_{\mathrm{at}}$.

The most direct implication is that one can tailor the cooperativity without the need of major alterations in the setup (like changing atomic species, the cavity geometry or the mirror's characteristics). This potential enhancement presents particular advantages if one aims to use the cavity as a single-photon storage device. As shown by Dicke [160], under certain conditions the reaction of the atoms to a radiation field can interfere constructively, giving rise to collective effects like superradiance. This can be exploited to boost the probability of photon-absorption of an atomic ensemble and increase the robustness of the subsequently created excitation. A cavity-coupled atomic ensemble can be then used as an efficient quantum memory [13, 161].

In a more realistic scenario, one must take into account the variation of coupling strength due to the atomic position (as we depicted in Eq. (4.6)). Thus, the coupling of an atom can be described as $g_i = g_0\,\psi(\mathbf{r}_i)$ — where $\psi(\mathbf{r}_i)$ contains the spatial information — while the collective one will be given

---

[12] At the time, the laser used to probe the cavity is also used in the MOT setup and as a reference in the locking chain. Therefore, a frequency scan cannot be applied directly at the laser, but only with an AOM after the outputs have been separated.

[13] As discussed in Sec. 3.2, we expect a reduction of up to 20 % in the average coupling due to a displacement of the 3D lattice in the cavity direction. The reason being that the trapping positions of the atoms in the blue-detuned trap do not overlap precisely with the antinodes of the resonant mode.

by [162]

$$g_N = g_0 \left(\sum_{i=1}^{N_{at}} g_i^2 / g_0^2 \right)^{1/2}.$$

The effects due to the position dependance can be absorbed by substituting N_{at} by an *effective atom number* N_{eff}, which stands for the number of maximally coupled atoms required to provide the collective coupling g_N. It is thus defined as $N_{eff} = \alpha N_{at}$ such that $g_N = g_0 \sqrt{N_{eff}}$. Here the parameter $\alpha = \sum_i \Psi^2(\mathbf{r}_i)/N$ depends only on the atoms' positions and the cavity-mode characteristics. As a result, the effective coupling strength of the system is described by the simple formula

$$g_N = g_0 \sqrt{\alpha N_{at}}. \tag{4.19}$$

The collective coupling of an ensemble of neutral atoms in a macroscopic cavity was first measured in an atomic-beam apparatus [151]; equivalent measurements for trapped atomic clouds were later perform using a MOT [158] and a Bose-Einstein Condensate (BEC) [101]. The recent development of fiber cavities has given rise to further results regarding strong collective-coupling of both a free-falling atom cloud [26] and a trapped BEC [25], where cooperativities as high as $C_N = 10^5$ were achieved due to the high density of the condensate combined with the reduced mode volume of the resonator. Here we offer a bottom-up approach, where we study how the system's cooperativity increases when we go from the single-atom case up to small ensembles of maximum $N_{at} = 10$ atoms distributed over the cavity mode, showing that the simplified model introduced above suffices to describe the behavior of our system.

Comparison between a Single Atom and a Small Ensemble

At the present time, our system cannot provide a deterministic loading of a particular number of atoms in the cavity mode (apart from the trivial case of $N_{at} = 1$). The best approach with the tools at hand is to load the optical lattice by using a long trapping time (MOT loading) and subsequently transport the atomic ensemble such that the area with the highest density coincides with the position of the cavity mode. To explore the characteristics of the ensemble and its effective coupling, we perform two experiments: In the first one we load a single atom and determine its coupling strength as a reference; this is similar to the previous procedures, with the difference that we measure the free-space fluorescence at the end of the scan (as explained below). For the second measurement we substitute the feedback scheme by a fixed-distance transport of a dense ensemble and measure the coupling when having several atoms in the resonator[14].

Examples of the typical VRS measurement for both cases can be found in Figure 4.7(a), where a clear improvement in terms of effective coupling appears when several atoms interact with the cavity. When contrasting those particular traces the coupling increases by a factor of two due to the collective effect of the ensemble. A real comparison of the behavior of the system in both scenarios involves an analysis of the full distribution of g. The corresponding distributions are shown in Figure 4.7(b), where we have included only those cases where the atom(s) survived the VRS measurement. Here we confirm that the spread of couplings follows indeed a Gaussian curve, as we assumed when reproducing the earlier experimental results.

For the single-atom case we obtain an average coupling of $\bar{g}_1 = 2\pi \times (59.8 \pm 0.4)\,\text{MHz}$, which is slightly better than the one previously reported (probably due to a realigning of one of the dipole-trap beams). One can also observe only a negligible amount of occurrences above the optimum strength value

---

[14] Both experiments where performed in different days, deviations might appear due to variations in the temperature and loading efficiency of the atoms.
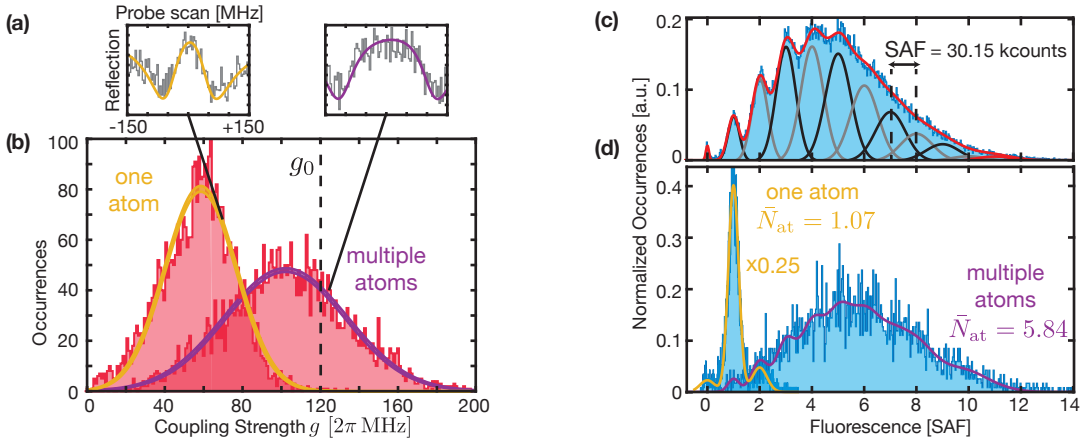
Figure 4.7: Comparison of the distributions of coupling strengths and fluorescence, for one and multiple atoms. **(a)** Sample of a typical VRS measurement for one (orange) and several atoms (purple). The probe light is scanned by ± 150 MHz. The colored curves represent a fit to the model, yielding values for (g, κ) of $2\pi \times (65, 86)$ MHz and $2\pi \times (122, 91)$ MHz respectively. **(b)** Histogram showing the distribution of g for both measurements (~ 3700 traces each). The colored curves are a fit to a Gaussian, and their linewidth marks the one-sigma confidence interval (see text for the extracted parameters). **(c)** Histogram of the fluorescence integrated over a $10\,\mu m \times 10\,\mu m$ region of interest, for all 25 ms pictures of the multi-atom measurement. The red line is a fit to the data, taking as free parameters the position and width of the background and one-atom peaks and the amplitude of all the peaks. The black and gray lines represent the contribution from different number of atoms. From the distance between peaks we estimate the SAF. **(d)** Histogram of the integrated fluorescence for the first image in the one- (orange) and multiple-atoms case (purple). From the fit to the model (taking into account up to 11 atoms) we extract an average of ~ 1 and ~ 6 atoms for each measurement.

of g_0, as expected. Both the width and the central value of the distribution increase when the cavity hosts several atoms; in particular we obtain $\bar{g}_N = 2\pi \times (102.2 \pm 0.6)$ MHz and $\sigma_g = 2\pi \times (31.3 \pm 0.6)$ MHz. Such behavior is qualitatively expected due to the collective enhancement of the ensemble; moreover, the wider spread of the curve as anticipated due to variations in the number of atoms.

A more quantitative analysis requires precise knowledge about number and positions of the atoms in the ensemble. Both parameters can in principle be estimated via the fluorescence imaging technique described in the previous chapter; for this reason, after the measurement of the collective coupling, we take a series of images to retrieve the corresponding atom-number information. In particular, we illuminate the atoms with $10 I_{\text{sat}}$ of light red-detuned from the D_2 line by 60 MHz, which is delivered by two counter-propagating beams in a lin$\perp$lin configuration. The light is collected by the high-NA intra-vacuum lens and focussed onto the EMCCD camera, which takes 20 exposures of 5 ms each in a stroboscopic manner. For the atom-number estimation we use the first 25 ms (5 pictures), which is on the order of the typical atom lifetime (~ 15 ms)[15].

As discussed in Section 3.2.1, the Single Atom Fluorescence (SAF) and the trapping losses are influenced by the presence of the resonator if the latter is tuned close to the illumination frequency. Such is the case during the VRS estimation and, although the cavity is tuned as far as possible (>450 MHz) before the imaging takes place, its influence is still evident due to the broad resonator linewidth ($\kappa \approx 2\pi \times 90$ MHz for this measurements). Additionally, the dependence of such effects on the coupling strength leads

---

[15] Integrating the fluorescences for longer times would include considerable atom losses and affect the outcome; additionally, taking into consideration only the first 5 ms decreases the SNR of the image information (and only leads to changes of the order of 5 % regarding the estimations of $\bar{N}_{\text{at}}$ and N_{eff}).

to spatially inhomogeneous fluorescence which, along with thermal hopping, makes it challenging to extract the precise number of atoms, let alone their particular position. The physical insight of this cavity-induced process, along with more quantitive details, can be found in Chapter 6, where we discuss the scattering properties of an atom coupled to the resonator.

Although, so far, we cannot obtain a precise correlation between the atoms' position and their corresponding collective coupling [163], the total fluorescence of the image still provides us with an estimation of the number of atoms (see Sec. 3.2.1). Figure 4.7(c) shows a histogram of the fluorescence of images taken under this particular illumination settings. This is obtained from integrating the photon counts of each frame over the particular region of interest. As introduced in the previous chapter, the histogram provides the calibration between fluorescence of an image and number of atoms in it[16].

Figure 4.7(d) shows specific histograms for the cases with one and multiple atoms in the cavity. The signal-to-noise is reduced due to the lower statistics, but knowing the SAF facilitates the fit to the model. From this fit one can extract the average number of atoms $\bar{N}_{at}$ which, as expected, is close to unity in the single-atom case[17]. When loading an ensemble we get on average $N_{at} \approx 6$ atoms; naively one would expect a collective coupling increased by a factor $\sqrt{6}$, but that is not the case if one compares the average coupling of both scenarios ($\bar{g}_N \approx 1.7\bar{g}_1$). We attribute this discrepancy mainly to the fact that we did not use feedback in the transport scheme of the second measurement, and therefore there is no pre-selection involved. It is thus convenient to compare single traces within the same (multi-atom) measurement. To that end, in the next lines, we will observe the correlation between coupling strength and number of atoms in the image.

Coupling for an Increasing Number of Atoms

To combine the information from both the VRS and the image fluorescence we compute a 2D histogram where each point on the plane represent the number of traces yielding a particular combination of effective coupling and fluorescence. The results are shown in Figure 4.8(a), along with the marginal distributions discussed earlier. We have included the cases where no atom was coupled to the cavity (or was lost during the VRS measurement), to avoid any post-selection bias on the results. As a consequence, two stark peaks appear in both 1D histograms corresponding to the no-atom case.

Despite the low density of the histogram (maximum 20 occurrences for a particular value), a clear trend can be observed as the effective coupling monotonically increases for traces with higher integrated fluorescence. Two particular examples in Figure 4.8(b,c) display the extreme cases: a single atom with a relatively low coupling and a small ensemble with a collective Rabi splitting as big as our frequency scanning window.

To guide the eye and uncover the underlying trend we create a cleaner version of the histogram: For each column we fit a Gaussian to the distribution of coupling strengths associated to that particular fluorescence; we normalize all the fits and plot the corresponding mean and width in Figure 4.8(d). We observe that the width of the distributions does not change much throughout the plotted region. Such behavior is expected and has indeed been reproduced when simulating a coupled ensemble with atoms randomly placed around the cavity mode region following a Gaussian distribution. The mean effective coupling in Figure 4.8(e) clearly displays the collective behavior described in Equation (4.19) for a increasing number of atoms in the region of interest. This becomes clear when fitting a curve of the type $g_0 \sqrt{\alpha N_{at}}$ to the extracted average coupling. By assuming $g_0 = 2\pi \times 120\,\text{MHz}$ we include the effect of

---

[16] For high number of atoms ($N_{at} \geq 7$) the distance between fluorescence peaks is equivalent to (or bigger than) their half-width, and their overlap reduces the precision when estimating the real amount of atoms in the picture, which then has to be taken as a rough estimation.

[17] This measurement was also used to characterize the fidelity of the single-atom transport scheme.
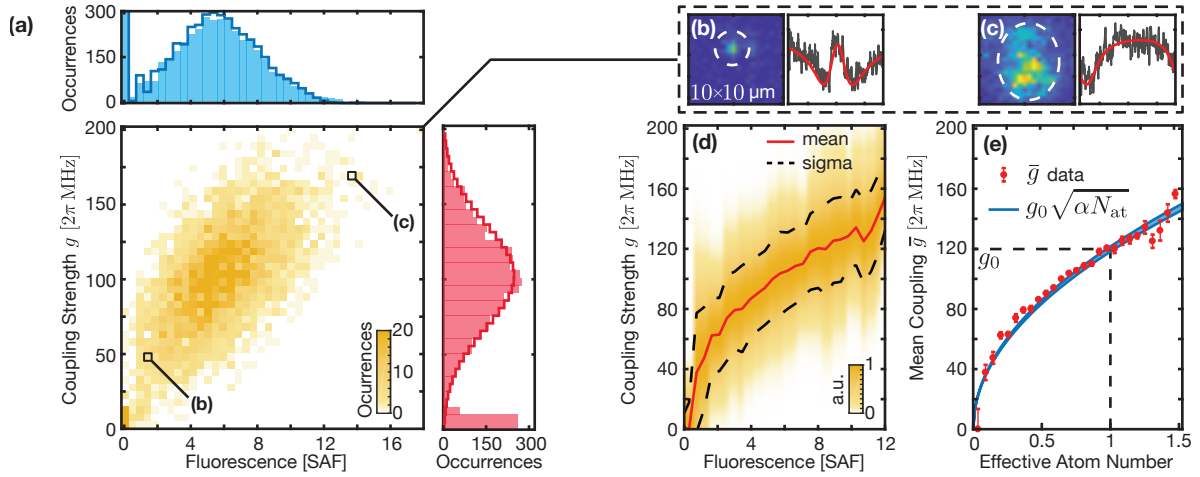
Figure 4.8: Collective coupling for different number of atoms. **(a)** 2D histogram showing the correlation between coupling strength (vertically) and estimated number of atoms (horizontally). The marginal distributions (and the corresponding fit) are the same as in the previous figure, with a wider binning and adding the cases with no atoms in the cavity (or weakly coupled). **(b)** and **(c)** are hand-picked examples where the fluorescence signal retained some spatial information: a single atom versus a small ensemble. They represent the two extreme cases highlighted in (a): (b) has low fluorescence (0.99 SAF) and coupling ($2\pi \times 49\,\text{MHz}$), while (c) displays higher values of both (13.93 SAF and $2\pi \times 168\,\text{MHz}$ respectively). **(d)** Shows the cleaned-up version of (a), where the vertical distributions have been replaced by their fit to a Gaussian. The red and dashed-black lines represent the average and width of each distribution respectively. In **(e)** we show the average value of the coupling and the fit to the model of Equation (4.19) with α as the only free parameter. We estimate $N_{\text{eff}} \approx 0.12 N_{\text{at}}$, which we use to rescale the horizontal axis.

different atom positions into the effective atom number, which is estimated to be $\sim 0.12 N_{\text{at}}$. This implies that the average coupling of a single atom is eight times smaller than the optimum, which we attribute to the fact that there is no deterministic transport to the regions of high coupling. In addition, there exist an unknown fraction of the atoms in the image that are not coupled to the resonator which further reduces N_{eff}.

We have then shown that the effective coupling of the system can be considerably enhanced by placing a small ensemble of atoms in the resonator, in particular we obtain cooperativities as high as 75 which would be on the order of ~ 250 if we considered the original cavity finesse. These values can be effectively improved further by performing compression techniques [84, 164] that allow a much higher filling factor of the two-dimensional trap. Furthermore, a recently implemented position-detection scheme [165] with potential single atom addressing [120] paves the way towards deterministic control of the collective coupling strength of our system.

Fast, Non-Destructive State Detection of a Single Atom with the Cavity

THE efficient state readout of a quantum system is a critical ingredient in the recipe towards feasible quantum computation protocols. Optically-trapped neutral atoms in particular, represent a promising platform not only due to their scalability and indistinguishability, but also thanks to the weak coupling to the environment. In this scenario quantum information is usually encoded into the hyperfine ground-states of the atoms.

In a typical quantum information procedure, after initializing the system and performing the necessary logic gates, the state of the atom(s) must be read out. With logic gates [166] and photon emission/storage schemes approaching the microseconds regime [167], the detection time quickly becomes the bottleneck and must therefore be reduced to the minimum. To reduce the experimental duty cycle, atom registers should be recycled after each protocol, which can only be achieved if the measurement process does not expel the atoms from the optical trap. The error in the estimation of the atomic state should be below that of the quantum logic gates, and ideally as low as $0.01\,\%$ to allow realistic quantum error correction schemes [168]. In summary, the state readout should be a fast and non-destructive process with a negligible estimation error [169].

A widely used method in the ion community consists in estimating the state via *state-dependent fluorescence* after performing electron shelving. The detection procedure employs a weak probe laser near-resonant with a cycling transition of the atom. The laser state-selectively excites the atom if it is initially in the resonant state (also known as *bright state*) which consequently scatters photons off the probe. In the opposite scenario, when the atom sits far off-resonance in the *dark state*, the amount of scattered photons is strongly reduced and in most cases negligible. The ability to differentiate between both situations by detecting the scattered light can lead to fidelities as high as $99.99\,\%$ for a $145\,\mu s$ detection window as it was shown for $^{43}Ca^+$ ions [170].

Implementing such a scheme is not straightforward for the case of neutral atoms. The separation between the excited state of the cycling transition and other energy levels is usually on the order of a few hundred MHz. As a consequence, polarization impurities lead to a transfer from the original internal state through off-resonant scattering processes; this detrimental effect called *population leakage* is the main contribution to detection errors. Figure 5.1(a) shows the relevant level scheme for the detection of ^{87}Rb hyperfine states, along with a representation of a common leakage path. In addition to population leakage, the shallower trapping potentials supplied by optical traps limit the amount of photons that can be scattered before the atom is lost, thus requiring much higher collection and detection efficiencies [171, 172]. In a previous version of our experimental setup, we showed that the high numerical aperture of the
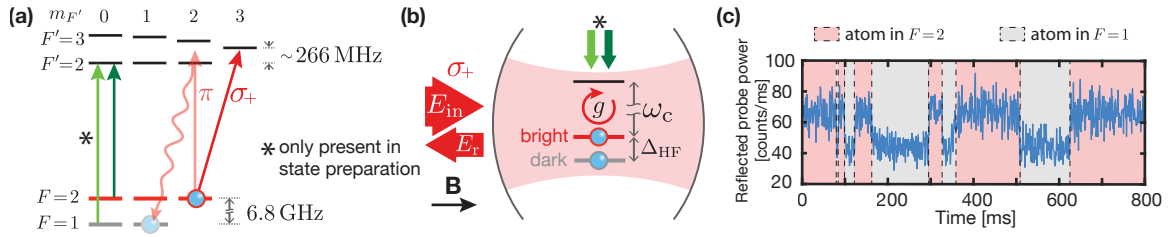
Figure 5.1: Cavity-based fluorescence state detection. **(a)** Relevant energy-level scheme of the D_2 line of ^{87}Rb: the hyperfine ground states with $F=1$ and $F=2$ represent the dark and bright states respectively; the small Zeeman splitting due to the bias field is not represented. The cycling transition $|2, 2\rangle \rightarrow |3', 3'\rangle$ is driven by a σ_+ probe beam (red arrow); residual π-polarized light may lead to off-resonant scattering from the $|F'=2\rangle$ manifold from where the originally bright atom can decay to the dark state (dimmed red arrows). The light (dark) green arrow represents the field driving the $|1\rangle \rightarrow |2'\rangle$ ($|2\rangle \rightarrow |2'\rangle$) transition, which along with the probe eventually pump the atom to the bright state $|2, 2\rangle$ (dark manifold). **(b)** Scheme for cavity-based state detection. A circularly polarized probe beam aligned with the bias magnetic field is reflected off the cavity, with the reflection depending on the atomic state; necessary repumping for state preparation is applied orthogonally to the cavity axis. **(c)** By using a weak $|1\rangle \rightarrow |2'\rangle$ repumper on a single atom coupled to the cavity, the probe reflection reveals quantum jumps between both states; the detection levels corresponds to those of an empty cavity on and off resonance. The colored bands are a guide to the eye representing the atom in the two different states.

in-vacuum lenses we utilize, combined with the efficiency of EMCCD cameras, provide enough photon collection to perform fast, non-destructive detection of the hyperfine state of a register of atoms. We achieved fidelities as high as 98% within $10\,\text{ms}$ of detection time with only 2% population transfer and 1% atom losses [40]. Such conditions can only be achieved through careful optimization of the probe polarization purity and the use of trap depths in the range of $3\,\text{mK}$.

In this chapter we employ the cavity to read out the state of single atoms, and show that the detection error can be further reduced without the need for thorough polarization optimization or deep traps. In our particular system we achieve a fidelity of 99.8% for a $5\,\text{ms}$ detection time, with 1% leakage and negligible atom losses (Section 5.2). In addition, as a proof of principle, in Sec. 5.3 we make use of the detection scheme to perform microwave spectroscopy of an atom under different confinement configurations inside and outside the fiber cavity, which yields valuable information about light-shifts introduced by the intracavity field.

5.1 Cavity-based State Detection

The coupling to a resonator induces an excited atom to emit a photon into the cavity mode rather than into free space, with the ratio given by the Purcell factor (Eq. (4.13)). The fast cavity regime thus portrays the resonator as a practical "funnel for photons" with efficiencies close to unity that overcome those of the best high numerical aperture objectives [173].

A first approach towards cavity-enhanced state detection consists in performing the standard fluorescence technique and replacing the usual collection optics by a suitable cavity. As it was shown for a ^{87}Rb atom–cavity system of $C_1 \simeq 0.2$ [174], this procedure can provide fidelities as high as 99.4% within $85\,\mu\text{s}$. Such a scheme does not require strong coupling and is robust against detuning of the probe light with respect to the atom; nonetheless it involves deep optical traps as the amount of scattered photons is still considerable.

Although effective, this method requires constant energy exchange between the atom and the detection

field. An alternative way that reduces the amount of scattering processes and takes advantage of high cooperativity values is that of detecting the atomic state by externally feeding the intracavity field (Fig. 5.1(b)). In practical terms, when pumping the cavity in a strongly coupled system, the difference in reflection between both atomic states corresponds to the contrast given by the reflection dip of the empty cavity. We saw that a strongly coupled atom drastically influences the reflection spectrum of the cavity; notably, the intracavity photon number is reduced by a factor $|1 + 2\tilde{C}|^2$ (see Eq. (4.15)). On the one hand, if the resonator and the probe light are on resonance with the cycling transition ($|2, 2\rangle \rightarrow |3', 3'\rangle$[1]) and the atom is in the bright state ($F = 2$), the cavity population is reduced by $\sim 4C_1^2$. The interference of this weak field with the cavity reflection becomes negligible and the system resembles that of an off-resonant empty cavity. On the other hand, an atom in the dark state ($F = 1$) is detuned from the intracavity field by $\Delta_{HF} \gg \kappa$ and the effective cooperativity drops to zero, leaving the cavity field intact. Figure 5.1(c) shows a single trace of the reflected probe power of our cavity for a coupled atom performing quantum jumps between both the bright and the dark states.

The simplest way to estimate the atomic state through the cavity field is by deciding on a threshold value for the reflected power that establishes the boundary of the two possible detection outcomes: if the reflected power is higher than the threshold the atom is in the bright state, otherwise the atom is in the dark state. Ideally, for longer interrogation times the signal to noise ratio should increase leading to a negligible detection error; nevertheless that is not the case when leakage is present. As we shall see, more elaborated state detection schemes based on Bayesian inference [40] or maximum likelihood [156, 170, 174] can increase the fidelity for similar detection times. This technique has been successfully applied in the community on both standard [175, 176] and fiber-based cavities [156], with the latter providing detection errors smaller than 0.1% for detection times below 100 μs. However in those cases the polarization-mode splitting present in their cavity made it impossible to drive the cycling transition.

It is worth noting that in the strong coupling regime, due to the highly reduced intracavity field, an atom in the bright state will only spontaneously scatter a fraction $\sim 1/C_1$ of the photons reaching the resonator (see e.g. App. D.2). This leads to a cavity-reduced population leakage since the cavity enhances the cycling transition strength but not the rest. The few photons present in the resonator give rise to a much smaller leakage probability and therefore the system becomes robust against polarization impurities. More importantly, the low scattering rate permits the use of state detection levels on the order of 10^6 photons with the bright atom spontaneously scattering less than a photon on average, giving rise to the possibility of measurements of the atomic state without the presence of energy exchange [29].

Experimental Sequence

To characterize the properties of our detection method we design an experimental sequence where an atom is prepared in one of the two states and subsequently undergoes a state detection procedure. The experimental setup corresponds to the one described in the previous chapter, where the system is interrogated by evaluating the cavity reflection.

The probe light reaching the fiber mirror is circularly polarized and on resonance with the cavity and the AC-Stark-shifted atoms. A bias magnetic field of ~0.5 G along the cavity defines the quantization axis and ensures that the probe light addresses the cycling transition (which could be either a σ_+ or σ_- transition due to the polarization ambiguity at the cavity). As long as the atom does not saturate, increasing probe intensities lead to higher signal-to-noise ratios of the detection levels due to the Poissonian shot-noise of the coherent state pumping [124]. Although this is limited by the leakage probabilities, higher illumination powers lead in general to faster optimum detection times. For that reason when performing

---

[1] We use short notation for the hyperfine and Zeeman sub-levels, e.g. $|F = 2\rangle = |2\rangle$ or $|F' = 3, m_{F'} = 3\rangle = |3', 3'\rangle$
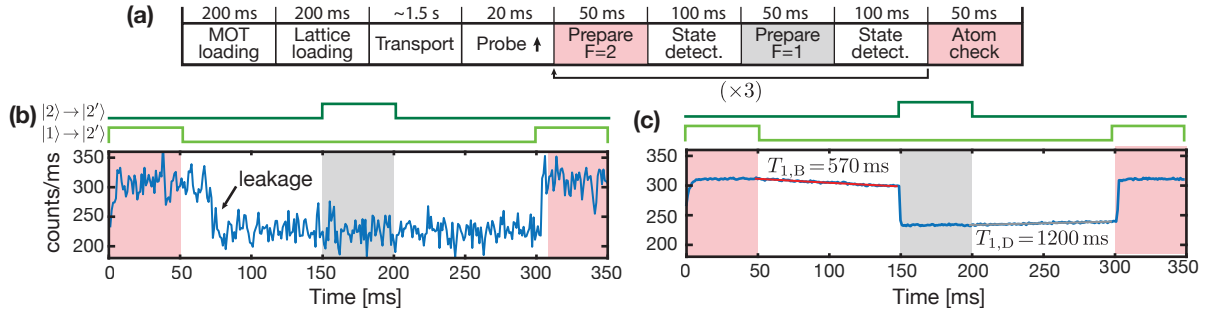
Figure 5.2: Measurement sequence to characterize the detection method. **(a)** Simplified flow-diagram of the modules used in the sequence (from right to left). Once the atom is in the cavity it undergoes a state preparation followed by a state detection measurement for both cases; the segment is repeated four times in total. **(b)** Single trace of a state detection characterization segment. The atom is pumped to the bright and dark states (red and gray areas) by using the corresponding repumping fields (light and dark green respectively). During the state detection only the probe light is on, an the atom can undergo a quantum jump and leak to the opposite state. The $F = 2$ pumping of the following repetition is also used to check the presence of the atom after the procedure. **(c)** Average of the 1300 independent runs. The average reflection count rate for both levels are $R_B = 311$ counts ms^{-1} and $R_D = 233$ counts ms^{-1}, each of them decaying with a time constant of (570 ± 70) ms and $(1\,200 \pm 190)$ ms respectively. The red and gray curves are exponential fits to the data.

such measurements we use probe powers[2] yielding a reflected count rate as high as 3×10^5 counts s^{-1}.

The sequence layout is presented in Figure 5.2(a). The MOT and trap loading times are short enough to create sparse loading of the lattice; in combination with the transport feedback this ensures that we couple a single atom in the cavity mode in most of the cases. The probe power reflection level is kept at $\sim 7 \times 10^4$ counts s^{-1} to avoid heating effects during the transport[3]. After the conveyor belt stops the probe power is increased and the state detection characterization starts.

The atom is initially pumped to the bright state by addressing the $|1\rangle \to |2'\rangle$ (free-space) transition with an intensity of $8\,I_{\text{sat}}$. The repumper is then shut down while the probe is kept on, initiating thus the state detection window. This step continues for 100 ms, during which the atom has a small probability of being off-resonantly pumped to the $F = 1$ manifold (see Fig. 5.2(b)). Subsequently a similar procedure takes place where the atom is prepared in the dark state and the corresponding state detection takes place. This cycle is performed four times for every atom before the sequence starts over.

The $F = 2$ pumping stage is also used for atom detection, such that we can select those detection cycles with atoms present before and after the procedure. In particular, we consider only the cases with rates above a threshold of 2.9×10^5 counts s^{-1}; this is higher than the optimum threshold for detection, and ensures the atom is well coupled. Nonetheless we reject fewer than 10 % of the traces, obtaining a total of 1300 successful state detection operations. The average is shown in Figure 5.2(c), from where we obtain the mean count rate of both states $r_{B,D}$ and the corresponding leakage probabilities, which emerge as a decay and a rise of the reflection signal respectively. The time constants of the exponential leakage, also known as T_1 times, are in our case on the order of one second; they can nevertheless be extended by optimizing the polarization purity of the probe light as well as the alignment of the cavity axis with the bias magnetic field and the dipole traps' electric fields.

---

[2] For this power, and with a cavity field decay of $\kappa \approx 2\pi \times 120$ MHz, the intracavity photon number is around $n_0/14$.

[3] When the atom approaches the cavity a strong near-resonant intracavity field is present that either attracts or repels the atom depending on the detuning; as the atom interacts with the cavity mode the intracavity field is reduced and eventually vanishes. This leads to a non-energy-conserving process which can heat the atom if the cavity is on resonance or slightly red-detuned.

5.2 Extracting the Information: Threshold vs Bayes

The Threshold Technique

The thresholding approach is the simplest way to evaluate the information, since it only requires knowledge about the number of counts c obtained during the interrogation or *binning time* t_b. By setting a particular threshold c_{th}, the measurement outcome is decided on wether the reflected counts are above (bright) or below the threshold (dark). In the absence of population leakage, the count distributions of both states are given by Poissonian curves $\mathcal{P}(c, c_i)$ with mean values c_i corresponding to the average number of counts of both states $c_{B,D} = t_b\, r_{B,D}$ (see Fig. 5.3(a)). The detection error, limited by the overlap of both curves, is minimized when the threshold sits near the crossing point of the distributions. In this case, increasing t_b would yield curves with smaller overlap and a decreasing detection error which eventually vanishes for long times.

This is unfortunately not the case when leakage processes take place, since longer illumination times increase the probability of changing the state of the atom, given by $1 - e^{-t_b/T_1}$. One must add the exponential decay behavior to the model [177], which leads to the following probability distribution for the counts of an atom in the bright state:

$$p_B(c) = e^{-t_b/T_{1,B}}\, \mathcal{P}(c, c_B) + \int_0^{t_b} \frac{e^{-t/T_{1,B}}}{T_{1,B}}\, \mathcal{P}\Big(c, c_B\, t/t_b + c_D(1 - t/t_b)\Big) dt\,. \tag{5.1}$$

The first element represents the original Poissonian distribution multiplied by the probability of the atom remaining in the initial state after the interrogation time. The second term stands for the counts detected after a leakage process: the probability of a quantum jump at time t multiplied by the count distribution associated to such an event, all integrated over the interrogation time [178]. An equivalent equation $p_D(c)$ is found for the dark state by using the corresponding T_1 time; both expressions reduce to the original Poissonian when $T_1 \to \infty$. We observe that the experimental histograms — in particular the bright-state case — fit better to a Gaussian with a width bigger than the Poissonian, and that the width linearly increases with the interrogation time. This is attributed to the distribution of coupling strengths experienced by the atom, as well as noise in the probe light power.

For interrogation times smaller than the leakage time, the distribution resembles a Gaussian plus a shallow tail extending towards the neighboring distribution, as shown in the inset of Figure 5.3(b). The overlap of these plateaus sets the detection fidelity for increasing interrogation times, and the optimum threshold does not sit in between both distributions anymore since the T_1 times are different for both states. The detection error is defined as $\epsilon = (\epsilon_B + \epsilon_D)/2$, where ϵ_B is the probability of detecting a dark state when the atom was originally in the bright state (i.e. the amount of bright counts below the threshold) and vice versa for ϵ_D. The optimum threshold is then the one that minimizes the error ϵ.

Figures 5.3(a,b) represent the count distributions along with their optimum thresholds for two cases of t_b where the error is dominated by either shot noise or leakage processes. To find the optimum detection time that maximizes the fidelity, we plot in Figure 5.3(c) the measured detection error for different interrogation times; a minimum of $\epsilon_{min} = (0.33 \pm 0.11)\,\%$ appears after 3 ms of detection, which is seven times smaller than the one we obtain through standard fluorescence collection [40]. Moreover, this illumination time corresponds to a probability of at most 0.5 % state transfer, such that our detection process can be considered as a continuous, projective quantum non-demolition measurement where the original state remains unchanged in 99.5 % of the cases [175]. An equivalent analysis performed for lower input powers (6.5×10^4 counts s^{-1}) displays an increase in the optimum detection time to 20 ms and of the minimum error to $(2.5 \pm 0.5)\,\%$.

In the same figure, the experimental result is compared to the theoretical prediction provided by finding
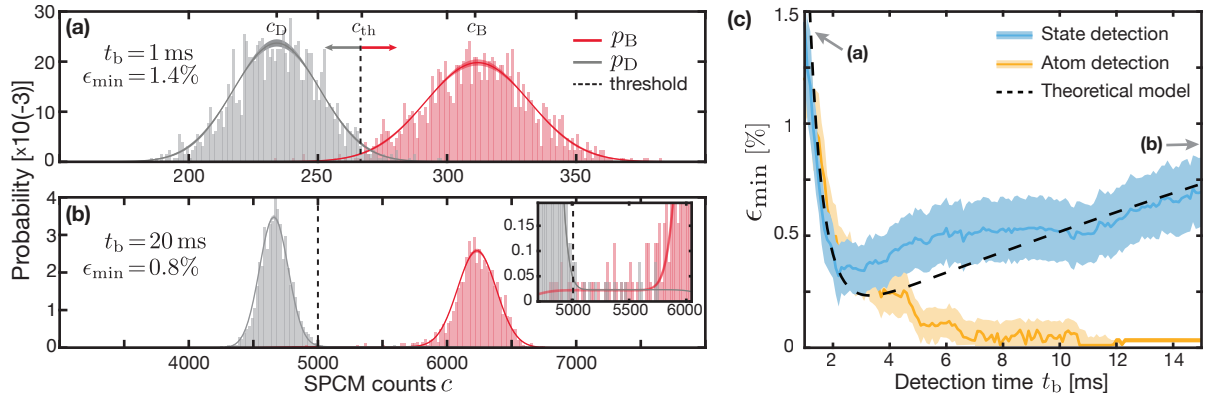
Figure 5.3: Count distributions and detection error for the threshold technique. **(a)** Histograms of the bright and dark count distributions obtained within the first millisecond of the state detection window. The solid lines represent a fit to the model in Equation (5.1) using a Gaussian distribution. The dashed vertical line symbolizes the optimum threshold that yields an error of $(1.4 \pm 0.3)\,\%$. **(b)** Corresponding distributions for a longer interrogation window of 20 ms; the threshold is shifted due to the bigger leakage probability of the bright state and the error is reduced to $(0.8 \pm 0.2)\,\%$. The inset shows a close-up view of the overlapping region. **(c)** Minimum detection error for different measurement times for the state (blue) and atom detection (yellow); the shaded areas are the one-sigma confidence intervals obtained by the bootstrap method. The atom-detection error is limited by shot noise that quickly vanishes with longer times; the state-detection error also contains a slowly raising contribution from leakage that yields optimum time window of 3 ms. The dashed line is the theoretical model from Equation (5.1), for a slightly longer T_1 times than the estimated.

the optimum threshold for the curves in Equation (5.1). We also considered the mentioned Gaussian behavior and the longest T_1 times within the uncertainty of our estimations from Figure 5.2(c). Despite the addition of such effects, the minimum error of the model is still 0.05 % smaller than the experimental one, we attribute this difference to unaccounted effects like imperfect state preparation and two-atom cases.

We further compare the time dependence of the error to the one obtained when the repumper $|1\rangle \rightarrow |2'\rangle$ is kept on. This is the situation when we want to detect the presence of an atom in the cavity, be it for the transport real-time feedback or to check the survival within a sequence. In this case leakage does not play a role as the atom is immediately pumped back, and the only contribution to the error is that of the shot noise, which quickly vanishes for increasing binning times. This shows that 10 ms binning times are enough to have a robust transport feedback.

The Bayesian Inference Approach

Once the optimum threshold is found, the interpretation of the data in the technique previously presented is quite straightforward. Nonetheless, the simplicity comes at the cost of casting off part of the information contained in the reflection counts: one distinguishes both states by the total amount of counts obtained during the measurement, regardless of how the photon arrivals are distributed in time.

In the absence of leakage, the threshold technique already provides the best estimate. Since both count distributions are Poissonian (or Gaussians in our case), their arrival times are distributed in the same way and all the information is therefore contained in the mean value, i.e. the count rate. Nevertheless, if there is a change in the atomic state during the interrogation time, the total count rate might render a value that corresponds to the wrong initial state. By looking at the relative time between photon counts one can
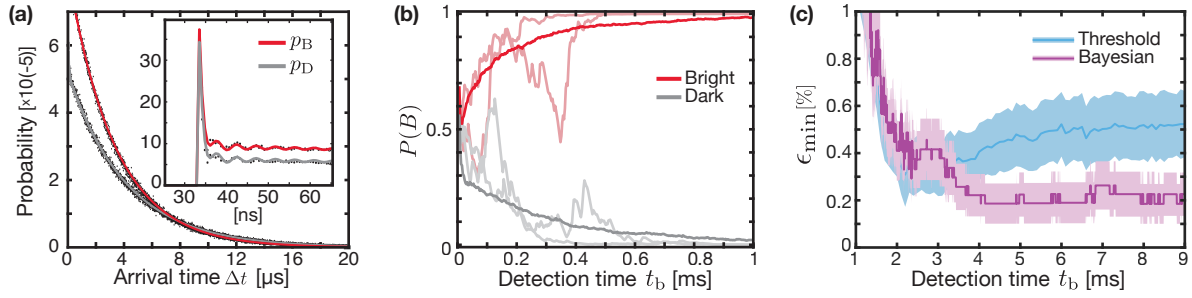
Figure 5.4: Probability distributions and detection error for the Bayesian technique. **(a)** Exponential probability distributions of the photon arrival time for both states (Eq. (5.3)) with mean arrival times of $\langle \Delta t \rangle_B = 3.3\,\mu s$ and $\langle \Delta t \rangle_D = 4.2\,\mu s$ (consistent with $R_{B,D}^{-1}$). The inset shows the complete model where we include a Heaviside step function to account for the detector dead time, an exponential rise due to *afterpulsing fluorescence* (see Sec. 6.4) and an oscillatory behavior attributed to impedance mismatch of the detector's output. **(b)** Time evolution of $P(B)$ for atoms in both states. The shaded curves represent single traces where one can appreciate discrete jumps due to the knowledge updating after a particular photon event. The average of all the digitalized traces (see text) is shown as a solid line. **(c)** Detection error obtained from the Bayesian method (purple) compared to the threshold technique error (blue). The optimum error is improved by almost a factor of two and shows less dependance on t_b.

detect these jumps, or design an estimation scheme which is robust against them.

We will use Bayesian inference to update our knowledge about the system after every photon click, which will provide us with a better detection fidelity with less dependence on interrogation time. Equivalent approaches make use of maximum likelihood schemes which have proved to yield similar results (e.g. [170]). Bayes' theorem, adapted to this particular application, states that if a photon click is detected after an idler time Δt, the probability of the atom being in the bright state is given by

$$P(B|\Delta t) = \frac{P(\Delta t|B)\, P_{pri}(B)}{P(\Delta t|B)\, P_{pri}(B) + P(\Delta t|D)\, P_{pri}(D)} \,. \tag{5.2}$$

This can be understood as the product between the *a priori* probability of the atom being in the bright state ($P_{pri}(B)$) and the probability of detecting a photon at time Δt when the atom is in such a state ($P(\Delta t|B)$). This is then normalized by the term in the denominator, which stands for the total probability of detecting an arrival time Δt considering the previous knowledge of the atom.

The arrival time probability distributions $P(\Delta t|B)$ and $P(\Delta t|D)$ can be retrieved from the state preparation traces, where we assume complete knowledge of the atomic state. They are obtained by creating a histogram of the relative time between photon clicks. For Poissonian distributed counts this is given by an exponential decay with an mean arrival time equal to the inverse of the detection count rate:

$$P(\Delta t|B) = p_B(\Delta t) = e^{-\Delta t \cdot R_B} \,, \tag{5.3}$$

and equivalently for the dark state. A more complete phenomenological model[4] including the detector characteristics can be found in Figure 5.4(a).

Once the distributions have been characterized, the inference scheme can be iteratively applied to the individual state-detection traces. The iteration process starts by assuming zero knowledge of the initial atomic state ($P_0(B) = 0.5$), which then gets revised as we use the data obtained from the first photon arrival

---

[4] $P(\Delta t|B) = H(\Delta t - t_{dead}) \cdot [A \exp(-\Delta t/t_{pulse}) + B \exp(-\Delta t \cdot R_B) + C \,\text{sinc}(D(\Delta t - t_0))]$ where $H(x)$ is the Heaviside step function, t_{dead} and t_{pulse} characterize the dead-time and afterpulsing time, and the sinc function describes the oscillatory behavior.

Δt_1, such that $P_1(B) = P(B|\Delta t_1)$. This is successively applied after every event until the predetermined interrogation time is over. Figure 5.4(b) shows individual traces of the probability evolution with time, for both bright and dark atoms.

After the detection time is over, the state estimation is acquired by digitalizing the trace, i.e. rounding up the final probability $P(B)$ to either 0 or 1. By calculating the average of all the digitalized traces for both states, one obtains the final detection error shown in Figure 5.4(c). This approach provides a smaller optimum error of $(0.19 \pm 0.08)\,\%$ for a longer window of detection times from 4 ms to 7 ms, proving higher robustness than the threshold technique. We consider the error to be limited by imperfect state preparation, variations in the coupling strength from shot to shot and cases with more than one atom present in the cavity.

It is worth noting that the Bayesian approach utilized here does not include the possibility of quantum jumps leading to leakage, therefore it does not exploit the full potential available in the count information. Nonetheless, as shown in the examples, the probability time-traces quickly saturate to values close to either 1 or 0 in less than a millisecond. Once those high (or low) values are reached, the knowledge update becomes robust[5] against state changes due to the *inertia* implicit in Equation (5.2).

Furthermore we observe that the optimum error provided by this technique is robust against jittering on detection starting times. For example, if the probe illumination is on for 3 ms before we start recording the photon counts, the threshold method will show an increased optimum error or 0.6 % due to the higher chances of the atom having undergone state leakage. On the other hand, the Bayesian inference will still provide us with the same error of 0.2 % for a slightly longer detection time; this becomes valuable when facing synchronization issues in the experiment, like those of slow mechanical shutters.

In summary, we have shown that with typical probe powers and no setup optimization required we can achieve detection errors one order of magnitude better than the best we can obtain in a fully-optimized free-space equivalent, and in shorter times. By improving the polarization purity, increasing the power of the illumination and reducing the state-preparation error, we are certain that another order of magnitude can be gained in the detection time [156]. The small mode volume of the cavity combined with our two-dimensional transport capabilities provide us with the necessary tools to expand the detection scheme to a 2D atom register, where the cavity can be used to locally detect and control single atoms placed in a 2D red-detuned lattice.

5.3 Application: Microwave Spectroscopy inside and outside the Cavity

The ability to detect the atomic hyperfine state has applications outside quantum information protocols. In general, analyzing the internal energy of an atom before and after a specific procedure sits at the heart of indispensable tools in this field, as is the case of spectroscopy. By illuminating an atom with a suitable electromagnetic field of varying frequency, its internal structure can emerge as a change in the final distribution of atomic population. The atom becomes a probe and the population transfer efficiency supplies information that would be otherwise inaccessible. Cavity-based state detection has been previously applied along these lines to characterize critical parameters of the system like the atom–cavity coupling [179] or AC Stark shifts [180]. In our case, as a proof of principle, we employ our detection scheme to retrieve information about an externally applied magnetic field. We address the hyperfine transitions with resonant microwave radiation and use the atom's magnetic structure as a probe.

---

[5] For an atom in the bright state, the probability $P(B)$ will reach values above 99 % after 1 ms. If the atom then "leaks" to the dark state, the factor proportional to $P_{\text{pri}}(B)$ in the denominator of Eq. (5.2) will out-weigh by two orders of magnitude the term proportional to $P_{\text{pri}}(D)$ and therefore the estimated probability $P(B)$ will remain close to unity for much longer times.

As we will see in the following lines, the extracted microwave spectrum also provides insight regarding the intracavity trapping field.

The presence of a static magnetic field B breaks the degeneracy of the magnetic sublevels of an atom. If the magnetic interaction is weak enough it can be considered as a perturbation; in that case the m_F levels split linearly according to the *Zeeman effect* with the energy term

$$H_B = \mu_B \, g_F \, m_F \, B \,,$$

where g_F is the hyperfine Landé g-factor and μ_B stands for the Bohr magnetron (we consider the atomic quantization axis to be along the magnetic field).

For the ground hyperfine levels of ^{87}Rb, we have that $g_2 = -g_1 = 1/2$ and therefore both hyperfine manifolds experience equivalent shifts with opposed sign. This effect translates into two opposing energy ladders as shown in Figure 5.5(a). From the nine permitted microwave transitions two are degenerate, giving rise to seven different resonance frequencies equally separated from the unperturbed transition ($\Delta_{\mathrm{HF}} \approx 6.8\,\mathrm{GHz}$). The distance between such resonances is proportional to the amplitude of the magnetic field, and it is given by

$$\Delta\omega_B = \frac{1}{2\hbar}\mu_B B \approx 0.7 \cdot B \,\, \mathrm{MHz\,G^{-1}} \,.$$

A measurement of the splitting yields then a direct estimation of the magnetic field at the position of the atom.

To obtain the spectrum we employ the same experimental setup introduced earlier in this chapter[6], with the difference that a stronger bias field is applied along the cavity direction to make sure the Zeeman splitting is visible, while the Earth's magnetic field is compensated in the other two directions. The microwave radiation (containing all polarizations) is applied by a waveguide a few centimeters away from the vacuum glass cell. The signal fed to the antenna is provided by a local oscillator (6.68 GHz) mixed with a variable frequency synthesizer which allows us to scan the frequency of the final amplified field (a detailed description can be found in [181]).

The sequence, described in Figure 5.5(b), consists in our usual procedure of coupling a single atom to the cavity followed by a number of spectroscopy cycles where the same atom is illuminated with different microwave frequencies. Prior to each of these cycles the atom is prepared in the dark state manifold. The probe field is then switched off and the magnetic field is raised; subsequently a squared microwave pulse of 2 ms is applied, followed by a state read-out window that detects the potential population transfer. The pulse duration is chosen to be long enough to wash out any coherent Rabo oscillation in the population and avoid *π-flips* that would leave the atomic state unaltered. The same sequence is performed but this time moving the atom 20 μm away from the cavity mode before applying the microwave pulse and bringing it back to perform state detection; this is used as a reference to uncover possible effects of the cavity.

In Figure 5.5(c) we show both spectra for a microwave frequency window containing four of the seven peaks, along with a fit to four equidistant Lorentzian curves. In the reference spectrum the frequency resolution is not fine enough to obtain a reliable estimation of the width of the peaks[7], although the outermost peak presents a wider feature (probably due to oscillations of the magnetic field value). Nonetheless the distance between the resonances provides us with an estimation of a total magnetic field

---

[6] We also used a smaller probe intensity of around $5.5 \times 10^4\,\mathrm{counts\,s^{-1}}$. The cavity field decay for this particular experiment was $\kappa \approx 2\pi \times 52\,\mathrm{MHz}$, which yields an intracavity photon number of $n = n_0/8$ and therefore provides similar state detection fidelities.

[7] Due to the low resolution, the fit to peak 2 ($0 \rightarrow 0$) was not reliable, we had to set a constraint to the width to ensure that the fitted curve is not wider than that of neighboring peaks, as expected for that transition.
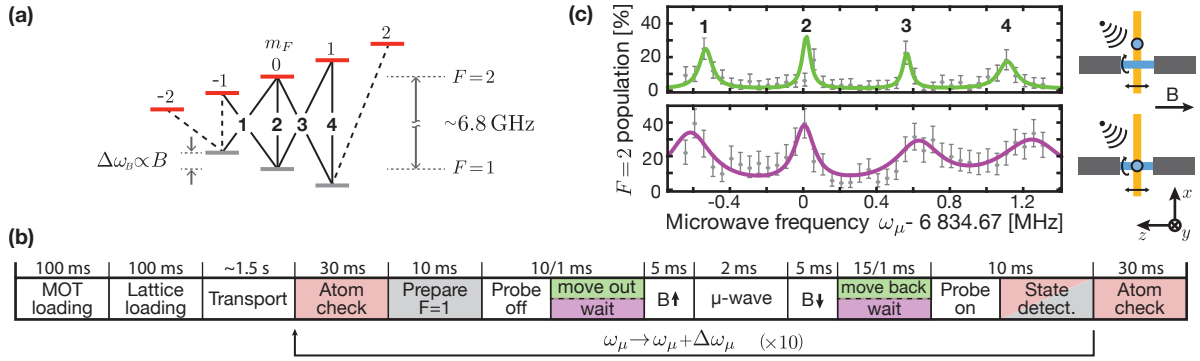
Figure 5.5: Microwave spectroscopy via cavity-based state detection. **(a)** Structure of the magnetic m_F sublevels for $F = \{1, 2\}$; the effect of the external bias field B appears as a linear shift with opposing sign for each manifold. Black lines represent all possible microwave transitions. The antenna emission contains all polarizations, as well as the repumper field used in the state preparation, nevertheless we focus our study on the four transitions marked as solid lines. **(b)** Simplified sequence layout. When the atom arrives at the cavity a total of 11 spectroscopy segments are applied; after each cycle the microwave frequency is increased by $\Delta\omega_\mu$. A total of 40 frequency values are used for the measurements (a non-multiple of 11, to avoid systematic drifts on the spectra). Depending on the measurement, the atom either waits in the cavity or it is transported away before the radiation pulse and brought back for the state detection. **(c)** Microwave spectra of the atom outside (green) and inside the cavity (purple); data is composed from a total of 1800 and 800 sequence runs respectively, the error bars represent the Clopper-Pearson confidence intervals. The colored lines are a fit to four equidistant Lorentzian peaks; their height depends on the degeneracy of the transition, the initial distribution in the dark manifold and the polarization of the microwave radiation.

of $B = (784 \pm 13)\,\mathrm{mG}$. This allows us to calibrate the magnetic coils and find the necessary values to compensate for residual fields.

The spectrum obtained when the atom remains in the cavity presents several differences. There is small shift of $2\pi \times 10\,\mathrm{kHz}$ in the position of the $|1, 0\rangle \rightarrow |2, 0\rangle$ transition (peak 2), which is at the limit of the data resolution. This is most probably induced by a *hyperfine-splitting scalar shift* (see e.g. [182]) that we expect to be in the range of $2\pi \times (1-20)\,\mathrm{kHz}$ depending on the position of the atom in the 3D trapping region. There are, nevertheless, more notable variations in the spectra, namely: the peaks are wider and the separation between them is slightly bigger ($\sim 2\pi \times 0.15\,\mathrm{MHz}$ longer). The variations in the outer peaks could be explained by the presence of a stronger and noisier magnetic field seen by the atoms. We do not expect, though, any changes in the amplitude or fluctuations of the external magnetic field between the cavity mode and the reference position. Moreover, the wavelength of the applied microwaves is around 4 cm, rendering the 20 μm distance negligible when it comes to radiation power differences. The only evident environmental difference between both scenarios is then the trapping potentials.

In the reference position outside the cavity, the atom is weakly trapped in a red-detuned 1D optical lattice ($\sim 0.25\,\mathrm{mK}$). Since the trapping conditions are the same for all atoms and the lattice field is π-polarized we only expect the already mentioned scalar shift. However, at the resonator, the atom is additionally trapped by the remaining two fields: while the MOT-transport lattice along y ($\sim 0.5\,\mathrm{mK}$) is also π-polarized, the deep trap of $\sim 1\,\mathrm{mK}$ provided by the intracavity lock field is circularly-polarized (as depicted in Figure 5.5(c)).

Off-resonant fields polarized in such a way give rise to a higher-order energy shift in the magnetic sublevels known as *vectorial light shift* [183, 184]. In the case of the ground hyperfine-states of alkali atoms, the effect is equivalent to that of a magnetic field applied in the direction of the light field

propagation[8]; this fictitious magnetic field B_f is proportional to the light's intensity at the position of the atom. Since the lock-field is blue detuned, the atom remains trapped in the regions where no light is present; nonetheless, mechanical oscillations associated with finite temperatures expose the atom to a fraction of the trapping light. In our case, from the increase in the splitting, we estimate that the effective light intensity seen by the atoms is responsible for the appearance of a fictitious field of average amplitude $B_f = (210 \pm 110)\,\text{mG}$. The growth in width of the resonances as we move from the central peak suggest that the average value oscillates by 25 %, most probably a inhomogeneous broadening consequence of the distribution of temperatures and positions in the 3D trap. This fictitious field represents a considerable fraction of our bias field, which emphasizes the importance of cooling methods when performing magnetically-sensitive procedures.

The $|1, 0\rangle \rightarrow |2, 0\rangle$ transition seems to present a wider peak at the cavity position, such a discrepancy could emerge due to an underestimation of either the corresponding width in the reference-position spectra (due to the low resolution of the particular measurement) or the expected scalar shifts induced by the deeper traps of the 3D confining regions. Another possible reason is the simplicity of the model used in our interpretations; so far we assumed that the bias magnetic field is perfectly aligned with both the cavity axis and the electric field of the red-detuned dipole traps. We also considered that we fully compensate residual fields present at the position of the cavity due to Earth's magnetic field and other environmental disturbances. However this is just an approximation as we did not yet perform a thorough optimization of the magnitude and direction of the total applied field, neither of the polarization purity of the dipole traps. Such experimental flaws may add up to a considerable fraction of the effects observed in the microwave spectrum, and therefore we should not attribute it entirely to the intracavity dipole trap.

In conclusion, we have shown that state detection can exploit the atom's sensitivity and use its internal structure as a magnetic gauge with spatial resolution (thanks to the transport capabilities). This can provide valuable information about residual magnetic fields or vectorial light shifts in specific locations of the cavity environment. Furthermore, precise spectroscopy under a bias field provides the necessary characterization for performing coherent population transfer within m_F-sublevels, which is critical for the initial state preparation in quantum information storage and/or processing protocols.

---

[8] This magnetic field is proportional to $\mathbf{E}^* \times \mathbf{E}$ and is a pseudovector, i.e. it does not flip under space reflection [185]; that means that the effect is not cancelled when the light beam is reflected, as it is the case in the intracavity field.

Tailoring the Atomic Emission: Purcell Enhancement and Cavity Back-Action

So far we used the cavity field as a probe to gain information about the coupled system. By looking at the reflection of an external pump, we characterized the influence of a single atom on the reflective properties of the resonator (Chap. 4), and used these effects to gain knowledge about the atomic internal state (Chap. 5). To see how the cavity affects the atomic emission properties, in this chapter we will go further and use the alternative probing method of directly driving the atom with an external light field, while monitoring the photons scattered into the cavity and in free space. This technique allows us to directly study the Purcell enhancement — one of the fundamental effects of cavity QED.

As discussed in the introduction to Chapter 4, the ratio between the probabilities of an excited quantum system emitting a photon into the cavity and into free space is given by the Purcell factor f_P, which is much bigger than unity in strongly coupled systems. The consequent directionality of the emitted radiation — which is efficiently collected by the cavity— along with the increase in the decay rate of the system, have established the Purcell enhancement as one of the key tools for the control of quantum emission since its first experimental demonstrations [186, 187]. Of particular interest is the use of cavities in the realization of efficient, high-bandwidth single photon sources [45]. Quantum dots coupled to micropillars have been the favored candidate due to their narrow spectral line shape and high tunability [188], yielding factors up to $f_P = 15$ for high finesse resonators [188]. However, the recent advancements on nanotechnology and microcavities [45] have made possible the realization of high Purcell enhancements in solid-state systems with much broader emission spectra [189–191], and its use to reduce by orders of magnitude the relaxation time of spins in solids [192].

The high-cooperativity and tunability offered by fiber-based Fabry–Pérot cavities has recently lead to the development of new, widely-tunable single-photon sources that combine fiber cavities with solid-state emitters such as quantum dots [32, 193], nitrogen-vacancy centers [33, 194] and carbon nanotubes [34]. Thanks to the open access that characterizes this type of resonators, trapped atoms can also be used as single-photon sources [48] by optically exciting them with an external driving field[1] and collecting most of the scattered photons through the fiber-coupled cavity output [26, 31, 195]. For high cooperativity systems, like those provided by fiber resonators containing spectrally-narrow atoms, the external optical driving of the atom leads to the phenomenon of *cavity back-action* [130, 196, 197], where the photons scattered into the resonator build up an intracavity field that — upon interference with the driving light —

---

[1] The Purcell effect is not restricted to spontaneous emission events, and in fact it also affects the coherent scattering processes of a far-detuned, externally illuminated atom.

can modify the total emission rate of the atom. Under resonant pumping, both driving and intracavity fields interfere destructively and the atomic emission is severely reduced (and can even vanish in a infinity-cooperativity system [198]). However, as we will show, for illumination frequencies detuned from the atomic resonance, the interference can be constructive and lead to a cavity-induced enhancement of the total scattering rate of the atom.

This chapter begins with a derivation of the scattering rates of a driven atom strongly coupled to a resonator (Sec. 6.1). We employ the quantum formalism introduced in Section 4.1 for the sake consistency, nonetheless the results derived here are fully consistent with the classical model presented in reference [130], as long as we consider a non-saturated two-level atom. The model successfully predicts the experimental results shown in Section 6.2.1 where we demonstrate that the fiber cavity can increase the total scattering rate of a single neutral atom by a factor of ~ 20 compared to the free-atom case (cavity back-action), and that more than 85 % of the photons scattered by the atom are emitted into the resonator mode despite the small solid angle that it covers (Purcell effect). The influence of the fiber cavity is further revealed as a broadening of the atomic line shape which corresponds to the expected enhancement of the atomic decay rate (Sec. 6.2.2). The wide optical access of our microcavity allows us to characterize on the influence of the cavity back-action in the atom's free-space scattering properties. In particular, in Section 6.3 we use the sub-micrometer spatial resolution of our imaging system to study how such effect varies for different positions of the atom in the cavity mode and, therefore, different coupling strengths. We conclude in Section 6.4 with an analysis of the statistics of the cavity output field to prove that, indeed, the emission collected by the resonator corresponds to single photons resulting from the relaxation of a single quantum emitter.

6.1 Scattering Properties of the Coupled System

We begin by analyzing the steady-state response of the system under external driving of the atom. In particular, we are interested on the amount of photons scattered by the atom into the resonator and in free space (see simplified experimental layout in Fig. 6.1(a)). Using the two-level-system approach introduced in Section 4.2, we can derive a simple analytical solution that describes the system qualitatively. The Hamiltonian of the system under free-space illumination is equivalent to that of Equation (4.14), if we replace the cavity pumping ϵ by a driving of the atom with a Rabi frequency of Ω, such that

$$\hat{H}_\Omega = \hat{H}_{JC} - i\hbar(\gamma\hat{\sigma}^\dagger\hat{\sigma} + \kappa\hat{a}^\dagger\hat{a}) + \frac{\Omega}{2}(\hat{\sigma}^\dagger + \hat{\sigma}).$$

By employing Heisenberg's equation on both cavity and atom amplitude operators ($\hat{a}^\dagger\hat{a}$ and $\hat{\sigma}^\dagger\hat{\sigma}$) one obtains the steady-state scattering rate of photons emitted in free-space and through the cavity (see App. D.2):

$$R_{\text{f-s}} = 2\gamma\langle\hat{\sigma}^\dagger\hat{\sigma}\rangle_s = \frac{\Omega^2/2\gamma}{1 + \Delta_a^2/\gamma^2} \frac{1}{|1 + 2\tilde{C}|^2} \tag{6.1a}$$

$$R_{\text{c}} = 2\eta_{\text{HT}}\kappa\langle\hat{a}^\dagger\hat{a}\rangle_s = \frac{2\eta_{\text{HT}}\kappa\Omega^2}{g^2} \frac{|\tilde{C}|^2}{|1 + 2\tilde{C}|^2}, \tag{6.1b}$$

where, as previously defined, $\Delta_{a/c} = \omega_{a/c} - \omega$ are the detuning of the atom/cavity with respect to the driving light, $\tilde{C}$ is the complex cooperativity of Equation (4.16) and η_{HT} denotes the probability that an intracavity photon leaves the cavity through the high-transmission fiber.

The two relations from Equations (6.1), which describe the rates of free-space scattering and cavity

output respectively, constitute the core of this chapter and provide both physical insight and a quantitative description of the influence of the cavity on the atomic emission. In order to assess such resonator-induced effects, we normalize both rates with respect to the scattering of a free atom in the absence of a cavity ($R_{\text{f-s}}^0$), which yields dimensionless figures of merit for the enhancement and/or inhibition of the atomic emission, independently of the incident driving power and frequency. $R_{\text{f-s}}^0$ can be obtained from Equation (6.1a) by setting $\tilde{C} = 0$, such that

$$R_{\text{f-s}}^0 = \gamma \frac{s}{1 + \Delta_{\text{a}}^2/\gamma^2} \, . \tag{6.2}$$

As expected, the emission rate of a free atom follows a Lorentzian curve with a width of γ and an amplitude proportional to the *saturation parameter*[2] $s = \Omega^2/4\gamma^2$.

The photon-collection capabilities of the resonator become clear when expressing the cavity output rate in terms of the free-space emission such as

$$R_{\text{c}} = \eta_{\text{HT}} \frac{2C_1}{1 + \Delta_{\text{c}}^2/\kappa^2} R_{\text{f-s}} \, . \tag{6.3}$$

Neglecting the technical factor η_{HT}, the ratio of the scattering rate into the cavity and in free space — when the cavity is on resonance with the illumination — is precisely the Purcell factor $R_{\text{c}}/R_{\text{f-s}} = 2C_1$. The denominator of Equation (6.3) denotes the extension of the Purcell effect for off-resonant cavities, which leads to zero collection efficiency for large detunings. Of particular interest is the fact that the atomic resonance (represented by Δ_{a}) does not play any role in the ability of the cavity to gather the scattered photons. As long as the illumination is resonant with one of the cavity longitudinal modes, a fraction $\eta = 2C_1/(1 + 2C_1)$ of the scattered light will be emitted into the resonator, even when the closest atomic resonance is largely detuned from the illumination frequency. This was shown in reference [199], where Purcell-like enhancement was observed for Rayleigh scattering of photons hundreds of nanometers away from any atomic transition. Notice that — under far-detuned illumination — the atom acts as a classical scatterer and its coherent interaction with the cavity is negligible; correspondingly, the dressed state formalism becomes unnecessary and we can resort to the classical description to provide a more intuitive picture [130]. By treating the atoms as dipoles which are driven by the classical illumination an cavity fields, the collection enhancement emerges as a consequence of the constructive interference of the atomic emission on successive roundtrips [129][3].

In the Rayleigh regime, the amount of light scattered — even when enhanced by the cavity — is negligible compared to the driving power (due to the small polarizability of the atomic dipole). Therefore, one does not expect the intracavity light — which consists of photons scattered by the atom — to have a substantial impact in the total field seen by the emitter. Such is not the case when we approach the atomic resonance, since the ratio between illumination power and scattering rate grows closer to unity. In this scenario, we encounter the cavity back-action regime, where photons scattered into the resonator build up an intracavity field that can be comparable to — or even as high as — the driving field (red and purple respectively in Figure 6.1(a)). The cavity output rate (represented in this chapter as red) can be used as a witness of the steady-state of the intracavity field. In Figure 6.1(b) we plot the resonator output for different detunings of the system, following the normalized version of Equation (6.1b). The resulting spectrum displays two clear high-intensity regions that correspond to the resonant excitation of the dressed-states of the coupled system (with eigenbands defined by $\Delta_{\text{a}}\Delta_{\text{c}} = g^2$). For our particular parameters, the scattering inside the resonator can be enhanced — with respect to the free-atom case

---

[2] $\ s \ll 1$ in this approximation.
[3] In this scenario, g denotes the overlap between the dipole emission pattern and the cavity mode.
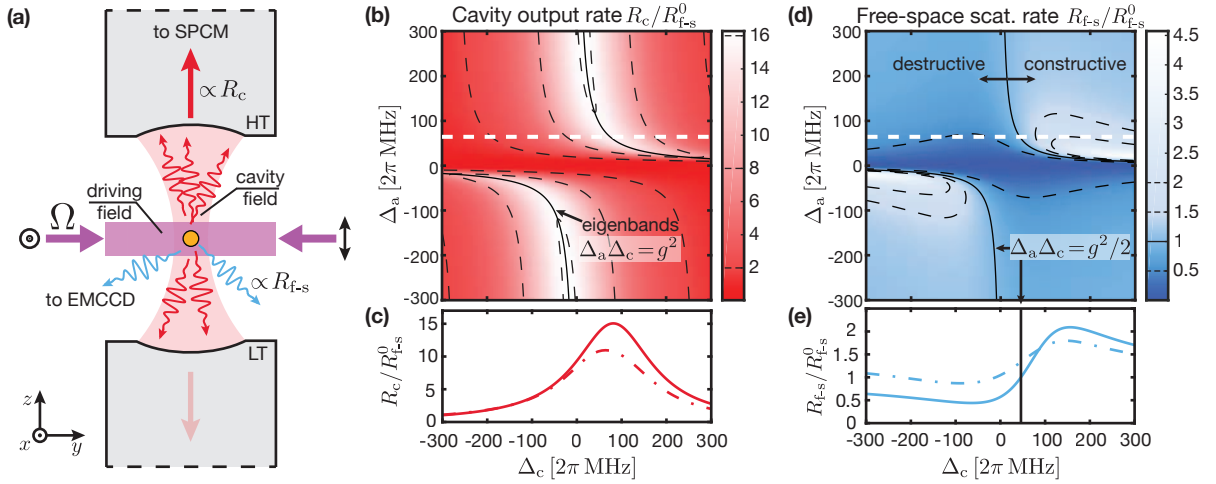
Figure 6.1: Scattering rates of the coupled system under external illumination of the atom for $(g, \kappa, \gamma) = 2\pi \times (70, 100, 3)$ MHz and $C_1 = 8.2$. **(a)** Simplified illustration of the atomic driving setup. Two counter-propagating driving beams (purple) illuminate the atom in a lin⊥lin configuration containing a $|1\rangle \to |1'\rangle$ repumper and red-detuned $|2\rangle \to |3'\rangle$ illumination light. The light scattered by the atom is detected by the SPCM (red) or by the EMCCD camera (blue) depending on the photons being collected by the cavity or the in-vacuum high-NA lens (perpendicular to the image plane), respectively. **(b)** Theoretical cavity output rate R_c (see Eq. (6.1b)) normalized to the scattering rate of a free-atom $R_{\text{f-s}}^0$, for different atom and cavity detunings (Δ_a and Δ_c, respectively). The dashed, black lines are contours of representative values, while the solid black lines denote the eigenbands of the undamped coupled system ($\Delta_a \Delta_c = g^2$). The latter correspond with the regions of highest intracavity intensities due to the resonant excitation of the dressed states with the illumination light. The white-dashed line marks out typical illumination detuning $\Delta_a = 2\pi \times 60$ MHz that corresponds to the inset shown below. **(c)** Cavity scan for our particular detuning showing the normalized cavity output rate for different resonator frequencies (solid line), reaching a maximum of $2C_1 \approx 16$. The dashed line represents the solution of the master equation for the same parameters, including saturation effects for an illumination of 250 nW (see main text). **(d)** Spectrum of the normalized free-space scattering rate $R_{\text{f-s}}/R_{\text{f-s}}^0$ (see Eq. (6.1b)), and representative contours (dashed black lines). Under resonant illumination ($\Delta_a = 0$) the free-space rate drops, yielding a *darker* atom. The rate is enhanced around the $\Delta_a \Delta_c = g^2/2$ bands (solid black lines), which mark the boundary between constructive and destructive cavity back-action. **(e)** The cavity detuning is scanned around resonance showing a two-fold enhancement of the free-space scattering rate. The dashed line represents the corresponding Master equation simulation.

— by factors as high as $2C_1 \approx 16$ (see Fig. 6.1(c)). A similar spectrum has been recently observed for a free-falling cloud of rubidium atoms weakly coupled to a micro-resonator, where the collective coupling provides cooperativity values of the same order as the one in our system [26].

The steady-state of the intracavity field is, as discussed, a result of the interplay between the driving field and the feedback from the photons scattered into the resonator. The interference between the fields can be both destructive or constructive depending on the relative dephasing between scattered photons ($\propto \Delta_a$) and the cavity buildup ($\propto \Delta_c$), which leads to either a reduction or an enhancement of the total field seen by the atom and, therefore, its total scattering rate. This classical-field picture applies to every coupling regime[4] and was recently employed to successfully describe a 10 % enhancement of the total emission of a single ion coupled to a fast fiber cavity [197], and the collective scattering of two neutral atoms strongly coupled to the same resonator [196].

---

[4] In fact, for a closed cavity ($\kappa = 0$), the driving field can be completely cancelled by the cavity mode such that the atom experiences no field at all [198].

The cavity back-action becomes more apparent when evaluating the free-space scattering rate (in this chapter represented by the color blue). In Figure 6.1(d) we show the normalized free-space emission, given by $R_{\text{f-s}}/R_{\text{f-s}}^0 = |1 + 2\tilde{C}|^{-2}$, for typical values of our system[5]. This ratio becomes smaller than unity for a resonant system (since $\tilde{C} \to C_1 > 0$), where one recovers the standard interpretation of the Purcell effect as the atom becomes *darker* in the presence of a resonant cavity. Nonetheless, as soon as the illumination is detuned from the atomic resonance ($\Delta_a \neq 0$), one can find a cavity detuning Δ_c that provides $|1 + 2\tilde{C}| = 1$ and therefore $R_{\text{f-s}} = R_{\text{f-s}}^0$. The detunings fulfilling such condition correspond with the bands given by $\Delta_a \Delta_c = g^2/2$, which set the boundary between constructive ($\Delta_a \Delta_c > g^2/2$) and destructive ($\Delta_a \Delta_c < g^2/2$) cavity back-action. This is shown in Figure 6.1(d) by the solid line separating both regimes, and in more detail in the horizontal section of Figure 6.1(e) where we see that for a typical red-detuned illumination with $\Delta_a = 2\pi \times 60\,\text{MHz}$, the presence of the cavity strongly modifies the normalized free-space scattering rate (all the way from 0.5 to 2).

It is worth noting that the population of the driven atom $\langle \hat{\sigma}^\dagger \hat{\sigma} \rangle$ in Equation (6.1a) resembles the population of an externally pumped cavity (see Eq.(4.15)) with the role of the main parameters swapped $(\gamma, \omega_a, \Omega/2) \leftrightarrow (\kappa, \omega_c, \varepsilon)$. Thus, the coupled-system's spectrum is correspondingly accessible by measuring the free-space fluorescence of a driven coupled atom, without the need of pumping or probing the cavity (as already shown in Fig 6.1(d)). As we shall see, the measurement of the vacuum Rabi splitting through free-space scattering is limited — in our case — by undesired optical pumping processes due to the resonant illumination. In particular, the population of m_F-levels with weaker coupling reduces the effective cooperativity of the system and, therefore, the visibility of the energy splitting. To the best of our knowledge the *free-space splitting* has not yet been observed in atoms, although it has been measured for solid state systems.

The simplified quantum model introduced in this section and its classical counterpart are valid as long as the cavity can host the polarization mode of the light and if all scattering processes are elastic; such assumptions are implicit when considering the two-level system and weak-excitation approximations. Nevertheless, our typical illumination scheme (shown in Fig. 6.1(a)) contains a mixture of linear polarizations with only one of them being compatible with propagation along the cavity axis. Furthermore, they address several of the atomic transitions, each with different coupling strengths. In Figures 6.1(c,e) the simplified model is compared to the master equation simulation for a typical set of parameters. Although both are evidently different, we observe that they follow the same qualitative behavior and, in fact, for the red-detuned illumination that we will use, the model from Equation (6.1) fits the simulation to a considerable degree by slightly changing the parameters g, κ. For that reason, we will use the simplified model to qualitatively study the behavior of our system, since the master equation simulations become computationally heavy when performing a multi-dimensional fit. In general, for low saturation intensities, the fit to the simplified model underestimates g by 5 % and overestimates κ and $R_{\text{f-s}}^0$ by 15 % and 25 % respectively. These corrections are thus applied to the parameters extracted from the fits to the following measurements in order to account for saturation and optical pumping effects.

6.2 Modifying the Scattering Rate of a Single Atom

Experimental Procedure

To measure the scattering properties of a single atom strongly coupled to the cavity we use the illumination scheme introduced in Figure 6.1(a). The core of this setup is the one that we already introduced in

---

[5] Interestingly enough, this factor appeared already in Section 4.2.1 (Eq.(4.15)) where we analyzed the effect that the atom has on the pumped intracavity field. Now we see that the cavity effect on the free-space emission of the atom is virtually the same.

Section 3.2, with the exception that in this case the cavity will be scanned through resonance. The light field used to drive (illuminate) the atoms is red-detuned by 46 MHz with respect to the free-space cycling transition (~60 MHz for the AC-Stark-shifted trapped atoms), which along with the absence of a bias B-field provides the best conditions for imaging when the cavity is far-detuned. The illumination beams are focused to 13 μm and counter-propagating in a lin⊥lin configuration that avoids intensity standing-wave patterns.

The photons scattered into the cavity mode are detected by the SPCM placed at the other side of the high-transmission cavity fiber, while a fraction of the free-space scattering is collected by one of the in-vacuum high-NA lenses and focussed onto the EMCCD camera. The photon losses involved in both optical paths are characterized by their corresponding detection efficiencies η_c and $\eta_{f\text{-}s}$.

As introduced in Section 3.2.2, we employ our transport feedback technique to ensure that only one atom couples to the cavity mode. The Signal-to-Noise Ratio (SNR) of the atom's scattering in free space is, however, reduced by the presence of other atoms in the proximity of the cavity mode (the fluorescence of which is also collected by the high-NA lenses). To avoid such contamination of the fluorescence, we push the atoms that are not coupled to the resonator out of the optical trap. This is done by first using the probe light to pump the atom in the cavity into the dark state (see Chap. 5) and, subsequently, performing a push-out pulse that expels off the trap all the undesired atoms remaining in the bright state. Next, the external illumination takes place for a duration of 100 ms during which we monitor both photodetectors. The whole sequence is repeated for different cavity detunings Δ_c in the range of -150 to 400 MHz. A more detailed description of the sequence can be seen in Figure 6.2(a).

6.2.1 Cavity Back-Action on a Single Atom

In Figure 6.2(b) we plot both the total SPCM counts received during the 100 ms illumination window (red) and the total amount of photons[6] detected on a region of the EMCCD chip (blue) that covers the full extent of the cavity mode. Contrary to our prediction shown in Figures 6.1(c,e), the measured curves from Figure 6.2(b) do not follow the expectations based on Equation (6.1), as the camera counts seem to be symmetric around zero detuning and the maximum of the cavity output is shifted by more than 100 MHz. The discrepancy, however, can be explained by a cavity dependent atom-loss rate. As discussed in Section 3.2.1, atoms escape the trap during the illumination time with an average trapping lifetime that depends on the cavity detuning. We attribute such detrimental effects to recoil-induced heating from the illumination beam. Photon recoil does not limit the trapping time when probing the system through the cavity (see Chap. 4.2.2), as only a few femtowatt of power are required (due to the efficient collection of the cavity output fiber) of which the atom scatters just a fraction. This is not the case under free-space illumination, since the collection efficiency of the optical system is much smaller and the signal can easily be buried by stray light and the dark counts of the camera. As a consequence, external illumination of the atom requires higher powers on the order of nanowatt; hence, the amount of recoil heating is no longer negligible, since in this case every photon reaching the detector has previously imprinted its recoil energy onto the atom. In the absence of 3D cooling, this leads to a trapping lifetime that depends on the total scattering rate of the atom, and therefore on the cavity detuning.

To obtain the atom-loss-corrected scattering rates, we first need to determine the trapping lifetime dependence on the cavity detuning. By averaging over multiple SPCM data traces for a fixed cavity frequency, we obtain an exponential decay that describes the atom loss rate, as shown in the inset of Figure 6.2(c). Since the coupling to the cavity affects the scattering rate — and therefore the trapping lifetime — we expect that a distribution of coupling strengths will lead to a distribution of exponential

---

[6] A thorough analysis of the camera response function [84] yields a calibration value of 87 photo-electrons (counts) per photon impinging on the detector.
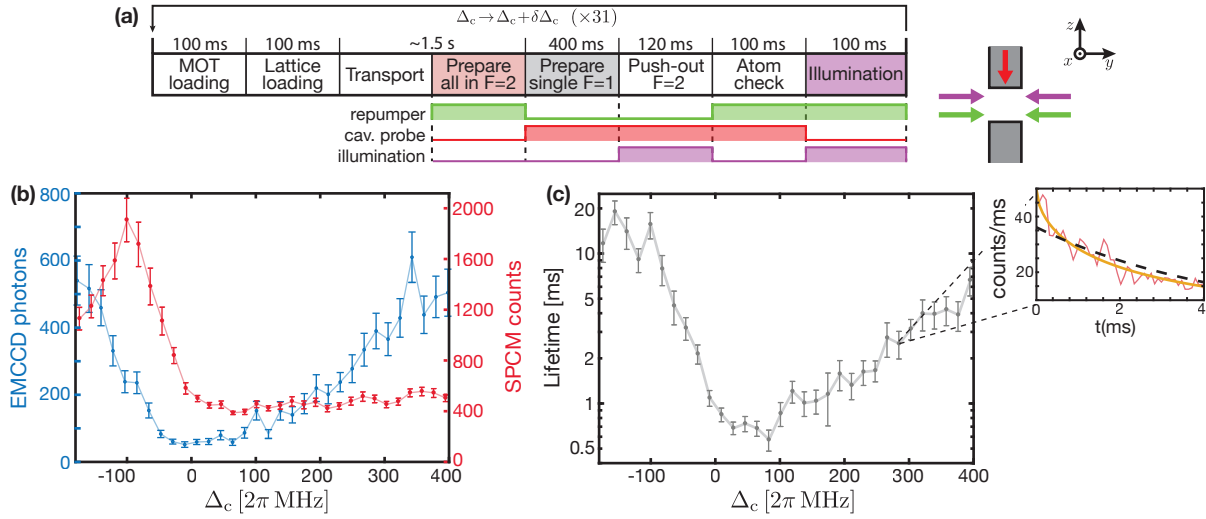
Figure 6.2: Main experimental sequence and measured integrated counts and lifetime for 100 ms of 250 nW illumination. **(a)** Simplified layout of the measurement sequence. After a single atom is coupled into the resonator, the repumper is shut down and the intracavity probe is switched on to induce leakage onto the dark state. This procedure does not affect the uncoupled atoms, which remain in the bright state and are expelled off the trap with a push-out beam. After checking that the coupled atom survived the push-out, the illumination window takes place. This is performed 32 times for different cavity lengths. **(b)** Total amount of photons detected by the SPCM (red) and the EMCCD camera (blue) during the illumination. Each data point is an average of ∼ 150 traces, the bars represent the statistical error of the mean. **(c)** Logarithmic plot of the trapping lifetime under illumination obtained by fitting a stretched exponential to the fluorescence for each cavity detuning, the error bars are obtained by bootstrapping resampling. Inset: example of an average trace for a fixed cavity frequency. The data (red) follows the solid, yellow line representing the fitted stretched exponential; the dashed, black line is a fitted simple exponential.

decays with different amplitudes and lifetimes. As a consequence, the average decay curve will not be a single exponential, but a distribution of them. For that reason we fit the data the more generic *stretched exponential*, which is defined by $A \exp[-(t/\tau)^\beta]$. This function represents the time evolution of a system that is driven by a distribution of decay processes, each with a different amplitude A_i and lifetime τ_i [200–202][7]. Although this particular function does not contain a full model of the heating mechanism, we find that this phenomenological approach is enough for the scattering rate evaluation.

The amplitude A of each average trace yields a direct estimation of the output rate of the cavity R_c, as it represents the scattering rate before the heating processes take place. In addition, the decay time of the curve corresponds to the trapping lifetime for the different cavity detunings (shown in Fig. 6.2(c)). It is not surprising that the atoms experience more heating when the cavity is on resonance with the illumination, since this is the region where we expect the maximum scattering rate due to the highest Purcell enhancement (see Eq. (6.3)). In addition, the lifetime is lower for blue-detuned cavities, which is a direct consequence of the asymmetry expected on $R_{\text{f-s}}$: For a blue-detuned cavity, a two-fold enhancement is expected in the free-space scattering; this increases the amount of photon recoil in the $x - y$ plane (perpendicular to the cavity) which corresponds to the directions where the repulsive intracavity lattice does not provide radial trapping. The estimation of $R_{\text{f-s}}$ is not straightforward, as we lack a time-resolved

---

[7] Note that $A = \langle A_i \rangle$ and that, for a delta function distribution of lifetimes centered in τ, one gets $\beta = 1$ and recovers the simple exponential.
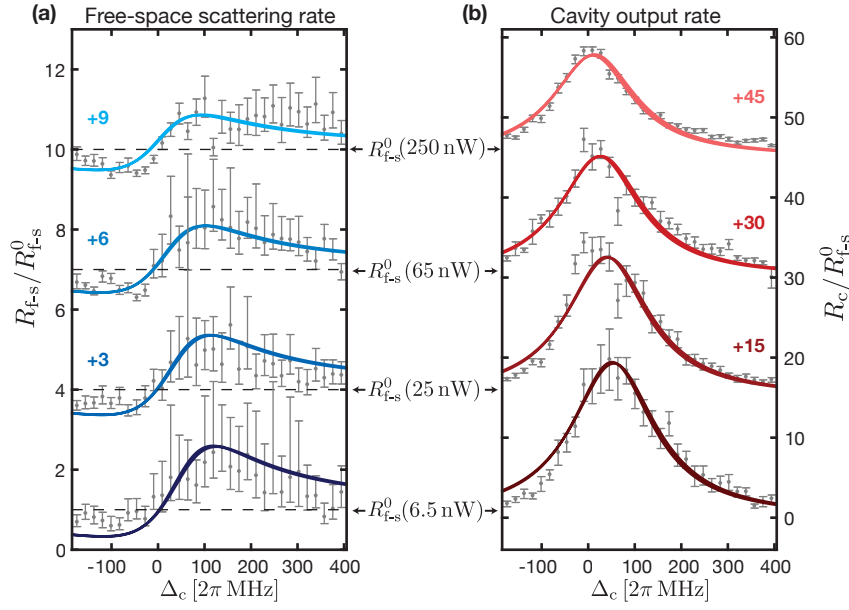
Figure 6.3: Experimental, lifetime-time corrected scattering rates for different cavity detunings (horizontal axis) and illumination powers (vertical offsets) in free-space **(a)** and through the cavity **(b)**. Both set of curves are normalized to the total scattering rate in the absence of a cavity ($R_{\text{f-s}}^0$). The error bars are obtained by bootstrapping resampling (for R_{c}) and by Montecarlo error propagation (for $R_{\text{f-s}}$). The latter are considerably bigger due to the small amount of photons reaching the camera when the lifetime is in the milliseconds regime and the low number of measured traces per point (100 to 300). The eight color curves represent the result of a single common fit to the theoretical model with seven free parameters: the cavity linewidth κ, the detection efficiencies of the SPCM (η_{c}) and camera ($\eta_{\text{f-s}}$) optical paths, and an average coupling strength g for each illumination power. The thickness of the curves represent the one-sigma confidence interval of the fit. During the fitting procedure a weighting factor of 1/10 is applied to the free-space curves to account for the bigger relative error bars. As a result we obtain decreasing coupling strengths of $2\pi \times [(86, 82, 76, 73) \pm 1]$ MHz for the increasing illumination powers. All curves are normalized to the scattering reference $R_{\text{f-s}}^0$ which is estimated from the fit and represented by the black-dashed horizontal lines (see main text for the rest of the parameter estimation and interpretation).

free-space rate due to the integration performed by taking a single image. However, we can still make use of the decay behavior obtained from the SPCM counts[8] and assume that the free-space scattering rate must be such that a single exposure of 100 ms yields the number of photons shown in Figure 6.2(b).

Both normalized scattering rates are plotted in Figure 6.3 for different illumination powers ranging from 6.5 to 250 nW, along with a fit to the simplified model of the previous section. The cavity back-action becomes visible in the free-space scattering rate, where both suppression and enhancement take place for different cavity detunings. Furthermore, the cavity output exhibits a high collection efficiency of ~85 % provided by the Purcell effect. Together, both spectra yield the total scattering of the atom that exhibit enhancements by factors as high as 20 in the presence of the cavity.

From the fit of Equations (6.1) to the experimental curves, one obtains estimations for the four parameters: $g, \kappa, \eta_{\text{c}}$ and $\eta_{\text{f-s}}$. After applying the corrections necessary due to the use of the simplified theoretical model, we retrieve a value of $\kappa = 2\pi \times (90 \pm 2)$ MHz for the cavity linewidth and average

---

[8] The lifetime will be same except for the cases of atoms that hop out of the cavity but stay within the field of view of the camera; nevertheless those atoms do not survive long as they are not trapped by the intracavity lock-light anymore.

coupling strengths $\bar{g}$ from $2\pi \times 86\,\text{MHz}$ down to $2\pi \times 73\,\text{MHz}$ for increasing illumination powers[9]. We attribute this gradual reduction of the effective coupling strength to the heating and hopping processes, which are proportional to the absolute scattering rate. The extracted detection efficiency of the cavity output is $\eta_c = (1.91 \pm 0.04)\,\%$, which deviates from the expected theoretical value $(3.1\,\%)$ even after applying the corrections predicted by the master equation; the theoretical estimation takes into account the relative transmission of the output mirror $\eta_{HT} = 18\,\%$, the cavity mode matching $\epsilon = 60\,\%$ and all the losses in the optical path $\eta_{eff} = 29\,\%$ (including fiber-couplers, filters and SPCM quantum efficiency). We attribute the discrepancy to the considerably big uncertainties in the fiber-mirror transmission, since we monitor the degradation with time of the finesse (see App. A.2), but not the particular properties of the output mirror. Other major contributions are the lack of knowledge regarding the precise spot-size and alignment of the illumination beam with respect to the cavity mode. Since atoms are distributed over a lattice as wide as the illumination beam, we assume the intensity seen by the atoms is the average of the Gaussian profile (not the peak intensity) which — along with power instabilities — can lead to further estimation errors. Finally, there exist a range of AC Stark shifts that the atoms experience for different positions in the trap.

Similar disparities appear for the extracted free-space collection efficiency $\eta_{f\text{-}s} = (2.91 \pm 0.05)\,\%$, which is $25\,\%$ larger than the theoretical prediction. To the aforementioned uncertainties we must add the lack of knowledge regarding the average dipole emission pattern of the atoms. For different cavity frequencies, the steady-state m_F population of the atoms changes and so does the polarization and pattern of the scattered light, which directly affects the fraction of photons collected by the imaging lens. In spite of the discrepancies, the curves notably follow the theoretical predictions. Although the scattering rate was not measure for a far-detuned cavity (due to technical reasons limiting the scanning range), the fit provides a precise estimation for such a reference, which reveals the enhancement factor of our system on the total emission rate.

We have therefore shown that the scattering properties of an atom can be strongly modified by tailoring the cavity resonance, as predicted by our simple model. Furthermore, we have demonstrated the high Purcell enhancement present in our system by showing that the emission into the fundamental cavity mode surpasses by one order of magnitude the one in free space. In the next paragraphs we explore the behavior of the system when scanning the illumination frequency instead of the cavity detuning.

6.2.2 Purcell Broadening of the Atomic Line Shape

The vacuum Rabi splitting can be observed in an alternative way to that shown in Chapter 4 by driving the atom and observing its free-space scattering. Both atom and cavity must be on resonance ($\Delta = \Delta_a = \Delta_c$) while the frequency of the probe laser is scanned. If the system is strongly coupled, both R_c and $R_{f\text{-}s}$ will display two peaks positioned around $\Delta = \pm g$, as shown in the examples of Figure 6.4(a). This curves correspond to a scan performed diagonally in the scattering rates of the previous Figure 6.1(b,d), with the difference that here we normalize with respect to the scattering rate of a resonant, uncoupled atom $R_{\max} = R_{f\text{-}s}^0(\Delta_a = 0)$.

For our particular system, the master equation solution suggest that near-resonant probe light depletes population of the outer most m_F levels of the ground state, while increasing that of $m_F = 0$ (Fig. 6.4(b)). Due to the weaker coupling associated with the $|2, 0\rangle \rightarrow |3', m_{F'}\rangle$ transitions the effective coupling of

---

[9] Note that the estimation of the average coupling strength here is considerably bigger than that presented in Section 4.2. We attribute the increase to a pre-selection effect of the push-out technique (only implemented in this measurement): The atoms with a better coupling have a higher probability of being pumped to the dark state before the push-out expels those in the bright state. Other factors that might affect the coupling estimation are the the presence of two-atom cases and any effect caused by the particular distribution of coupling strengths.
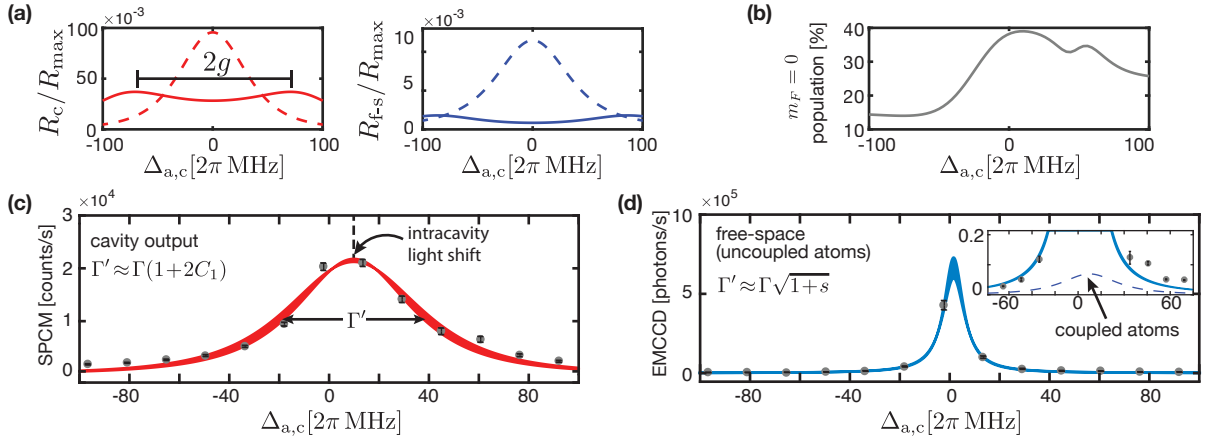
Figure 6.4: Emission line shape of an atom resonantly coupled to the cavity when scanning the illumination frequency ($\Delta_{a,c} = \Delta_a = \Delta_c$). **(a)** Theoretical prediction of the simplified model for the scattering rate of a coupled atom in both the cavity (left, red) and free-space (right, blue); the rates are normalized to that of an atom in free space resonant with the probe light (R_{max}). Two cases are shown for different cooperativities of $C_1 = 8$ (solid lines) and $C_1 = 4$ (dashed lines); in the first case the splitting is visible as two peaks appear around the resonance, with a separation given by $2g$. In all cases, the emission rate is always much smaller than that of an uncoupled, resonant atom. **(b)** Steady-state population of the $m_F = 0$ sub-level of the atomic ground state obtained via the master equation simulation for our typical parameters. The increase in population near resonance implies a reduction of the effective coupling, due to the lower strengths of the associated transitions. **(c)** Line shape of a coupled atom measured through the cavity output. The red curve is a fit to the theoretical model (Eq. (6.1b)) and its thickness represents the one-sigma confidence interval. The effect of the cavity appears as a broadening of the original width Γ. **(d)** Free-space emission line shape for coupled and uncoupled atoms. The power-broadened emission of the uncoupled atoms (blue Lorentzian fit) dominates the spectrum. The peak displays a smaller light shift than the cavity output line shape in (c) associated with the lack of intracavity trap for the uncoupled atoms. The Purcell effect suppresses the emission of coupled atoms rendering it negligible, as shown in the the inset. The dashed line represents the expected emission of the coupled atoms for the parameters extracted from (c).

the atoms is severely reduced and smaller than the cavity linewidth ($g < \kappa$). Under such conditions, our system enters the fast-cavity regime, where the effect of the resonator on the atoms is just a perturbative change on the atomic response. In this regime both cavity [26] and free-space spectra [31, 197] are reduced to a Lorentzian line shape with a broadened width of $\Gamma' = \Gamma \sqrt{(1+2C_1)^2 + s}$, where s is again the illumination saturation parameter. The system can yet be described by the model of Equation (6.1) if one considers the lower effective coupling and slight changes in the atomic resonance due to the different light-shifts.

To characterize the modified atomic line shape, we perform a similar sequence to that of the last measurement with the difference that the cavity is tuned to the light-shifted atomic resonance, while the illumination frequency is scanned by ± 100 MHz. In order to have a wider frequency tuning we use the probe laser as the source to externally illuminate the atoms. The lack of intracavity probe light implies that the cavity reflection is not monitored during the experiment and, therefore, a deterministic single-atom loading is not available. Furthermore, we lack the previously used push-out technique and atoms not coupled to the cavity remain during the illumination window and strongly contribute to the free-space emission rate.

The cavity output rate — shown as the red curve in Figure 6.4(c) — is extracted by the amplitude of the decay curves, as in the previous section. The data agrees with the predictions when accounting

for a reduced effective coupling of $2\pi \times (43 \pm 2)$ MHz and an increase on the AC Stark shift of $2\pi \times (10 \pm 2)$ MHz, both a consequence of the m_F pumping. By using the path efficiency η_c obtained from the previous measurement, we estimate that the illumination power at the position of the atoms yields a saturation parameter of $s \approx 1.4$. As a result, the emission recorded by the SPCM resembles a Lorentzian curve which is widened by a factor of $1 + 2C_1 \approx 8$ as compared to the free atom case. We do not include power broadening effects as the Purcell enhancement affects also to the saturation intensity, such that $s' = s/(1 + 2C_1)^2$ (see App. D.4).

The complementary curve of the free-space scattering, shown in Figure 6.4(d), does not display the cavity-induced widening. Instead, the measured line shape resembles that of an uncoupled atom with a power-broadening of $s = 1.7 \pm 0.4$ (which is consistent with our illumination power). The reason we do not observe the influence of the cavity is that, as previously mentioned, the atoms that are not coupled to the cavity mode are not expelled off the trap. When those atoms are illuminated with resonant light, they scatter two orders of magnitude more photons than the ones affected by the cavity, which are darker due to the Purcell effect[10]. As a consequence, the emission spectrum of the free atoms dominates the measured counts, rendering negligible the effect of the broadened peak of the coupled atoms, as shown in the inset of Figure 6.4(d). We therefore lack information about the free-space emission of the coupled atom, although the expected behavior is equivalent to the one observed though the cavity output. A more elaborate scheme with single atoms in their outermost m_F level would allow us to observe the full splitting in both channels. It is, nonetheless, experimentally challenging to obtain such a clean system when illuminating the atoms perpendicularly to the quantization axis.

6.3 Cavity Back-Action in Different Coupling Regimes

So far we traced out the spatial information provided by the camera by integrating all the photons detected over the region of interest. As a consequence we increase the SNR, which is particularly critical due to the small amount of photons emitted into free space for such short trapping lifetimes. Nonetheless, by doing so, we cast off information about the atomic position in the cavity mode, which is directly related to the effective interaction strength of the coupled system. This knowledge would allow us to correlate the system's cooperativity to the influence of the cavity on the scattering rate. To keep the SNR without loosing the spatial resolution, we transport as many atoms as possible to the region of the cavity mode and — as opposed to the previous experiment — we do not perform any push-out. In addition, we only bin the images along one of the two dimensions, thus obtaining a 2D map of the free-space scattering rate, not only for different cavity frequencies but also for different positions of the atom in the cavity mode (i.e. different coupling strengths).

In general, due to the larger amount of number of atoms inside the cavity, we observe a considerable raise of total scattered photons. Qualitatively, the rates of free-space scattering and cavity output follow the curves predicted by the model in Equation (6.1), except for an slight increase in the total rate for blue detunings of the cavity. This deviation from the single atom model is not yet fully understood and further efforts are required to account for many-body interference effects as it has been already observed in similar systems [163, 196]. Nonetheless, in the following we will keep using the simplified model, which still provides a good estimation of the coupling strength as we shall see in the following paragraphs.

As discussed, the trapping lifetime for our particular illumination conditions is reduced when the cavity is resonant or slightly blue-detuned ($\Delta_c \geq 0$). Therefore, when imaging the atoms with exposure times longer than the typical lifetime range, the influence of the near-resonant cavity appears as a reduced

---

[10] This can be seen on the vertical scale of Figures 6.4(a), where the rate is normalized to that of free atoms on resonant with the light (R_{max}).
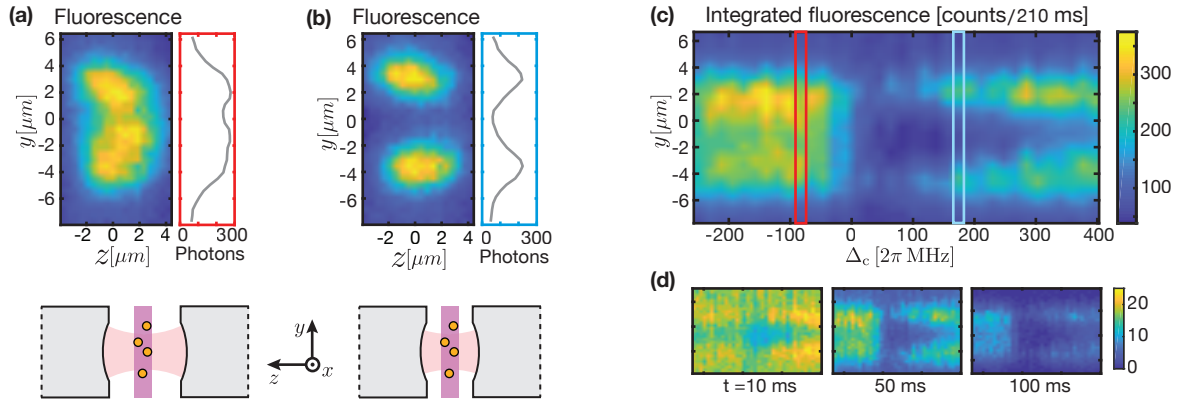
Figure 6.5: Fluorescence imaging of atoms strongly coupled to a cavity. **(a)** Average of ~80 images of an atomic ensemble transported to the mode of the red-detuned cavity, with ~65 nW of red-detuned illumination during 210 ms. The bright central region corresponds to atoms in trapped in the 3D optical lattice. The side plot displays the fluorescence integrated along the z-direction. **(b)** Equivalent image for a blue-detuned cavity. The heating processes induced by the cavity expel the atoms with higher coupling (in the central band). **(c)** Vertically-binned fluorescence (columns) for different cavity detunings (rows) for the same imaging parameters. The red and blue boxes mark the cavity detuning used in (a) and (b), respectively. Darker areas correspond to shorter lifetimes due to either the resonant-cavity effect (center) or atoms outside the 3D trapping region (top and bottom). **(d)** Sample frames of 10 ms duration after 0, 40 and 90 ms of illumination.

number of photons reaching the detector. Figures 6.5(a,b) show an average long-exposure image of the atomic ensemble in the cavity region for both a red- and blue-detuned cavity. In Figure 6.5(a) we observe that the atoms trapped in the 3D-lattice region exhibit in general longer illumination lifetimes, which manifests as the bright area in the center of the image. If the resonator is blue-detuned (Fig. 6.5(b)), the bright area is composed of two independent lobes separated by a darker region that corresponds to atoms with a stronger coupling and — due to the blue detuning — higher heating rates. Figure 6.5(c) shows the gradual behavior of the fluorescence profile as we scan the cavity around resonance. The dark bands at the top and the bottom correspond to atoms that are not in the resonator mode and therefore not axially-trapped in the z−direction; in this case their lifetime and scattering rate are independent of the cavity detuning. The required 2D map of the scattering rate cannot be provided by the SPCM — which lacks information about the atom's position — and must be acquired by using the EMCCD camera in a stroboscopic manner (to obtain the desired time resolution). To that end, we develop an experimental sequence where, after transferring an atomic ensemble to the cavity-mode region, we take a series of 21 pictures of 10 ms each. Figure 6.5(d) shows the average fluorescence after different exposure times: as time increases, only atoms in a red-detuned cavity survive, while those coupled to a blue-detuned resonator — or not coupled at all — quickly escape the trap. This time evolution yields the decay of the fluorescence of each "pixel", from which we can extract the corresponding lifetime and scattering rate amplitudes by fitting to a binned version of the stretched exponential model. Figures 6.6(a,b) show the 2D maps of both the lifetime and the photon-detection rate retrieved from the temporal decays. The lifetime map resembles the total fluorescence behavior previously shown and, when averaging over all positions, we obtain a lifetime curve really similar to that of the previous section[11] (see Fig. 6.2(c)).

---

[11] Notice that the average of the lifetimes is not necessarily the same as the lifetime of the average decay; in other words, for a stretched exponential $A \exp[-(t/\tau)^{\beta}]$ with a distribution of decay times τ_i, it generally follows that $\tau \neq \langle \tau_i \rangle$. That is the reason why the 1D lifetime curve shown here is not as asymmetric as the one in Figure 6.2(c).
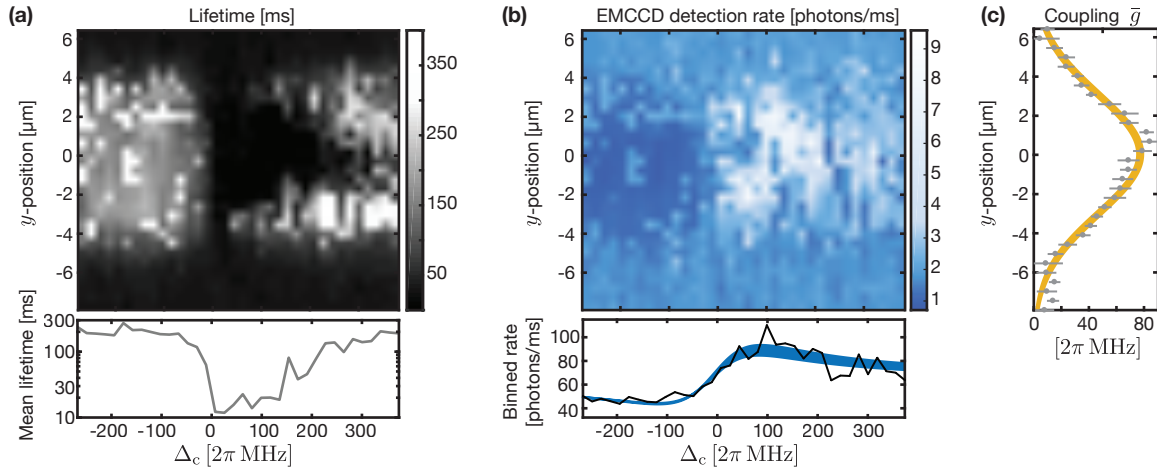
Figure 6.6: 2D maps of the atomic decay properties for different positions (rows) and cavity detunings (columns). **(a)** Trapping lifetime extracted from the stroboscopic-imaging time-evolution. The bottom graph is a semilogarithmic plot of the average lifetime in the central cavity region ($\pm 2.5\,\mu$m). **(b)** Free-space detected photons scattered by the illuminated atoms. The uniform rate of the uncoupled atoms (top and bottom homogeneous regions) gets either enhanced (blue detuning) or reduced (red detuning) when the coupling strength increases (central $y = 0$ region) due to the cavity back-action. The bottom graph shows the total count rate for each cavity frequency and a fit to the model (blue) from Eq. (6.1a) (the thickness represents the fit's confidence interval). The two fitting parameters are the average coupling $\bar{g} = 2\pi \times (46 \pm 2)$ MHz and the scattering rate reference $R_{\text{f-s}}^0$, from which we estimate an average of 7.5 ± 0.2 atoms loaded into the whole region (including those which are not coupled). **(c)** Coupling strength for different positions in the cavity mode, extracted from fitting each row of data to the theoretical model. For each fit we consider as free parameters the coupling g and fluctuations of $R_{\text{f-s}}^0$ of $\pm 10\,\%$ due to different AC Stark shifts and inhomogeneous illumination. The yellow, solid line is a fit to a Gaussian distribution. The error bars are extracted from the one-sigma confidence interval of each fit.

The free-space scattering rate for the different positions of the atom displays a clear transition between two extreme scenarios. On the one hand, the uniform regions at the top and bottom correspond to the emission from atoms not coupled to the resonator; the rate does not depend on the cavity frequency and constitutes the constant reference of the free-atom scattering (apart from small deviations in AC Stark shifts). On the other hand, the middle region represents the emission of atoms strongly coupled to the resonator that exhibits a prominent cavity back-action effect, which appears as a clear asymmetry between red and blue detunings of the cavity. In fact, the detected rate binned for all atom positions follows the qualitative curve expected for the enhanced scattering (as shown in the bottom inset). The transition between the two different regimes becomes more visible by independently fitting each row to the model from Equation (6.1a) and extracting the corresponding average coupling strength $\bar{g}$. The distribution, shown in Figure 6.6(c), follows a Gaussian curve of amplitude $g = 2\pi \times (77 \pm 2)$ MHz that reveals the underlying cavity-mode profile. The fit to a Gaussian profile yields an estimated cavity-mode waist of $(4.2 \pm 0.4)\,\mu$m, which is consistent with our independent geometrical calculation of $\sim 4.4\,\mu$m.

In summary, we have observed a spatially-resolved map of the back-action of our fiber resonator with sub-micrometer precision. By using the correspondence between interaction strength and position in the cavity mode, we have shown the influence of the cavity on the spectral properties of an atom in the different coupling regimes — from the "free" atoms in the outer regions to the strongly coupled ones at the center of the cavity mode — which is in excellent agreement with cavity back-action model and the predicted geometry of our resonator.

Imaging under the Purcell Effect

Assuming that a three-dimensional cooling scheme is available — such that the recoil-induced losses can be ignored — one could use the cavity back-action to increase the amount of free-space scattering of an atom under illumination, making the imaging process faster. Nevertheless, this effect would just be equivalent to increasing the illumination intensity, and the enhancement effect of the cavity would come in handy only in situations where illumination power is a scarce resource. In addition, the dependance on cavity detuning that we have observed severely reduces the duty cycle of this particular imaging scheme, as it requires shifting the cavity to the blue region every time the imaging is required. The robustness of this scheme would also be compromised as the amount of fluorescence collected by the camera depends on the atomic coupling strength (i.e. its position and temperature); furthermore, for atomic ensembles, the fluorescence does not scale linearly with the number of atoms due to interference effects on the intracavity field [196].

In conclusion, if one requires a fast, robust imaging technique that yields a consistent amount of single-atom fluorescence, the illumination light must be far-detuned with respect to the cavity to avoid any back-action (as discussed in Section 3.2.1 when discussing the D_1-line illumination). Instead of fluorescence imaging, one could try to use the enhanced scattering rate of the atom to perform absorption imaging with an improved SNR. Nevertheless, the absorption rate of an atom coupled to a cavity (for any detuning or cooperativity) is always smaller than that of a an atom in free space illuminated with resonant light. In fact, as we show in Appendix D.4, the maximum absorption cross section of the coupled atom gets actually reduced by the Purcell factor, which in this case constitutes a detrimental scenario.

6.4 Application: Atom–Cavity System as an Efficient Single-Photon Source

Single-photon sources are a crucial element in the majority of quantum communication and cryptography protocols [203]. The ideal source should meet a set of criteria, namely the fully deterministic, efficient and fast generation of single photon states which are indistinguishable amongst each other [204]. Independently of the nature of the source, its efficiency can be increased by improving the collection capabilities of the system; this is generally achieved by coupling the emitter to a photonic structure that channels a considerable fraction of the light. Resonators are a natural choice for the task [20, 205, 206]: As we have seen, in a high-cooperativity system the cavity collects most of the atomic emission and — under constant off-resonant illumination — the total emission rate can be enhanced due to the cavity back-action. In particular, the small mode volume of fiber-based cavities can provide strong coupling while having a higher mirror transmission. This type of open cavity is therefore a suitable candidate for highly efficient, high-bandwidth single-photon sources. As shown in recent experiments, single-photon generation using fiber cavities can be performed in a variety of platforms, including single ions [195, 197] and nitrogen-vacancy centers [33, 194]. In this section we show, as a proof of principle, that this also applies for neutral atoms. In particular, we continuously illuminate a coupled atom and collect its emission with the cavity, which constitutes a stepping stone towards the triggered generation (and/or absorption) of a single photon by coherent population transfer (see e.g. [167, 207] and Chap. 7). By characterizing the photon statistics of the cavity output, we demonstrate the quantum nature of the light emitted by our system, indicated by a clear photon antibunching.
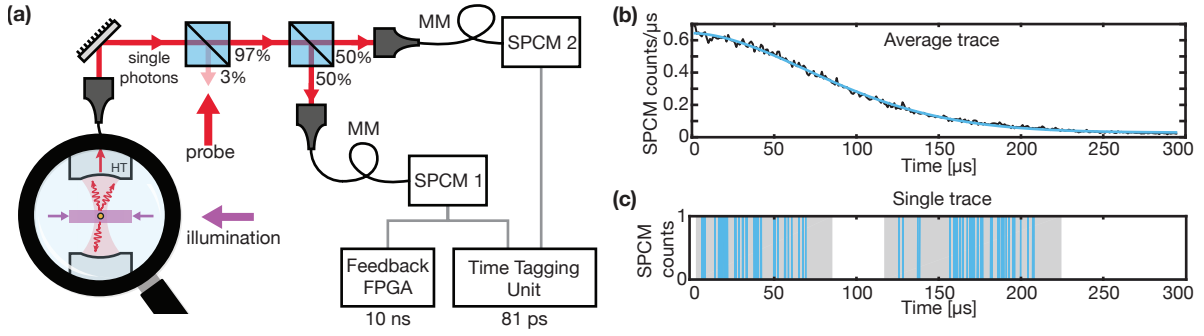
Figure 6.7: Single-photon generation experiment. **(a)** Simplified sketch of the experimental setup. A single atom scatters single photons from the illumination beams into the cavity (magnified drawing). The light is then guided through the fiber to a 97%/3% beam splitter used to couple the probe into the cavity during the feedback transport. The single photons are split and sent to both multi-mode (MM-) fiber-inputs of the detectors. The signal from SPCM1 is also sent to the FPGA. **(b)** Average emission rate of the atom during illumination. The data follows a stretched exponential with a time decay of $107\,\mu s$ (blue curve). **(c)** Example of the counts detected on a single trace. The gray shading marks the selected time windows for the subsequent data analysis. The empty regions correspond to the atom being in the dark state or leaving the cavity mode due to heating effects.

Experimental Procedure

For this procedure we employ the same experimental scheme used to analyze the scattering properties of the atom (see previous section). As depicted in Figure 6.7(a), we place a single atom in the cavity mode and continuously shine a strong, near-resonance illumination field along with a suitable repumper. This gives rise to a more or less constant stream of single photons that boosts the data rate, which is critical in our case due to the short trapping times of the atoms. The cavity collects and channels most of the photons through the high-transmission fiber. In this case though, the output of the cavity is sent to two different fiber-coupled SPCMs[12] by placing a 50%/50% non-polarizing beam splitter in the single photon path. As we will see, this allows us to obtain the photon statistics of the emitted light without the drawbacks of using a single detector. To increase our photon timing resolution we use a time tagging unit[13] that provides a bin size of 81 ps. The output of one of the SPCMs is split and sent to the FPGA such that we can still trigger the transport stop mechanism and have a single atom in the cavity.

In order to reduce the impact of background counts on the single-atom emission, we illuminate with strong counter-propagating beams of $18\,I_{sat}$ each which are red-detuned by $\sim 27\,\text{MHz}$. This leads to a high atomic scattering rate and translates, on average, to 6×10^5 counts s^{-1} reaching the detectors, which renders the $\sim 1\,\text{kHz}$ background count rate negligible[14]. The strong scattering rate dramatically reduces the lifetime of the atom as one can see in the average trace of Figure 6.7(b).

We record 3500 traces of $300\,\mu s$ each, and obtain an accumulated trace of single-atom emission of one second duration. Due to the large amount of time bins ($>10^9$), we reduce the computing time required to obtain the correlation statistics by selecting only the time windows where the average scattering rate is over a certain threshold, as shown in Figure 6.7(c). This excludes from the analysis the periods when the atom is not scattering, namely when the atom undergoes quantum jumps due to low repumping or in the presence of hopping/trap-loss due to heating.

---

[12] SPCM1: *COUNT-250N* (Laser Components). SPCM2: *SPCM-AQR-14* (PerkinElmer).

[13] 8-channel time-to-digital converter: *ID800* (IDQuantique).

[14] This scattering rate is a factor of two more than expected, attributed to errors in the estimations of illumination power and the cavity optical path efficiency η_c, which is affected by the decay in finesse. In this measurement $\kappa \approx 2\pi \times 75\,\text{MHz}$.

The Quantum Character of the Cavity Output Field

The distinction between the emission patterns of a weak classical field and a single quantum emitter can be challenging, particularly when using a detection scheme that projects the incoming light state onto the two subspaces of zero and one-or-more photons (as is the case for SPCMs). An indication commonly used to identify true single-photons coming from a quantum system is the so-called *antibunching* [208], a character of the photon statistics of a field that can only be explain resorting to the particle nature of light. To gain an intuitive understanding of such an effect we assume the simple case of a two-level atom which is being illuminated by a resonant beam. When the atom absorbs one of the incoming photons it populates the excited state for a finite amount of time. During this period, which is on average given by the atomic lifetime τ_{at} — and that is reduced in the presence of a cavity due to the Purcell enhancement — the atom is unable to scatter more photons and remains dark[15]. It is this *emission dead-time* that gives rise to the photon antibunching, yielding a lack of simultaneous or consecutive detections on the SPCM. This is not the case for a weak classical field, which is governed by Poissonian statistics where the simultaneous detection of more than one photon is still possible.

The photon statistics necessary to observe antibunching can, in principle, be provided by a single detector; in particular by its second order intensity correlation function

$$g_a^2(\tau) = \frac{\langle c(t)\, c(t+\tau)\rangle}{\langle c(t)\rangle^2}\,,$$

where $c(t)$ is the number of counts detected at time t (either 0 or 1), $\langle\rangle$ is the time average for sufficiently long periods and the subindex a stands for *autocorrelation*. This time-correlation is a normalized histogram of all the time periods elapsed between photon arrivals. It describes the conditional probability of detecting a photon at time $t+\tau$ having detected one at time t (independently of what happened in between). For the emission of a single atom the antibunching appears as a characteristic dip in the intensity correlation for $|\tau| < \tau_{at}$ and $g^{(2)}(0) = 0$, as it was first shown in 1977 [209]. The lack on detection coincidences is in contrast to the behavior expected for a coherent source, where no correlations take place and $g^{(2)}(\tau) = 1$. Unfortunately, real detectors entail certain technical drawbacks — like limited time resolution or afterpulsing fluorescence — which can generate artificial bunching (see e.g. [210]). More importantly, after a detection is triggered, the detector requires a certain *detection dead-time*. This blind period is in our case on the order of 30 to 50 ns, which is bigger than the relaxation time of an atom coupled to the cavity.

In Figures 6.8(a,b) we show the autocorrelation of one of the detectors for both a coherent field and the single-atom emission. Although the expected dip is not visible at the center, the single-atom displays a bunching behavior with a decay time (~260 ns) which is not compatible with the short afterpulsing fluorescence of the detector. This type of "bunching" is attributed to insufficient optical power of the repumper which causes the atom to spend a considerable fraction of the time in the dark state (see sample trace in Fig. 6.7). The emission pattern is thus comprised of emission windows separated by "dark" periods, and the compression or "clustering" of photons in packets leads to the bunching observed in Figure 6.8(b)[16]. Such behavior can also appear as a consequence of the Rabi oscillations of the atom due to the external driving field; the emission probability of the atom (collected by the cavity) follows a damped oscillatory behavior characterized by the corresponding illumination Rabi frequency [197, 209, 213]. We do not expect such strong Rabi oscillations for our mixed atomic population, and we attribute

---

[15] This picture of the atom populating the excited state applies for more complex internal structures, but requires near-resonant illumination or high saturation values that ensure the scattering is inelastic.

[16] Bunching is also present in sources based on molecules and solid state systems where shelving leads to similar effects [194, 211, 212].
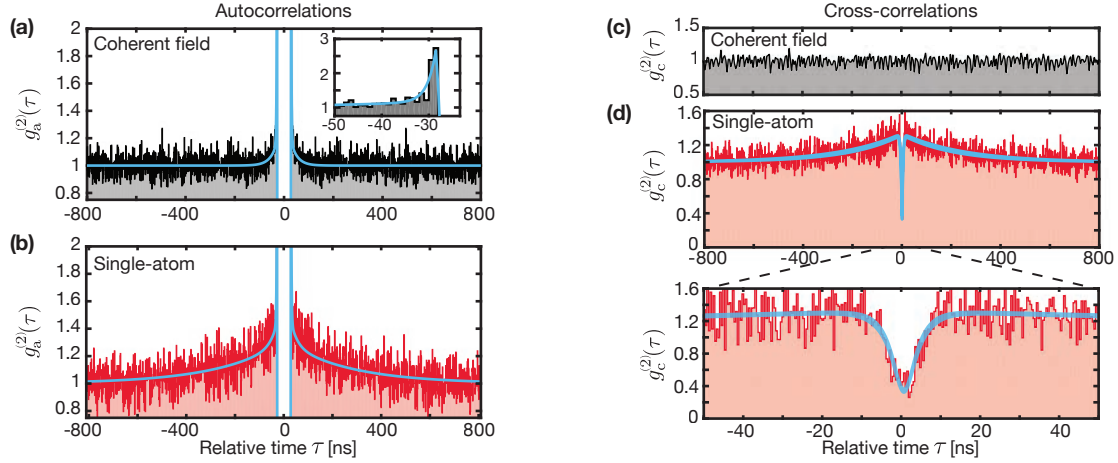
Figure 6.8: Second order correlation functions of the system. **(a)** Autocorrelation of SPCM2 for a coherent field, obtained from the cavity reflection of the weak probe laser. Each time bin corresponds to 1.2 ns. The dead time of ±28 ns erases information in the central region. Inset: A sharp bunching feature due to afterpulsing fluorescence appears during the next nanoseconds after the dead time. The blue line is a fit to a model containing both effects. **(b)** Autocorrelation of SPCM2 for the single-atom emission, for a total of one second of data. The much longer bunching of ~260 ns is attributed to optical pumping effects. **(c)** Cross-correlation between both SPCMs for a coherent field where we observe the expected correlation-free behavior of the underlying Poissonian statistics. The afterpulsing and dead-time effects are not present anymore. **(d)** Cross-correlation for the single-atom emission. The central region is now unveiled and shows the expected antibunching dip. The curve is a fit to the phenomenological model described by Eq. (6.4). The width of the curve represents the one-sigma confidence interval. Close-up: The expected sharp dip is washed out by the detectors jittering, and the correlation function drops only to ~0.3. Each time bin corresponds to 0.4 ns.

the bunching to the weak repumper field applied.

To overcome the limitations of the detector's dead-time, we separate the incoming photon stream into two indistinguishable paths (with a non-polarizing beam splitter) and place two independent detectors, as originally performed by Hanbury Brown and Twiss in 1956 [214]. When a detector is now in the blind period, the second one can still detect half of the incoming photons. In this way a more complete description of the photon statistics can be obtained through the *cross-correlation* function of detectors *1* and *2* as

$$g_c^{(2)}(\tau) = \frac{\langle c_1(t) \, c_2(t+\tau) \rangle}{\langle c_1(t) \rangle \langle c_2(t) \rangle} \, .$$

Figures 6.8(c,d) show the cross-correlation between both SPCMs for both a classical field and the single-atom emission respectively. The coherent field features a flat correlation function of unity, as expected for Poissonian photon statistics. On the other hand, the single-atom emission shows the bunching that we already observed plus a clear dip at $\tau = 0$ (as shown in the close-up). The behavior can be described phenomenologically by a simple model given by [211, 212]

$$g_c^{(2)}(\tau) = 1 - (1+a)e^{-\tau/\tau_{at}} + ae^{-\tau/\tau_b} \, , \tag{6.4}$$

where a and τ_b describe the amplitude and decay time that characterize the photon bunching. We must account for the limited time resolution of the detectors by convolving Equation (6.4) with a Gaussian of

$\sigma = 1.35$ ns, which describes the specified detectors' jittering.

A fit to the data reveals an atomic decay time of $\tau_{at} = (3.3 \pm 0.5)$ ns, almost an order of magnitude faster than that of an atom in free space. This cavity-induced reduction of the atomic lifetime yields an estimated coupling strength $g \approx 2\pi \times 40$ MHz which is consistent with the range of effective couplings obtained in previous measurements and with the fact that the intracavity trap-depth was much lower during this measurement. As a consequence, we estimate a collection efficiency of $\eta \approx 78\,\%$ (see Eq. (4.13)), which can be improved by future cooling and optical pumping techniques. The fast atomic decay and the considerable bunching amplitude ($a = 0.33$) reduce the width of the antibunching dip. In combination with the detectors jittering, we observe that the feature is washed out and the central value of the fit model rises from 0 to $g_{c}^{(2)}(0) = 0.34 \pm 0.05$, which is consistent with the recorded data.

In conclusion, the lack of detection coincidences ($g_{c}^{(2)}(0) < 0.5$) confirms the expected antibunching behavior in the photon statistics of this particular light field, thus indicating the non-classical nature of the single photons emitted by a single atom. Furthermore, the cavity does not only provide a collection efficiency of the atomic emission much larger than standard optics, but also enhances the atomic decay rate by almost an order of magnitude and, therefore, the available emission bandwidth of the source. The next step towards a deterministic single-photon source consists in replacing the continuous driving by a pulsed coherent population transfer, that allows triggered single-photon generation [167, 195, 207].

Outlook

I N this thesis I presented the realization of strong coupling and high cooperativity between an optically-trapped atomic ensemble and a fast fiber-based microcavity. The resonator — consisting of two dielectric mirrors machined on the end facet of optical fibers — was manufactured and characterized in-house, and designed to display a high-finesse and a micrometric mode volume. The cavity was integrated into a robust atom-microscope system where the tight confinement of neutral atoms in a 3D optical lattice, combined with the control of their position with a 2D optical conveyor belt, provides strong and deterministic single-atom coupling strengths of up to 100 MHz. The interaction manifests as a clear vacuum Rabi splitting of the system's energy spectrum that is further enhanced by collective effects when placing an atomic ensemble at the resonator. The strong light–matter interaction was exploited to perform a fast, non-destructive read out of the atomic internal state through the cavity. Additionally, due to the high cooperativity of the system, the cavity was used to efficiently collect single photons emitted by an externally-pumped coupled atom. A clear observation of the Purcell effect and the cavity back-action in excellent agreement with the simplified quantum model was possible due to the high collection efficiency of the in-vacuum lenses. In addition, the spatial resolution of the atom-microscope shows how the influence of the fiber cavity on the atomic free-space emission varies for different coupling regimes.

The CQED platform presented here offers the possibility to both globally and locally address tens of indistinguishable atoms equally coupled to the same well defined cavity mode. This few-particle quantum system represents a test bed for the creation and investigation of multiparticle entanglement and other types of non-classical states. In the next paragraphs we describe the next immediate technical steps required in the present setup in order to provide a well controlled, single-atom qubit register [38]. The two sections that follow contain two relevant and feasible applications that would make use of the high collective cooperativity of our system and that form part of our mid- and long-term goals.

Atomic Ensembles as a Single-Atom Qubit Register

Dicke states and other types of multi-particle entanglement can be achieved through the collective interaction of indistinguishable atoms mediated by a single cavity mode [215–217]. This section contains the next steps towards the generation of dense 3D atomic ensembles and the ability to perform precise local operations on them, with the two basic building blocks being the spatial compression of the ensemble and the individual optical addressing of its constituents.

The present limitation in the density of our atomic ensembles is the sparse loading of the transport lattice which, as discussed in Section 4.2.3, cannot provide more than 6 atoms in the resonator on

average[1]. A technique to increase the filling factor of a 1D optical lattice was realized in reference [164], where a spatial compression of the atomic distribution was performed by exploiting the oscillation of the ensemble around the waist of one of the trapping beams[2]. The technique was successfully implemented in our previous rubidium experiment [84] (employing the same focussing high-NA aspheric lenses and a similar MOT size) yielding compressions of the loading region down to ~10 μm. Although the trap depths employed here are lower, the presence of the second red-detuned trap (in the perpendicular direction) can lead to an even more compact final distribution. Furthermore, the large amount of lattice sites inside the 3D optical lattice reduces events of multiple occupancy which typically lead to losses during the compression sequence. As a consequence, we expect to place tens of atoms inside the cavity mode after a few compression sequences.

Since the final distribution of atoms depends on their initial temperature, a cooling mechanism is required in between different compression intervals. To that end, and as discussed in Section 4.1.2, we will use the intracavity lock field along with an additional external beam to perform 3D carrier-free Raman cooling of the atoms coupled to the resonator [150]. This cooling technique will also drastically reduce the trap losses of our fast high-resolution imaging (see Sec. 3.2.1). By imaging the ensembles from an additional perpendicular direction (using one of the available in-vacuum lenses) we will be able to obtain a full 3D reconstruction of the position of each atom in the cavity mode. The ability to retrieve the position and internal state information of each individual atom at once (which was already shown in our group [40]) will facilitate the characterization and analysis of any target entangled state.

Additionally, the strong focussing provided by our in-vacuum lenses opens the possibility for single atom addressing inside the resonator. A proof of principle of atom addressing was recently demonstrated in our experimental apparatus [120] which, combined with our 2D optical transport capabilities, paves the way towards selection and preparation of specific atomic patterns and the possibility of arbitrary local operations. The addition of these tools will upgrade our setup into a proving ground for the investigation of collective radiation effects [163, 196] for a controlled growing number of atoms and the realization of well defined Dicke states.

Bandwidth Matching between a Fast Single Photon and an Atomic Ensemble

Quantum information processing and communication relies on the efficient performance of each of its components. For every particular purpose there is an ideal platform, e.g. : photons are good for the transfer of information, while solid-state systems are fast information processing tools. It is the goal of quantum-enabled technologies to build devices that can simultaneously perform each of these tasks. Hybrid quantum systems, which combine several platforms, are the natural candidate [218]. Of particular interest, is the link between solid-state Quantum Dots (QD) and neutral atom ensembles. While QD constitute fast and tunable single-photon sources that can be triggered on demand, optically-trapped atomic ensembles display a group of weakly interacting spins that can serve as a long-lived quantum memory [9]. However, the efficiency of energy conversion between them is limited by the discrepancies in their bandwidth; this can be solved by interfacing both systems with an impedance matching element, e.g. a fast cavity [219].

One of our mid-term goals (in collaboration with the group of O. Schmidt) is the bandwidth-matched coupling of a GaAs QD (~1 GHz linewidth) to a neutral-rubidium based memory (6 MHz), by exploiting the coupling of a dense atomic ensemble to an open fiber cavity. As a first approach, we plan to use the

---

[1] The main reason being the large size of the MOT region (~60 μm) compared to the cavity-mode waist.

[2] The compression is done by adiabatically lowering one of the lattice arms such that the atoms start oscillating around the waist of the remaining single trap beam. After a multiple of a quarter of the oscillation period, the lattice is brought back and the atoms are captured when passing through the central region.
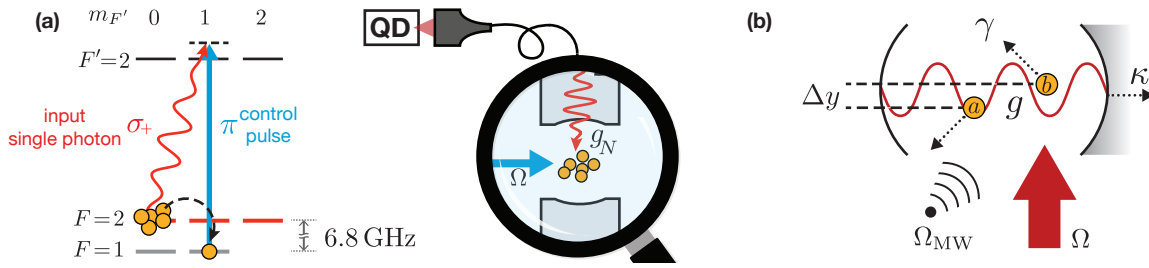
Figure 7.1: Applications for high cooperativity CQED with atomic ensembles. **(a)** Simplified energy-level scheme of the fast photon storage process. A "fast" photon (wavy red arrow) from a QD is coupled into the cavity and collectively (g_N) absorbed by the ensemble. The excitation follows a STIRAP process mediated by a free-space control pulse (Ω, blue arrow). As a result the input photon is stored in the population of the $|F=1\rangle$ ground state (dashed black arrow). **(b)** Simplified sketch of the main requirements for the deterministic entanglement of the internal hyperfine states of two atoms coupled to a resonator. The driving optical field (Ω) and microwave (Ω_{MW}) fields must be applied globally. The protocol requires a phase difference of the laser driving field of π between the two atoms, i.e. $\Delta y = (2n+1)\lambda/2$. See reference [221] for details.

present high bandwidth of our resonator ($\sim$100 MHz) to allow a considerable fraction of the fast photons to build up inside the cavity, where the high collective light–matter interaction ensures the efficient absorption of single-photon pulses much shorter than the natural atomic decay [50, 220]. A simplified sketch of the storage process is shown in Figure 7.1(a): All constituents of the atomic ensemble are prepared in the $|F=2, m_F=0\rangle$ state through a combination of optical and microwave pumping. A single photon, coming from a frequency stabilized QD resonant with the cavity, is coupled through the input fiber with circular polarization, such that it drives the $|F=2\rangle \rightarrow |F'=2\rangle$ σ-transition. A free-space *control beam* illuminates the atoms previous to the arrival of the single photon, and is subsequently switched off adiabatically in order to create an optimum STIRAP process [51] that transfers one of the atoms into the $|F=1\rangle$ ground state. The photon is then stored as a collective excitation (due to the indistinguishability of the atoms) with an efficiency increasing with the effective cooperativity of the ensemble. It can be later retrieved on demand through the same input/output fiber by illuminating the atoms once more with the classical control beam.

The temporal variation of the control beam during the storage process is tailored by a fast-switching EOM which allows the creation of arbitrary pulses with sub-nanosecond features. A similar setup is employed to create weak classical fields with less than a photon on average that can be used to simulate single photons with arbitrary bandwidth. These pulse-shaping setups will be used to characterize the efficiency of the storage scheme for a wide range of parameters and to benchmark the present simulated theoretical predictions in the limit of high-bandwidth input photons, providing a better understanding of the process and the optimal configuration for this type of hybrid link.

Cavity-based Dissipative Entanglement of Two Atoms

As discussed in Chapter 1, the deterministic generation of entanglement is essential for the realization of quantum-enabled technologies. The two main challenges that entanglement protocols face nowadays are their scalability to large system sizes and their robustness agains perturbations. The setting of CQED with densely pack atoms in optical lattices represent a fair candidate for multi-particle controlled systems up to the mesoscopic regime. However, the robustness of the cavity-based protocols performed so far, typically based on unitary operations, is limited by the precision of individual gate operations, well-defined initial states and a complete environment decoupling (e.g. [222]).

In this section we discuss the future implementation of a dissipative entanglement protocol where the intrinsic cavity-decay processes are exploited, rather than suppressed, as a mean to deterministically entangle two or more atoms strongly coupled to the resonator. The simplest scenario, consisting in the entanglement of a pair of atoms coupled to a cavity, can be achieved by globally addressing the two particles with classical fields (optical and microwave), as described in the proposal by Reiter et al. [221]. The model predicts that a final stationary state can be achieved that consists of the entangled singlet of the hyperfine ground-states of both atoms (*a* and *b*)

$$|S\rangle = (|0\rangle_a |1\rangle_b - |1\rangle_a |0\rangle_b) / \sqrt{2}.$$

The dissipative character of the process makes the entangled state an attractor of the open-system dynamics, leading to robustness against perturbations and arbitrary initial conditions.

As summarized in Figure 7.1(b), the only technical requirements for this particular deterministic entanglement are — apart from the classical global fields — the controlled relative position of the atoms with respect to the driving field and their equal coupling to a cavity. The system must display high cooperativity values as it has been shown that the fidelity of entanglement by cavity dissipative processes scales as $F \sim 1/C$ [223], thus displaying a better scaling than unitary protocols.

With the high cooperativity of our system and the recently implemented addressing scheme, we fulfill all necessary conditions to ensure the strong coupling of atom pairs with specific target relative positions. By employing the spatially-resolved state-detection method provided by our integrated in-vacuum lenses, a full tomographic reconstruction of the collective atomic state can be performed that will yield important benchmarks of the practical capabilities of the dissipative method. As a long-term goal, our plan is to investigate how this approach can contribute to the existing set of quantum optics tools to produce high-fidelity multi-particle entanglement. By expanding the Hilbert space of our system to three atoms, we plan to realize (through purely dissipative means) the preparation of three-atom states such as GHZ, squeezed states or W-states, which are relevant for the collective enhancement of single-photon generation, other unitary protocols or the field of quantum metrology (see [39] and references therein).

New Production Facility and Novel Approaches for Fiber Micromirrors

A new setup is being implemented to substitute and improve on the existing in-house facility for fiber-mirror manufacturing (introduced in Sec. 2.2), as part of the shared project *Fiber Lab* in cooperation with the groups of M. Köhl and S. Linden. The goal is to exploit the scalability and intrinsic miniaturization possibilities of optical fibers in order to facilitate the integration of quantum information devices with existing telecommunication infrastructure.

The new optical setup for mirror micromachining consists of a CO_2-laser capable of delivering up to $40\,W$ of power at $9.4\,\mu m$, which corresponds to the wavelength for optimal absorption in fused silica. The polarization and power of the laser output are controlled with state-of-the-art optical and mechanical components, while the position of the target surface is mounted on high-precision pneumatic translational stages that provide reproducible transport between the ablation region and the focal plane of a built-in Mirau interferometer. The system will allow real-time surface topography that can be used as feedback during the process of surface modification with several ablation pulses. With such techniques we will be able to manufacture concave mirrors with a large diameter [63] that can be used to form long resonators with low clipping losses (see Sec. 2.3.1), of particular relevance in ion-trap experiments. With the use of precision fiber tools the machined surfaces can be combined with and attached to different types of optical fiber cables; this includes the possibility of annexing GRIN lenses that would serve as integrated mode-matching optics to provide near-unity incoupling efficiency in long resonators [64].

Bibliography

[1] J. Gallego, S. Ghosh, S. K. Alavi, W. Alt, M. Martinez-Dorantes, D. Meschede and
L. Ratschbacher,
"High-finesse fiber Fabry-Pérot cavities: stabilization and mode matching analysis",
Applied Physics B: Lasers and Optics 122.3 (2016) 47 (cit. on pp. iv, 2, 18, 30, 36, 37, 134, 141).

[2] R. P. Feynman, "Simulating physics with computers",
International Journal of Theoretical Physics 21.6-7 (1982) 467 (cit. on p. 1).

[3] C. H. Bennett and G. Brassard,
"Quantum Cryptography: Public Key Distribution, and Coin-Tossing",
Proc. 1984 IEEE International Conference on Computers, Systems, and Signal Processing, 1984
175 (cit. on p. 1).

[4] P. W. Shor, "Polynomial-Time Algorithms for Prime Factorization and Discrete Logarithms on a
Quantum Computer", SIAM Journal on Computing 26.5 (1997) 1484 (cit. on p. 1).

[5] V. Giovannetti, "Quantum-Enhanced Measurements: Beating the Standard Quantum Limit",
Science 306.5700 (2004) 1330 (cit. on p. 1).

[6] M. A. Nielsen and I. L. Chuang, *Quantum Computation and Quantum Information*,
Cambridge University Press, 2010 702 (cit. on p. 1).

[7] H. J. Kimble, "The quantum internet", Nature 453.7198 (2008) 1023 (cit. on p. 1).

[8] J. I. Cirac, P. Zoller, H. J. Kimble and H. Mabuchi, "Quantum State Transfer and Entanglement
Distribution among Distant Nodes in a Quantum Network",
Physical Review Letters 78.16 (1997) 3221 (cit. on p. 1).

[9] A. I. Lvovsky, B. C. Sanders and W. Tittel, "Optical quantum memory",
Nature Photonics 3.12 (2009) 706 (cit. on pp. 1, 114).

[10] J. I. Cirac and P. Zoller, "Quantum Computations with Cold Trapped Ions",
Physical Review Letters 74.20 (1995) 4091 (cit. on p. 1).

[11] M. H. Devoret and J. M. Martinis,
"Implementing qubits with superconducting integrated circuits",
Experimental Aspects of Quantum Computing, 2005 163 (cit. on p. 1).

[12] H. Briegel, W. Dür, J. I. Cirac and P. Zoller,
"Quantum Repeaters: The Role of Imperfect Local Operations in Quantum Communication",
Physical Review Letters 81.26 (1998) 5932 (cit. on p. 1).

[13] L.-M. Duan, M. D. Lukin, J. I. Cirac and P. Zoller,
"Long-distance quantum communication with atomic ensembles and linear optics",
Nature 414.6862 (2001) 413 (cit. on pp. 1, 2, 7, 77).

[14] N. Sangouard, C. Simon, H. de Riedmatten and N. Gisin,
      "Quantum repeaters based on atomic ensembles and linear optics",
      Reviews of Modern Physics 83.1 (2011) 33 (cit. on p. 1).

[15] S. Haroche and D. Kleppner, "Cavity quantum electrodynamics", Physics Today 42.1 (1989) 24
      (cit. on p. 1).

[16] E. M. Purcell, "Spontaneous Emission Probabilities at Radio Frequencies",
      Physical Review 69 (1946) 681 (cit. on pp. 1, 61).

[17] S. Haroche and J.-M. Raimond, *Exploring the Quantum: Atoms, Cavities, and Photons*,
      Oxford University Press, 2006 (cit. on pp. 1, 66, 149).

[18] J. Simon, H. Tanji, S. Ghosh and V. Vuletić,
      "Single-photon bus connecting spin-wave quantum memories", Nature Physics 3.11 (2007) 765
      (cit. on p. 1).

[19] H. P. Specht, C. Nölleke, A. Reiserer, M. Uphoff, E. Figueroa, S. Ritter and G. Rempe,
      "A single-atom quantum memory", Nature 473.7346 (2011) 190 (cit. on p. 1).

[20] J. McKeever, "Deterministic Generation of Single Photons from One Atom Trapped in a Cavity",
      Science 303.5666 (2004) 1992 (cit. on pp. 1, 108).

[21] W. Chen, K. M. Beck, R. Bucker, M. Gullans, M. D. Lukin, H. Tanji-Suzuki and V. Vuletic,
      "All-Optical Switch and Transistor Gated by One Stored Photon", Science 341.6147 (2013) 768
      (cit. on pp. 1, 40).

[22] A. Reiserer, N. Kalb, G. Rempe and S. Ritter,
      "A quantum gate between a flying optical photon and a single trapped atom",
      Nature 508.7495 (2014) 237 (cit. on pp. 1, 40).

[23] S. Ritter, C. Nölleke, C. Hahn, A. Reiserer, A. Neuzner, M. Uphoff, M. Mücke, E. Figueroa,
      J. Bochmann and G. Rempe,
      "An elementary quantum network of single atoms in optical cavities",
      Nature 484.7393 (2012) 195 (cit. on p. 1).

[24] R. Dicke, "Coherence in spontaneous radiation processes", Physical Review 24.1 (1954) 99
      (cit. on p. 1).

[25] Y. Colombe, T. Steinmetz, G. Dubois, F. Linke, D. Hunger and J. Reichel,
      "Strong atom-field coupling for Bose-Einstein condensates in an optical cavity on a chip",
      Nature 450.7167 (2007) 272 (cit. on pp. 1, 2, 4, 40, 78).

[26] Y. H. Lien, G. Barontini, M. Scheucher, M. Mergenthaler, J. Goldwin and E. A. Hinds,
      "Observing coherence effects in an overdamped quantum system",
      Nature Communications 7 (2016) 13933 (cit. on pp. 1, 2, 9, 66, 68, 78, 95, 98, 104).

[27] D. Hunger, T. Steinmetz, Y. Colombe, C. Deutsch, T. W. Hänsch and J. Reichel,
      "A fiber Fabry–Perot cavity with high finesse", New Journal of Physics 12.6 (2010) 065038
      (cit. on pp. 2, 4, 7, 9, 20, 23, 140).

[28] M. Uphoff, M. Brekenfeld, G. Rempe and S. Ritter, "An integrated quantum repeater at telecom
      wavelength with single atoms in optical fiber cavities", Applied Physics B 122.3 (2016) 46
      (cit. on p. 2).

[29] J. Volz, R. Gehr, G. Dubois, J. Estève and J. Reichel,
      "Measurement of the internal state of a single atom without energy exchange.",
      Nature 475.7355 (2011) 210 (cit. on pp. 2, 85).

[30] M. Steiner, H. M. Meyer, C. Deutsch, J. Reichel and M. Köhl,
"Single Ion Coupled to an Optical Fiber Cavity", Physical Review Letters 110.4 (2013) 043003
(cit. on pp. 2, 31).

[31] H. Takahashi, E. Kassa, C. Christoforou and M. Keller,
"Cavity-induced anticorrelated photon-emission rates of a single ion",
Physical Review A 96.2 (2017) 023824 (cit. on pp. 2, 95, 104).

[32] A. Muller, E. B. Flagg, M. Metcalfe, J. Lawall and G. S. Solomon,
"Coupling an epitaxial quantum dot to a fiber-based external-mirror microcavity",
Applied Physics Letters 95.17 (2009) 173101 (cit. on pp. 2, 95).

[33] R. Albrecht, A. Bommer, C. Pauly, F. Mücklich, A. W. Schell, P. Engel, T. Schröder, O. Benson,
J. Reichel and C. Becher, "Narrow-band single photon emission at room temperature based on a
single nitrogen- vacancy center coupled to an all-fiber-cavity",
Appl. Phys. Lett 105.073113 (2014) (cit. on pp. 2, 95, 108).

[34] A. Jeantet, Y. Chassagneux, C. Raynaud, P. Roussignol, J. S. Lauret, B. Besga, J. Estève,
J. Reichel and C. Voisin,
"Widely Tunable Single-Photon Source from a Carbon Nanotube in the Purcell Regime",
Physical Review Letters 116.24 (2016) 247402 (cit. on pp. 2, 95).

[35] N. E. Flowers-Jacobs, S. W. Hoch, J. C. Sankey, A. Kashkanova, A. M. Jayich, C. Deutsch,
J. Reichel and J. G. E. Harris, "Fiber-cavity-based optomechanical device",
Applied Physics Letters 101.22 (2012) 221109 (cit. on p. 2).

[36] R. Grimm, M. Weidemüller and Y. B. Ovchinnikov, "Optical Dipole Traps for Neutral Atoms",
Advances in Atomic, Molecular and Optical Physics 42.C (2000) 95 (cit. on pp. 2, 44).

[37] S. Nussmann, M. Hijlkema, B. Weber, F. Rohde, G. Rempe and A. Kuhn,
"Submicron positioning of single atoms in a microcavity",
Physical Review Letters 95.17 (2005) 173602 (cit. on pp. 2, 40).

[38] D. Schrader, I. Dotsenko, M. Khudaverdyan, Y. Miroshnychenko, A. Rauschenbeutel and
D. Meschede, "Neutral Atom Quantum Register", Physical Review Letters 93.15 (2004) 150501
(cit. on pp. 2, 113).

[39] F. Reiter, D. Reeb and A. S. Sørensen,
"Scalable Dissipative Preparation of Many-Body Entanglement",
Physical Review Letters 117.4 (2016) 040501 (cit. on pp. 2, 116).

[40] M. Martinez-Dorantes, W. Alt, J. Gallego, S. Ghosh, L. Ratschbacher, Y. Völzke and
D. Meschede, "Non-destructive parallel readout of neutral atom registers in optical potentials",
(2017), arXiv: 1706.00264 (cit. on pp. 2, 52, 61, 84, 85, 87, 114).

[41] A. Alberti, C. Robens, W. Alt, S. Brakhane, M. Karski, R. Reimann, A. Widera and D. Meschede,
"Super-resolution microscopy of single atoms in optical lattices",
New Journal of Physics 18.5 (2016) (cit. on pp. 2, 49, 52, 53).

[42] Y. Wang, X. Zhang, T. A. Corcovilos, A. Kumar and D. S. Weiss,
"Coherent Addressing of Individual Neutral Atoms in a 3D Optical Lattice",
Physical Review Letters 115.4 (2015) 043003 (cit. on p. 2).

[43] D. Schrader, S. Kuhr, W. Alt, M. Müller, V. Gomer and D. Meschede,
"An optical conveyor belt for single neutral atoms", Applied Physics B 73.8 (2001) 819
(cit. on pp. 2, 39, 48).

[44] S. Kuhr, W. Alt, D. Schrader, M. Müller, V. Gomer and D. Meschede,
      "Deterministic Delivery of a Single Atom", Science 293.5528 (2001) 278 (cit. on pp. 2, 39, 48).

[45] K. J. Vahala, "Optical microcavities", Nature 424.6950 (2003) 839 (cit. on pp. 3, 95).

[46] G. Rempe, R. J. Thompson, H. J. Kimble and R. Lalezari,
      "Measurement of ultralow losses in an optical interferometer", Optics letters 17.5 (1992) 363
      (cit. on pp. 3, 133).

[47] A. E. Siegman, *Lasers*, University Science Books, 1986 (cit. on pp. 4, 6, 27).

[48] C. K. Law and H. J. Kimble, "Deterministic generation of a bit-stream of single-photon pulses",
      Journal of Modern Optics 44.11-12 (1997) 2067 (cit. on pp. 7, 95).

[49] M. J. Kastoryano, F. Reiter and A. S. Sørensen,
      "Dissipative Preparation of Entanglement in Optical Cavities",
      Physical Review Letters 106.9 (2011) 090502 (cit. on p. 7).

[50] M. Fleischhauer, S. Yelin and M. Lukin,
      "How to trap photons? Storing single-photon quantum states in collective atomic excitations",
      Optics Communications 179.1-6 (2000) 395 (cit. on pp. 7, 115).

[51] J. Dilley, P. Nisbet-Jones, B. W. Shore and A. Kuhn,
      "Single-photon absorption in coupled atom-cavity systems",
      Physical Review A 85.2 (2012) 023834 (cit. on pp. 7, 115).

[52] I. Dotsenko, "Single atoms on demand for cavity QED experiments",
      PhD thesis: Universtät Bonn, 2007 (cit. on pp. 7, 23, 30).

[53] D. Hunger, C. Deutsch, R. J. Barbour, R. J. Warburton and J. Reichel,
      "Laser micro-fabrication of concave, low-roughness features in silica",
      AIP Advances 2.1 (2012) 012119 (cit. on pp. 7, 9, 12, 133, 134).

[54] J. I. Cirac, S. J. van Enk, P. Zoller, H. J. Kimble and H. Mabuchi,
      "Quantum Communication in a Quantum Network", Physica Scripta T76.1 (1998) 223
      (cit. on p. 7).

[55] M. Trupke, E. A. Hinds, S. Eriksson, E. A. Curtis, Z. Moktadir, E. Kukharenka and M. Kraft,
      "Microfabricated high-finesse optical cavity with open access and small volume",
      Applied Physics Letters 87.21 (2005) 211106 (cit. on p. 8).

[56] A. Laliotis, M. Trupke, J. P. Cotter, G. Lewis, M. Kraft and E. A. Hinds,
      "ICP polishing of silicon for high-quality optical resonators on a chip",
      Journal of Micromechanics and Microengineering 22.12 (2012) 125011 (cit. on p. 8).

[57] D. Najer, M. Renggli, D. Riedel, S. Starosielec and R. J. Warburton,
      "Fabrication of mirror templates in silica with micron-sized radii of curvature",
      Applied Physics Letters 110.1 (2017) 011101 (cit. on p. 8).

[58] J. Goldwin, M. Trupke, J. Kenner, A. Ratnapala and E. Hinds,
      "Fast cavity-enhanced atom detection with low noise and high fidelity",
      Nature Communications 2 (2011) 418 (cit. on pp. 9, 56).

[59] A. Muller, E. B. Flagg, J. R. Lawall and G. S. Solomon,
      "Ultrahigh-finesse, low-mode-volume Fabry-Perot microcavity",
      Optics letters 35.13 (2010) 2293 (cit. on pp. 9, 133).

[60] B. Brandstätter, A. McClung, K. Schüppert, B. Casabone, K. Friebe, A. Stute, P. O. Schmidt,
      C. Deutsch, J. Reichel, R. Blatt and T. E. Northup,
      "Integrated fiber-mirror ion trap for strong ion-cavity coupling",
      Review of Scientific Instruments 84.12 (2013) 123104 (cit. on pp. 9, 20, 23, 31, 133–135).

[61] H. Kaupp, T. Hümmer, M. Mader, B. Schlederer, J. Benedikter, P. Haeusser, H. C. Chang,
      H. Fedder, T. W. Hänsch and D. Hunger, "Purcell-Enhanced Single-Photon Emission from
      Nitrogen-Vacancy Centers Coupled to a Tunable Microcavity",
      Physical Review Applied 6.5 (2016) (cit. on p. 9).

[62] H. Takahashi, J. Morphew, F. Oručević, A. Noguchi, E. Kassa and M. Keller,
      "Novel laser machining of optical fibers for long cavities with low birefringence",
      Optics Express 22.25 (2014) 31317 (cit. on pp. 9, 16, 20).

[63] K. Ott, S. Garcia, R. Kohlhaas, K. Schüppert, P. Rosenbusch, R. Long and J. Reichel,
      "Millimeter-long fiber Fabry-Perot cavities", Optics Express 24.9 (2016) 9839
      (cit. on pp. 9, 16, 20, 116).

[64] G. K. Gulati, H. Takahashi, N. Podoliak, P. Horak and M. Keller,
      "Fiber cavities with integrated mode matching optics", Scientific Reports 7.1 (2017) 5556
      (cit. on pp. 9, 116).

[65] R. Kitamura, L. Pilon and M. Jonasz, "Optical constants of silica glass from extreme ultraviolet
      to far infrared at near room temperature", Applied Optics 46.33 (2007) 8118 (cit. on p. 9).

[66] L. Greuter, S. Starosielec, D. Najer, A. Ludwig, L. Duempelmann, D. Rohner and
      R. J. Warburton,
      "A small mode volume tunable microcavity: Development and characterization",
      Applied Physics Letters 105.12 (2014) 121105 (cit. on p. 9).

[67] E. Mendez, K. M. Nowak, H. J. Baker, F. J. Villarreal and D. R. Hall,
      "Localized CO2 laser damage repair of fused silica optics", Applied optics 45.21 (2006) 5358
      (cit. on p. 9).

[68] C. Deutsch,
      "High finesse fibre Fabry-Perot resonators. Production , characterization and applications",
      Diplomarbeit: Ludwig-Maximilians Universität München, 2008 (cit. on pp. 9, 10, 17).

[69] F. M. Seidler, "Aufbau einer Maschine zur Bearbeitung von Glasfaser-Endflächen",
      BSc thesis: Universität Bonn, 2012 (cit. on pp. 10, 11).

[70] N. Thau, "Optical fiber cavities", MSc thesis: Universität Bonn, 2012 (cit. on p. 13).

[71] M. Costantini, "A novel phase unwrapping method based on network programming",
      IEEE Transactions on Geoscience and Remote Sensing 36.3 (1998) 813 (cit. on p. 15).

[72] M. Uphoff, M. Brekenfeld, G. Rempe and S. Ritter,
      "Frequency splitting of polarization eigenmodes in microscopic Fabry–Perot cavities",
      New Journal of Physics 17.1 (2015) 013053 (cit. on pp. 17, 23).

[73] A. Bick, C. Staarmann, P. Christoph, O. Hellmig, J. Heinze, K. Sengstock and C. Becker,
      "The role of mode match in fiber cavities", Review of Scientific Instruments 87.1 (2016) 013102
      (cit. on p. 18).

[74] M. Steiner, "A Single Ion Inside a Miniature Cavity",
      PhD thesis: University of Cambridge, 2014 (cit. on p. 20).

[75]   J. Benedikter, T. Hümmer, M. Mader, B. Schlederer, J. Reichel, T. W. Hänsch and D. Hunger,
       "Transverse-mode coupling and diffraction loss in tunable Fabry–Pérot microcavities",
       New Journal of Physics 17.5 (2015) 053051 (cit. on p. 21).

[76]   W. B. Joyce and B. C. DeLoach, "Alignment of Gaussian beams",
       Applied Optics 23.23 (1984) 4187 (cit. on pp. 22, 25, 26, 29, 139–141).

[77]   T. W. Lynn, "Measurement and Control of Individual Quanta in Cavity QED",
       PhD thesis: California Institute of Technology, 2003 (cit. on pp. 23, 62).

[78]   J. L. Hall, J. Ye and L.-S. Ma, "Measurement of mirror birefringence at the sub-ppm level:
       Proposed application to a test of QED", Physical Review A 62.1 (2000) 013815 (cit. on p. 23).

[79]   C. J. Hood, H. J. Kimble and J. Ye, "Characterization of high-finesse mirrors: Loss, phase shifts,
       and mode structure in an optical cavity", Physical Review A 64.3 (2001) 033804
       (cit. on pp. 23, 26).

[80]   T. Hansch and B. Couillaud,
       "Laser frequency stabilization by polarization spectroscopy of a reflecting reference cavity",
       Optics Communications 35.3 (1980) 441 (cit. on p. 24).

[81]   C. E. Wieman and S. L. Gilbert, "Laser-frequency stabilization using mode interference from a
       reflecting reference interferometer", Optics Letters 7.10 (1982) 480 (cit. on p. 25).

[82]   D. A. Shaddock, M. B. Gray and D. E. McClelland,
       "Frequency locking a laser to an optical cavity by use of spatial mode interference",
       Optics Letters 24.21 (1999) 1499 (cit. on p. 25).

[83]   W. Alt, "An objective lens for efficient fluorescence detection of single atoms",
       Optik 113.3 (2002) 142 (cit. on p. 33).

[84]   M. Martinez-Dorantes,
       "Fast non-destructive internal state detection of neutral atoms in optical potentials",
       PhD thesis: Universität Bonn, 2016
       (cit. on pp. 33, 34, 41, 43, 44, 49, 50, 52, 53, 81, 100, 114, 153).

[85]   D. A. Steck, "Rubidium 87 D Line Data", (2015) (cit. on p. 35).

[86]   H. Mabuchi, J. Ye and H. Kimble, "Full observation of single-atom dynamics in cavity QED",
       Applied Physics B: Lasers and Optics 68.6 (1999) 1095 (cit. on p. 36).

[87]   R. W. P. Drever, J. L. Hall, F. V. Kowalski, J. Hough, G. M. Ford, A. J. Munley and H. Ward,
       "Laser phase and frequency stabilization using an optical resonator",
       Applied Physics B Photophysics and Laser Chemistry 31.2 (1983) 97 (cit. on p. 37).

[88]   E. L. Raab, M. Prentiss, A. Cable, S. Chu and D. E. Pritchard,
       "Trapping of Neutral Sodium Atoms with Radiation Pressure",
       Physical Review Letters 59.23 (1987) 2631 (cit. on pp. 39, 40).

[89]   M. H. Anderson, J. R. Ensher, M. R. Matthews, C. E. Wieman and E. A. Cornell,
       "Observation of Bose-Einstein Condensation in a Dilute Atomic Vapor",
       Science 269.5221 (1995) 198 (cit. on p. 39).

[90]   K. B. Davis, M. O. Mewes, M. R. Andrews, N. J. Van Druten, D. S. Durfee, D. M. Kurn and
       W. Ketterle, "Bose-Einstein condensation in a gas of sodium atoms",
       Physical Review Letters 75.22 (1995) 3969 (cit. on p. 39).

[91] A. Ashkin, "Acceleration and Trapping of Particles by Radiation Pressure",
      Physical Review Letters 24.4 (1970) 156 (cit. on p. 39).

[92] S. Chu, J. E. Bjorkholm, A. Ashkin and A. Cable,
      "Experimental observation of optically trapped atoms", Physical Review Letters 57.3 (1986) 314
      (cit. on p. 39).

[93] I. Dotsenko, W. Alt, M. Khudaverdyan, S. Kuhr, D. Meschede, Y. Miroshnychenko, D. Schrader
      and A. Rauschenbeutel, "Submicrometer position control of single trapped neutral atoms",
      Physical Review Letters 95.3 (2005) 033002 (cit. on pp. 39, 48).

[94] C. J. Hood, T. W. Lynn, A. C. Doherty, A. S. Parkins and H. J. Kimble,
      "The atom-cavity microscope: single atoms bound in orbit by single photons",
      Science 287.5457 (2000) 1447 (cit. on p. 40).

[95] P. W. H. Pinkse, T. Fischer, P. Maunz and G. Rempe, "Trapping an atom with single photons",
      Nature 404.6776 (2000) 365 (cit. on p. 40).

[96] A. C. Doherty, T. W. Lynn, C. J. Hood and H. J. Kimble,
      "Trapping of single atoms with single photons in cavity QED", Physical Review A 63.1 (2001) 1
      (cit. on p. 40).

[97] S. Nußmann, K. Murr, M. Hijlkema, B. Weber, A. Kuhn and G. Rempe,
      "Vacuum-stimulated cooling of single atoms in three dimensions", Nature Physics 1.2 (2005) 122
      (cit. on pp. 40, 69).

[98] A. Reiserer, C. Nölleke, S. Ritter and G. Rempe,
      "Ground-state cooling of a single atom at the center of an optical cavity",
      Physical Review Letters 110.22 (2013) 223003 (cit. on p. 40).

[99] K. M. Fortier, S. Y. Kim, M. J. Gibbons, P. Ahmadi and M. S. Chapman,
      "Deterministic loading of individual atoms to a high-finesse optical cavity",
      Physical Review Letters 98.23 (2007) (cit. on p. 40).

[100] M. Khudaverdyan, W. Alt, I. Dotsenko, T. Kampschulte, K. Lenhard, A. Rauschenbeutel,
      S. Reick, K. Schörner, A. Widera and D. Meschede,
      "Controlled insertion and retrieval of atoms coupled to a high-finesse optical resonator",
      New Journal of Physics 10.7 (2008) 073023 (cit. on p. 40).

[101] F. Brennecke, T. Donner, S. Ritter, T. Bourdel, M. Köhl and T. Esslinger,
      "Cavity QED with a Bose-Einstein condensate", Nature 450.7167 (2007) 268 (cit. on pp. 40, 78).

[102] K. Baumann, C. Guerlin, F. Brennecke and T. Esslinger,
      "Dicke quantum phase transition with a superfluid gas in an optical cavity",
      Nature 464.7293 (2010) 1301 (cit. on p. 40).

[103] R. Landig, L. Hruby, N. Dogra, M. Landini, R. Mottl, T. Donner and T. Esslinger,
      "Quantum phases from competing short- and long-range interactions in an optical lattice",
      Nature 532.7600 (2016) 476 (cit. on p. 40).

[104] W. D. Phillips and H. Metcalf, "Laser Deceleration of an Atomic Beam",
      Physical Review Letters 48.9 (1982) 596 (cit. on p. 40).

[105] S. Chu, L. Hollberg, J. E. Bjorkholm, A. Cable and A. Ashkin,
      "Three-dimensional viscous confinement and cooling of atoms by resonance radiation pressure",
      Physical Review Letters 55.1 (1985) 48 (cit. on p. 40).

[106] D. J. Wineland and W. M. Itano, "Laser cooling of atoms", Physical Review A 20.4 (1979) 1521 (cit. on pp. 40, 69).

[107] W. Alt, "Optical control of single neutral atoms", PhD thesis: Universität Bonn, 2004 (cit. on pp. 44, 52).

[108] I. Bloch, J. Dalibard and S. Nascimbène, "Quantum simulations with ultracold quantum gases", Nature Physics 8.4 (2012) 267 (cit. on p. 44).

[109] C. Monroe, "Quantum information processing with atoms and photons.", Nature 416.6877 (2002) 238 (cit. on p. 44).

[110] Y. Wang, A. Kumar, T.-Y. Wu and D. S. Weiss, "Single-qubit gates based on targeted phase shifts in a 3D neutral atom array", Science 352.6293 (2016) 1562 (cit. on pp. 44, 45).

[111] C. Cohen-Tannoudji, J. Dupont-Roc and G. Grynberg, *Atom—Photon Interactions: Basic Process and Applications*, Wiley-VCH Verlag GmbH, 2004 (cit. on pp. 44, 62).

[112] D. G. Grier, "A revolution in optical manipulation", Nature 424.6950 (2003) 810 (cit. on p. 45).

[113] M. Endres, H. Bernien, A. Keesling, H. Levine, E. R. Anschuetz, A. Krajenbrink, C. Senko, V. Vuletic, M. Greiner and M. D. Lukin, "Atom-by-atom assembly of defect-free one-dimensional cold atom arrays", Science 354.6315 (2016) 1024 (cit. on p. 45).

[114] W. Hänsel, J. Reichel, P. Hommelhoff and T. W. Hänsch, "Magnetic conveyor belt for transporting and merging trapped atom clouds", Physical Review Letters 86.4 (2001) 608 (cit. on p. 48).

[115] M. Keil, O. Amit, S. Zhou, D. Groswasser, Y. Japha and R. Folman, "Fifteen years of cold matter on the atom chip: promise, realizations, and prospects", Journal of Modern Optics 63.18 (2016) 1840 (cit. on p. 48).

[116] S. Kuhr, "A controlled quantum system of individual neutral atoms", PhD thesis: Unisversität Bonn, 2003 (cit. on p. 49).

[117] M. Gehm, K. O'Hara, T. Savard and J. Thomas, "Dynamics of noise-induced heating in atom traps", Physical Review A 58.5 (1998) 3914 (cit. on pp. 49, 143).

[118] J. F. Sherson, C. Weitenberg, M. Endres, M. Cheneau, I. Bloch and S. Kuhr, "Single-atom-resolved fluorescence imaging of an atomic Mott insulator", Nature 467.7311 (2010) 68 (cit. on p. 49).

[119] L. W. Cheuk, M. A. Nichols, M. Okan, T. Gersdorf, V. V. Ramasesh, W. S. Bakr, T. Lompe and M. W. Zwierlein, "Quantum-gas microscope for fermionic atoms", Physical Review Letters 114.19 (2015) 193001 (cit. on p. 49).

[120] E. Uruñuela, "Imaging and addressing of neutral atoms inside a fiber cavity", MSc thesis: Universität Bonn, 2017 (cit. on pp. 50, 53, 55, 81, 114).

[121] M. Martinez-Dorantes, W. Alt, J. Gallego, S. Ghosh, L. Ratschbacher and D. Meschede, "State-dependent fluorescence of neutral atoms in optical potentials", 2017 (cit. on pp. 51, 69).

[122] J. B. Pawley, "Points, Pixels, and Gray Levels: Digitizing Image Data",
Handbook Of Biological Confocal Microscopy, Boston, MA: Springer US, 2006 59
(cit. on p. 53).

[123] Y. Miroshnychenko, D. Schrader, S. Kuhr, W. Alt, I. Dotsenko, M. Khudaverdyan,
A. Rauschenbeutel and D. Meschede,
"Continued imaging of the transport of a single neutral atom", Optics Express 11.25 (2003) 3498
(cit. on p. 53).

[124] P. Horak, B. G. Klappauf, A. Haase, R. Folman, J. Schmiedmayer, P. Domokos and E. A. Hinds,
"Possibility of single-atom detection on a chip", Physical Review A 67 (2003) 043806
(cit. on pp. 56, 58, 62, 85).

[125] T. Puppe, I. Schuster, A. Grothe, A. Kubanek, K. Murr, P. W. H. Pinkse and G. Rempe,
"Trapping and observing single atoms in a blue-detuned intracavity dipole trap",
Physical Review Letters 99.1 (2007) 013002 (cit. on p. 56).

[126] G. Grynberg, A. Aspect and C. Fabre,
Introduction to Quantum Optics: From the Semi-classical Approach to Quantized Light,
Cambridge University Press, 2010 (cit. on pp. 62, 63).

[127] L. A. Lugiato, "II Theory of Optical Bistability", *Progress in Optics*, ed. by E. Wolf, vol. XXI,
Elsevier Science Publishers, 1984 69 (cit. on p. 62).

[128] H. J. Kimble, "Strong interactions of single atoms and photons in cavity QED",
Physica Scripta 76 (1998) 127 (cit. on p. 62).

[129] J. P. Dowling, "Spontaneous emission in cavities: How much more classical can you get?",
Foundations of Physics 23.6 (1993) 895 (cit. on pp. 62, 97).

[130] H. Tanji-Suzuki, I. D. Leroux, M. H. Schleier-Smith, M. Cetina, A. Grier, J. Simon and
V. Vuletic,
"Interaction between Atomic Ensembles and Optical Resonators: Classical Description",
Advances in Atomic, Molecular, and Optical Physics 60 (2011) 53 (cit. on pp. 62, 95–97).

[131] E. Jaynes and F. Cummings, "Comparison of quantum and semiclassical radiation theories with
application to the beam maser", Proceedings of the IEEE 51.1 (1963) 89 (cit. on p. 63).

[132] B. R. Mollow, "Power Syectrum of Light Scattered by Two-Level Systems",
Physical Review 188.5 (1969) 1969 (cit. on p. 64).

[133] J. J. Sanchez-Mondragon, N. B. Narozhny and J. H. Eberly,
"Theory of Spontaneous-Emission Line Shape in an Ideal Cavity",
Physical Review Letters 51.7 (1983) 550 (cit. on pp. 65, 70).

[134] H. J. Charmichael,
Statistical Methods in Quantum Optics 1: Master Equations and Fokker-Planck Equations,
Springer, 2002 (cit. on p. 65).

[135] S. M. Tan, "A computational toolbox for quantum and atomic optics",
J. Opt. B: Quantum Semiclass. Opt 1.99 (1999) 424 (cit. on pp. 66, 151).

[136] S. M. Tan, *A Quantum Optics Toolbox for Matlab 5* (cit. on pp. 66, 151).

[137] K. M. Birnbaum, "Cavity QED with Multilevel Atoms",
PhD thesis: California Institute of Technology, 2005 (cit. on pp. 66, 151, 153).

[138] N. Moiseyev, "Quantum theory of resonances: calculating energies, widths and cross-sections by complex scaling", Physics Reports 302.5-6 (1998) 212 (cit. on p. 66).

[139] C. W. Gardiner and P. Zoller, *Quantum noise*, 3rd Ed, Springer-Verlag, 2004 (cit. on p. 66).

[140] A. Kuhn and G. Rempe,
"Optical cavity QED: Fundamentals and application as a single-photon light source",
Experimental Quantum Computation and Information, ed. by F. D. Martini and C. Monroe, 2002
37 (cit. on p. 66).

[141] G. Khitrova, H. M. Gibbs, M. Kira, S. W. Koch and A. Scherer,
"Vacuum Rabi splitting in semiconductors", Nature Physics 2.2 (2006) 81 (cit. on p. 66).

[142] D. E. Grant and H. J. Kimble, "Optical bistability for two-level atoms in a standing-wave cavity",
Optics Letters 7.8 (1982) 353 (cit. on p. 67).

[143] G. Hechenblaikner, M. Gangl, P. Horak and H. Ritsch,
"Cooling an atom in a weakly driven high-Q cavity", Physical Review A 58.4 (1998) 3030
(cit. on p. 69).

[144] V. Vuletić and S. Chu, "Laser Cooling of Atoms, Ions, or Molecules by Coherent Scattering",
Physical Review Letters 84.17 (2000) 3787 (cit. on p. 69).

[145] J. Ye, D. W. Vernooy and H. J. Kimble, "Trapping of Single Atoms in Cavity QED",
Physical Review Letters 83.24 (1999) 4987 (cit. on p. 69).

[146] P. Maunz, T. Puppe, I. Schuster, N. Syassen, P. Pinkse and G. Rempe,
"Cavity cooling of a single atom", Nature 428.6978 (2004) 50 (cit. on p. 69).

[147] V. Vuletić, H. W. Chan and A. T. Black,
"Three-dimensional cavity Doppler cooling and cavity sideband cooling by coherent scattering",
Physical Review A 64.3 (2001) 033405 (cit. on p. 69).

[148] K. Murr, S. Nußmann, T. Puppe, M. Hijlkema, B. Weber, S. C. Webster, A. Kuhn and G. Rempe,
"Three-dimensional cavity cooling and trapping in an optical lattice",
Physical Review A 73.6 (2006) 063415 (cit. on p. 69).

[149] T. Kampschulte, W. Alt, S. Manz, M. Martinez-Dorantes, R. Reimann, S. Yoon, D. Meschede,
M. Bienert and G. Morigi,
"Electromagnetically-induced-transparency control of single-atom motion in an optical cavity",
Physical Review A 89.3 (2014) 033404 (cit. on p. 69).

[150] R. Reimann, W. Alt, T. Macha, D. Meschede, N. Thau, S. Yoon and L. Ratschbacher,
"Carrier-free Raman manipulation of trapped neutral atoms",
New Journal of Physics 16.11 (2014) 113042 (cit. on pp. 69, 114).

[151] R. J. Thompson, G. Rempe and H. J. Kimble,
"Observation of normal-mode splitting for an atom in an optical cavity",
Physical Review Letters 68.8 (1992) 1132 (cit. on pp. 70, 78).

[152] J. J. Childs, K. An, M. S. Otteson, R. R. Dasari and M. S. Feld,
"Normal-Mode Line Shapes for Atoms in Standing-Wave Optical Resonators",
Physical Review Letters 77.14 (1996) 2901 (cit. on pp. 70, 71).

[153] C. J. Hood, M. S. Chapman, T. W. Lynn and H. J. Kimble,
"Real-Time Cavity QED with Single Atoms", Physical Review Letters 80.19 (1998) 4157
(cit. on p. 70).

[154] A. Boca, R. Miller, K. M. Birnbaum, A. D. Boozer, J. McKeever and H. J. Kimble, "Observation of the Vacuum Rabi Spectrum for One Trapped Atom", Physical Review Letters 93.23 (2004) 233603 (cit. on p. 70).

[155] P. Maunz, T. Puppe, I. Schuster, N. Syassen, P. W. H. Pinkse and G. Rempe, "Normal-Mode Spectroscopy of a Single-Bound-Atom–Cavity System", Physical Review Letters 94.3 (2005) 033002 (cit. on p. 70).

[156] R. Gehr, J. Volz, G. Dubois, T. Steinmetz, Y. Colombe, B. L. Lev, R. Long, J. Estève and J. Reichel, "Cavity-based single atom preparation and high-fidelity hyperfine state readout", Physical Review Letters 104.20 (2010) 203602 (cit. on pp. 70, 85, 90).

[157] K. Murr, "On the suppression of the diffusion and the quantum nature of a cavity mode. Optical bistability: forces and friction in driven cavities", Journal of Physics B 36.12 (2003) 2515 (cit. on p. 71).

[158] A. K. Tuchman, R. Long, G. Vrijsen, J. Boudet, J. Lee and M. A. Kasevich, "Normal-mode splitting with large collective cooperativity", Physical Review A 74.5 (2006) 053821 (cit. on pp. 71, 78).

[159] M. Tavis and F. W. Cummings, "Exact Solution for an N-Molecule—Radiation-Field Hamiltonian", Physical Review 170.2 (1968) 379 (cit. on p. 77).

[160] R. H. Dicke, "Coherence in Spontaneous Radiation Processes", Physical Review 93.1 (1954) 99 (cit. on p. 77).

[161] J. Sherson, B. Julsgaard and E. S. Polzik, "Deterministic Atom-Light Quantum Interface", *Advances in Atomic, Molecular and Optical Physics*, vol. 54, C, 2007 81 (cit. on p. 77).

[162] H. J. Carmichael and B. C. Sanders, "Multiatom effects in cavity QED with atomic beams", Physical Review A 60.3 (1999) 2497 (cit. on p. 78).

[163] A. Neuzner, M. Körber, O. Morin, S. Ritter and G. Rempe, "Interference and dynamics of light from a distance-controlled atom pair in an optical cavity", Nature Photonics 10.5 (2016) 303 (cit. on pp. 80, 105, 114).

[164] M. T. DePue, C. McCormick, S. L. Winoto, S. Oliver and D. S. Weiss, "Unity Occupation of Sites in a 3D Optical Lattice", Physical Review Letters 82.11 (1999) 2262 (cit. on pp. 81, 114).

[165] R. Jindra, "Positioning of Single Atoms in a Dipole Trap", MSc thesis: Technischen Universität Wien, 2014 (cit. on p. 81).

[166] D. Jaksch, J. I. Cirac, P. Zoller, S. L. Rolston, R. Cote and M. D. Lukin, "Fast quantum gates for neutral atoms", Physical Review Letters 85.10 (2000) 2208 (cit. on p. 83).

[167] M. Mücke, J. Bochmann, C. Hahn, A. Neuzner, C. Nölleke, A. Reiserer, G. Rempe and S. Ritter, "Generation of single photons from an atom-cavity system", Physical Review A 87.6 (2013) 063805 (cit. on pp. 83, 108, 112).

[168] E. Knill, "Quantum computing with realistically noisy devices", Nature 434.7029 (2005) 39 (cit. on p. 83).

[169] D. P. DiVincenzo, "The Physical Implementation of Quantum Computation", Fortschritte der Physik 48.9-11 (2000) 771 (cit. on p. 83).

[170] A. H. Myerson, D. J. Szwer, S. C. Webster, D. T. C. Allcock, M. J. Curtis, G. Imreh, J. A. Sherman, D. N. Stacey, A. M. Steane and D. M. Lucas, "High-Fidelity Readout of Trapped-Ion Qubits", Physical Review Letters 100 (2008) 200502 (cit. on pp. 83, 85, 89).

[171] A. Fuhrmanek, R. Bourgain, Y. R. P. Sortais and A. Browaeys, "Free-Space Lossless State Detection of a Single Trapped Atom", Physical Review Letters 106.13 (2011) 133003 (cit. on p. 83).

[172] M. J. Gibbons, C. D. Hamley, C.-Y. Shih and M. S. Chapman, "Nondestructive Fluorescent State Detection of Single Neutral Atom Qubits", Physical Review Letters 106.13 (2011) 133002 (cit. on p. 83).

[173] C. Robens, S. Brakhane, W. Alt, F. Kleißler, D. Meschede, G. Moon, G. Ramola and A. Alberti, "High numerical aperture (NA = 0.92) objective lens for imaging and addressing of cold atoms", Optics Letters 42.6 (2017) 1043 (cit. on p. 84).

[174] J. Bochmann, M. Mücke, C. Guhl, S. Ritter, G. Rempe and D. L. Moehring, "Lossless State Detection of Single Neutral Atoms", Physical Review Letters 104 (2010) 203601 (cit. on pp. 84, 85).

[175] M. Khudaverdyan, W. Alt, T. Kampschulte, S. Reick, A. Thobe, A. Widera and D. Meschede, "Quantum Jumps and Spin Dynamics of Interacting Atoms in a Strongly Coupled Atom-Cavity System", Physical Review Letters 103 (2009) 123006 (cit. on pp. 85, 87).

[176] R. Reimann, "Cooling and Cooperative Coupling of Single Atoms in an Optical Cavity", PhD thesis: Universität Bonn, 2014 (cit. on pp. 85, 143).

[177] M. Acton, K. A. Brickman, P. C. Haljan, P. J. Lee, L. Deslauriers and C. Monroe, "Near-Perfect Simultaneous Measurement of a Qubit Register", Quantum Information & Computation 6.6 (2005) 165 (cit. on p. 87).

[178] R. Gehr, "Cavity based high-fidelity and non-destructive single atom detection on an atom chip", PhD thesis: Laboratoire Kastler-Brossel, 2011 (cit. on p. 87).

[179] M. Khudaverdyan, "A controlled one and two atom-cavity system", PhD thesis: Universität Bonn, 2009 (cit. on p. 90).

[180] J. Bochmann, "Coherent Dynamics and State Detection of Single Atoms in a Cavity", PhD thesis: Technischen Universität München, 2010 (cit. on p. 90).

[181] L. Paulet, "Raman and Microwave Manipulation of Small Atomic Ensembles", PhD thesis: Universität Bonn, 2014 (cit. on p. 91).

[182] S. Kuhr, W. Alt, D. Schrader, I. Dotsenko, Y. Miroshnychenko, A. Rauschenbeutel and D. Meschede, "Analysis of dephasing mechanisms in a standing-wave dipole trap", Physical Review A 72.2 (2005) 023406 (cit. on p. 92).

[183] B. S. Mathur, H. Tang and W. Happer, "Light shifts in the alkali atoms", Physical Review 171.1 (1968) 11 (cit. on p. 92).

[184] C. Cohen-Tannoudji and J. Dupont-Roc, "Experimental Study of Zeeman Light Shifts in Weak Magnetic Fields", Physical Review A 5.2 (1972) 968 (cit. on p. 92).

[185] F. Le Kien, P. Schneeweiss and A. Rauschenbeutel, "Dynamical polarizability of atoms in arbitrary light fields: general theory and application to cesium", The European Physical Journal D 67.5 (2013) 92 (cit. on p. 93).

[186] P. Goy, J. M. Raimond, M. Gross and S. Haroche,
"Observation of Cavity-Enhanced Single-Atom Spontaneous Emission",
Physical Review Letters 50.24 (1983) 1903 (cit. on p. 95).

[187] D. J. Heinzen, J. J. Childs, J. E. Thomas and M. S. Feld,
"Enhanced and inhibited visible spontaneous emission by atoms in a confocal resonator",
Physical Review Letters 58.13 (1987) 1320 (cit. on p. 95).

[188] J. Gérard, B. Sermage, B. Gayral, B. Legrand, E. Costard and V. Thierry-Mieg,
"Enhanced Spontaneous Emission by Quantum Boxes in a Monolithic Optical Microcavity",
Physical Review Letters 81.5 (1998) 1110 (cit. on p. 95).

[189] I. Aharonovich, D. Englund and M. Toth, "Solid-state single-photon emitters",
Nature Photonics 10.10 (2016) 631 (cit. on p. 95).

[190] H. Sumikura, E. Kuramochi, H. Taniyama and M. Notomi,
"Purcell enhancement of fast-dephasing spontaneous emission from electron-hole droplets in
high-Q silicon photonic crystal nanocavities", Physical Review B 94.19 (2016) 195314
(cit. on p. 95).

[191] D. Ding, L. M. C. Pereira, J. F. Bauters, M. J. R. Heck, G. Welker, A. Vantomme, J. E. Bowers,
M. J. A. de Dood and D. Bouwmeester,
"Multidimensional Purcell effect in an ytterbium-doped ring resonator",
Nature Photonics 10.6 (2016) 385 (cit. on p. 95).

[192] A. Bienfait, J. J. Pla, Y. Kubo, X. Zhou, M. Stern, C. C. Lo, C. D. Weis, T. Schenkel, D. Vion,
D. Esteve, J. J. L. Morton and P. Bertet, "Controlling spin relaxation with a cavity",
Nature 531.7592 (2016) 74 (cit. on p. 95).

[193] J. Miguel-Sánchez, A. Reinhard, E. Togan, T. Volz, A. Imamoglu, B. Besga, J. Reichel and
J. Estève, "Cavity quantum electrodynamics with charge-controlled quantum dots coupled to a
fiber Fabry–Perot cavity", New Journal of Physics 15.4 (2013) 045002 (cit. on p. 95).

[194] J. Benedikter, H. Kaupp, T. Hümmer, Y. Liang, A. Bommer, C. Becher, A. Krueger, J. M. Smith,
T. W. Hänsch and D. Hunger,
"Cavity-Enhanced Single-Photon Source Based on the Silicon-Vacancy Center in Diamond",
Physical Review Applied 7.2 (2017) 024031 (cit. on pp. 95, 108, 110).

[195] M. Steiner, H. M. Meyer, J. Reichel and M. Köhl,
"Photon Emission and Absorption of a Single Ion Coupled to an Optical-Fiber Cavity",
Physical Review Letters 113.26 (2014) 263003 (cit. on pp. 95, 108, 112).

[196] R. Reimann, W. Alt, T. Kampschulte, T. Macha, L. Ratschbacher, N. Thau, S. Yoon and
D. Meschede, "Cavity-Modified Collective Rayleigh Scattering of Two Atoms",
Physical Review Letters 114.2 (2015) 023601 (cit. on pp. 95, 98, 105, 108, 114).

[197] T. G. Ballance, H. M. Meyer, P. Kobel, K. Ott, J. Reichel and M. Köhl, "Cavity-induced
backaction in Purcell-enhanced photon emission of a single ion in an ultraviolet fiber cavity",
Physical Review A 95.3 (2017) 033812 (cit. on pp. 95, 98, 104, 108, 110, 135).

[198] P. M. Alsing, D. A. Cardimona and H. J. Carmichael,
"Suppression of fluorescence in a lossless cavity", Physical Review A 45.3 (1992) 1793
(cit. on pp. 96, 98).

[199] M. Motsch, M. Zeppenfeld, P. W. H. Pinkse and G. Rempe,
       "Cavity-enhanced Rayleigh scattering", New Journal of Physics 12.6 (2010) 063022
       (cit. on p. 97).

[200] R. Kohlrausch, "Theorie des elektrischen Rückstandes in der Leidener Flasche",
       Annalen der Physik und Chemie 167.1 (1854) 56 (cit. on p. 101).

[201] G. Williams and D. C. Watts, "Non-symmetrical dielectric relaxation behaviour arising from a
       simple empirical decay function", Transactions of the Faraday Society 66 (1970) 80
       (cit. on p. 101).

[202] K. B. Lee, J. Siegel, S. Webb, S. Lévêque-Fort, M. Cole, R. Jones, K. Dowling, M. Lever and
       P. French,
       "Application of the Stretched Exponential Function to Fluorescence Lifetime Imaging",
       Biophysical Journal 81.3 (2001) 1265 (cit. on p. 101).

[203] N. Gisin, G. Ribordy, W. Tittel and H. Zbinden, "Quantum cryptography",
       Reviews of Modern Physics 74.1 (2002) 145 (cit. on p. 108).

[204] A. Kuhn and D. Ljunggren, "Cavity-based single-photon sources",
       Contemporary Physics 51.4 (2010) 289 (cit. on p. 108).

[205] M. Keller, B. Lange, K. Hayasaka, W. Lange and H. Walther,
       "Continuous generation of single photons with controlled waveform in an ion-trap cavity system",
       Nature 431.7012 (2004) 1075 (cit. on p. 108).

[206] M. Hijlkema, B. Weber, H. P. Specht, S. C. Webster, A. Kuhn and G. Rempe,
       "A single-photon server with just one atom", Nature Physics 3.4 (2007) 253 (cit. on p. 108).

[207] P. B. R. Nisbet-Jones, J. Dilley, D. Ljunggren and A. Kuhn,
       "Highly efficient source for indistinguishable single photons of controlled shape",
       New Journal of Physics 13.10 (2011) 103036 (cit. on pp. 108, 112).

[208] H. Paul, "Photon antibunching", Reviews of Modern Physics 54.4 (1982) 1061 (cit. on p. 110).

[209] H. J. Kimble, M. Dagenais and L. Mandel, "Photon Antibunching in Resonance Fluorescence",
       Physical Review Letters 39.11 (1977) 691 (cit. on p. 110).

[210] S. Manz, "Heterodyne spectroscopy with single atoms in a high-finesse optical cavity",
       PhD thesis: Universität Bonn, 2012 (cit. on p. 110).

[211] S. C. Kitson, P. Jonsson, J. G. Rarity and P. R. Tapster,
       "Intensity fluctuation spectroscopy of small numbers of dye molecules in a microcavity",
       Physical Review A 58.1 (1998) 620 (cit. on pp. 110, 111).

[212] E. Neu, D. Steinmetz, J. Riedrich-Möller, S. Gsell, M. Fischer, M. Schreck and C. Becher,
       "Single photon emission from silicon-vacancy colour centres in chemical vapour deposition
       nano-diamonds on iridium", New Journal of Physics 13.2 (2011) 025012 (cit. on pp. 110, 111).

[213] M. Dagenais and L. Mandel,
       "Investigation of two-time correlations in photon emissions from a single atom",
       Physical Review A 18.5 (1978) 2217 (cit. on p. 110).

[214] R. Hanbury Brown and R. Q. Twiss,
       "Correlation between Photons in two Coherent Beams of Light", Nature 177.4497 (1956) 27
       (cit. on p. 111).

[215]   F. Haas, J. Volz, R. Gehr, J. Reichel and J. Esteve,
        "Entangled States of More Than 40 Atoms in an Optical Fiber Cavity",
        Science 344.6180 (2014) 180 (cit. on p. 113).

[216]   R. McConnell, H. Zhang, J. Hu, S. Ćuk and V. Vuletić,
        "Entanglement with negative Wigner function of almost 3,000 atoms heralded by one photon",
        Nature 519.7544 (2015) 439 (cit. on p. 113).

[217]   G. Barontini, L. Hohmann, F. Haas, J. Esteve and J. Reichel,
        "Deterministic generation of multiparticle entanglement by quantum Zeno dynamics",
        Science 349.6254 (2015) 1317 (cit. on p. 113).

[218]   G. Kurizki, P. Bertet, Y. Kubo, K. Mølmer, D. Petrosyan, P. Rabl and J. Schmiedmayer,
        "Quantum technologies with hybrid systems",
        Proceedings of the National Academy of Sciences 112.13 (2015) 3866 (cit. on p. 114).

[219]   H. M. Meyer, R. Stockill, M. Steiner, C. Le Gall, C. Matthiesen, E. Clarke, A. Ludwig,
        J. Reichel, M. Atatüre and M. Köhl,
        "Direct Photonic Coupling of a Semiconductor Quantum Dot and a Trapped Ion",
        Physical Review Letters 114.12 (2015) 123001 (cit. on p. 114).

[220]   A. V. Gorshkov, A. André, M. D. Lukin and A. S. Sørensen,
        "Photon storage in Λ-type optically dense atomic media. I. Cavity model",
        Physical Review A 76.3 (2007) 033804 (cit. on p. 115).

[221]   F. Reiter, M. J. Kastoryano and A. S. Sørensen,
        "Driving two atoms in an optical cavity into an entangled steady state using engineered decay",
        New Journal of Physics 14.5 (2012) 053022 (cit. on pp. 115, 116).

[222]   L. Viola and S. Lloyd, "Dynamical suppression of decoherence in two-state quantum systems",
        Physical Review A 58.4 (1998) 2733 (cit. on p. 115).

[223]   M. J. Kastoryano, F. Reiter and A. S. Sørensen,
        "Dissipative Preparation of Entanglement in Optical Cavities",
        Physical Review Letters 106.9 (2011) 090502 (cit. on p. 116).

[224]   H.-J. Cho, M.-J. Shin and J.-C. Lee,
        "Effects of substrate and deposition method onto the mirror scattering",
        Applied optics 45.7 (2006) 1440 (cit. on p. 134).

[225]   E. Atanassova, T. Dimitrova and J. Koprinarova,
        "AES and XPS study of thin RF-sputtered Ta2O5 layers",
        Applied Surface Science 84.2 (1995) 193 (cit. on p. 134).

[226]   D. Gangloff, M. Shi, T. Wu, A. Bylinskii, B. Braverman, M. Gutierrez, R. Nichols, J. Li,
        K. Aichholz, M. Cetina, L. Karpa, B. Jelenković, I. Chuang and V. Vuletić, "Preventing and
        reversing vacuum-induced optical losses in high-finesse tantalum (V) oxide mirror coatings",
        Optics Express 23.14 (2015) 18014 (cit. on pp. 135, 136).

[227]   C. Klempt, T. van Zoest, T. Henninger, O. Topic, E. Rasel, W. Ertmer and J. Arlt, "Ultraviolet
        light-induced atom desorption for large rubidium and potassium magneto-optical traps",
        Physical Review A 73.1 (2006) 013410 (cit. on p. 137).

[228]   Y. Zhao, Y. Wang, H. Gong, J. Shao and Z. Fan, "Annealing effects on structure and
        laser-induced damage threshold of Ta2O5/SiO2 dielectric mirrors",
        Applied Surface Science 210.3-4 (2003) 353 (cit. on p. 138).

[229] P. A. M. Dirac, "The Fundamental Equations of Quantum Mechanics",
Proceedings of the Royal Society A 109.752 (1925) 642 (cit. on p. 146).

[230] V. Fock, "Konfigurationsraum und zweite Quantelung",
Zeitschrift für Physik 76.11-12 (1932) 852 (cit. on p. 146).

[231] D. Meschede, *Optics, Light and Lasers: The Practical Approach to Modern Aspects of Photonics and Laser Physics*, 3rd Ed, Wiley-VCH Verlag, 2017 (cit. on p. 154).

[232] W. Jhe, A. Anderson, E. A. Hinds, D. Meschede, L. Moi and S. Haroche, "Suppression of spontaneous decay at optical frequencies: Test of vacuum-field anisotropy in confined space",
Physical Review Letters 58.7 (1987) 666 (cit. on p. 154).

Dielectric Coating of the Fiber Mirrors: Specifications and Degradation

A.1 High-Reflectivity Dielectric Coating

The laser-machined fiber end facets must be provided with a reflective coating in order to reach the high finesse values required for typical cavity QED experiments. Although metallic coatings are in general easier to produce, their reflectivity is usually below 95 %. A more suitable choice is that of dielectric coatings. By depositing several layers of alternating dielectric materials (each with a thickness of $\lambda/4$), the constructive interference between the multiple reflections from each interface results in reflectivities beyond 99.99 %. The precise deposition of dielectric material can be implemented via *ion-beam sputtering*, a widely used technique that has so far provided the macroscopic mirrors with lowest amount of losses [46] and that was also employed to obtain fiber-based cavities with finesse values above 10^5 [53, 59, 60] for the infrared domain.

For the coating procedure to succeed, the target surfaces must be kept clean and mounted perpendicular to the sputtering stream. A custom-made sample holder was developed in cooperation with *Laseroptik GmbH* to mount up to a hundred of our 1 m long fibers and several reference substrates. The mounting procedure was performed in a dust-free environment, where the fibers were included immediately after the ablation process. The coating consists of alternating deposits of Ta_2O_5 ($n = 2.10$) and SiO_2 ($n = 1.45$), with the particular number of layers depending on the desired transmission coefficient $\mathcal{T}$. As discussed in Section 2.1.2, the directionality of the cavity output can be increased by employing mirrors with different transmissivities. To that end we performed two coating runs, previously coined as HT and LT, designed to have transmissions of 120 ppm and 10 ppm respectively. The high reflectivity of the coating is maintained for a broad spectrum of frequencies of approximately $770 - 820$ nm that covers the two main spectroscopic (D_1 and D_2) lines of rubidium and the the 770 nm laser used to stabilize the cavity length (see Sec. 2.4.2). A summary of the coating properties can be found in Table A.1.

The coefficient $\mathcal{T}$ of the coated surfaces can be estimated by coupling light through the uncoated end of the fiber and directly measuring how much gets transmitted through the mirror. The simple setup consists of a diode laser at 780 nm coupled to a commercial FC/APC-connected optical fiber[1] which is then spliced[2] to the uncoated end of the sample fiber mirror (optical losses in the splicing region are typically below 0.15 dBm). The resulting values from the measurement realized for fibers from both coating runs yield the coefficients $\mathcal{T}_{HT} = (126 \pm 13)$ ppm and $\mathcal{T}_{LT} = (13 \pm 3)$ ppm (after the annealing

---

[1] Single Mode Patch Cable, 780 - 970 nm, FC/APC: *P3-780A-FC* (Thorlabs Inc).
[2] Fusion splicer for polarization maintaining fibers: *FSU 995 PM* (Ericcson Cables AB).

Table A.1: Main parameters of the two coating runs. The coated targets include a few flat (non-machined) fibers (18 and 9 for the two sets) and fused-silica reference substrates. The $Ta_2O_5-SiO_2$ layers have a thickness of $\lambda_{780}/4$ each (except for the ones immediately after the substrate), and the HT coating features an extra Ta_2O_5 surface layer. The specified values for transmission ($\mathcal{T}$) and losses ($\mathcal{L}=\mathcal{A}+\mathcal{S}$) were provided by *Laseroptik GmbH* (only for 780 nm). Experimental transmission coefficients measured after annealing procedure (see text). Losses extrapolated from finesse measurements of Sec. 2.3, with this technique absorption and scattering losses are indistinguishable.

	Fibers SM/MM	Layers $(Ta_2O_5+SiO_2)$	Wavelength (nm)	Transmission $\mathcal{T}$ spec./meas. (ppm)	Losses $\mathcal{L}$ spec./meas. (ppm)
HT	53/27	16	780 nm	$(120 \pm 20)/(126 \pm 13)$	$20/(26 \pm 5)$
			850 nm	————/(490 ± 30)	
LT	95/9	17	780 nm	$(10 \pm 2)/(13 \pm 3)$	$16/(25 \pm 5)$
			850 nm	————/(140 ± 20)	

procedure introduced later).

Impurities and irregularities on the coated surface give rise to undesired absorption ($\mathcal{A}$) and scattering losses ($\mathcal{S}$). The absorption probability depends on the coating characteristics, in particular the material of the last dielectric layer, since it is proportional to the penetration depth of the reflected light field. Although it is challenging to precisely measure the absorption coefficient, a study of the thermal properties of our fiber mirrors yields an estimation of $\mathcal{A}\sim 10$ ppm [1]. The detrimental scattering processes are directly related to the surface roughness[3] of the coating, which in turn depends on the underlying fiber surface [224] and on the quality of the coating procedure. For laser-machined fiber surfaces, it has been observed that the surface roughness can increase after the coating is performed [53]. This has been nevertheless attributed to the quality of the coating procedure itself and — as reported in references [53, 60] — coated fiber mirrors provide same losses as superpolished mirrors (roughness < 1 Å) coated under the same conditions. Measurements on the scattering properties of our fiber mirrors are not available, however the finesse measurements discussed in Section 2.3 yield information about the total losses $\mathcal{L}$ (as shown in Tab. A.1). These estimations suggest values of $\mathcal{S}\sim 15$ ppm, which correspond to the expected surface roughness.

A standard procedure employed to improve the quality of mirrors with dielectric coatings is to thermally cure them. This technique, known as *annealing*, leads to an homogenization of the oxide layers that causes a reduction in absorption losses [225]. The method has been successfully transferred to fiber-based mirrors, although some issues have been reported regarding the surrounding copper coating (see [60]). We typically perform a 300 °C curing of our mirrors for 3 to 5 h, by placing the first millimeters of the fiber tip (with no copper coating) in a temperature stabilized metal heat-bath. The improvement of the coating manifests as an increase on the mirror's transmission coefficient, which for the HT coating run typically rises from ~70 ppm to the nominal value of 126 ppm.

A.2 Finesse Decay and Partial Recovery

The optical quality of the dielectric coating of our mirrors is one of the critical elements providing the high cooperativity required in our system. In addition, a rise in reflection losses that is not cause by a

---

[3] Scattering losses for a given RMS roughness σ are given by $S=(4\pi\sigma/\lambda)^2$ (see e.g. [53]).

transmission increase will lead to a general loss of information (cavity leakage), which becomes relevant when rapid atomic state detection or efficient photon storage is necessary. It is thus important to monitor any decay or unexpected behavior of the finesse of our cavity, and to try to gain insight about the physical mechanisms underneath those processes. In general we observe a decay of the finesse of our FFPC after being placed under high-vacuum conditions ($\sim 10^{-9}$ mbar). The type of decay and the time scales involved can be strongly influenced by the presence of ultraviolet (UV) light shone onto the mirrors; in particular we observe that UV radiation can turn a rapid exponential decay of the finesse into a slower decline with a time constant increased by orders of magnitude.

Decay in Vacuum

Degradation of the optical coating of high-reflectivity cavity mirrors under vacuum conditions has been observed for both macroscopic resonators [226] and FFPCs [60, 197]. In the literature it is usually attributed to the depletion of oxygen of the surface coating layer which creates inhomogeneities and brakes the stoichometry of the oxide (with Ta_2O_5 being much more sensitive than SiO_2), thus increasing the absorption losses. In a standard air environment, oxygen atoms can also be absorbed from the surroundings, making the loss/recovery process symmetric. This is not the case under vacuum conditions, where the depleted oxygen is quickly diffused and cannot be reabsorbed. It has been shown that the increase in losses is reversible and can be fully or partially recovered by exposing the coating to air (or preferably oxygen atmosphere) [60], and that the process can be catalyzed either by increasing the substrate temperature[4] or illuminating it with ultraviolet light [226]. However, the time scales and type of decay observed in our system do not correspond to the ones expected for this type of process, as we will see in the following.

The fiber cavity that we employed in the experiments — which had an initial finesse of 32 800 — was placed under vacuum conditions where two bake-out processes took place in order to ensure the cleanliness of the system (in both cases at 100 °C during two days, see Sec. 3.1.1). After the thermal curing, the system was maintained at the laboratory temperature of 21 °C (except for any heating of the mirrors induced by the strongly focussed dipole trap beams). No recording of the finesse was performed during that period, since the cavity properties did not show evident variations after the bake-out. However, after two months, the losses of the mirrors began to increase leading to a sudden and rapid decay of the finesse reaching slopes of more than 1 % reduction per hour. By exposing the vacuum chamber to pure oxygen atmosphere[5] the finesse immediately recovered (within seconds), rising from less than 10 % to almost 80 % of its original value. By illuminating the cavity — still in the presence of oxygen — with UV light (see last section for technical details), the finesse increased further by around 5 % in two days. It is worth noticing that Non-Evaporable Getter (NEG) pumps — when activated and after having been exposed to constant presence of alkali materials — become highly reactive to pure oxygen atmospheres, possibly due to the incomplete passivation of the alkali atoms (rubidium in our case). Due to the large surface area that characterizes these pumps, the exothermal oxidation processes quickly undergo a "chain reaction" that, in our case, lead to temperatures above the fusion of the porous material (ZrVFe) and therefore the immediate destruction of the pump[6]. The spread of microscopic fragments of the getter material in the vacuum system did not affect the cavity mirrors, the finesse of which was immediately recovered in the presence of oxygen.

In order to study the decay and recovery processes in more detail we implemented a finesse monitoring scheme (see last section) that allows us to continuously measure the finesse of the cavity at the frequency

---

[4] Equivalently, an increase in temperature under vacuum conditions leads to faster degradations (see references in main text).

[5] O_2 purity 99.9995 %: *ALPHAGAZ 2 OXYGEN* (Air Liquide).

[6] The recommended procedure consists on a previous passivation of the system by flushing the vacuum apparatus with argon.
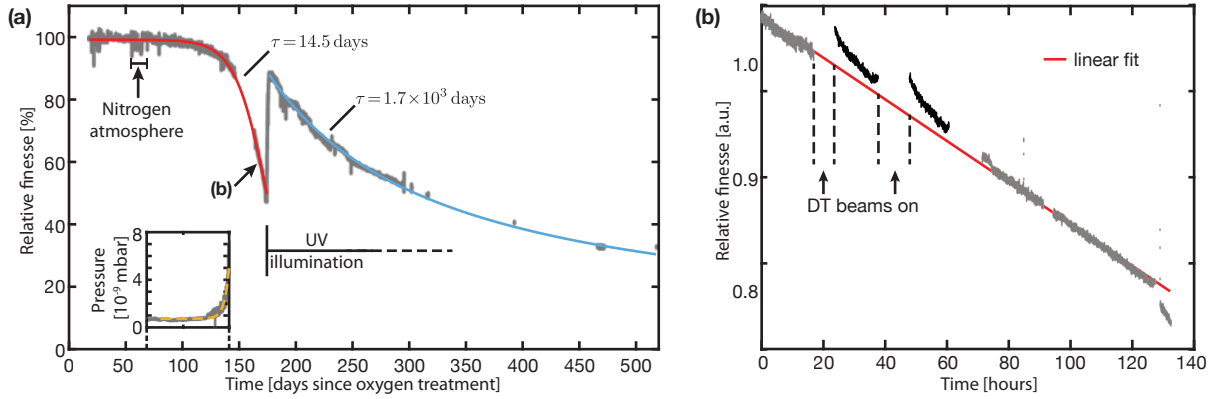
Figure A.1: Decay of the finesse under vacuum after the first oxygen treatment. **(a)** Monitored finesse at 770 nm represented as a percentage of the initial value. The initial decay is fitted to the model of Eq. (A.1) (red curve) yielding a time constant of 14.5 days. The vacuum was flushed with nitrogen once during this period, which did not affect the finesse evolution. The pressure (inset) showed a similar exponential rise (orange, dashed line) correlated with the finesse decay (reasons still unknown). With constant UV illumination the finesse was quickly recovered (sudden positive slope) and the decay process slowed down, following the curve predicted by the oxygen depletion model of Eq. (A.2) (blue) with a time constant of ~ 1670 days. The sporadic spikes are due to artifacts of the monitoring program. **(b)** Closeup of the fast decay of the finesse (marked in (a)). The monitoring periods are performed during the night, where the slope of the decay seems to be affected by the use of the dipole trap. The finesse decays $\sim 33\%$ faster when the cavity has been heat up by the dipole trap beams during the previous hours (black data). However it seems that the initial value of the finesse at the end of each day is higher when the beams are on, leading to a total effective slope (red line) that remains the same (at least at this time scales).

of the lock light (770 nm) given that no experimental sequence is taking place. Figure A.1(a) shows the recordings — under vacuum, after the recovery — expressed in percentage of the finesse value right after the oxygen and UV treatment (which is $\sim 80\%$ of the original). The behavior of the first decay (in red) resembles the one previously described, characterized by a constant plateau with no visible changes and a sudden decay of the finesse in a few days time scale. In particular, the finesse follows a curve of the type

$$\mathcal{F}(t) = \frac{2\pi}{\mathcal{L}(t)} = \frac{2\pi}{\mathcal{L}_0 + \Delta\mathcal{L} \cdot \exp\,(t/\tau)} \tag{A.1}$$

which yields a decay time of ~ 14.5 days. This type of exponential rise in the losses is in contrast to the one expected due to oxygen depletion which — according to the Arrhenius-type model suggested and experimentally corroborated in reference [226] — should be a saturating curve of the form

$$\mathcal{L}(t) = \mathcal{L}_0 + \Delta\mathcal{L}\,(1 - \exp\,(-t/\tau))\,. \tag{A.2}$$

The clear discrepancies in the type of decay and its time scale (which are typically hundreds of days for depletion at room temperature) — along with the almost instantaneous recovery — suggest that oxygen defects are not the only degradation mechanism contributing to the increase in absorption losses of the mirrors. This is further suggested by the fact that no bake-out took place when creating the vacuum environment after the oxygen treatment. Additionally, although we observe heating of the cavity due the dipole trap beams[7], there is no apparent effect on the general slope of the fast finesse decay (as shown in Fig. A.1(b)).

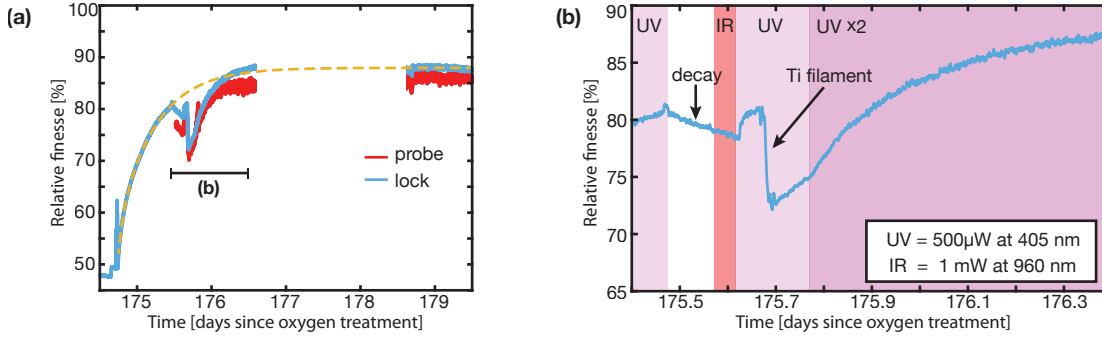[7] The cavity resonance shifts by a few GHz when the trap beams are on.

Figure A.2: UV-mediated finesse recovery under vacuum. **(a)** Cavity finesse for 770 nm (blue) and 780 nm (red) during the first hours with UV illumination, both normalized to their respective value after the oxygen treatment. The recovery rates and relative values are similar, the probe finesse seems more sensitive to the decay mechanisms (lower relative values), which is reasonable taking into account the smaller initial losses at 780 nm. The general trend follows a saturated rising that is fit (orange) to a double exponential of the form $\mathcal{F}_0 + \Delta\mathcal{F}\,[1 - \exp(-(t - t_1)/\tau_1)] \cdot [1 - \exp(-(t - t_2)/\tau_2)]$. The small features correspond to different tests performed during the recovery process to gain insight. A close up with more details is shown in **(b)** (the powers stated in the inset where measured before coupling into the LT fiber).

Although the evidence points at additional loss processes being involved, it remains unclear what are the mechanisms underneath. A candidate would be the constant deposition of certain absorbent impurities that increase the losses and that are reactive to oxygen. This assumption would be in agreement with the fact that the finesse exponential drop happened at the same time as a similar increase in pressure (see inset of Fig. A.1(a)), which might imply deposits due to outgassing of components close by, like the glues used in the cavity assembly (see Sec. 2.4.1).

Partial Recovery and Slower Decay under UV Illumination

This (second) fast exponential decay of the cavity finesse under vacuum was recovered within a few hours by constant illumination of the mirrors with UV light ($<1\,\mathrm{kW\,cm^{-2}}$). As shown in Figure A.1(a), the finesse could be recovered in a few hours back to 90 % (of the value preceding the fast drop). Additionally, by keeping the illumination on, the degradation process slowed down showing a decay that follows the oxygen depletion model, both qualitatively and quantitatively in terms of time scales (in this case the decay is of 1.6×10^3 days). The clear influence of UV radiation suggests a partial or even total prevention of the yet unknown mechanism leading to fast degradation of the finesse. The remaining increase in losses is attributed to vacuum-induced oxygen depletion which cannot be recovered unless in the presence of high contents of oxygen.

A possible cause for the effects of the illumination is that UV radiation reduces the detrimental deposition of impurities on the mirrors by catalyzing desorption mechanisms. A detailed evolution of the recovery process can be seen in Figure A.2(a) where the finesse shows a saturated rise which can be described by a double exponential curve with time constants of 0.62 h and 9.93 h. The process is too slow to be a consequence of Light-Induced Atomic Desorption (LIAD) effects, that usually occur in the millisecond regime [227], suggesting that slower mechanisms like diffusion might be involved.

The amount of UV light slightly affects the slope (and therefore the duration) of the recovery process, but no apparent effect was observed in the final saturation value of the finesse. To discard that the process is caused by temperature changes, we illuminated the mirrors with similar powers of laser light at 960 nm, which resulted in no clear influence (see details in Fig. A.2(b)). In fact, in the absence of UV,

the finesse starts decreasing with a similar slope, suggesting that the UV illumination should be kept to prevent additional losses. It is worth noticing that the temporal usage of the Titanium sublimation pump lead to an immediate decrease of the finesse even in the presence of the UV illumination. The only explanation so far is attributed to heating on the copper fibers (which are placed close to the filament) that leads to a temperature rise at the fiber-mirrors tips. The higher temperatures might change the characteristics of the coating and produce misalignments of the fibers (additional clipping losses). This temporal increase in losses is not attributed to oxygen depletion, as it was recovered after the filament cooled down. Due to technical reasons (see next section), the finesse of the probe cannot be monitored at all times. Nevertheless, we realized a parallel measurement of the (relevant) probe finesse to ensure that the recovery process was equivalently effective (as shown in Fig. A.2(a)).

Finesse Monitoring and UV illumination

The finesse of the FFPC inside the vacuum apparatus is monitored by scanning the cavity length through a full FSR with a repetition rate of 20 Hz while recording the reflection dip of the lock light with a digital oscilloscope every few seconds. The lock beam is sideband-modulated at 250 MHz (see Section 2.4.2), which can be used as a reference to extract the linewidth (and therefore the finesse) for both probe and lock light, given that the resonator's length is known. In order to keep the cavity resonance within the scanning range (and within the oscilloscope window), a simple digital feedback loop was developed to maintain the position of the resonance by shifting the offset voltage of the scanning shear piezos, thus allowing continuous recordings for long periods of time. This monitoring is not possible during the realization of measurements in the experimental setup, which require the cavity length to be locked. Furthermore, most of the finesse recordings are done employing only the lock light, while probe finesse measurements are performed sporadically to characterize any quantitative differences between both[8]. In general we assume that the characteristic time of the variations in the coating losses will be similar in both cases (probe and lock finesse), although the final saturation values or the amplitude of the changes might differ due to the distinct wavelengths.

The light source for the UV illumination of the fiber mirrors is a high-power diode laser at 405 nm. A small fraction of the output (500 μW to 1 mW) is coupled into a UV single-mode fiber[9] which, at its other end, is connected to the LT fiber of the FFPC through a mating connection[10]. Since our copper coated fibers have a cutoff wavelength much higher than UV, we expect a considerable power loss and a combination of transversal modes before the light reaches the cavity. Assuming no losses and no mode distortion, we obtain an upper boundary for the power dose[11] on the fiber mirrors of ~1 kW cm^{-2}. A fraction of the UV light is coupled onto the opposed HT mirror and is guided to the lock-chain optical setup, where it is suppressed by the laser-line filters. However, we observe that the illumination creates — along its propagation through both fibers — broadband fluorescence containing 780 nm light. The desired constant UV illumination must then be temporarily interrupted whenever a sensitive measurement is performed (especially when atoms are coupled to the resonator). In general we keep the UV light on during MOT loading and atom transport periods, which can be extended to ensure that the illumination is present at least half of the time during an experiment cycle.

---

[8] The reflection of the probe light is monitored by an SPCM (as opposed to the lock which is measured by an amplified photodiode) due to the small amount of power required in the experiments (see e.g. Chapter 4.2). Any finesse measurement requires changes in the optical components of our locking scheme, and therefore cannot be perform often.

[9] 405 - 532 nm FC/APC Single Mode Patch Cables: *P3-405B-FC-1* (Thorlabs Inc).

[10] FC/APC to FC/APC Narrow-Key-Slot Mating Sleeves: *ADAFC3* (Thorlabs Inc).

[11] Much smaller than typical damage thresholds for UV light on this type of dielectric stack [228].

Mode Matching in Fiber-based Cavities

This appendix contains the analytical evaluation of the mode overlap coefficients α and β, introduced in Sec. 2.3.2, that allows us to study the properties of the reflective line shape in FFPCs and its influence on the optimal fiber-cavity alignment providing the best mode matching. The derivations shown here consist on the definition of the Gaussian modes involved in the problem and the calculation of their overlap integral at a particular projection plane; a sketch containing all the relevant geometrical and optical factors can be found in Figure B.1(a).

In general, for the calculation of the mode-matching efficiency $\epsilon = |\langle \psi_f^+ | \psi_{cav} \rangle|^2$, the choice of the integration plane is arbitrary [76] as the power overlap between both modes does not vary at different positions of the propagation z-axis. However, the phase of the associated complex amplitude α does depend on the z-position, and equivalently for β. Since the interference effects under investigation depend on the addition of both complex amplitudes (see Eq. (2.20)), it is critical to evaluate both integrals at the same plane. Although a different plane can be chosen for each geometric configuration and alignment angle of the fiber-cavity system, it is more convenient to perform all calculations for a particular z-plane. This allows us to examine the reflective properties of an FFPC for different angles of the cavity mode with a single analytical expression. For that reason we decide to use as a projection plane the z point located at the bottom of the mirror structure (see Fig. B.1); as we will see, this means that we need to propagate the cavity mode into the fiber.

The overlap integrals of interest, defined in Equations (2.14), are all of the form $\langle \psi_f^\pm | \phi \rangle$ (or its complex conjugated). Here $|\psi_f^\pm\rangle$ is the fiber-core mode and $|\phi\rangle$ represents either the intracavity or the reflected modes at the $(x, y, 0)$ plane. Since all of them are considered as fundamental (Gaussian) modes, their overlap integral over the (x, y)-plane can be expressed as the product of two independent 1D overlap integrals, such that:

$$
\begin{aligned}
\langle \psi_f | \phi \rangle &= \int_{-\infty}^{+\infty} \int_{-\infty}^{+\infty} \psi_f^*(x, y)\, \phi(x, y)\, dx\, dy \\
&= \int_{-\infty}^{+\infty} \psi_{f,x}^*(x)\, \phi_x(x)\, dx \int_{-\infty}^{+\infty} \psi_{f,y}^*(y)\, \phi_y(y)\, dy \ .
\end{aligned}
$$

The one-dimensional distribution of the fiber-core mode at the surface of the fiber is given by

$$
|\psi_{f,x}^\pm(x)\rangle = \left(\frac{2}{\pi w_f^2} \right)^{1/4} e^{-\frac{x^2}{w_f^2}} \ ,
$$

where w_f is the MFD/2 of our SM fibers and we have used our freedom of choice of the phase of the fiber
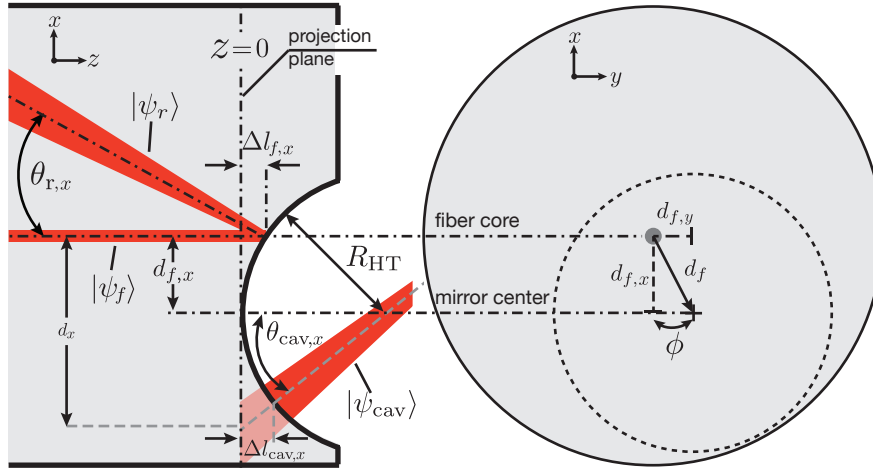
Figure B.1: Geometrical and optical considerations for the calculations of the overlap integrals. Black dotted lines represent fixed geometrical axes or planes, gray dashed lines represent axes that depend on the cavity-mode angle $\theta_{\text{cav},x}$. Displacements and angles have been exaggerated for a better clarity of the sketch.

mode such that $\psi_f^{\pm} = \psi_f \in \mathbb{R}$. The fiber-core position in the (x, y)-plane is used to the define the origin of both axes. The reflected- and cavity-modes, on the other hand, can in general be described by a Gaussian with a certain wavefront curvature R and beam radius w (for a particular z-point) and, if necessary, a displacement $d = (d_x, d_y)$ and tilt $\theta = (\theta_x, \theta_y)$, such that[1]

$$|\phi_x(k, w, R, d, \theta)\rangle = \left(\frac{2}{\pi w^2}\right)^{1/4} \exp\left[-\frac{(x-d)^2}{w^2} - ik\left(\frac{(x-d)^2}{2R} - (x-d)\theta\right)\right],$$

where k stands for the light's wave vector in the medium where the integration takes place (k_0 for vacuum or $k_f = 1.45 k_0$ for the $textSiO_2$ coating layer of the fiber).

The overlap between both (in the x-axis) is then given by

$$\langle\psi_{f,x}|\phi_x\rangle = 2\left(w_f w\left(\frac{ik}{R} + 2\left(\frac{1}{w_f^2} + \frac{1}{w^2}\right)\right)\right)^{-1/2} \exp\left(-\frac{k^2 R\, w_f^2 w^2 \theta^2 + d^2(4R + 2ikw^2) - 4ik R\, w^2\, d\theta}{4R(w_f^2 + w^2) + 2ik\, w_f^2 w^2}\right).$$
(B.1)

By considering the overlap in both x, y-directions, and calculating its absolute value squared one obtains the mode-matching efficiency between the fiber-core mode and a tilted decentered intracavity mode

$$\epsilon = \epsilon_0\, e^{-2d^2/d_e^2}\, e^{-2\theta^2/\theta_e^2}.$$
(B.2)

Here ϵ_0 is the mode-matching efficiency for a perfectly centered and aligned cavity [27, 76]

$$\epsilon_0 = \frac{4}{\left(\frac{w_f^2}{w^2} + \frac{w^2}{w_f^2}\right)^2 + \left(\frac{k\, w_f\, w}{2R}\right)^2},$$

where the first term in the denominator represents the waist overlap between modes and the second

---

[1] Note that the wavevector here contains the information about the propagation medium. If the integral is performed inside the fiber, the corresponding index of refraction must be included.
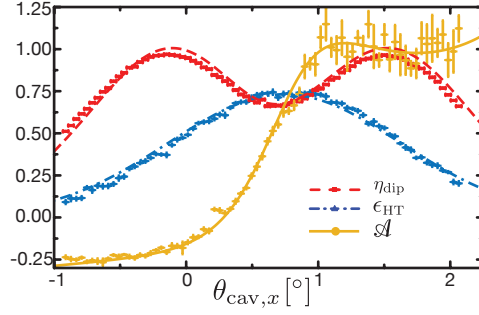
Figure B.2: Fit between experimental data and analytical model from Section 2.3.2 (see text there and compare to Figure 2.17). The decentration of the mirror has been added as a free parameter to show a much better agreement (see Supplemental Material in [1] for more details).

stands for the miss-match originated by the different wavefront curvatures (which would be zero for a flat mirror). The two extra terms of Equation (B.2) contain the matching losses due to decentration and tilt described by the effective length d_e and angle θ_e which depend on the geometry of the system (see [76] or Supplemental Material in [1]).

As discussed, the cavity and reflected modes must be "propagated" towards the integration plane. We define the characteristics of their wavefront and spot size at the position of the fiber surface (which is typically at $z > 0$) and then calculate the phase shift of the extra optical path required to reach $z = 0$[2]. The cavity mode, at the mirror, presents a wavefront curvature which is given by the mirror's ROC ($R_{cav} = -R_{HT}$) and waist w_m which depends on the ROC of both the mirrors and the cavity length (see Equation (2.6)). For different cavity-mode angles θ_{cav}, the separation between cavity and fiber-core modes will be a combination between the original core-mirror decentration d_f and the angular displacement of the intracavity field such that $d = R_{HT} \sin(\theta_{cav}) - d_f$. Additionally, a certain phase is accumulated inside the fiber before reaching $z = 0$ due to the extra path (shown in Figure B.1), which is given by[3] $\Delta l_{cav} = R_{HT} \theta_{cav}^2 / 2$. The final expression for the (one-dimensional) cavity mode at the plane of interest is then:

$$|\psi_{cav,x}\rangle = \left|\phi_x \left(k_f, w_m, -R_{HT}, R_{HT} \sin(\theta_{cav,x}) - d_{f,x}, \theta_{cav,x}\right)\right\rangle \exp\left(-ik_f \frac{R_{HT} \theta_{cav,x}^3}{2}\right). \qquad (B.3)$$

Same considerations apply to the reflected mode, which features the same waist a the input fiber-mode (w_f) and that, upon reflection on the curved fiber surface, acquires a wavefront curvature with radius $R_r = -R_{HT}/2$ along the new direction tilted by $\theta_r = -2d_f / R_{HT}$. Considering the propagation to $z = 0$, which is given by $\Delta l_f = d_f^2 / 2R_{HT}$, the final reflected mode is:

$$|\psi_{r,x}\rangle = \left|\phi_x \left(k_f, w_f, -R_{HT}/2, 0, -2d_{f,x}/R_{HT}\right)\right\rangle \exp\left(-ik_f \frac{d_{f,x}^2}{2R_{HT}}\right). \qquad (B.4)$$

Both expressions (B.3) and (B.4) provide the corresponding complex amplitudes α and β (respectively) when used in Equation (B.1). The formalism provides analytical expressions for the reflective line shape under arbitrary geometries and alignment conditions, yielding the model used in Section 2.3.2 to fit our experimental data. As an example of the agreement between both, in Figure B.2 we show the results of

---

[2] Since the surface depression is typically less than 2 μm, we do not consider changes in the spot size w, the wavefront radius of curvature R or the decentration d when propagating from the surface to $z = 0$.

[3] The calculation of both lengths Δl_{cav} and Δl_f are calculated up to second order of all transverse angles and coordinates.

such experimental results being fitted to the model when the decentration is added as an additional free parameter.

Optical Transport of Neutral Atoms

This appendix contains a brief description of the electronic components employed in our system to steer the frequency of our red-detuned dipole traps.

Fine Tuning of Optical Frequencies

The necessary control over the frequency of the dipole trap beams is achieved through the AOMs that also steer the trapping power (see Section 3.1.2). We use the first refractive order of each AOM in single-pass configuration, resulting in a change $\Delta\nu$ of the RF driving frequency and, equivalently, a shift of the optical frequency of the beam. Therefore, to achieve sub-micrometer precision during the transport, the differential driving frequency between both AOMs must be controlled well below 1 Hz. In addition, their relative phase is directly mapped onto the spatial phase of the dipole trap: sudden changes or jittering in that phase will shake the lattice and can lead to heating or even the loss of the atom [117].

To minimize the phase noise and to meet the precision requirements we use a Dual Digital Frequency Synthesizer (DDFS) to drive both AOMs at their central frequency of $\nu_0 = 80$ MHz. This evaluation board contains two Direct Digital Synthesizers[1] chips (DDS) synchronized to a common reference clock (400 MHz). Each of the DDS chips features an RF output channel with a frequency range from DC up to 160 MHz with a resolution of 0.09 Hz. The relative frequency between both channels can be changed in a phase-coherent way, and arbitrary frequency ramps can be programmed. A detailed analysis about the relative phase noise between both outputs of the DDFS board can be found in reference [176]. For our trapping parameters, the heating rates extracted from the measured DDFS phase-noise would restrict the trapping times to about ~20 s, which is about four times larger than the limit due to background gas collisions (see Sec. 3.2.1). As a result, this phase-noise induced heating can be safely neglected.

Flexible Transport Configurations

In a typical transfer sequence, two linear ramps are pre-loaded in the memory on the DDFS board: a raising ramp that sweeps the output frequency from ν_0 to $\nu_0 + \Delta\nu$ and a lowering ramp that brings the frequency back to the original. When the board receives the triggering signal, the raising ramp is activated and the transport starts. After a short acceleration time the ramp finishes and the output frequency remains shifted. The constant velocity period usually continues for hundreds of milliseconds until a stop signal is received. This triggers the lowering ramp that brings the transport to a halt within a few microseconds (less than a nanometer stopping distance). A sketch of the process can be seen in Figure C.1(a).

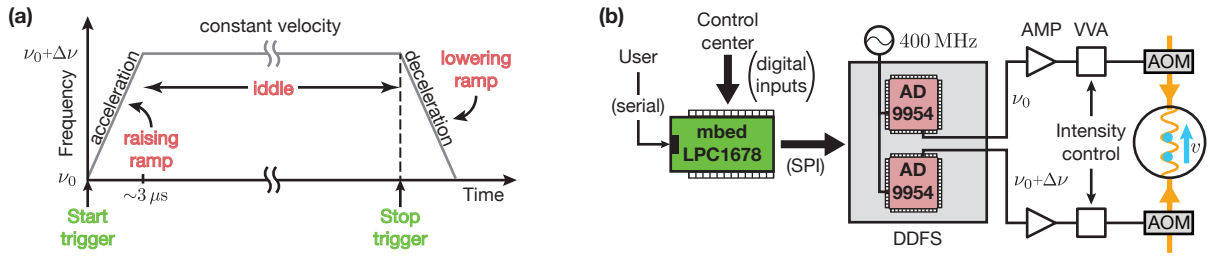[1] DDS: *AD9954* (Analog Devices Inc).

Figure C.1: Transport scheme. **(a)** Frequency output of one of the channels in a typical transport sequence. The mbed sends the start/stop signals (green) that trigger the output of the respective frequency ramps (red). **(b)** Simplified layout of the conveyor belt electronics. The control center communicates with the DDFS via the mbed microcontroller. The RF outputs are amplified and their power is controlled by the intensity stabilization system. In general it is more convenient to shift the frequency of only one of the beams.

The communication with the board is mediated by an *mbed* microcontroller[2] that reacts to the external start/stop signals with sub-microsecond precision. It also contains several types of transport (distance, time, acceleration...) that can be loaded onto the DDFS within a few tens of milliseconds. The user can access and modify the transport properties through serial communication. A set of digital inputs in the mbed allow the control center to select the type and direction of the transport and to trigger the start/stop commands (see Fig. C.1(b)). In this way, the transport sequence is synchronized with the rest of the experimental cycle. This allows real-time feedback that can stop the transport whenever the demanded target is achieved. As we show in Section 3.2.2, we can use the cavity reflection to detect wether an atom has arrived to the cavity-mode region. This signal can trigger the command for the conveyor belt to stop before the atom continues moving out of the region of interest. An identical setup is implemented for the other dipole trap DT_x.

---

[2] Microcontroller development board: *mbed NXP LPC1768* (ARM Ltd).

Theoretical Considerations in Cavity QED

D.1 The Quantization of Light

The most elementary solution of Maxwell's equations (when no source is present) is given by a mode of the electromagnetic field defined by its wave vector $\mathbf{k}$ and the perpendicular unitary vector $\boldsymbol{\epsilon}$. In the case of a traveling wave[1] of linearly polarized monochromatic light (of frequency ω), the electromagnetic field is given by:

$$
\begin{aligned}
\mathbf{E}(\mathbf{r}, t) &= \boldsymbol{\epsilon} \left(\mathcal{E}(t)\, e^{i\mathbf{k}\cdot\mathbf{r}} + \mathcal{E}^*(t)\, e^{-i\mathbf{k}\cdot\mathbf{r}} \right) \\
\mathbf{B}(\mathbf{r}, t) &= \frac{\mathbf{k}\times\boldsymbol{\epsilon}}{\omega} \left(\mathcal{E}(t)\, e^{i\mathbf{k}\cdot\mathbf{r}} + \mathcal{E}^*(t)\, e^{-i\mathbf{k}\cdot\mathbf{r}} \right),
\end{aligned}
\tag{D.1}
$$

where $\mathcal{E}(t) = \mathcal{E}(0)\, e^{-i\omega t}$ is the complex amplitude of the field that includes the time varying component. The energy $\mathcal{H}$ of the mode is then given by the amplitudes of both electric and magnetic fields, such that

$$
\mathcal{H} = \frac{\varepsilon_0}{2} \int_V d^3 r \left(\mathbf{E}^2 + c^2 \mathbf{B}^2 \right) = 2\varepsilon_0 V |\mathcal{E}(t)|^2 ,
$$

where V represents a fictitious volume over which we perform the integration. In the case of traveling waves it can be considered as a cube with a length such that $L = 2\pi n_i / k_i$ in the three directions $i = (x, y, z)$. Nevertheless in the case of a cavity, V represents the actual mode volume of the standing wave inside the resonator (see Eq. (2.7)).

We define the *normal mode amplitude* $\alpha(t)$ of the field such that

$$
\mathcal{E}(t) = i\mathcal{E}_0 \alpha(t).
\tag{D.2}
$$

Here $\mathcal{E}_0$ is an arbitrary constant with no concrete assigned value yet. The quadratures corresponding to the field with such amplitude are proportional to its real and imaginary parts such that

$$
\begin{aligned}
Q(t) &= \sqrt{\frac{\hbar}{2}} \left[\alpha(t) + \alpha^*(t) \right] \\
\mathcal{P}(t) &= -i \sqrt{\frac{\hbar}{2}} \left[\alpha(t) - \alpha^*(t) \right].
\end{aligned}
$$

---

[1] The derivations shown in the following consider traveling waves, nevertheless the results apply equivalently to the standing wave present inside a cavity.

The choice of the pre-factor $\sqrt{\hbar/2}$ in the definition above is not arbitrary, as it ensures the right commutation relations when quantizing the system. It is straightforward that the energy of the system can be re-expressed in a more compact and convenient way as

$$\mathcal{H} = 2\varepsilon_0 V \frac{\mathscr{E}_0^2}{2\hbar}(Q^2 + \mathcal{P}^2)\,.$$

We can now use our freedom of choice for the constant $\mathscr{E}_0$ such that the hamiltonian resembles that of a mechanical oscillator with the dimensionless quadratures Q and $\mathcal{P}$ as position and momentum variables:

$$\mathscr{E}_0 = \sqrt{\frac{\hbar\omega}{2\varepsilon_0 V}} \implies \mathcal{H} = \frac{\omega}{2}(Q^2 + \mathcal{P}^2)\,. \tag{D.3}$$

Notice that the value of $\mathscr{E}_0$ actually corresponds to the intensity of a field with a single photon of energy $\hbar\omega$ spread over a volume V. This shows that the choice of pre-factor is not arbitrary but necessary to make the model consistent with the already known quantum properties of radiation.

It can be shown that the Hamiltonian equations of motion yield the very same dynamics for the field that Maxwells equations provide, proving that indeed the quadratures of the system form a pair of canonically conjugated variables. It is this fact that allows us to perform the so-called *canonical quantization*, where each variable is associated with its corresponding operator. In this case

$$\left.\begin{array}{c} Q \to \hat{Q} \\ \mathcal{P} \to \hat{P} \end{array}\right\} \implies \hat{H} = \frac{\omega}{2}(\hat{Q}^2 + \hat{P}^2) \text{ with } [\hat{Q}, \hat{P}] = i\hbar$$

from which the dynamics of the quantized electromagnetic mode derive. The temporal dependency of the classical quadratures can be included either in the new operators or in the state defining the system, depending on which picture of quantum mechanics we decide to use. It is more convenient though, to express such Hamiltonian in terms of the new operator $\alpha \to \hat{a} = (\hat{Q} + i\hat{P})/2\hbar$ such that

$$\hat{H} = \hbar\omega_c\left(\hat{a}^\dagger\hat{a} + \frac{1}{2}\right) \text{ with } [\hat{a}, \hat{a}^\dagger] = 1\,. \tag{D.4}$$

These two equations, the formalism of which was first introduced by Dirac [229], define the structure of the electromagnetic mode and the starting point of quantum optics.

From here one can find the eigenstates of the system $|n\rangle$ usually referred as *Fock states* [230] or *number states* (since their eigenvalues are the natural numbers). They fulfill the following conditions

$$\hat{H}|n\rangle = n|n\rangle$$
$$\hat{a}|n\rangle = \sqrt{n}|n-1\rangle$$
$$\hat{a}^\dagger|n\rangle = \sqrt{n+1}|n+1\rangle\,,$$

where $|n\rangle$ corresponds to the state of the radiation mode that contains n photons. The effect of the operator $\hat{a}$ ($\hat{a}^\dagger$) is that of retrieving (adding) a single photon from the mode; for that reason they are respectively referred as annihilation and creation operators.

Of particular interest is the ground state of the radiation field $|0\rangle$ corresponding to zero photons in the mode (also called *vacuum state*). By definition one cannot retrieve a photon from this state ($a|0\rangle = 0$),

and any other number state can be expressed in terms of the vacuum:

$$|n\rangle = \frac{(a^\dagger)^n}{\sqrt{n!}}|0\rangle .$$

To extract the properties of this particular state, one can calculate the mean value and variance of the main observable of the system: the electric field amplitude. By inserting the operator version of the relation (D.2) in Equation (D.1) one gets

$$\hat{\mathbf{E}} = \boldsymbol{\epsilon}\,\mathscr{E}_0\left(e^{i(\mathbf{k}\cdot\mathbf{r}-\omega t)}\hat{a} + e^{-i(\mathbf{k}\cdot\mathbf{r}-\omega t)}\hat{a}^\dagger\right). \qquad (D.5)$$

The mean value of this operator in vacuum turns out to be null as one would expect, nevertheless the variance $(\Delta E)^2$ is non-zero and given by $\mathscr{E}_0^2$. This is known as *vacuum fluctuations* and it is one of the most fundamental and striking results of quantum optics, since it implies that even in the absence of photons, the electric filed amplitude still takes non-zero values that vary with time. The variance of the field can be related to that of $\hat{Q}$ and $\hat{P}$ which are canonically conjugated variables. Therefore vacuum fluctuations can be seen as a direct consequence of the limits set by Heisenberg's uncertainty principle applied to the field quadratures. This property is responsible for several effects unaccounted for in semi-classical theories, amongst them the more relevant for us is *spontaneous emission*: It is the coupling of the atom with the fluctuating radiation vacuum that makes it possible for the atom to decay from an *excited state* in the absence of any external field, even though such *excited state* is an eigenvector of the atomic Hamiltonian.

The formalism developed so far is for a single mode of radiation, for a more realistic description one must take into account the various modes usually present in the radiation field of interest. It can be shown that different modes l (with different frequency, polarization or propagation direction) are orthogonal and do not interact; this leads to the absence of cross terms in the total Hamiltonian, such that $\hat{H} = \sum_l \hat{H}_l$. If we now take into account the infinity modes of radiation available, the $1/2$ term of Equation (D.4) diverges to infinity, and so do the fluctuations of the vacuum electric field! This divergence though can be fixed through renormalization theory, which provides finite and precise predictions for observable effects like the Lamb shift.

It is worth mentioning yet another particular radiation state: the eigenstates of the annihilation operator, also known as the *coherent states*. These are defined by $\hat{a}|\beta\rangle = \beta|\beta\rangle$ and can be expressed in the Fock basis as

$$|\beta\rangle = e^{-|\beta|^2/2} \sum_{n=0}^{\infty} \frac{\beta^n}{\sqrt{n!}}|n\rangle.$$

Their phase is well defined, but not the number of photons since they are not eigenstates of the Hamiltonian (except for the vacuum state, which happens to be both a Fock and a coherent state). One can find that the probability of finding a certain number of photons is given by a Poissonian distribution and that the expected value of the electric field of such a state is

$$\langle\beta|\hat{\mathbf{E}}(\mathbf{r},t)|\beta\rangle = \boldsymbol{\epsilon}\mathscr{E}_0\left(\beta\,e^{i(\mathbf{k}\cdot\mathbf{r}-\omega t)} + \beta^* e^{i(\mathbf{k}\cdot\mathbf{r}+\omega t)}\right),$$

which resembles that of a classical field (see Equation (D.1)); although the variance is a non-zero value given by that of the vacuum field.

A coherent state then presents an amplitude given by $|\beta|\mathscr{E}_0$ and fluctuations on the order of $\mathscr{E}_0$. This is why they are also called *quasi-classical states*, as for high values of $|\beta|$ the relative amplitude of the fluctuations become negligible ($\mathscr{E}_0 \ll |\beta|$) and the state can be reasonably approximated by a

classical field with the same average amplitude. As it turns out, quasi-classical states are commonly found in the laboratory, as they describe the state produced by a laser. This knowledge, along with the approximation mentioned above will be used in the coming sections whenever we introduce a laser field in our Hamiltonian.

D.2 A Single Excitation in the Open Atom–Cavity System

Excited Atom in a Cavity

Let us assume an interacting, open atom–cavity system with maximum one excitation as we introduced in Section 4.1.2. We will focus on the two-level system represented by the doublet $|\pm_1\rangle$, which can be described heuristically by the non-Hermitian Hamiltonian:

$$\hat{H}_{\text{diss}} = \hat{H}_{\text{JC}} - i\hbar\hat{\Gamma}. \tag{D.6}$$

The damping component of the Hamiltonian is given by

$$\hat{\Gamma} = \gamma\hat{\sigma}^\dagger\hat{\sigma} + \kappa\hat{a}^\dagger\hat{a},$$

which can be interpreted as the quantum equivalent of introducing losses in a system by adding an imaginary term to the energy.

The matrix form of the Hamiltonian in the uncoupled basis given by $(1, 0)^{\text{T}} = |e, 0\rangle$ and $(0, 1)^{\text{T}} = |g, 1\rangle$ reads

$$\hat{H}_{\text{diss}} = \begin{bmatrix} \omega_{\text{a}} - i\gamma & -g \\ -g & \omega_{\text{c}} - i\kappa \end{bmatrix}.$$

The eigenvalues $\tilde{\omega}_\pm$ can be obtained by diagonalizing the matrix, i.e. : solving the quadratic equation $|\det(\hat{H}_{\text{diss}} - \mathbb{1}\tilde{\omega})| = 0$ which reads:

$$\tilde{\omega}^2 - \tilde{\omega}(\omega_{\text{c}} + \omega_{\text{a}} - i(\kappa + \gamma)) + (\omega_{\text{a}} - i\gamma)(\omega_{\text{c}} - i\kappa) - g^2 = 0$$

the solution of which is

$$\tilde{\omega}_\pm = \omega_a + \frac{\Delta_c - i(\kappa + \gamma)}{2} \pm \sqrt{g^2 + \left(\frac{\Delta_c - i(\kappa - \gamma)}{2}\right)^2}.$$

A generic state can be expressed in the uncoupled basis by $\Psi(t) = (c_{\text{e}}(t), c_{\text{g}}(t))$, where the components $c_j(t)$ represent the complex amplitudes of the atomic and photonic populations, i.e. :

$$c_{\text{e}}(t) = \langle e, 0| \Psi(t) |e, 0\rangle$$
$$c_{\text{g}}(t) = \langle g, 1| \Psi(t) |g, 1\rangle.$$

The time evolution of each component $c_j(t)$ will be given by its coordinates in the new basis (A_j, B_j), each of them evolving with the corresponding eigenvalue, i.e.

$$c_j(t) = A_j e^{-i\tilde{\omega}_+ t} + B_j e^{-i\tilde{\omega}_- t}, \text{ with } j = \{g, e\}. \tag{D.7}$$

Let us assume that the system starts originally in the state $|e, 0\rangle$. The initial conditions of the system can be obtain via Schrödinger equation applied to the Hamiltonian in Equation (D.6). In this case we

get $\Psi(0) = (1, 0)$ and $\dot{\Psi}(0) = (-\gamma, -i\,g)$; which along with (D.7) yields the solution[2] of the amplitude coefficients for both atom and cavity excitations

$$
\begin{aligned}
c_{\mathrm{e}}(t) &= e^{-i\tilde{\omega}_- t} + \frac{\gamma - i\tilde{\omega}_-}{i(\tilde{\omega}_+ - \tilde{\omega}_-)}\left(e^{-i\tilde{\omega}_+ t} - e^{-i\tilde{\omega}_- t}\right) \\
c_{\mathrm{g}}(t) &= \frac{g}{\tilde{\omega}_+ - \tilde{\omega}_-}\left(e^{-i\tilde{\omega}_+ t} - e^{-i\tilde{\omega}_- t}\right).
\end{aligned}
\tag{D.8}
$$

From these amplitudes we can extract the corresponding excited atom and cavity populations ($\rho_{\mathrm{a}} = |c_{\mathrm{e}}(t)|^2$ and $\rho_{\mathrm{c}} = |c_{\mathrm{g}}(t)|^2$) or the occupation of the ground state ($\rho_{00} = 1 - \rho_{\mathrm{a}} - \rho_{\mathrm{c}}$). Since there is no external driving, the steady state will of course correspond to $\rho_{00} = 1$; nonetheless equations (D.8) provide us with the full transient solution. Pertinent approximations are used in the main text in Section 4.1.2, and can also be found in the literature (see e.g. [17]).

Externally Driven Cavity

The two-level system abstraction used so far is not valid anymore if we decide to drive the system with a weak laser, since we require then to include the external driving effect that pumps the system from the ground state back into the dressed doublet. We need therefore to expand our system of interest to the lowest triplet formed by $|g, 0\rangle$ and $|\pm_1\rangle$. As we mentioned in Section D.1, a laser field can be described as a coherent state with certain phase and amplitude given by a complex number (in this case ε). Furthermore, for high intensities, the effect of the corresponding creation and annihilation operators can be substituted by the mean value of the field's amplitude (via the semi-classical approximation), such that $\hat{a}, \hat{a}^\dagger \to \varepsilon, \varepsilon^*$. By choosing a convenient phase we can moreover consider $\varepsilon = \varepsilon^*$.

Therefore, if we pump into the cavity a coherent field of amplitude ε, the dissipative Hamiltonian of Equation (D.6), expressed in the frame rotating at the frequency of the probe laser ω_{p}, transforms into

$$
\hat{H}_\varepsilon = \hat{H}_{\mathrm{JC}} - i\hbar(\gamma\hat{\sigma}^\dagger\hat{\sigma} + \kappa\hat{a}^\dagger\hat{a}) + \varepsilon(\hat{a}^\dagger + \hat{a}).
$$

If we include the ground state, our generic state $\Psi(t)$ is now:

$$
|\Psi(t)\rangle = c_{\mathrm{e}}(t)|e, 0\rangle + c_{\mathrm{g}}(t)|g, 1\rangle + c_0(t)|g, 0\rangle,
$$

and applying once more Schrödinger's equation we obtain the coupled differential equations for both complex amplitudes of interest:

$$
\begin{aligned}
\dot{c}_{\mathrm{e}} &= -(\gamma + i\Delta_{\mathrm{a}})c_{\mathrm{e}} + igc_{\mathrm{g}} \\
\dot{c}_{\mathrm{g}} &= -(\kappa + i\Delta_{\mathrm{c}})c_{\mathrm{g}} + igc_{\mathrm{e}} + i\varepsilon,
\end{aligned}
\tag{D.9}
$$

where we have introduced the cavity and atomic detunings with respect to the probe laser $\Delta_{\mathrm{c,a}} = \omega_{\mathrm{c,a}} - \omega_{\mathrm{p}}$.

A simple full analytical solution is not available. Yet, unlike the previous case, the driven system reaches a steady state which is non-trivial and contains relevant information. Thus, by assuming $\dot{c}_{\mathrm{e}} = \dot{c}_{\mathrm{g}} = 0$ we find

$$
\begin{aligned}
c_{\mathrm{e,s}} &= \frac{ig\varepsilon}{(\kappa + i\Delta_{\mathrm{c}})(\gamma + i\Delta_{\mathrm{a}}) + g^2} \\
c_{\mathrm{g,s}} &= \frac{\varepsilon}{(\kappa + i\Delta_{\mathrm{c}}) + g^2/(\gamma + i\Delta_{\mathrm{a}})},
\end{aligned}
$$

---

[2] We assume $\tilde{\omega}_+ \neq \tilde{\omega}_-$; this is true except for the particular case where $g = (\kappa - \gamma)/2$.

We first focus on $\rho_c = |c_{g,s}|^2$ since the cavity field is more accessible to interrogation. For a cavity with no atom, the number of photons is $n_{empty} = \varepsilon^2/(\kappa^2 + \Delta_c^2)$ and the intracavity field is represented by a Lorentzian of width κ as shown in Section 4.2.1.

When placing an atom though, one gets

$$n_{coupled} = \frac{n_{empty}}{\left|1 + 2\tilde{C}\right|^2}$$

where we make use of the *complex cooperativity* introduced in the main text and given by

$$\tilde{C} = \frac{g^2}{2(\kappa + i\Delta_c)(\gamma + i\Delta_a)} \; .$$

On resonance and in the presence of an atom, the intracavity power will then be reduced by a factor of $(1 + 2C_1)^2$ and therefore drastically affect the reflection and transmission properties of the driving field (as we mention in the motivation of Section 5). As we scan the probe frequency (with $\Delta_c = \Delta_a$), a double peaked feature substitutes the original Lorentzian curve, representing the energy bands of the coupled system; i.e. , the coupling makes it possible to address both photonic and atomic excitations by only pumping the cavity.

So far we talked about the intracavity photon number, nevertheless the real accessible parameter is, in our case, the reflection of the pumping field from the input cavity mirror. If we assume an input rate of photons R_{in} on a cavity with perfect mode matching and symmetric mirrors, the uncoupled cavity on resonance will host a field of amplitude $\varepsilon = \sqrt{R_{in}\kappa/2}$ (as we saw in the discussion of Section 4.2.1). The reflected photon rate in this simple-cavity model is given by

$$R_{ref} = \left| -\sqrt{R_{in}} + \sqrt{\kappa}c_{g,s} \right|^2 \; .$$

Both theoretical and experimental results regarding the reflected power of the driven cavity can be seen in the main text, including a more complete model of the cavity line shape.

Regarding the atomic population, we can use the expression of $c_{e,s}$ to obtain the rate of spontaneous emission of the atom in free space, given by $2\gamma\rho_a$. In the simple case of a resonant system ($\Delta_c = \Delta_a = 0$), and for strong coupling regime ($C_1 \gg 1$) one gets

$$2\gamma\rho_a \simeq 2\gamma\frac{\varepsilon^2}{g^2} = \frac{\varepsilon^2}{\kappa C_1} = \frac{R_{in}}{2C_1} \; .$$

Therefore the atom scatters only a fraction $1/2C_1$ of the incoming probing power, which is what makes the coupled cavity a useful, non-intrusive probe of the atomic state.

Externally Driven Atom

One can use an equivalent formalism to depict the evolution of the system when the external driving is applied to the atom instead of the cavity field. Applying our simple model for light–matter interaction depicted already in Equation (4.3) and choosing a convenient driving phase, the Hamiltonian of the system becomes

$$\hat{H}_\varepsilon = \hat{H}_{JC} - i\hbar(\gamma\hat{\sigma}^\dagger\hat{\sigma} + \kappa\hat{a}^\dagger\hat{a}) + \frac{\Omega}{2}(\hat{\sigma}^\dagger + \hat{\sigma}),$$

where Ω is the Rabi frequency corresponding to the atom-field interaction. The application of Schrödinger's equation leads to a system of equations similar to that of (D.9)

$$\dot{c}_e = -(\gamma + i\Delta_a)c_e + igc_g + i\Omega/2$$
$$\dot{c}_g = -(\kappa + i\Delta_c)c_g + igc_e\,,$$

and the corresponding steady state solution for the populations

$$\rho_a = \frac{(\Omega/2)^2}{\left|(\gamma + i\Delta_a) + g^2/(\kappa + i\Delta_c)\right|^2}$$
$$\rho_c = \frac{g^2\,(\Omega/2)^2}{\left|(\gamma + i\Delta_a)(\kappa + i\Delta_c) + g^2\right|^2}\,.$$

By re-writing them as a function of the complex cooperativity and including the decay rates, one obtains the expressions presented in Equations (6.1) for the scattering rate in free space ($R_{\text{f-s}} = 2\gamma\rho_a$) and outside the cavity ($R_c = 2\kappa\rho_c$).

D.3 The Master Equation

In this section we discuss the details of the model used to describe the master equation of our system. As mentioned in the main text, this formalism contains all the dynamics of the open atom–cavity system. Nevertheless the complexity of the equation usually requires a numerical treatment and some additional approximations. In the following we discuss the main considerations and processes included in our model; the implementation is then performed using the Quantum Optics toolbox for Matlab [135, 136]. The approach shown here is an adaptation of that developed in ref. [137], which discusses in detail the case for a cesium atom coupled to a birefringent high-finesse cavity.

The basic Jaynes-Cumming Hamiltonian shown in Section 4.1.1 assumes a two-level atom coupled to a single mode of a resonator. The two-level system approximation is good enough when optical pumping to the cycling transition is present. As we discuss in Section 4.2.2, that is the case when we drive the cavity with circularly polarized light. Nonetheless, when such pumping is not possible, the atomic hyperfine substructure has to be taken into account to obtain a full description of the phenomena and the effect of different polarizations of the light fields (as it is the case in Section 6).

With that in mind, we expand the Hamiltonian of Equation (4.4) by including the hyperfine states of the D_2 line ($F = 1, 2$ and $F' = 1, 2, 3$) and their corresponding Zeeman sub-levels. This is done by substituting the dipole operator $\hat{d}$ of the two levels by a more complete dipole transition operator $\hat{D}_p(F, F')$ which describes the strength of the transitions between F and F' coupled through a light field of polarization $p = (-1, 0, 1) \equiv (\sigma_-, \pi, \sigma_+)$ [137]. This new operator is, in our case, given by

$$\hat{D}_p(F, F') = \sum_{m_F=-F}^{F} |F, m_F\rangle \langle F, m_F| \hat{d}_p |F', m_{F'} + p\rangle \langle F', m_{F'} + p|$$

where $\hat{d}_p$ is the dipole operator for the polarization p, normalized to that of the cycling transition.

If the cavity is near-resonant with the cycling transition it is safe to assume that it only couples to those starting from $F = 2$ (which is reasonable, as $g \ll \Delta_{\text{HFS}} = 6.83\,\text{GHz}$). After applying the rotating wave approximation, the Hamiltonian becomes:

$$\hat{H} = \omega_{\mathrm{c}}\hat{a}^{\dagger}\hat{a} + \sum_{F'=1}^{3}\sum_{m_{F'}}\omega_{F',m_{F'}}\,|F',m_{F'}\rangle\langle F',m_{F'}|$$

$$+g\sum_{F'=1}^{3}\hat{a}^{\dagger}\hat{D}_{p,a}(2,F') + \hat{D}_{p,a}^{\dagger}(2,F')\,\hat{a}\,,$$

where $\omega_{F',m_{F'}}$ is the frequency of the transition $F=2 \to F', m_{F'}$ and the subindex p,a stands for the polarization of the cavity mode represented by the operator $\hat{a}$.

In general, Fabry–Pérot resonators can host two modes with orthogonal polarizations if the cavity does not feature any polarization-mode splitting (as it is in our system). Therefore, the interaction of the atom with a single mode must be expanded to take into account both polarizations represented by the operators $\hat{a}$ and $\hat{b}$. This yields the final version of the Hamiltonian of the open atom–cavity system with no external drivings:

$$\hat{H}_{0} = \omega_{\mathrm{c}}(\hat{a}^{\dagger}\hat{a} + \hat{b}^{\dagger}\hat{b}) + \sum_{F'=1}^{3}\sum_{m_{F'}}\omega_{F',m_{F'}}\,|F',m_{F'}\rangle\langle F',m_{F'}|$$

$$+g\sum_{F'=1}^{3}\hat{a}^{\dagger}\hat{D}_{p,a}(2,F') + \hat{D}_{p,a}^{\dagger}(2,F')\,\hat{a}$$

$$+g\sum_{F'=1}^{3}\hat{b}^{\dagger}\hat{D}_{p,b}(2,F') + \hat{D}_{p,b}^{\dagger}(2,F')\,\hat{b}\,,$$

where $p,b \perp p,a$ and we have assumed that both modes are degenerate with frequency ω_{c}.

As we mentioned, the most accessible information provided by the master equation is obtained through the steady state solution ($\hat{\mathcal{L}}\hat{\rho}_{\mathrm{s}} = 0$). In this particular case, with no external driving whatsoever, such a solution is trivial and leads to a completely relaxed system with no excitations. We therefore move on to the more practical scenario where an external driving is applied.

We discussed already in the previous section how to introduce both cavity and atom external drivings. This was done by means of coherent states ε and $\Omega_{\mathrm{p}}/2$ that pump the intracavity field or drive Rabi oscillations on the atom respectively. We must add the same terms we used before, adapted to the new extended scenario. We will assume that the external atomic driving is done around the cycling transition and that we additionally shine a repumper field Ω_{r} resonant to the $F=1 \to F'=1$ transition to address the dark state of the atom. Considering all that, the expression for a generic Hamiltonian containing all possible external drivings is the following

$$\hat{H}_{\mathrm{ext}} = \hat{H}_{0} + \varepsilon_{a}(\hat{a}^{\dagger} + \hat{a}) + \varepsilon_{b}(\hat{b}^{\dagger} + \hat{b})$$

$$+\Omega_{\mathrm{p}}/2\sum_{F'=1}^{3}\hat{D}_{p,\mathrm{p}}(2,F') + \hat{D}_{p,\mathrm{p}}^{\dagger}(2,F')$$

$$+\Omega_{\mathrm{r}}/2\sum_{F'=1}^{3}\hat{D}_{p,\mathrm{r}}(1,F') + \hat{D}_{p,\mathrm{r}}^{\dagger}(1,F')\,.$$

The particular polarization of the cavity modes and the external fields can be π, σ or a combination of both, and it will depend on the quantization axis that we choose. In the presence of an external bias magnetic field, it is usually convenient to define the axis to be parallel to the field to avoid precession of m_F populations. Therefore, depending on the particular experimental setup, the final expression of the
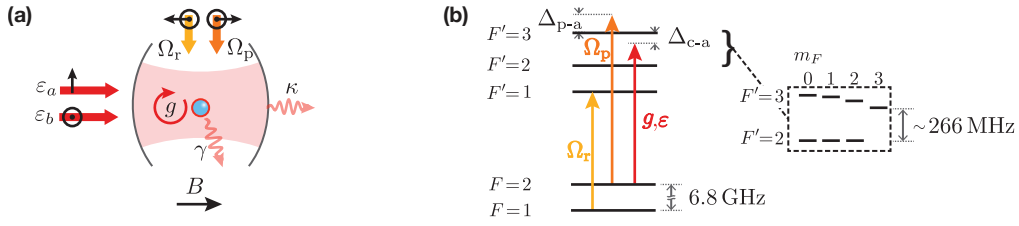
Figure D.1: Considerations for the master equation model. **(a)** Configuration of the possible external driving fields. The cavity can be pumped with one or both of the polarization modes by a coherent field of amplitude $\varepsilon_{a,b}$. The atom's external driving is a combination of both the probe Ω_p and repumper Ω_r lasers, which are usually linearly polarized. The external magnetic field can be applied in any direction, here we show the typical configuration parallel to the cavity axis. **(b)** Relevant energy-levels of the D_2 line. The fine levels show the transitions addressed by each of the three fields. Both cavity and probe resonances can be scanned over the cycling transition ω_a ($\Delta_{p,c} = \omega_{p,c} - \omega_a$). The inset shows the relative effect of the AC Stark shift induced by a π-polarized dipole trap (more quantitative details can be found in ref. [84]).

operators will vary.

In Figure D.1(a) we show an schematic of the main parameters and configuration of the system as well as the optical access typically used for the external driving. Additionally, in Figure D.1(b) one can see the relevant hyperfine levels of the atom along with the addressing of each field. We have also include the effect of the AC Stark shift on all the Zeeman sublevels; although this is not shown in the expression of $\hat{H}_{\text{ext}}$, one can easily implement it by modifying the resonant frequencies $\omega_{F',m_{F'}}$ according to their particular shift.

The final expression of the master equation will be that shown in Equation (4.8) substituting the collapse operator $\hat{C}$ by $\sum_{p,q} \hat{C}_{p,q}$ [137] where

$$\hat{C}_{p,q} = \sqrt{2\gamma} \sum_{F,F'} \hat{D}_p(F,F') + \sqrt{2\kappa}\,\hat{a}_q\,,$$

being $p = (-1, 0, 1)$ and $\hat{a}_q = (\hat{a}, \hat{b})$.

From the steady-state solution characterized by $\dot{\rho}_s = 0$, one can obtain the expectation value of any operator $\hat{O}$ in the steady-state given that $\langle \hat{O} \rangle = \text{Tr}(\hat{\rho}_s \hat{O})$. This allows us to extract valuable information like the intracavity photon number ($\langle \hat{a}^\dagger \hat{a} \rangle$) and the population of a given atomic level F' ($\langle \sum_p \hat{D}_p^\dagger(F,F')\hat{D}_p(F,F') \rangle$) or any of its Zeeman sublevels. In turn, such populations provide information about the output rate of the cavity field and the free-space scattering rate of the atom. The list continues with other physical quantities such as the properties of the scattered light, correlation functions of the cavity output, etc.

D.4 Cavity-reduced Absorption Cross Section

Considering the measurements presented in Section 6.3, one could think of exploiting the enhancement of the total scattering rate (which can be on the order of 20 in our case) to perform some kind of cavity-enhanced absorption imaging of the coupled atom. Although it is true that the cavity back-action can in general enhance the number of scattered photons for a given illumination, this only occurs when the light is detuned from the atomic resonance. As we saw in Figures 6.4(a), for a system on resonance the total scattering is much smaller than the one in the absence of the cavity (which we called R_{max}). In

fact, the total scattering rate of a coupled atom for any illumination and cavity detunings is never higher than R_{max}; this statement applies to every coupling regime. It might seem unintuitive at a first glance, as one would expect that the Purcell enhancement of the natural decay rate Γ automatically increases the absorption cross section of the atom σ_0. Nevertheless, it can be shown that σ_0 in fact gets reduced in the presence of the cavity, by an amount which is precisely the Purcell factor.

In general, for an absorber illuminated by a field of intensity I_{in}, the absorption cross section is defined as the ratio between the scattered power and the input intensity $P_{\mathrm{sc}}/I_{\mathrm{in}}$. It has units of m^2, as it represents the effective area the scatterer would have if it absorbed every photon arriving to the region. For a two-level atom illuminated by resonant light with frequency ω, the scattered power P_{sc} can be obtained from Equation (6.2) such that $\sigma_0 = \hbar\omega\Gamma/2I_{\mathrm{sat}}$. The saturation intensity depends on the atomic properties, and in particular $I_{\mathrm{sat}} \propto \Gamma^2/\mu^2$ where μ is the dipole matrix element of the particular transition (also known as the transition strength). This leads to the more specific expression

$$\sigma_0 = \frac{\omega\mu^2}{c\epsilon_0\hbar\Gamma},$$

where ϵ_0 is the electric permittivity and c the speed of light, both in vacuum.

For the case of an atom placed in free space, the decay rate is calculated using Weisskopf-Wigner's theorem (see e.g. [231]), and one obtains

$$\Gamma = \frac{\omega^3\mu^2}{3\pi\epsilon_0\hbar c^3}. \tag{D.10}$$

The spontaneous emission rate increases with the transition strength, since the latter represents the interaction between the atom and the vacuum modes. This implies the well known fact that the resonant absorption cross section of a two-level system does not depend on the transition properties, and is in fact given by $\sigma_0 = 3\lambda^2/2\pi$.

Let us assume that the atom is now weakly coupled to a cavity such that no dressed-states splitting occurs. In this scenario we saw that the cavity modifies the density of states of the surrounding vacuum such that the excited state decay rate is enhanced by the factor $1+2C_1$. Nevertheless, the matrix element μ of the interaction between the atom and a photon coming from free-space remains unchanged since the cavity only alters the electromagnetic vacuum and not the atomic structure. As a consequence, the resonant absorption cross section is modified and now includes the extra factor $\sigma' = \sigma_0/(1 + f_P)$. In classical terms, the external damping of the oscillating atomic dipole is enhanced while the spring constant is kept the same; this leads to broader line shapes with less response at the line center. This effect is similar to those situations where non-radiative processes increase the total decay rate, like is the case in collisional broadening.

Results from the master equation show that this Purcell-reduction of the cross section is present for every coupling regime, including those where the dressed-state picture takes place. Interestingly enough, this also implies that in the regime of Purcell inhibition, where the cavity is off-resonant with the atom and occupies a considerable solid angle of its emission [232], the absorption cross section can be arbitrarily big. This would turn a single atom into a perfect absorber[3].

---

[3] In those scenarios, though, the optical access to the intracavity region is severely reduced as the mirrors separation must reach wavelength scales. Furthermore, the close-to-unity absorption would only happen for low powers, as the saturation intensity would get enhanced by the resonator.

Acknowledgements

This work is the culmination of one of the most intense and precious experiences that I had so far. The long way that brought me here was sometimes hard, but not as challenging as compressing all my gratitude in just these few paragraphs.

First of all, I would like to thank Prof. Dr. Dieter Meschede for giving me the opportunity to take part in such an exciting field and guiding and motivating me through the process, but most importantly, for welcoming me in such a fantastic, dynamic and diverse group that he gathered. I am also grateful to Prof. Dr. Michael Köhl for his support in being my second thesis advisor, and the fruitful interchange of ideas with his group members.

My special thanks go to Dr. Lothar Ratschbacher, for the constant motivation and strong driving. I never met someone so passionate and with such ability to keep the big picture in mind. I am grateful that I had the opportunity to share so many hours with him in the lab (especially those with explosions and vacuum snow falls involved). I would also like to thank Dr. Wolfgang Alt for sharing his incredible technical knowledge (and his chocolates) with us and for being able to solve week-long problems with just a few intuitive arguments.

I am forever grateful to The Office members, I never thought I would feel like home being so far from Spain. To Carsten, meine kleine, for coming to my help during the "2π-incident" or when I needed the RGB code of the color *red*. To Stefan, mein deutscher Vater, with whom I shared the love for beer, *little May* and Thorlabs catalogues. To Tobi StatafulaiMacha, my Morty and humor-doppelganger, I never needed to tell the jokes out loud because he already knew what I was thinking about. To Gautam and Sajid, my Edeka companions, despite the continuous unending disputes, every single conversation was genuinely interesting. To El Maxo, my writing pal, for sharing with me some "crazy" weekends and literally hundreds of cat GIFs. I thank the rest group members (Eduardo, Manolo, Deepak...) for all the help and good times. I am indebted to everyone involved in proofreading this thesis, and I wish the best of luck to the new FCQED crew: Deepak, Tobi, Eduardo and Elvira. I am confident that the lab is in good hands and that exciting times are coming.

I am grateful to the rest of the group for all the help and support that they provided, particularly Annelise Miglo, Fien Latumahina and Dietmar Haubrich, and the staff members of the mechanical and electronic workshops.

Estoy en deuda con Miguel — el hermano mayor que nunca tuve (ni quise) — por aguantar mis continuos fastidios incluso en los peores de sus días, y por demostrarme que hay versiones del castellano más feas que el murciano. Ha sido un placer compartir tantas horas con él y con Miriam. A la Manada de Murcia y Madrid no les agradezco nada en absoluto, su única contribución durante estos años han sido las depresiones de dos semanas que me daban después de cada visita. Os odio; excepto a Ricardo, que hizo el viaje de penitencia y sufrió a mi lado, sin faltar a la milenaria tradición del carajillo de los sábados.

No tengo palabras para expresar mi gratitud hacia Lucie, que ha estado a mi lado en cada momento, apoyándome y dándome energías cuando más lo necesitaba. Atesoro cada beso, lágrima y locura que hemos compartido, y espero de corazón vivir miles de pequeñas y grandes aventuras a su lado.

Este camino no habría sido el mismo sin el constante apoyo de mi familia. Por eso, éstas últimas

palabras las dedico a los pilares de mi juventud, que me dieron la vida y me vieron crecer ante sus ojos: mis padres, cuya historia es la que merece ser plasmada en papel. Siempre os agradeceré vuestro amor incondicional, y vuestra eterna lucha y sacrificio por darnos — a mí y a mis hermanas — la oportunidad de elegir nuestro propio camino. Nuestros logros son vuestros logros, y por eso os dedico con humildad mi pequeña contribución.